DEPARTAMENT OF
MATERIALS SCIENCE

SERS-BASED BIOSENSOR FOR ON-SITE DETERMINATION OF PANCREATIC CANCER BIOMARKERS

YUSELIS CASTAÑO GUERRERO

Master in Biochemistry

DOCTORATE IN NANOTECHNOLOGIES AND NANOSCIENCE

NOVA University Lisbon

April, 2024

DEPARTAMENT OF
MATERIALS SCIENCE

SERS-BASED BIOSENSOR FOR ON-SITE DETERMINATION OF PANCREATIC CANCER BIOMARKERS

YUSELIS CASTAÑO GUERRERO

Master in Biochemistry

Adviser:	Maria Goreti Ferreira Sales *Full Professor,* University of Coimbra
Co-advisers:	Hugo Manuel Brito Águas *Associate Professor*, NOVA University Lisbon

Examination Committee:

Chair:	Pedro Miguel Ribeiro Viana Baptista *Full Professor*, NOVA University Lisbon
Rapporteurs:	Tito da Silva Trindade, *Full Professor*, University of Aveiro Rúben Miguel Pereira Fernandes, *Full Professor*, Fernando Pessoa University
Adviser:	Maria Goreti Ferreira Sales, *Full Professor*, University of Coimbra
Members:	Maria João Dantas Ramalhosa Ferreira, *Adjunct professor*, Polytechnic of Porto - School of Engineering Manuela Maria Teixeira Basto de Faria Frasco, *Guest Research Assistant*, University of Coimbra Pedro Miguel Cândido Barquinha, *Associate Professor*, NOVA University Lisbon Pedro Miguel Ribeiro Viana Baptista *Full Professor*, NOVA University Lisbon

DOCTORATE / MASTER IN NANOTECHNOLOGIES AND NANOSCIENCE

NOVA University Lisbon
April, 2024

SERS-based biosensor for on-site determination of Pancreatic cancer biomarkers

Copyright © Yuselis Castaño Guerrero, NOVA School of Science and Technology, NOVA University Lisbon.

The NOVA School of Science and Technology and the NOVA University Lisbon have the right, perpetual and without geographical boundaries, to file and publish this dissertation through printed copies reproduced on paper or on digital form, or by any other means known or that may be invented, and to disseminate through scientific repositories and admit its copying and distribution for non-commercial, educational or research purposes, as long as credit is given to the author and editor.

ACKNOWLEDGMENTS

Writing a few words of gratitude is always a moment of reflection and a new starting point in our lives. It marks the end of one stage of my life and at the same time the beginning of another, which I look forward to with great anticipation. This stage leaves me with an enormous sense of satisfaction on a professional and personal level that cannot be expressed in a few words. Many people were involved in this professional work and I would like to thank them.

First and foremost, I would like to thank my supervisor Prof. Maria Goreti Ferreira Sales for giving me the opportunity to be part of Biomark and to continue my academic career with the development of this work. I also thank Felismina Moreira for encouraging me to continue with the research and giving me the opportunity to learn from her knowledge. My co-supervisor Hugo Aguas for accepting me under special circumstances.

I would also like to thank my lab colleagues who have accompanied me during these challenging years, especially Gabi for the calmness that characterizes her and that has helped me to see the good side in every experimental result. Aninhas, who infected everyone with his passion for research. Mariana, for the laughter that refreshes the soul and for allowing me to be a small part of Beca. Sara, for all the days together and the clarity in your ideas. Daniela, for becoming that special little person who occupies a part of my heart.

Thank you to my friends who have supported me in my life without often understanding that they were an essential part of making this time complete. Especially to my dear friend Daniela Almeida, who, without knowing me, opened the doors of her life to me and let me in. She became a wonderful treasure that Portugal gave me for my life.

I thank family, especially my husband Robert, for the good days and the not so good days, and for always being willing to share with me and help me dream of a better future. My daughters Carolina and

Camila, who have taught me to be happy. My mother, my father, my grandmothers, my brother, my cousin and my aunts, who make my life beautiful and have supported me throughout the years.

ABSTRACT

Pancreatic cancer is the most lethal cancer disease, as an outcome of its late diagnosis. Biomarkers in body fluids offer an alternative approach to earlier diagnosis, prognosis, and progress of cancer treatment. This includes circulating vesicles, miRNA, cell, and protein, which have been identified for the specific case of pancreatic cancer. Commonly, a specific clinical evaluation requires the analysis of more than one biomarker, meaning that it is important to define methods that are capable of providing a combined response for more than a single biomarker. In addition, it is also important that the analytical results are reliable and avoid false analytical results, which may be achieved by combining multiple transducers and biorecognition elements.

Thus, this work is developing a new generation of biosensors sensitive to pancreatic cancer biomarkers, using molecularly imprinted polymer and immunosensing-based strategies. The biorecognition of the biomarkers is established in two-stages, thereby ensuring high accuracy and sensitivity in the final device, making use of both electrochemical and surface-enhance Raman spectroscopy (SERS) readings. The first stage is electrochemical sensing, which captures the target compound, and the second stage includes SERS sensing, by a suitable Raman tag. Natural or plastic antibodies are combined herein, also involved in multi-analyte detection.

Keywords: biosensors, electrochemical detection, Raman spectroscopy, SERS, MIPs, immunosensor, reporters, pancreatic cancer.

RESUMO

O cancro de pâncreas é a doença oncológica de elevada letalidade, tipicamente em resultado do seu diagnóstico tardio. A análise de biomarcadores em fluidos corporais podem oferecer uma abordagem alternativa para um diagnóstico precoce, prognóstico e acompanhamento do tratamento deste tipo de cancro. Incluem-se aqui vesículas circulantes, miRNA, células e proteínas, que foram identificadas para o caso específico do cancro de pâncreas. Normalmente, uma avaliação clínica específica requer a análise de mais do que um biomarcador, o que significa que é importante definir métodos que sejam capazes de fornecer uma resposta mais alargada. Além disso, é também importante que os resultados analíticos sejam fiáveis, evitando-se a ocorrência de resultados analíticos falsos, o que pode ser conseguido através da combinação de múltiplos transdutores e elementos de bioreconhecimento.

Neste sentido, este trabalho descreve o desenvolvimento de uma nova geração de biossensores sensíveis a biomarcadores do cancro pancreático, utilizando polímeros molecularmente impressos e estratégias baseadas em imunossensores. O bioreconhecimento dos biomarcadores é estabelecido em duas etapas, garantindo alta precisão e sensibilidade no dispositivo final, fazendo uso de leituras eletroquímicas e de espectroscopia Raman (do inglês, *surface-enhanced Raman spectroscopy,* SERS). O primeiro estágio diz respeito à deteção eletroquímica, que captura o composto alvo, e o segundo estágio inclui a deteção por SERS, por meio de uma molécula sinalizadora de Raman adequada. Neste trabalho combinam-se anticorpos naturais ou plásticos, também envolvidos na deteção de múltiplos analitos.

Palavras-chaves: biossensores, detecção eletroquímica, espectroscopia de Raman, SERS, MIPs, imunossensor, reporters, cancro do pâncreas.

TABLE OF CONTENTS

LIST OF FIGURES

LIST OF TABLES

ACRONYMS

AFM	Atomic force microscopy.
AgNCs	Silver nanocapsules.
AgNPs	Silver nanoparticles.
3AP	3-aminophenol.
4-ATP	4-aminothiophenol.
AuNSs	Gold nanostars.
AuNPs	Gold nanoparticles.
Au-SPEs	Gold screen-printed electrodes.
CA 19-9	Carbohydrate Antigen 19-9.
CBB	Coomassie brilliant blue.
CE	Counter electrode.
CEA	Carcinoembryonic Antigen.
CMEs	Chemically modified electrodes.
CNS	Central nervous system.
CPE	Carbon paste electrode.
C-SPEs	Carbon screen-printed electrodes.
CV	Cyclic voltammetry.
Cys	Cysteamine hydrochloride.
DNA	Deoxyribonucleic acid.
DPV	Differential pulse voltammetry.
EIS	Electrochemical impedance spectroscopy.

ELISA	Enzyme-linked immunosorbent assay.
EXOs	Exosomes.
FBS	Foetal bovine serum.
FDA	Food and drug administration.
FIR	Far infrared.
FTIR	Fourier Transformed Infrared Spectroscopy.
GSH	Glutathione.
GPC1	Glypican-1.
L1CAM	L1 cell adhesion molecule.
LLLR	Lower limit of linear range.
MBA	4-mercaptobenzoic acid.
MBN	4-mercaptobenzonitrile.
MES	2-(*N*-morpholino)ethanosulfonic acid.
MIPs	Molecularly imprinted polymer.
MMP7	Metalloproteinase 7.
MIR	Mid-infrared.
MUC4	Mucin 4.
MWCNTs	Multiwall carbon nanotubes.
NADH	Nicotinamide adenine dinucleotide.
NHS	*N*-hydroxysuccinimide.
NIP	Non-imprinted polymer.
NIR	Near-infrared.
NPs	Nanoparticles.
PAH	Poly(allylamine hydrochloride).
PBS	Phosphate buffered saline.
PDDA	Poly(diallyldimethylammonium chloride).
PC	Pancreatic cancer.
PhB	Phosphate buffer
PS	Polystyrene.

PTH	Polythionine.
PVP	Polyvinylpyrrolidone.
RE	Reference electrode.
RIA	Radioimmunoassay.
RNA	Ribonucleic acid
RT-PCR	Reverse transcription polymerase chain reaction.
SEM	Scanning electron microscopy.
SERS	Surface enhanced Raman spectroscopy.
SPEs	Screen-printed electrodes.
SPR	Surface plasmon resonance.
SR	Scan rate.
SWV	Square wave voltammetry.
TEM	Transmission electron microscopy.
TH	Thionine.
Tspan8	Tetraspanin 8.
UV	Ultraviolet.
VIS	Visible.
WE	Working electrode.

SYMBOLS

E_{pa}	Anodic peak potential.
E_{pc}	Cathodic peak potential.
δ	Scissoring
hv_0	Incident laser energy.
hv_{vib}	Vibrational energy.
Ω	Ohm.
ρ	Rocking.
R_{ct}	Charge-transfer resistance.
R_s	Resistance of the solution.
S_0	Ground electronic state.
S_1	Excited electronic state.
τ	Twisting.
υ	Stretching modes.
Δ**v**	Raman shift.

υ_{as}	Asymmetric stretching modes
υ_{s}	Symmetric stretching modes.
υ_{n}	Vibrational states.
υ_{vib}	Vibrational frequencies.
W	Warburg impedance.
ω	Wagging.
Z	Impedance.

Chapter 1. Motivation and aim of the thesis.

This chapter describes the motivation and the main goal of this work.

1.1 Motivation

With the increasing incidence of cancer, its prevention becomes a major public challenge. Currently, many of the existing cancers have a high chance of cure if they are diagnosed early and treated correctly [1]. However, this does apply to Pancreatic Cancer (PC), which remains the deadliest cancer. It is one of most aggressive neoplasms, spreading rapidly to neighbouring organs, due to late diagnosis and lack of specific symptoms [2].

Biomarkers circulating in blood, urine and saliva may turn out an alternative way to reach an earlier diagnosis, also contributing the prognosis and progress of cancer treatment. Screening specific markers offers the additional advantages of allowing a non-invasive and relatively inexpensive process to detect cancer. The biomolecules used as tumour markers include cell-free DNA, cell-free RNA, tumour proteins and, more recently, exosomes (EXOs) [3], [4].

Biomarkers for PC are categorized as diagnostic and prognostic, which provide information about the patient's overall cancer outcome, regardless the therapy. Moreover, there are predictive ones, providing information on the effect of a therapeutic intervention [5]. The ideal would be to be able to differentiate healthy subjects from patients with PC in the early stages, but this has been a challenge in the scientific community [5]. The classical cancer biomarkers (such as the Carbohydrate Antigen 19–9; CA 19–9 or the Carcinoembryonic Antigen; CEA) are unreliable for prognosis and detection of early-stage of PC. However, they are relevant to monitor the response of patients undergoing treatment [6], [7].

Potential exosomal markers for the early detection of PC include miRNA-155, miRNA-21 [8], [9], tetraspanin 8 (Tspan8) [10] and cell surface proteoglycan, glypican-1 (GPC1) [11]. The simultaneous detection of more than one of these biomarkers has been shown fundamental to provide valuable information in clinical context. Together with the unequivocal confirmation that these biomarkers are present in the sample, thereby avoiding false positive and negative data. Thus, a simple system combining the ability of screening more than one biomarker at the same time in an accurate way becomes fundamental.

The most common ways of targeting cancer cells in biosensors include antibodies. Antibodies contain specific regions that are able to interact with a given target with a considerable selectivity, especially if of monoclonal origin [12]. These natural compounds may also be replaced by biomimetic materials obtained by Molecularly Imprinted Polymer (MIPs) technology [13], [14], [15]. Compared to natural antibodies, these materials offer higher stability and lower cost, but lower selectivity of binding. The selection of the most suitable antibody-based approach depends on the intended targets. So far, there are many reports on the use of MIPs for a wide range of different molecules [16].

In terms of detection, Surface enhanced Raman spectroscopy (SERS) was established as a powerful technique for the discrimination, identification, and quantification of samples of biological origin, even allowing single molecule detection [17], [18]. It employs metal nanostructures to enhance the signal of suitable Raman reporters with fingerprint information, thereby enhancing the accuracy of the detection.

1.2 Objectives

The main goal is to develop a low-cost sensing-platform for screening protein biomarkers in PC. It uses (i) screen printed electrodes (SPEs), (ii) modified with biorecognition elements that capture the biomarkers, which is signalled after by (iii) specially designed Raman tags. This platform is expected to offer exceptional accuracy features, as there are two stages of biorecognition for the same analyte.
The specific goals are:
(a) Preparing suitable biosensing supports and Raman tags.
(b) Using suitable biorecognition elements.
(c) Enable suitable SERS detection for single and multiple analytes.

1.3 Thesis Outline

The thesis is organized into eight chapters.

CHAPTER 1. Described the motivation of this thesis and list the objectives of the work.

CHAPTER 2. address about the cancer disease and focusses on most relevant biomarkers for PC. One of the possible solutions to detect PC early are biosensors, so electrochemical and optical based in SERS, are potential tools to solve this problem. The introduction of nanomaterials improves the performance of sensors, and this part resumes the uses of nanometal structures in several applications.

CHAPTER 3. shows the ability of nanomaterials like gold nanostars (AuNSs) to produce a Raman signal. The gold screen-printed electrode (Au-SPEs) was a surface used to assembly the immunosensor. The dual detection was a system applied to recognize CEA, using electrochemical and SERS detection on the same spot. The Au-SPEs was modified with an antibody producing an electrochemical signal. The following stages, on the same surface, consisted in binding a second antibody linked to AuNSs with a suitable Raman reporter to generate a relevant enhancement of the Raman signal.

In **CHAPTER 4.** the use of polythionine (PTH) as an electroactive compound is considered to be employed in the construction of an electrochemical biosensor. PTH is further explored as an electrochemical probe in a biosensor to detect CA 19-9 on two different substrates, carbon and gold, using differential pulse voltammetry (DPV) as a reading technique in phosphate buffer (PhB) solution. The biosensor was assembled using the MIPs technology. The Raman spectra of PTH films on gold (substrates or AuNSs) and carbon (substrates) are also presented and discussed as a potential use for SERS reading as complementary information to electrochemical data.

With prior knowledge of the properties of PTH, in the **CHAPTER 5.** the MIPs was built on top of a carbon screen-printed electrode (C-SPEs) using Thionine (TH) as monomer. To detect L1, cell adhesion molecule (L1CAM) uses the combination of SERS with MIPs technologies is employed. The synthesis of the Ag nanocapsules (AgNCs) coated with porous silica starts by using a Au core as a seed and using polystyrene (PS) beads as a template. Then, these Au cores were covered with Ag, obtaining nanostructures with high plasmonic capacity. The plasmonic AgNCs were then modified with the Raman reporter, 4-mercaptobenzoic acid (MBA) and antibody for L1CAM, to recognize the selective sites in the MIPs by SERS.

Due to the high efficiency obtained in the detection of biological markers using MIPs with SERS, **CHAPTER 6.** explores a similar approach for another biomarker. The MIPs was built on the surface of C-SPEs using 3-aminophenol (3AP) as monomer. The novelty of this work consisted on the use of Coomassie brilliant blue (CBB) to protect the protein during the MIPs formation and give more stability and reproducibility to the sensor. Particularly, 4-mercaptobenzonitrile (MBN) was used as Raman tag to modify the AgNCs. The Raman peak of MBN is in the so-called "silent region" allow following the strong peak without interference from competing vibrations.

In **CHAPTER 7.** a multi-detection platform was built using the electropolymerization and previous knowledge. The MIPs for GPC1 and CA 19-9 were developed and used to capture on the same surface both biomarkers, to be detected by a differentiated SERS signal. The Raman reporters 4-ATP and MBN, were used to modify the surface of AgNCs. The SERS tags were marked with the specific antibodies to recognize the antigens captured in the MIPs on the biosensor.

Finally, **CHAPTER 8.** summarizes the most relevant aspects of the work and indicates probable future investigation routes.

1.4 List of publications

1.4.1 Chapter in books

- Martins, G.V.; **Castaño-Guerrero, Y.**; Santos.S.; Sales, M G. F., Molecularly imprinted electropolymerized carbon electrodes. Semiconducting Polymer Materials for Biosensing Applications. Woodhead Publishing Series in Electronic and Optical Materials (2024), 85-121. https://doi.org/10.1016/B978-0-323-95105-0.00004-8
- Martins, G.V.; Khan, M. Azizur R.; Piloto, A. M. L.; Guerreiro, J. R.L.; **Castaño-Guerrero, Y.**; Moreira, F. T.C.; Sales, M G. F., Chapter 8: Molecularly imprinted polymers in electrochemical sensing - A step closer to achieving technology readiness. Molecularly Imprinted Polymers (MIPs). Commercialization Prospects (2023), 143-215. doi: 10.1016/b978-0-323-91925-8.00017-x

1.4.2 Papers in international scientific journals

- **Castaño-Guerrero, Y**., Romanguera-Barcelay, Y., Moreira, F., Brito, W., R., Fortunato, E., Sales, M.G., Poly (Thionine)-Modified Screen-Printed Electrodes for CA 19-9 Detection and Its Properties in Raman Spectroscopy. Chemosensors (2022), 10 (3), 92. doi: 10.3390/CHEMOSENSORS10030092/S1
- Vaz, R., Serrano V.M., **Castaño-Guerrero, Y**., Cardoso, A.R., Frasco, M.F, Sales, M.G., Breaking the classics: Next-generation biosensors for the isolation, profiling and detection of extracellular vesicles. Biosensors and Bioelectronics: X, (2022),10, 200115. doi: 10.1016/J.BIOSX.2022.100115

- **Castaño-Guerrero, Y**., Moreira, F., Sousa-Castillo, A., Correa-Duarte, M., A., Sales, M.G., SERS and electrochemical impedance spectroscopy immunoassay for carcinoembryonic antigen. Electrochimica Acta (2021), 366, 137377. doi: 10.1016/J.ELECTACTA.2020.137377

1.4.3 Communications in national and international scientific conferences

- **Castaño-Guerrero, Y.,** Moreira, F., Fortunato, E., Sales, M.G., Cost-effective ways to detect L1CAM. Biosensors on-line. Poster, 2021.
- **Castaño-Guerrero, Y.,** Moreira, F., Fortunato, E., Sales, M.G., Poly(thionine) modified screen-printed carbon electrode and its application to detect CA19-9. Biosensors on-line. Poster, 2021.
- **Castaño-Guerrero, Y.,** Moreira, F., Fortunato, E., Sales, M.G., SERS-based biosensors for on-site determination of pancreatic cancer biomarkers. Ciencia’21 on-line (Lisboa). Poster, 2021.
- **Castaño-Guerrero, Y**., Moreira, F., Correa-Duarte, M., A., Sales, M.G., SERS-based immunosensing layer for cancer biomarker detection in point-of-care. RICI8, Aveiro. Oral, 2019.

Chapter 2. Introduction

This chapter reviews the main theoretical topics that support the work developed throughout this thesis. Relevant concepts about cancer diseases with particular focus on PC biomarkers are highlighted. The main components of biosensors are addressed, along with a summary of the main concepts underlying the operation of electrochemical and SERS-based sensor devices. Finally, this chapter reviews the topics of nanomaterials that involve electrochemical polymerization and metal nanostructures used in SERS-based devices.

2.1 STATE OF ART

2.1.1 Cancer diseases

Cancer is a result of the abnormal cell division that proliferates in an uncontrolled manner, without responding to the normal control signals during the cell division process. As a result of uncontrolled and unregulated proliferation, numerous cancer cells grow, continue to divide, and invade normal tissues [19].

Abnormal cell proliferations are called tumours, which can be benign or malignant. Benign tumours remain retained in their primary location, do not invade nearby tissues, or spread to other parts of the body. In contrast, malignant tumours invade healthy tissues and spread throughout the body in the circulatory systems causing metastasis. The capability of malignant tumours to cause metastasis makes it a dangerous and aggressive disease, and very difficult to treat locally. While benign tumours can be surgically removed as they are retained in a specific site in the body [19].

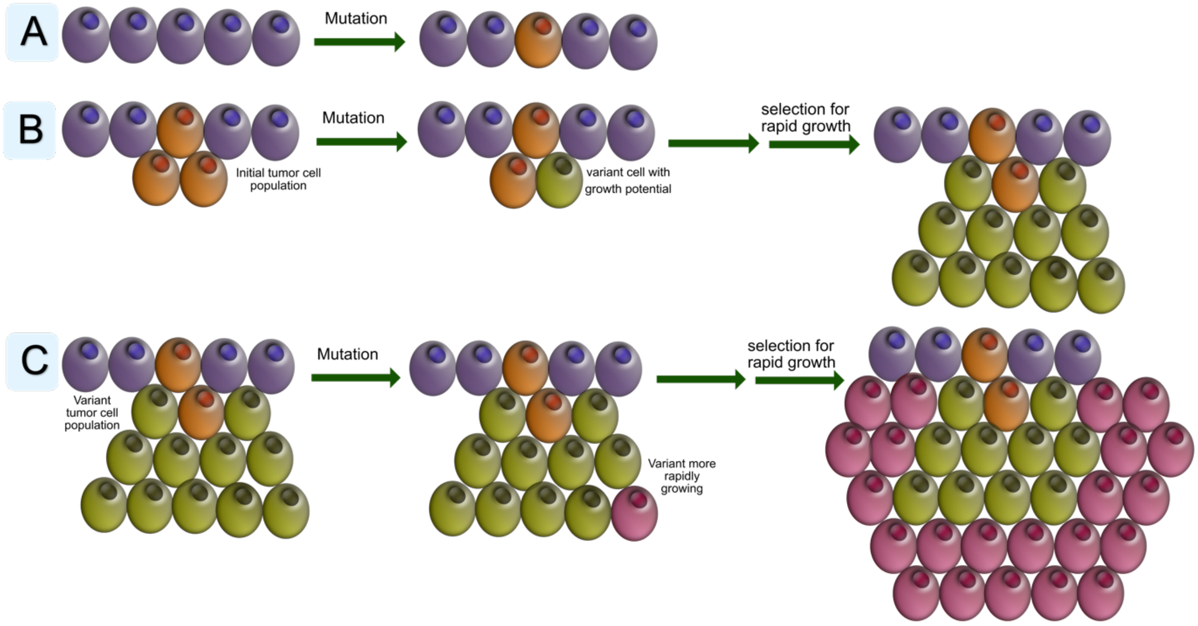

Figure 1: Stages of tumour proliferation. A) initiation of mutation of one cell, B) appear more mutation of cells and growing fast, C) progression with several mutations and accelerated growing.

The process of cancer development at the cellular level involves a series of steps beginning with the mutation of a cell Figure 1 A. The first step described the initiation of the tumour, abnormal cells are produced as a consequence of a genetic alteration. Next, in the cell proliferation phase population of tumour grow up very fast through cell division of the original abnormal cell. During the tumour progression, additional mutations are added to the tumour population, Figure 1 B [19]. The mutations involve selective advantage transmitted to descending cells, such as accelerated growth, survival, or invasion. Consequently, cell descendants become dominant in the tumour population Figure 1 C, a process called clonal selection. Clonal selection is responsible for the fast-growing and increasingly aggressive characteristics of cancer [19].

The main differences between normal cells and cancer cells are evidenced in communication with the immune system, like cell repair and death, function, and blood supply. Cancer cells are more easily mobilized than normal cells, so they move to nearby tissues to form new clones and become in metastasis [20].

Nowadays, the probability of surviving of cancer are increasing [21] thanks to the knowledge about the disease, along with advances in early detection [22], treatments and prevention [23]. However, some types of cancer are still a severe problem, mostly because are caused by intrinsic DNA replication, problems that are not modifiable and affect all human beings [23].

2.2 Pancreatic Cancer

"*Pancreatic cancer cells are difficult to detect, making early diagnosis the exception*", the statement describes a figure of PC cells in the article written by the Eric Bender, a science writer in Newton, Massachusetts, 2020 in Nature journal [24]. The statement a few years later, is not far from reality. Nowadays, PC continues to be a challenge in science in the search for early detection to obtain better prognosis for life in patients.

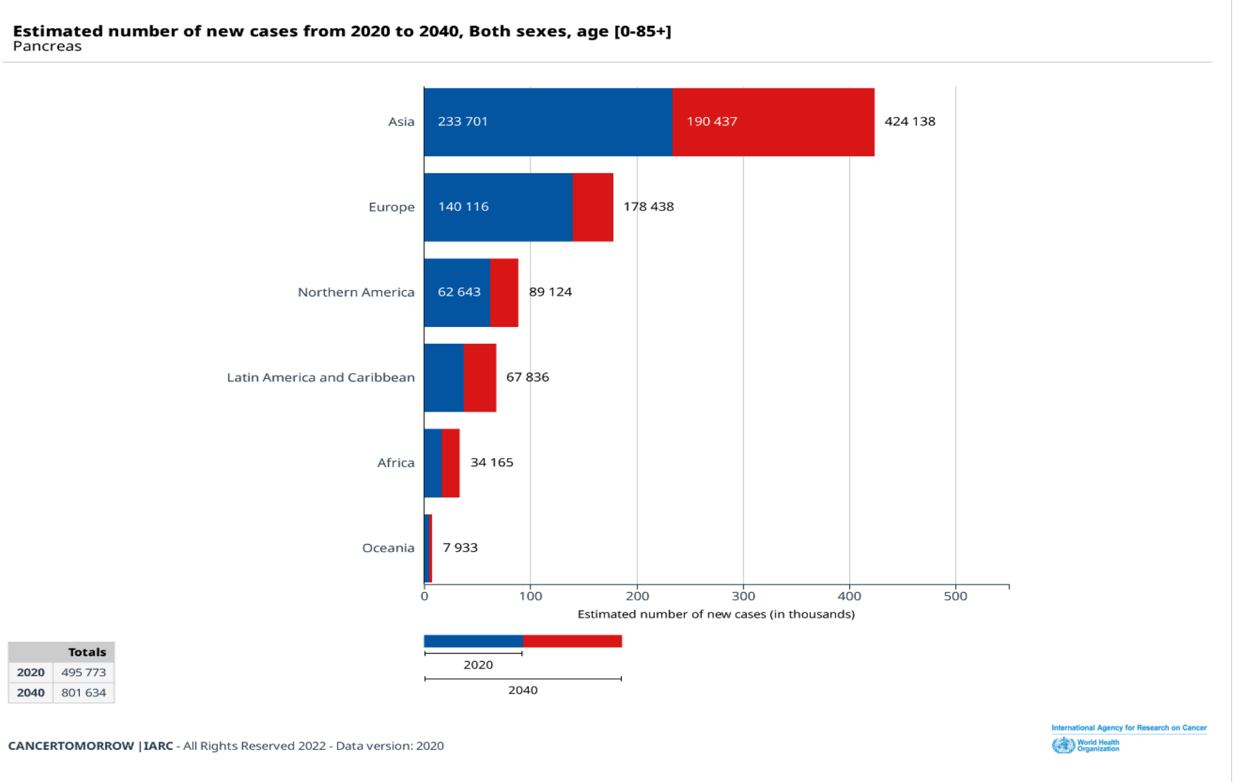

Figure 2: Representation from Global Cancer Observatory of estimated number of new cases of pancreatic cancer in 2040, comparative with 2020.

The Global Cancer Observatory [25], predicted for 2040 the world population will experiment an increase of +61.7% the incidence of PC in both sexes, from 495 773 cases in 2020 to 801 634 in 2040, Figure 2.

Although PC is a rare occurrence, it does not have a history of success in medicine, with most people diagnosed with it being sentenced to death [24]. Living without the pancreas is quite difficulty, which is one of the reasons of PC is so deadly. Another reason is the anatomical position of the pancreas, behind the stomach, makes it difficult to access by scanning tools in the search for tumours. All these disadvantages contribute to PC detection being too late in most clinical cases [24].

The pancreas is an organ with exocrine and endocrine functions, hence pancreatic tumours have been divided into non-endocrine and endocrine tumours. Benign tumours of endocrine are called: adenoma, cystadenomas, lipomas, fibromas, haemangioma, lymphangioma and neuromas. While among malignant tumours are ductal adenocarcinoma, cystadenocarcinoma, among others with histological characteristics of malignant tumours [26].

Published studies on the risk factors for PC show the existence of modifiable and non-modifiable risks. Non-modifiable risks are age, gender, ethnicity, blood group, gut microbiota, diabetes, and family history along with genetic susceptibility. Among the modifiable risks are alcohol, smoking, obesity, diet, and infections [27].

2.2.1 Biomarkers

In the initial stages of PC, most patients are asymptomatic, clinical evidence appears in very advanced stages of the disease. The survival of patients diagnosed with PC is between four and six months, and in resected pancreatic patients the survival rate is 30–58% in 5 years [28], [29]. However, when the disease is detected early, the survival rate is significantly higher compared to more advanced stages. Hence, the diagnosis in the initial stages of the disease is one of the most relevant aspects for success in the treatment of PC [30].

However, early detection continues to be a challenge due to the absence of symptoms and adequate tests for diagnosis. Biomarkers emerge as a possible tool for cancer diagnosis and monitoring during the treatment phase [30]. Particularly for PC, biomarkers are of great importance due to the high impact they can have in clinical practice. Biomarkers are a molecular structure that can be measured to predict the incidence or outcome of a disease. A biomarker is defined as: "*a biological molecule found in blood, other body fluids, or tissue that is a sign of a normal or abnormal process, or of a condition or disease*," according to the National Cancer Institute [31]. Testing to find biomarkers are targeted to genes, proteins, and other molecules that can provide common information about cancer more personalized to each person. A great variety of biomarkers can be found (Figure 3) include proteins (enzyme or receptor), nucleic acids (microRNA, DNA), antibodies, and peptides, among other categories [32].

CA19-9 is considered as a biological marker in the diagnosis of PC. However, it is not specific or sensitive enough to be used for screening without the need for additional tests to confirm the diagnosis [29]. Many other biomarkers are reported in the literature and here we will be reviewing some of them. Biomarkers can be found in serum, biliary fluid, pancreatic juice, urine, faeces and cystic fluid, and these analysis methods present complexity associated with their invasiveness, sensitivity, and specificity [29].

The characteristics looking for an ideal biomarker would be the ability to isolate with non-invasive and economical processes, high sensitivity in early stages together with high specificity to discriminate pathologies [33]. In the search for specific biomarkers of early release has been found abundant biological material, mainly is detected proteins expressed in high quantity. Another biological material in less quantity is quite difficult of detect. For this reason, instead of continuing to search for quantitative changes in a single biological marker, the search has been redirected to a multiple panel of biomarkers [34].

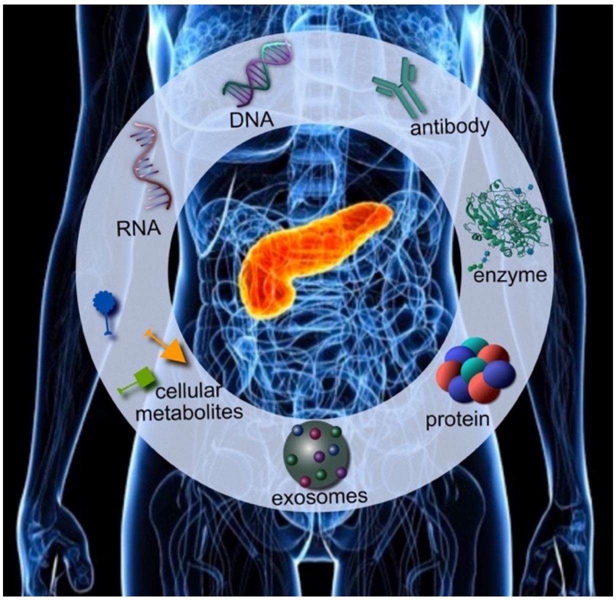

Figure 3: Scheme of several biomarkers for cancers, like exosomes, RNA, DNA, antibody, enzyme, protein and cellular metabolites. Adapted from a photograph of a BBC Science Focus Magazine [35].

The idea of a single biomarker with enough information about a type of cancer would be very favourable in the clinic. However, due to the complexity of tumours, particularly PC, the best approach for a solid diagnosis is a panel of biomarkers together with the clinical evaluation of the patient's history [33].

2.2.1.1 Carbohydrate antigen 19-9

The Food and drug administration (FDA) in 2002 approved the use of CA 19-9 as a biomarker for PC, being the only marker for pancreatic cancer authorized for clinical use [36] at the time. CA 19-9 is already established in the clinical routine as a marker and combined with other biomarkers it is expected to bring an improvement in diagnostic accuracy and robustness. The use of panels of biomarkers allows a better sensitivity for cases where CA 19-9 fails to be specific enough [33].

CA 19-9 is found on the surface of cancer cells. It was initially described in 1979 [37] as a tumour antigen and is the best-known serological biomarker in the diagnosis of PC [38]. CA 19-9 is not specific for PC and has been found expressed in other cancer cells such as colon, gastric and biliary tract [39], [40]. Its clinical use has been described to monitor the progress of the disease or the response to treatment [41], since it has been found elevated in blood in 80% of patients with PC [42]. Its use is however limited for detecting the disease [29]. The serum sensitivity and specificity of CA 19-9 are between 79-81% and 82-90%, respectively, for the diagnosis of PC in symptomatic patients [42], [43], [44].

CA 19-9 has been used to evaluate treatment in patients with metastatic PC. One of the studies aimed to evaluate actual use by monitoring results of CA 19-9 levels in serum of patients with metastasis. The database used includes patients diagnosed with PC metastasis between 2015-2020 [41]. Independent of treatment, elevated CA 19-9 levels at the start of treatment correlated with poorer survival. Increased CA 19-9 levels in the treatment phase were also associated with decreased survival. On the other hand, the decrease in CA 19-9 in weeks 8 of treatment served as a predictive marker for the efficacy of chemotherapy. CA 19-9 became more useful in radiological evaluations to identify patients with a higher survival rate. In conclusion, the trial reported that a greater than 20% reduction in CA 19-9 levels at week 8 predicted highly significant survival [41].

In the literature we find specific biosensors for the detection of CA 19-9. One of the most recent publications presents [45] an electrochemical immunosensor for CA 19-9 using a self-assembled membrane on the surface of Au-SPEs, for detection in real samples. The immunosensor responds in the range of 0.05 to 500 u/ml showing a linear response dependent on the concentration of CA 19-9. The researchers accomplish a stability study of the immunosensor after 7 days. The sensor response decreased by 3.1% past 7 days in relation to the current response. The evaluation of the immunosensor after 3 weeks shows values of 85% of the initial values, indicating a great stability in storage at 4 ºC of the immunosensor [45].

Another work based on electrochemical immunosensor for the detection of CA 19-9, presents the applications of PTH and gold nanoparticles (AuNPs) [46]. DPV was used to measure the electrochemical response of the immunosensor over a range of CA 19-9 concentrations from 6.5 to 520 u/ml. The decrease in currents showed a linear concentration-dependent relationship with R=0.9989, efficiently presenting an electrochemical immunosensor sensitive to CA 19-9.

2.2.1.2 Carcinoembryonic antigen

Gold and Freedman [47] in 1965 experimentally found in adenocarcinomas of the human colon the presence of unique tumour antigens absent in normal colonic tissues. They were referring exactly to a CEA isolated for the first time in 1965 from colorectal cancer [47]. CEA is a glycoprotein with a molecular weight of 180–200 kDa that isolated from different tumours maintains a similar amino acid and carbohydrate composition [48]. CEA is composed by 29 genes divided into two groups, mainly cell adhesion molecules and subgroups of pregnancy-related glycoproteins. The fact that CEA is an adhesion molecule suggests that it has an important role in the processes of invasion and metastasis of cancer [49].

CEA levels in patients with PC can increase up to 60%. Along with other biomarkers, CEA is related to a poor prognosis of PC. However, the possibility of being indicative of the prognosis and evolution of PC has been being studied [50]. CEA cut-off value of 7.2 ng/ml determined the survival outcome after surgical resection for locally advanced PC. This finding suggests that CEA level could be used as an additional marker in the selection of patients for surgery [50].

CEA is a non-specific marker related to various types of cancer as colorectal cancer [51], breast cancer [49], [52], lung cancer [53], ovarian cancer [54], and PC. The CEA serum level is not a definitive marker to differentiate the origin of cancer. So, the use of other diagnostic tools to confirm the type of cancer is alternatively recommended. However, it is being used in targeted therapies against cancer [55], [56]. Along with CA 19-9, serum CEA levels continue to be used to predict late-stage PC diagnosis. *Manen et al*, also agree the optimal cut-off value of CEA is 7.0 ng/ml for better survival prognoses in patients with advanced PC after surgery [57].

2.2.1.3 L1 cell adhesion molecule

L1 antigen was described, for the first time in 1984, *by Rathjen and Schachner* [58]. L1 was identified as a cell adhesion molecule (CAM) component involved in cell [58]. L1CAM is a member of the immunoglobulin-like cell-adhesion molecule superfamily, also known as CD171. It is composed of six Ig-like domains and five fibronectin Type III repeats followed by a transmembrane region and a highly conserved cytoplasmic tail [59].

L1CAM is a transmembrane glycoprotein of 200-220 kDa, with a large extracellular part and a short intracellular cytoplasmic domain. This protein can be digested by metalloproteinases, releasing a soluble ectodomain of 200 kDa and a transmembrane peptide of 32 kDa [60]. Originally it was described in the nervous system but has been a cross-border process into its expression in cancer cells [61]. The relationship of L1CAM with neural biology has been elucidated little by little since its discovery. It is described as a promoter of neuronal adhesion, determining the migration of neuronal cells [62]. Also, mediate the adhesion of neurons to Schwann cells along axons, intervenes in process of myelination and stimulated the survival of neurons [63].

As expected, due to the important role it plays in the central nervous system (CNS), the mutations in L1CAM cause serious abnormalities [64]. Moreover, L1CAM gene mutation described as X-linked hydrocephalus are responsible of neonatal lethality caused by hydrocephalus [65], [66]. Its expression and relative specificity in neural tissue, promotes its used as a neuronal surface marker [67]. Many studies present L1CAM as a marker of the CNS [68], [69] and as potential diagnosis to identify types of tumours [64], [70].

Outside of the CNS, L1CAM emerges as a predictor and possible target in tumour therapies [71]. The ectodomain soluble is a marker of poor prognosis, in various cancer types: in renal cell cancer, endometrial, ovarian carcinomas, melanoma, glioblastoma, colon cancer, pancreatic ductal adenocarcinoma, and small cell lung cancer [72]. It is really to be expected the normal functions of L1CAM, adhesion and migration, will be found in the same way in tumours. So, it is questioned whether the behaviour of cancer cells, such as invasion, growth, and metastasis, are related in some way to the levels of expression of L1CAM [73].

The overexpression of L1CAM in tumours have been detected different techniques like immunohistochemistry, ELISA [74], [75], RT-PCR [76], [77], or Western blot. Although not commonly used in clinical practice, L1CAM emerges as a diagnostic marker for human cancers [73]. Many immunohistochemical studies emerge in the literature using L1CAM as a positive marker, to detect glioblastomas [78], neuroendocrine carcinoma [79], breast cancer [80], endometrial cancer [81], and gastric cancer [82] to name a few.

The first report to detect L1CAM in epithelial tumours from serum samples was by *Fogel et al in 2003* [70]. The authors present L1CAM as clinical predictor in ovarian and uterine tumours using immunohistochemistry techniques [70]. L1CAM overexpression in certain cancers appears to provide antiapoptotic protection to cells against drug treatment [83]. Findings in this study corroborate the role of L1CAM in the malignancy of PC tumours [84]. These studies suggest that the high expression of L1CAM in the PC induce chemoresistance to the treatments [84], [85].

2.2.1.4 Glypican-1

GPC1 is a membrane-anchored protein associated with several types of cancer, including PC. The protein is one of six members of the heparan sulphate family of proteoglycans [86]. In general, glypicans have a nucleus of around 70 kDa and conserved cysteine residues. Other characteristics are the binding regions to the heparan sulphate chains located in the C-terminal regions [87]. The protein is highly expressed in the membrane and has an extracellular part that can be release in a soluble form [88]. Several studies confirm the overexpression of GPC1 in different tumour tissues associated with cancer development [88], [89], [90].

The GPC1 biomarker has been detected exclusively in the membrane of cancer EXOs [91]. EXOs origin is determined by integrins expression involved in the development of metastasis. Many publications reveal proteins and protein receptors in cancer related to EXOs [92], [93], [94], [95], [96]. These extracellular vesicles are attracting attention based on their surface protein patterns and cargo [97]. Recent studies [98] have shown the overexpression of GPC1 protein and specific mRNA in PC, even in early stages of the disease. Results indicate a correlation of GPC1 with an unfavourable diagnosis and prognosis in PC, although it could be used as a therapeutic marker for cancer progression [98], [99].

In 2015, GPC1 was identified for the first time with a specificity and sensitivity of 100% between healthy and PC patients [91]. The report generated interest and in 2018 [100] was published the first biosensor for the detection of GPC1 based on the thiol-modified antibody immobilization technique. Using the DPV as electrochemical reading, GPC1 antigen was detected in a concentration range of 100 pg/µL to 5000 pg/µL in undiluted human serum [100].

Nanomaterials have been widely used in the fabrication of biosensors. Mostly because its high performance and great combination with different analyte detection techniques. The authors combined the nanomaterials with the photoelectrochemical detection method to detect GPC1. For a more precise diagnosis of PC, they used three biomarkers GPC1, CEA and glutathione (GSH) simultaneous [101]. The selectivity of the immunosensor was studied using different interfering species demonstrating an excellent specificity. The precision of the sensor to detect GPC1, CEA and GSH was evaluated against cell models, mice, and patients. Molecules targets were detected simultaneously with high precision and sensitivity in all models [101].

Overall, it is critical to address and develop new devices for sensing complex biomarkers as proteins signalling PC, for which biosensors are well-suited. Biosensors are intrinsically related to the devices employed for detecting biomarkers, making use of a wide range of nanomaterials that ensure a good discrimination of a given biomarker in the presence of various other compounds.

2.3 Biosensors

The general term *sensor* is employed for a device to detects changes like pressure, heat, or electrical, and converts them into signals that we can detect and analyse. The transducer is the element responsible for converting the signal from the sensor into a measurable form [102]. Sensors must possess certain characteristics such as sensitivity, selectivity, high resolution, reproducibility, repeatability, and response time. They can be divided into several categories considering various parameters, for example the detection signal. According to the methods used for detection signal, sensor is divided in physical, chemical, thermal, and biological. Considering the way used for signal identification, appears the term biosensors referring to biological sensors [102].

According UPAC, a biosensor is "*a device that uses specific biochemical reactions mediated by isolated enzymes, immunosystems, tissues, organelles or whole cells to detect chemical compounds usually by electrical, thermal or optical signals*" [103]. Biosensors are composed of a bioreceptor, a transducer and a signal processing system, as shown in

Figure 4. Bioreceptors are the elements that recognize the analyte, like enzymes, antibodies, plastic antibodies, cells, or microorganisms. Transducers are responsible to convert the results of biological interactions into measurable parameters. Finally, the signal processor (or detector) allows reading signals and interpreting them [104]. Overall, they constitute a valuable analysis and detection technique for monitoring signals from biological processes that include interactions of proteins, DNA, enzymes, or cellular communication entities [105], by combining the recognition properties of bioreceptors and the sensitivity of transducers.

In general, biosensors can be classified in four groups according to the transducer: optical, thermal, piezoelectric, and electrochemical [106]. The optical biosensors are based on the response of light after interaction with a molecule. Its foundation is based on the optical properties of light such as absorption, fluorescence, luminescence, and resonance of surface plasmons. Among the best-known optical techniques, we can mention Raman, Fourier Transformed Infrared Spectroscopy (FTIR), fibre optics and surface plasmon resonance (SPR) [107]. Thermal biosensors measure temperature changes produced in the biological reactions. Since enthalpy changes occur in most chemical reactions, it is possible to measure heat changes using biosensors. The best-known example of a device that measures temperature body or environmental is the thermometer [108]. Piezoelectric biosensors measure mass changes produced by interactions between molecules. The voltage produced by apply mechanical stress to a material is known as the piezoelectric effect [107].

In terms of biorecognition element, biosensors are classified as enzymatic, immunosensors, based in aptamer and nucleic acid, and the biosensor of whole cell [109]. Bioreceptors can be of natural origin like antibodies and enzymes, taking advantage of their naturally developed biological interactions to achieve analyte specificity in the construction of biosensors. Otherwise, synthetic bioreceptors are developed to mimic natural physiological interactions [110].

As an element of synthetic biorecognition, MIPs are often employed, using a polymeric matrix to imprint the complementary shape of the targeted biomarker. The polymeric matrix encapsulates the bioanalyte to form synthetic recognition patterns between the analyte and the polymeric matrix. In other words, MIPs use polymers to obtain synthetic biorecognition elements with “molecular memory” in the presence of a target molecule used as a template [110].

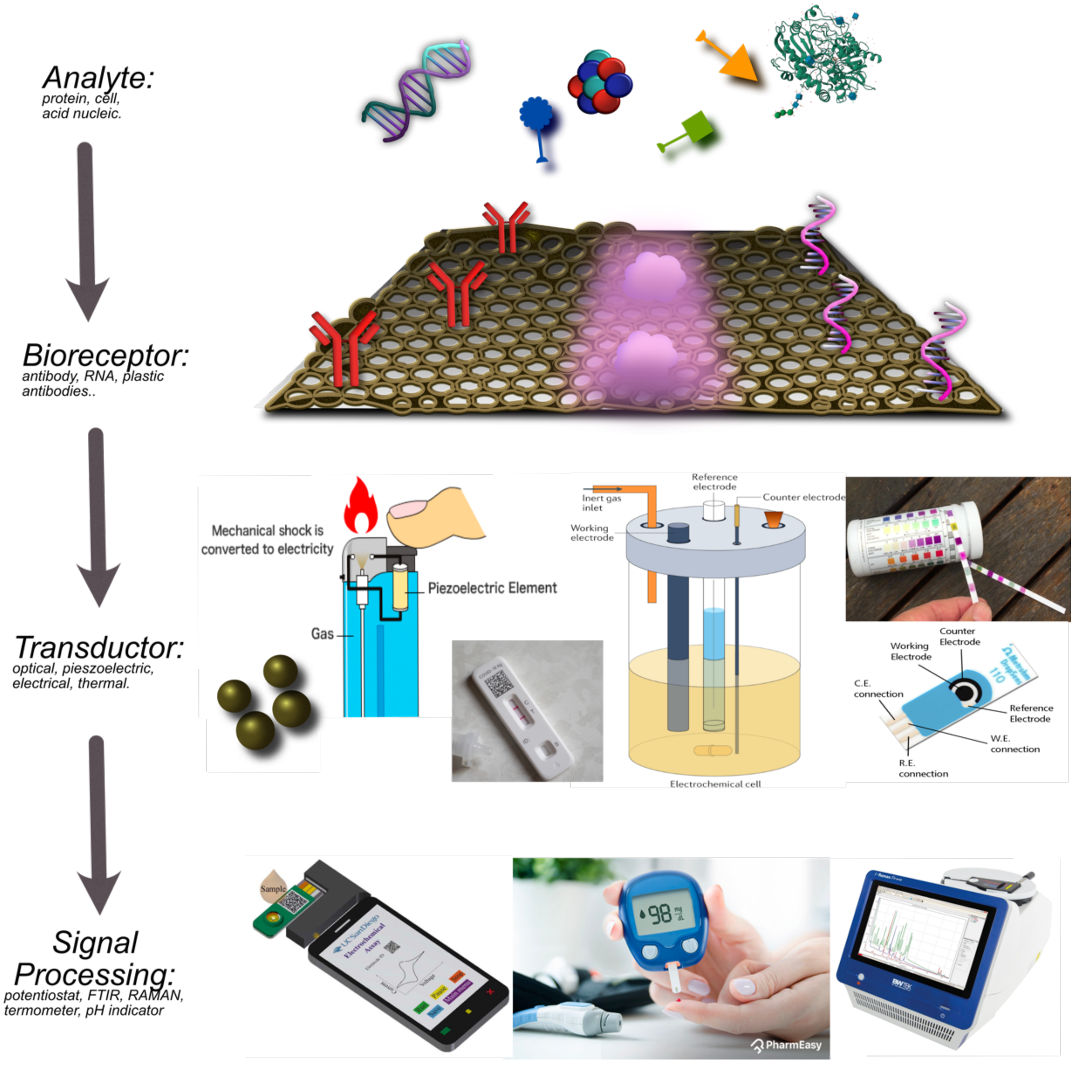

Figure 4: Elements of biosensor: analytes, bioreceptor, transductor and detector.

MIPs are prepared by molecular imprinting technology, which involves the formation of a complex between the target molecule and the functional monomers. Then, functional monomers are polymerized in presence of target molecule [111]. This target molecule is then removed from the polymeric network, giving rise to cavities in the polymer that hold complementary features to the imprinted molecule. These cavities are structurally and chemically like the template and are used for the selective binding of the original analyte [112].

For the purposes of this plan, electrochemical and SERS detection were combined, sequentially for producing accurate, sensitive, and reproducible analytical data. Having a dual detection system offers the advantage of an improved accuracy since each biosensing system is operating on a different scientific background, and the possibility of having a given sample component playing a severe interfering role on both detection systems is very small. On the other hand, using SERS offers the capacity of having highly sensitive responses, due to the use of nanomaterials that enhance the response of Raman reports. These nanomaterials may also be tailored specially with the purpose of intensifying the regular enhancement of the Raman signal.

2.3.1 Electrochemical biosensing

Electrochemical biosensors are typically composed by a three-electrodes system, containing working electrode (WE), reference electrode (RE) and counter electrode (CE). The biorecognition takes place at the WE. The CE completes the circuit by sending/receiving current to/from the WE. The RE is responsible for setting a given potential [113]. The WE can be built in different types of materials, as glassy carbon [114], [115], [116], [117], platinum [118], [119], Au [120], Ag [120], mercury [121], in different formats, from conventional screen-printing [122] to packed carbon paste [123], [124], [125]. The selectivity of the electrochemical response is granted by modifying the conductive material on the WE [122], [126], [127], [128] with a suitable nanomaterial, as antibodies, enzymes, or biomimetic materials [129], [130], [131], [132], [133], [134]. Nanomaterials with conductive properties may also be employed with the purpose of enhancing the sensitivity of the analytical reading.

Electrochemical biosensors use electrochemical transducers to measure current, potential, conductance and/or impedance (Z), operating in the form of an amperometric, potentiometric, impedimetric, conductometric or impedimetric system [109]. The first electrochemical biosensor was set in 1962 for detecting glucose by monitoring the current linked to an enzymatic reaction [135]. Since then, the technological advances of electrochemical devices were huge [105], which includes the miniaturization of laboratory devices to detect molecules in vivo and in situ [106]. Potentiometric biosensors measure the potential difference between two electrodes. The conductometric biosensors measure the ability of the analyte to conduct electrical current between two electrodes under (near-)zero current. Otherwise, the amperometric/voltametric follow the current changes produced by the redox reaction of an electroactive species. In the case of impedimetric, the variation in the charge-transfer resistance (R_{ct}) is measured [136].

The techniques often employed to follow the response of a given biosensor include cyclic voltammetry (CV), DPV, square wave voltammetry (SWV) and electrochemical impedance spectroscopy (EIS), along with potentiometry and conductometry [106]. Voltametric and impedimetric strategies are the most widely used in the detection of cancer biomarkers [137], [138]. The CV is one of the electroanalytical methods whereby varying the potential and measuring the resulting current we obtain information about the target molecule [139]. In addition to being a technique used for analysis, it is used in the characterization and synthesis of chemical compounds or polymeric film [140].

Among the electrochemical biosensors, voltametric and impedimetric strategies are the most widely used in the detection of cancer biomarkers. Potentiometric biosensors measure the potential difference between two electrodes, unlike conductometric biosensors that measure the ability of the analyte to conduct electric current between electrodes. On the other hand, the amperometric/voltametric follow the current changes produced by the redox reaction of an electroactive species. In the case of impedimetric, the variation in the R_{ct} is measured [136].

Sensing with electrochemistry often requires polymeric materials, which in specific conditions may be tailored in-situ. This involves initiating the polymerization via the application of suitable electrical conditions. These polymers may have different uses, including acting as antibodies of synthetic nature. This topic is addressed later in section 2.4.1.

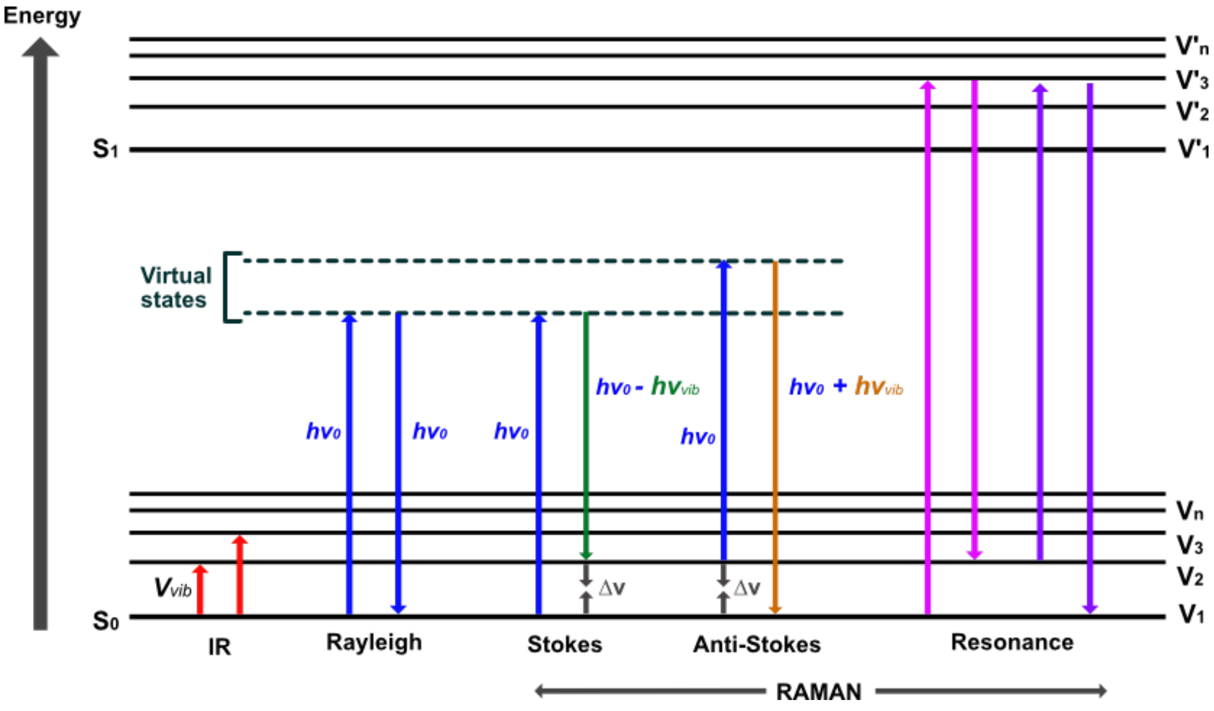

Figure 5: Jablonski energy diagram showing the transitions during the infrared absorption, Rayleigh, Raman Stokes, anti-Stokes and Resonance Raman scattering. The vibrational states (V_n) of a molecule in the ground electronic state (S_0) directly measuring the absolute frequency (IR absorption) or the relative frequency or Raman shift (Stokes and anti-Stokes) of the allowed transitions. Resonance Raman also involves the vibrational states (V'_n) of the excited electronic state (S_1). hv_0= incident laser energy, hv_{vib}= vibrational energy, Δv = Raman shift and v_{vib}= vibrational frequencies. Reproduced by [141].

2.3.2 SERS-based biosensing

Raman spectroscopy is based on the inelastic scattering of light. The scattering events of the photons when interacting with molecules generate loss or gain of energy is called the Raman shift and is represented by wavelength numbers. In Raman spectroscopy, the sample is illuminated with a monochromatic laser and when incise in the molecules causes light scattering in all directions. The Raman spectrum is constructed with the scattered light that comes out at different frequency from the incident light, called inelastic scattering (see Figure 5). The scattered radiation that has the same frequency as the incident radiation is called Rayleigh scattering or elastic scattering. In the case of the scattered frequency being less than the incident frequency, the Stokes lines in the Raman spectrum is originate. Otherwise, when the frequency of the scattered radiation is higher than the incident radiation then anti-Stokes lines appear in the Raman spectrum [142], [143]. The effect known as Raman resonance occurs whenever the energy of the incident photon causes the electron to reach a true electronic state of the molecule [143].

For excitation in Raman spectroscopy, a laser light source from ultraviolet (UV) to infrared (IR) light can be used. As a result, the Raman spectrum include the spectral range of UV, visible (VIS) and near-infrared (NIR) regions (see Figure 6). Most of the spectra are built in the normal vibrational range of organic molecules with modes of vibration between 400 – 4000 cm^{-1}. Raman has been widely used for the identification of organic materials, so the spectrum between 200 – 2000 cm^{-1} is known as the finger-print region [144].

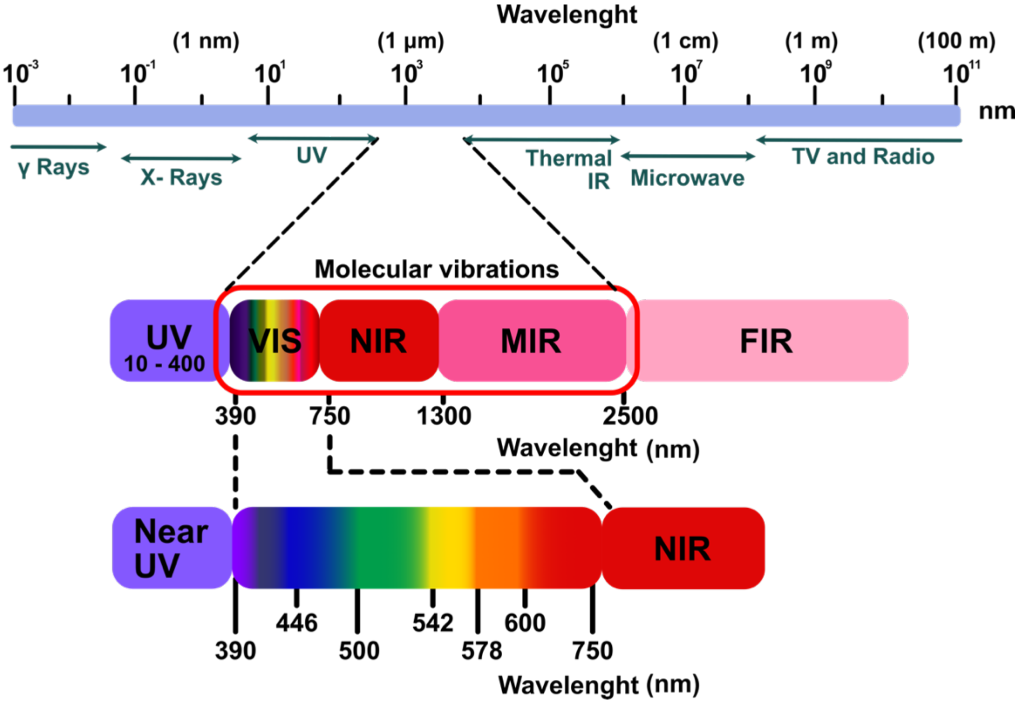

Figure 6: Spectral range for: ultraviolet–visible (UV/Vis), near-infrared (NIR), mid-infrared (MIR), far infrared (FIR), microwaves and radio waves. Adapted from [145].

The Raman laser wavelength is selected according to the type of application and the sample to be analysed. The lasers that can be used range from the UV region through the visible region to the near IR. The excitation wavelength determines the intensity of the Raman scattering. For the most part, lasers with longer wavelengths in the NIR region are correlated with a low intensity scattering signal. Unlike short excitation wavelengths where higher magnitude Raman intensities have been observed. For example, a UV excitation wavelength produces higher intensity than a NIR laser. For NIR lasers, longer acquisition times are normally used with high accumulation numbers. These acquisition parameters are much smaller for lasers with visible excitation channels. However, the excitation of molecules in UV-vis regions often causes greater fluorescence emission than the Raman effect. Fluorescence is the pain point for Raman lasers [146], [147].

Excitation lasers with wavelengths in the visible range have been used in cancer phototherapy [148], [149] and in retinal laser therapies [150], [151], to name a few examples. As few biological fluorophores are known to have their maximum emission peak in the NIR region, this region is the most selected as excitation source for clinical instruments. Making the data processing simpler by not having the emission peaks of the biological markers overlapping with the normal vibrations of the components of the biological samples [152].

The 532 nm laser offers high Raman excitation energy combined with low fluorescence intensity. Longer wavelength lasers are often used, such as 785 nm and 1064 nm, with the aim of obtaining a greater reduction of the fluorescence effect. In the case of carbon materials, a good option is to resort to 532 nm lasers, obtaining the additional benefit of Raman resonance, unlike 785 nm where the sample may burn [146]. The 523 nm laser are suggested to use for analysing metallic oxides or inorganic materials.

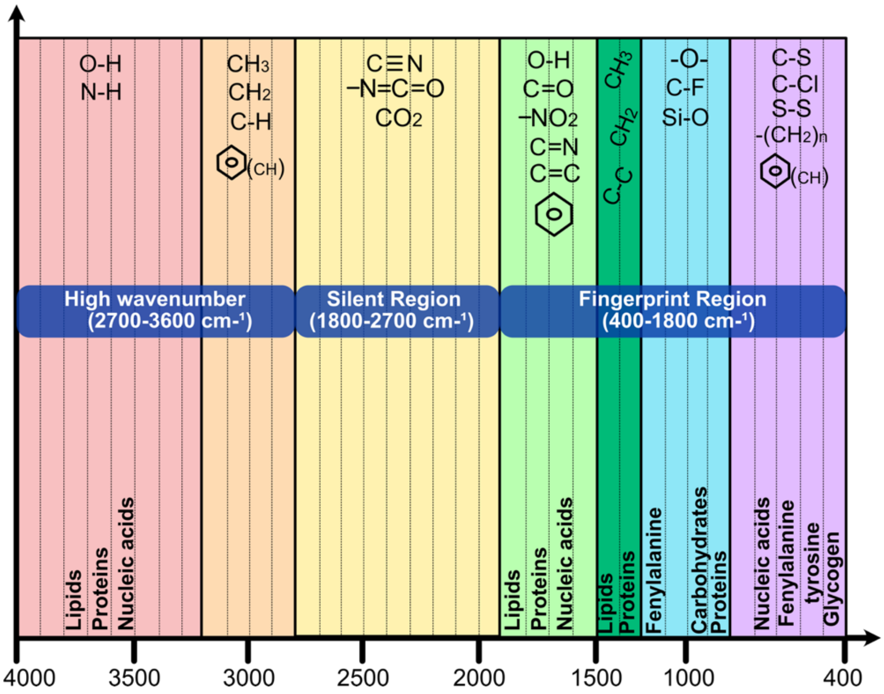

Figure 7: Raman shift for functional groups correspond to the fingerprint region, silent region, and high wavenumber region. Adapted from [153].

As an advantage the 523 nm laser cover the entire range of 65 cm^{-1} until 4000 cm^{-1}. The 785 nm laser have an equilibrium between potential of signal and fluorescence emitted, also in the efficient for acquiring spectrum of organic materials. The 1064 nm laser has the greatest advantage when samples have fluorescence at other wavelengths [152].

The heterogeneity of biological samples, particularly the large number of vibrational modes in Raman, make difficult extracting relevant information from the spectra [154]. The Raman spectrum presents three main regions: fingerprint (400-1800 cm-1), the silent one (1800-2700 cm-1) and the high wavenumber (2700-3600 cm-1) see Figure 7. Most of the peaks in biological samples appear in the region of the fingerprint, because of the molecular vibrational modes originating from proteins, lipids, carbohydrates, and nucleic acids. The region known as silent coincides with the free region of the peaks of the biological material, except for the bands coming from triple bond functional groups such as alkynes. The high wavenumber region presents the peaks of stretching modes of C-H, C-H2, O-H and N-H groups [155], [156].

The bond of a molecules experiences multiplex types of vibrations and rotations. The different vibrational modes are represented in the Figure 8, stretching vibration (symmetrical and asymmetrical), and four bending vibrations (rocking, scissoring, twisting, and wagging). When a change occurs in the distance between atoms along the axis of the bond, it is known as stretching vibration. Otherwise, we have the bending vibration that occurs when a change in the angle between two bonds is observed. [157]. Unfortunately, the literature is not uniform regarding the nomenclatures to describe Raman modes and their vibrations, often resulting in contradictions. For more simplest is present the followed nomenclature: stretching modes (υ), symmetric (υ_s) and asymmetric (υ_{as}), scissoring (δ), rocking (ρ), wagging (ω) and twisting (τ).

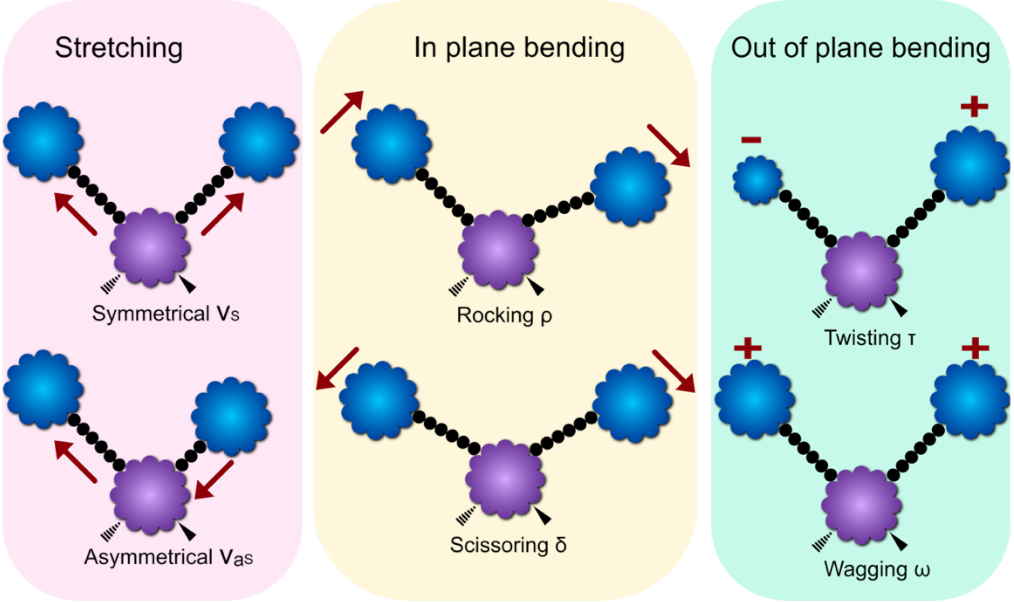

Figure 8: Possible vibrational modes of molecules: Stretching, in plane bending and out of plane bending. Adapted from [157].

The Raman scattering is enhanced when the target molecule is in contact with the surface of metallic nanostructures, resulting in the SERS phenomenon [158]. During the last decades the number of chemical applications, particularly the life sciences, have been increasing [159].

SERS was first observed in 1973 for pyridine adsorbed on a rough silver electrode. The rapid growth in knowledge about SERS was largely due to advances and increasing knowledge in nanofabrication and Raman instrumentation, combining research areas such as chemistry, physics, life, and materials sciences [159]. SERS, unlike Raman, needs metal nanostructures as a component with the objective of increasing Raman scattering and consequently its signal. While Raman only is considered the interactions between light and molecules, in SERS we must also consider the interactions of light with different forms of metallic nanostructures Figure 9 [159].

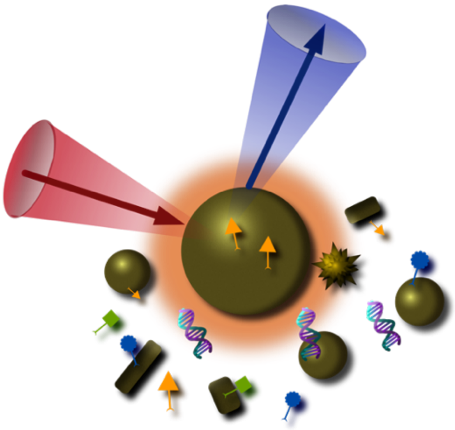

Figure 9: Scheme metallic nanostructures used in SERS: nanoparticles, nanorods and nanostars.

Two separate mechanisms are involved in enhancing the SERS signal: the chemical mechanism and the electromagnetic mechanism. The chemical mechanism is determined by the chemical interaction of the molecules with the surface of the metal. While the electromagnetic mechanism is responsible for the enhancement of the electric field caused by the metal [160]. In the chemical mechanism the molecules can be absorbed on the surface of the metal. This adsorption is modulated by the electronic interaction with the metal, the chemical nature of the molecule and the surface selection rules [160].

The proximity of the molecules to the surface of metallic structures stimulates the excitation of surface plasmons in the substrate [158]. The plasmonic behaviour of metallic NPs involves multiple factors, the theories of electromagnetic field and the resonance of the plasmon metals [160]. The electromagnetic enhancement is caused by excitations of the surface plasmons in a NPs. The surface excitation improves the local field of the molecule adsorbed on the metal surface. The increase in the local electric field is not so intense, however the inelastic scattering of light increases causing a noticeable SERS effect [161]. In summary, the electromagnetic mechanism is the main responsible for the improvement in SERS, and it is independent of the bond established between the molecule and the metal surface [160].

Metallic NPs are synthesized in different sizes and shapes to enhance intensity in SERS. A great variety of geometric shapes have been synthesized over time such as: spheres [162], [163], nanostars [164], [165], [166], and rods (Figure 9) [167], [168], [169].

The work presented by [170] is an example of the utility of SERS in the clinical diagnosis of PC. They presented a dual-SERS-based biosensor to detect microRNA in exosomes and plasma supernatants from blood samples. The Ag NPs synthetized with a Fe_3O_4 core was used as substrate for the capture of the SERS nanostructure. The SERS nanostructure was synthesized using Ag with Au as core and the DTNB as a Raman reporter. The nanostructure between the substrate and SERS increased the Raman signal due to the magnetic concentration of the metallic structures. The dual-SERS biosensor distinguishes accurately between patients with PC and normal controls and the quantifications in order of attomolar concentration of biomarker was detected [170].

Recently, a research article combining SERS and immunosensors techniques for detection of exosomes in PC was published. The authors assembly a pyramidal matrix to obtain uniform Ag NP deposition. The pyramidal structure used as SERS substrate provides a greater number of hot spots due to the ordered distribution of plasmonic Ag. Thus, the phenomenon of superposition of the SERS substrate together with the proximity of the SERS probe produced an increase in the Raman signal, increasing the sensitivity to detect exosomes [171].

In multiplex detection studies of pancreatic biomarkers, SERS spectroscopy has also shown its usefulness. By means of directed matrices made of polydimethylsiloxane, it was possible to control the direction of the capturing antibody. In each direction, the specific antibody for each biomarker (CA19-9, matrix metalloproteinase 7 (MMP7) and Mucin 4 (MUC4)) was carefully immobilized on a single platform. Followed by SERS using extrinsic Raman tags, was detected these three different biomarkers in the serum of the patient with PC [172].

2.4 Nanomaterials

The nanomaterials employed are a critical element of the biosensor assembly. In a simple perspective, they should display the desired features to grant detection with suitable selectivity and sensitivity features. Usually, they are employed to modify the WE with the purpose of conferring a biorecognition ability or amplifying the analytical response. A MIPs assembly is being considered in electrochemical biosensing, in which a polymerization is taking place in-situ. This is the critical aspect of the technology because it is responsible for forming the imprinted cavities against the target biomarker. For the purposes of SERS-signal amplification, metal-based nanostructures are always employed to ensure the plasmon effect of a suitable Raman reporter. These are detailed next.

2.4.1 Polymerization in situ

The term polymerization was first mentioned in 1863, in a conference in Paris by Berthelot (1827-1907). Berthelot, based on combustion observed that certain compounds became polymers, by a reaction that was called “polymeric transformation”, known as “polymerization” [173]. He postulated: "*all compounds capable of adding hydrogen, hydrogen chloride or water, must be able to add identical molecules to themselves”,* meaning that these molecules should be polymerizable [173]. The first description of a polymerization process was made by Eduard Simon, in 1893, by observed a liquid from banana becoming increasingly viscous with the time, until a solid very similar to glass appeared [173].

Free-radical polymerization is behind the overall process, which includes the successive formation of free upon addition of a new component. Usually, the first step called initiation is responsible to form radicals, followed the propagation involve the addition of monomers to make growing polymer chain, and the last step is termination where the active centre is destroyed [174].

The initiation of a given polymerization is a critical step, for being the one responsible generating radicals that are later involved in the formation of the polymeric network. It involves a compound that may undergo the formation of a radical species upon an external stimulus, as shown in Figure 10. The stimulus can be chemical, electrical, optical (usually UV radiation) and/or thermal [175].

Focused on thermal initiation, some monomers could polymerize at high temperatures, such as styrene and methyl methacrylate. After being exhaustively reviewed it was shown that by ultraviolet spectroscopy the initiation process of styrene polymerization came from the formation of an initial Diels-Alder dimer. The free radical is formed by the transfer of a hydrogen to a styrene molecule from the previously formed dimer [175].

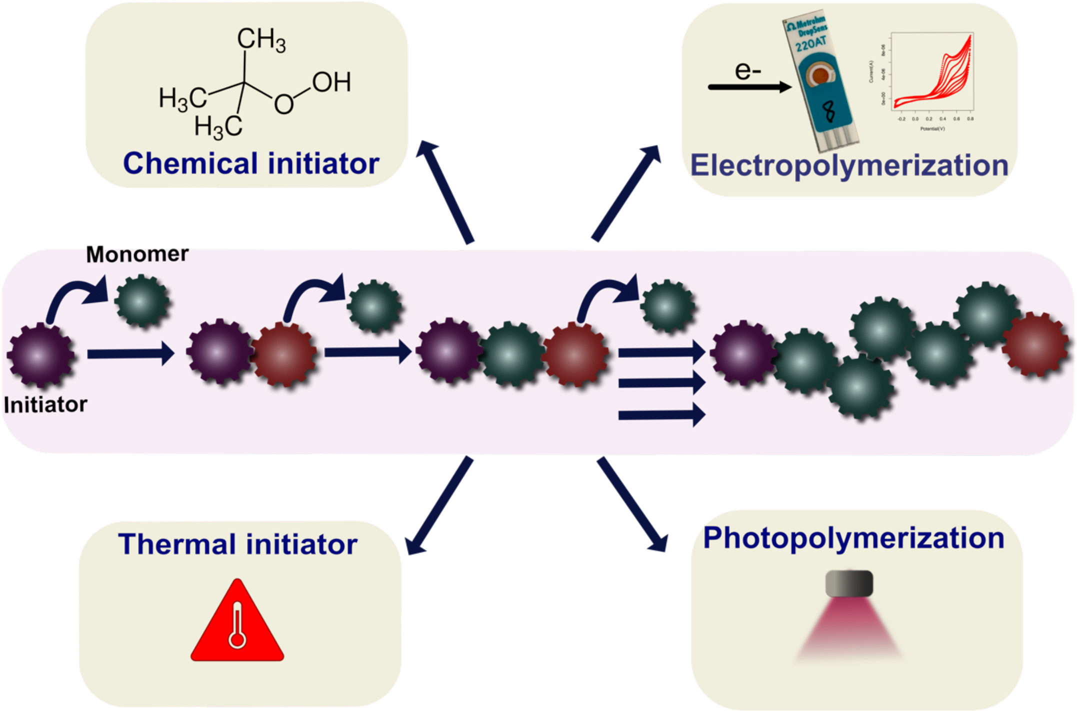

Figure 10: Polymers formation stages: initiation, propagation, and termination. Sources of free radical initiator involved into the polymerization process.

Another form of initiation originates photopolymerization, where light is used in the formation of radical species. The most prominent advantage over conventional initiation methods is the light source involved. Light, being an ecological method, releases less solvents and can produce polymer in mild conditions. For its part, there is also a limitation to consider, which is the depth of penetration of the light, depending largely on the wavelength used [176]. The photoinitiation process take place when photoinitiators are subjected to UV irradiation. The phenomenon occurs when photons convert absorbing molecules into their activated form, and they rapidly disintegrate into radicals, initiating polymerization reactions [177]. More efficient polymer combinations have recently been proposed using photopolymerization with thermal initiators [176]. The phenomenon of heat release in the form of energy from photopolymerization prompted these authors to add a thermal initiator, generating an additional source of radical initiators that allow higher monomer conversions to be achieved.

In electrical initiation, there are radicals being formed in a solution containing both monomers and electrolytes upon electrical stimulus. At the cathode, the monomer molecule receives an electron to form a radical anion. At the anode, the monomer molecule gives up an electron, forming a radical anion. The radical ions formed then initiate free or ionic radical polymerization or both, depending on the electrolysis conditions [178].

In the area of electrochemical biosensors, electropolymerization is mostly used to polymerize directly on the surface of the electrodes [179], [180], [181]. The electropolymerization is a simpler process that integrates into the surface of the electrode all the materials. Polymers as electrical insulators were a well-conceptualized idea. Only with the emergence of organic polymers a new conception of conductive polymers with electrical and optical properties appears [182]. The parameters used in electrochemistry allow the formation of conductive and non-conductive polymers [183]. Conductive polymers include those derived from aniline, pyrrole, thiophene, or thiazine [182]. In contrast, polymers derivative from phenols or aminophenols correspond to films with insulating properties [183]. The electrical properties of polymers have become very useful tools in the construction of electrochemical sensors.

The controlled process of polymer synthesis by electrochemistry can be carried out through three methods: galvanostatic, potentiostatic and potentiodynamic. In the galvanostatic and potentiostatic methods, a constant potential is applied to the WE for a determined time. While the potentiodynamic mode is applied a few cycles in a determined potential range. The thickness of the polymeric film depends on the number of applied potential cycles. The potentiodynamic is the most used method in the electropolymerization process [183].

The electropolymerization allows to control the parameters of the growth of the polymer doing the synthesis more controlled and precise [184]. The thickness of the polymeric film can be controlled by varying the solvent, monomer concentration, electrode material, applied potential, time, and scanning speeds better known as scan rate [185].

In the Figure 11 A-D, the electropolymerization of 3AP is shown as an example at different scan rate, 10, 20, 30 and 50 mv/s. In the graph of electropolymerization using CV, it is observed how as consequence of increases the speed of scan rate increase the current in the oxidation peak at 0.5 V. At higher current in the peak is observed minor Z values in the Nyquist Plot Figure 11 E, meaning a polymer with less resistance to the passage of current is producing. Thus, we verified how only altering the scan rate in the CV directly affects the polymeric film deposited on the surface of the electrodes, being polymers with different conductive properties.

In the production of polymers, the voltametric potential range influences the properties of the polymer formed. The electropolymerization method could be summarized by the application of a potential on the WE cover-up by the monomer. As result of potential applied occurs the oxidation of the monomer generates free radicals responsible for initiate the growth process of the polymer chain, depositing a polymer film on the surface of the WE [186].

Polyaniline is the material of choice for electronic technologies, among the advantages its easy production predominates. Using the electropolymerization of aniline we will briefly explain the steps involved in the production of the aniline polymer [186].

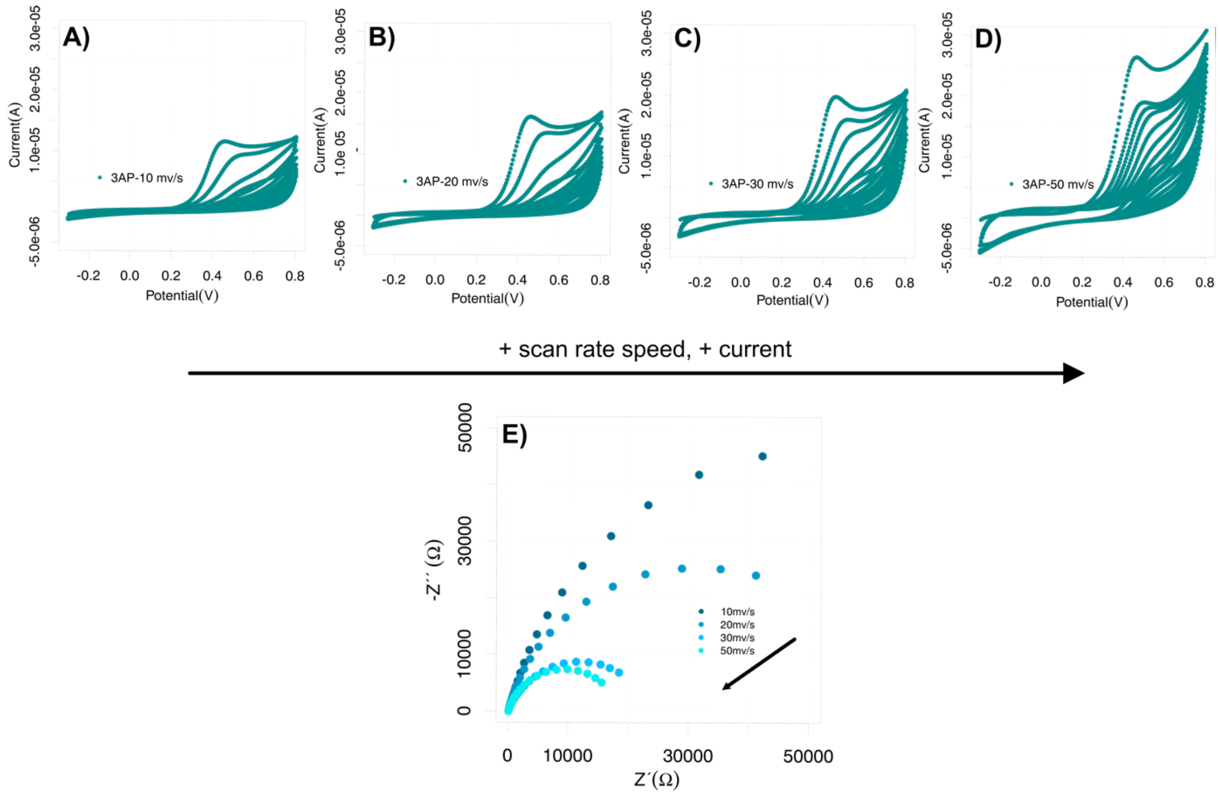

Figure 11: Electropolymerization of 3AP at different speed of scan rate: 10, 20, 30 and 50 mv/s A) to D) respectively, at potential range between -0.3 to 0.8 and the result of electropolymerization E) in the Nyquist Plot.

In the first step when the CV potential sweep occurs, oxidation occurs on the surface of the WE and a radical cation is formed. The Figure 12 shows a study of electropolymerization of aniline on a gold surface, there are observed the anionic peaks and the cationic peak. Peaks a1, a3 and C1 appear because of gold electrode oxidation since it disappears in successive cycles. As the next voltammetry cycles continue, it is more evident that the anionic peak a2 at 0.9 V is due to the irreversible oxidation of aniline and is responsible for generating cationic radicals. The greater the number of cycles, the more pronounced other redox couples appear, which increase the current as the cycles increase, evidencing the growth of polyaniline [187], [188].

The electropolymerization process of aniline passes from the oxidized state to the reduced state. Non-conductive polyaniline is formed first in the oxidized state (the oxidation of leucoemeraldine to emeraldine), and then semiconductive polyaniline in the reduced state (the reduction of emeraldine to leucoemeraldine) [186].

The EIS, like the CV, is a widely used technique to analyse the electrical characteristics of polymers. EIS measures current in response to an applied potential of alternate current [189]. In electrochemical cell, the interactions between the reactive species and the electrode are reflected R_{ct}, mass transfer, electrolyte resistance, and electroactive species, from the solution to the electrode surface. EIS is used to study to known if the characteristics of materials influence in the conductance, resistance, or capacitance of the electrochemical system. All the electrochemical changes on the surface of the WE like the resistance of the solution (R_s), the R_{ct} and the Warburg impedance (W) are shown in Nyquist plots, see Figure 11. The Z represented in the Nyquist graphs is divided into a real part and an imaginary part. Nyquist plots are the graphical representation of all data collected during the EIS and can generate different curves such as one semicircle or two semicircles for a specific electrochemical event [137].

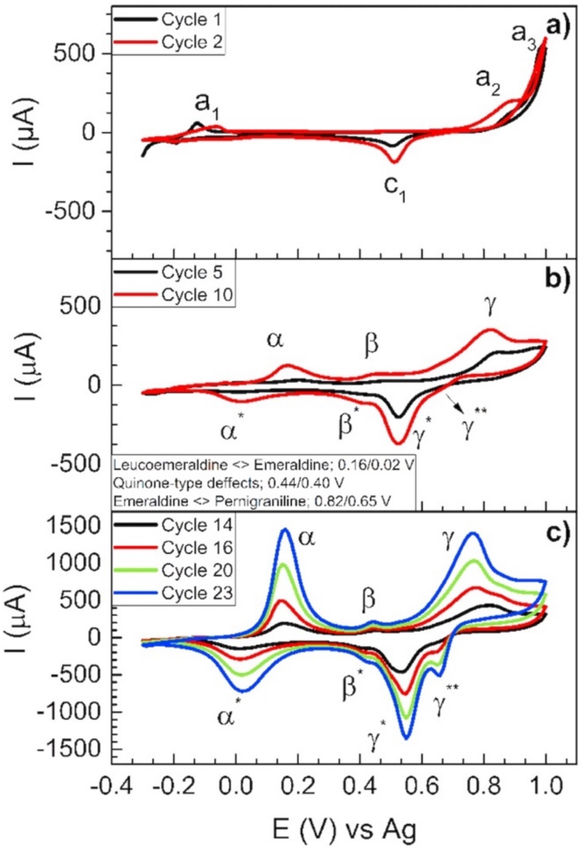

Figure 12: Electrochemical deposition of PANI via CV on Au-SPEs. (a) Starting cycles; (b) the first occurrence of PANI formation and (c) further growth of PANI on Au-SPEs. Reproduced from [188].

The functionalization of the WE surface has been widely used to obtain biosensors with higher sensitivity. Nanomaterials are heavily involved in applications as biosensors for electrochemical detection since they offer advantages such as increased surface area, high mechanical resistance, and greater electrical conductivity. Hence its utility to improve the performance of the biosensor, amplifying the electrochemical readings and lower detection limits. We also found the greatest stability on the surface of the immobilized biorecognition elements [190].

One pathway to synthesis MIPs are electrochemical techniques. Since the preparation of synthetic polymers to produce plastic antibodies as biorecognition elements was first reported, their use in the construction of biosensors has not stopped [191], [192], [193], [194] . The recognized by MIPs has been combined with several types of transducers, among them electrochemical and optical transducers predominate. The construction steps of the MIPs and the analysis of the responses against the presence of the target molecule can be measured by redox conversion in an electrode, fluorescence, or Raman spectroscopy [138], more recently used SERS [195], [196].

2.4.2 Metal-based nanostructures

The basic SERS mechanism is based on the optical properties of metal nanoparticles (NPs) [155], as described above 2.3.2. To be more exact, none of the surface-enhanced optical techniques would exist without the properties of metals such as Ag and Au. The most widely used plasmonic metals to improve the Raman response are Au and Ag and have been used in various medical fields and research [197].

The optical properties of metallic materials are characterized by the dielectric function. The dielectric function varies in function of the frequency of the light and the wavelength. The electromagnetic properties are defined based on the geometry of the materials and varies depending on geometry of metal. Metals with different shapes have different resonances, one of the properties that makes metals unique at the nano-optical level [197]. Studies carried out with different size and shape of the NPs demonstrate that each geometry can be clearly identified with optical signature. As expected, the spectra of asymmetric particles with more edges tend to be more complex, the optical properties are size-dependent [198], [199].

Regarding the electrostatic approximation, the size of the nanospheres is not relevant when the sphere size is increased or decreased near 10 nanometres. However, for sizes between 30 – 100 nm there will be effects that vary depending on the size [197]. Particularly, the noble metallic NPs (Au, Ag, Platinum (Pt), and Palladium (Pd)) in the range of 2 – 100 nm present a strong localized surface plasmon resonance (LSPR) suitable for a wide range of applications. Whereas the NPs below 2 nm loses the effect of LSPR [200].

SERS is a technique widely used in biomedical applications. For example, using Ag NPs it was possible to detect ctDNA in several serum samples from patients for primary and non-primary lung adenocarcinoma. The SERS platform incorporates a film of Ag NPs linked to a probe that specifically recognizes the ctDNA biomarker of lung cancer [201]. In the pandemic of COVID-19 one of effective methods use to detection of virus was SERS. The SERS sensor was development by assembly DNA to Ag nanorod to capture the RNA of COVID-19 [202]. SERS have been used to detect several biological samples like DNA or microRNA, to identified biomarkers of breast cancer [203], [204], miRNA-155 for pancreatic carcinoma [205], or miRNA-499, miRNA-328, and miRNA-208 for myocardial infarction [206]. SERS can be useful in the diagnosis of virus dengue in blood samples. Employing Ag nanorods was constructed an array to capture NS1 protein in the serum of patient. The SERS portable platform turned out to be efficient in the early and in situ diagnosis of dengue with high sensitivity and reproducibility [207] .

Briefly, this part of the report described some of advances in application of metallic NPs in SERS. It is possible to detect important biochemical species and especially the medical biomarkers, with great signal. The use of metallic particles in SERS spectroscopy is a recent and advantageous option that may lead to an improvement in many of the analytical techniques used in medical, biochemical, and biological analysis.

Chapter 3. SERS and electrochemical impedance spectroscopy immunoassay for carcinoembryonic antigen

The results presented in this chapter are based on the publication *“SERS and Electrochemical Impedance Spectroscopy Immunoassay for carcinoembryonic antigen*“ by **Castaño-Guerrero, Y**., Moreira, F., Sousa-Castillo, A., Correa-Duarte, M., A., Sales, M.G., Electrochimica Acta (2021), 366, 137377. **doi: 10.1016/J.ELECTACTA.2020.137377**. This chapter includes a brief introduction about the conventional methods to detect CEA and the description/discussion of the research work about an innovative dual detection approach, combining electrochemical and SERS sequential readings, on Au-SPEs. This simple principle was proven successful in the CEA detection.

3.1 Introduction

As explained before, many of the existing cancers have a high chance of cure when early diagnosed [208]. An earlier identification may result in a higher probability of survival, which includes monitoring diverse biomarkers as cell-free DNA, cell-free RNA, tumour proteins and extracellular vesicles [209], [210], [211]. This includes several overexpressed glycoproteins, among which CEA can be found.

CEA is a cancer biomarker that is currently employed in clinical context. It is a glycoprotein of 200 kD that has been associated mostly with colon and gastric cancer diseases [212], but may also be linked to breast, ovarian and lung cancers. Normal CEA levels range 3-5 ng/ml, but these may reach 10 ng/ml in specific benign diseases and CEA levels above 20 ng/ml before therapy are commonly linked to metastatic state [213]. Thus, the routing monitoring of CEA may contribute to the early detection of cancer diseases, while also contributing to follow-up the therapy.

It is therefore clear that quick and low-cost methods are required for CEA screening. Conventional methods for CEA screening include enzyme-linked immunosorbent assay (ELISA) (*Human CEA ELISA Kit)* as, radioimmunoassay (RIA) [214] and fluoroimmunoassay [212]. These are reliable and accurate but require a long time to retrieve a response, trained personal, and expensive equipment, being therefore too expensive to be implemented under routing analytical procedures.

Alternative methods for monitoring CEA include electrochemical immunosensors, which combine the quick response of electrochemistry methods with the great selectivity of antibodies, yielding sensitivity, accurate and inexpensive analysis [215], [216]. These methods have been currently employed in the detection of a wide variety of biomolecules, including cancer biomarkers [217] and also CEA. Different technical approaches are employed for this purpose. This includes using different electrodes, as gold [218], transparent oxides [219], [220] or carbon-based [221] materials. Different chemical entities are also employed to improve the detection features, such as poly(sulfanilic acid), chitosan, TH, toluidine blue, methylene blue [222], [223], [224], as well as titanium dioxide nanomaterials, AuNPs, porous nanogold, Janus NPs of gold/silica [225], magnetic DNA nanoprobes [226] and different composites of organoclay nanogold [227] or graphene/Nafion [228].

In terms of biorecognition, electrochemical immunosensing of CEA may be established by the direct reading of the antigen binding, usually leading to changes in the electrical current of a standard redox probe [229]. However, if another protein in a complex sample would adsorb non-specifically to the sensing surface, it would also contribute to the detected signal, thereby leading to a positive error. This may be minimized by combining electrochemical immunosensors with sandwich approaches [230], in which labelled antibodies in a solution are added after antigen binding and prior to detection. Labels used for this purpose that contribute for the electrochemical detection include metallic/redox-based compounds or labelled enzymes (horseradish peroxidase), or a combination of both [224], [231], [232]. CEA has a single polypeptide chain with an NH terminal domain of 107 amino acids, in addition to three highly homologous domains of 178 amino acids. Most likely, these homologous domains are responsible for the presence of repetitive epitopes in CEA, meaning that one antigen molecule can bind simultaneously to more molecules of the same monoclonal antibody [233].

The two stages of incubation (the antigen and the labelled antibody) required in sandwich-based methods are an excellent opportunity to establish dual detection approaches. This would further validate the analytical readings, thereby ensuring the desired accuracy of these sandwich-based methods in highly complex samples. The first stage could remain of electrochemical nature, as this is non-destructive. The second stage could rely on SERS, a versatile approach that is attracting much attention in the field of biosensing, including for CEA detection [234].

Overall, this work reports for the first time an immunosensor combining electrochemical and SERS sequential readings on the same sensing surface, thereby yielding quantitative/qualitative data and further contributing to the accuracy of the data so obtained. Some research work has been reported in the literature describing the integration of electrochemical and SERS techniques for testing the interaction between anticancer drugs and DNA [235], [236] but it was never used before for the immunosensing of tumour markers. To this end, the immunosensor was assembled and optimized on a commercial Au-SPEs. The first detection stage is obtained after CEA binding and concerns electrochemical signals produced by EIS. Then, the labelled antibody linked to AuNSs with 4-aminothiophenol (4-ATP) (yielding a specific and well-established Raman signal) was incubated on the WE and SERS data were collected. The analytical performance of immunosensor was tested with spiked serum.

3.2 Experimental Section

3.2.1 Equipment

Electrochemical measurements were made in a potentiostat/galvanostat from Metrohm Autolab, equipped with an impedimetric module and controlled by NOVA 2.0 software [237]. Commercial Au-SPEss were used (DropSens, 220AT), combining WE and CE made of gold, and RE and electrical contacts made of silver. The switch box interfacing these SPEs and the potentiostat was obtained from BioTID, Portugal. Raman spectra were collected in a Thermo Scientific DXR Raman with a confocal microscope and a 785 nm excitation laser.

Transmission electron microscopy (TEM) was performed using a JEOL JEM 1010 transmission electron microscope operating at an acceleration voltage of 100 kV.

3.2.2 Reagents and solutions

All chemicals were of analytical grade and water ultrapure Milli-Q laboratory grade. Potassium hexacyanoferrate III ($K_3[Fe(CN)_6]$), potassium hexacyanoferrate II ($K_4[Fe(CN)_6]$) trihydrate, sodium phosphate dibasic dihydrate (Na_2HPO_4), and *Ortho*-phosphoric acid 85% (H_3PO_4) were obtained from Riedel-de-Häen; *N*-(3-dimethylaminopropyl)-*N'*-ethyl-carbodiimide hydrochloride (EDAC), Polyvynilpirrolidone (10 000 MW), *N,N*-Dimethylformamide, trisodium citrate dihydrate ($C_6H_5Na_3O_7{\cdot}2H_2O$), tetrachloroauric acid trihydrate ($HAuCl_4$ x $3H_2O$), ethanol absolute (C_2H_5OH) ≥99.9% and monoclonal antibody for CEA produced in mouse were obtained from Sigma-Aldrich; *N*-hydroxysuccinimide, potassium chloride (KCl), glycine and cysteamine hydrochloride were obtained from Merck; Phosphate buffered saline (0.01 M, pH 7.4) solution, sodium chloride (NaCl), potassium dihydrogenphosphate (KH_2PO_4), and hydrochloric acid (HCl) were obtained from Panreac; foetal bovine serum and glucose were obtained from Alfa Aesar. Sulphuric acid (H_2SO_4) was obtained from BDH; 2-(*N*-morpholino)ethanosulfonic acid (MES) from AppliChem; ethanol 96% from Labsolve; 4-aminothiophenol 96% from Acros Organics; CEA, 25 µg, from EastCoastBio; and creatinine from Fluka.

3.2.3 Electrode pre-treatment

SPEs should be cleaned prior to their first use, to ensure that the resulting immunosensor displays stable and reproducible readings [238]. To this end, the electrodes were subject to an electrochemical cleaning stage, made by CV cycling, in H_2SO_4 solution. It was expected that this electrochemical approach eliminated organic contaminants through their oxidation [239], [240]. After the cleaning procedure, the electrodes showed average R_{ct} values of ~180 Ω (*n*=8), a reproducible feature among the SPEs used herein.

3.2.4 Assembly of the immunosensor

The steps involved in the assembly of the immunosensor are shown in Figure 13 A. The WE was electrochemically cleaned with H_2SO_4, 0.5 M, by CV, from -0.2 V to +1.5 V, at a scan rate of 50 mV/s. Then, a cysteamine (Cys) (100 mM) solution was casted on the WE area for 1 hour. In parallel, the Ab-CEA underwent a reaction with NHS (50 mM) and EDAC (250 mM) for 30 min at 4ºC, too activate the carboxylic acid groups. The activated Ab-CEA was then added to the Cys functionalized electrode (Au-SPEs/Cys) and incubated overnight at 4ºC. Finally, the electrode Au-SPEs/Cys/Ab-CEA was incubated with glycine (Gly) (50 mM) for 1 h at room temperature, to block non-specific binding sites in the sensing film. These steps of electrode construction were monitored by EIS and CV. EIS was performed from 10^5 to 10^{-1} Hz, using a number of frequency of 50 with amplitude of 0.01, and CV used a potential applied range from −0.4 V to 0.6 V, at a scan-rate of 50 mV/s.

3.2.5 Electrochemical measurements

Electrochemical measurements for CEA calibration were made in a 5mM $[Fe(CN)_6]^{3-/4-}$solution, prepared in Phosphate buffered saline (PBS 0.01 M), of pH 4.5, conducted with EIS at frequency of 10 Hz and with step potential of 2.5 mV (Figure 13 B). The PBS solution was composed of 0.01 M Na_2HPO_4, 0.0027 M KCl, 0.137 M NaCl, and 0.0018 M KH_2PO_4, with the final pH adjusted to the desired value with H_3PO_4, 1M.

Calibration curves used CEA standard solutions ranging from 0.25 to 250 ng/ml, prepared in PBS buffer (pH 4.5) and foetal bovine serum (FBS) diluted by 1:10 in PBS (pH 4.5, 0.1 M). Each solution was let stand for 30 minutes at the electrode surface (Figure 13 B). The selectivity study was performed by incubating interfering species in a similar way. The solutions selected for this purpose were 1.0×10^{-4} g/ml of glucose, 1.0×10^{-3} g/ml of creatinine, also prepared in PBS buffer.

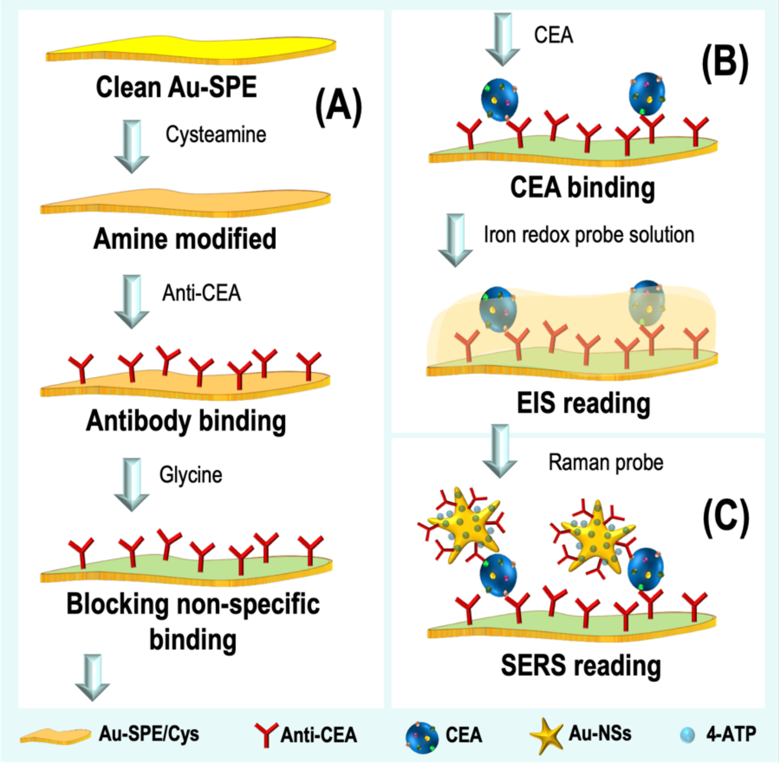

Figure 13: Schematic representation of the assembly of the immunosensor (A) and its electrochemical (B) and SERS (C) readings, after incubation of CEA (and reading by the iron redox probe) and the Raman probe, respectively. The antibody binding in the assembly stage was made after modifying the Ab-CEA with EDAC/NHS chemistry.

3.2.6 Synthesis of the goldnanostars

The synthesis of the AuNSs started by producing the Au-seeds. For this purpose, a 0.5 mM HAuCl4 aqueous solution was boiled, under continuous stirring and added 10 ml of 1% citrate solution. The reaction was allowed to proceed at the same temperature for 20 min and, after this, the resulting solution allowed to cool down. Then, 10 ml of a 2.5 mM PVP solution was added, under continuous stirring, and the Au-seeds were formed overnight.

The second part of the procedure was made according to [241]. In this, the Au-seeds were centrifuged (4500 rpm, 45 min), suspended in ethanol, and concentrated to 1.5 mM. The AuNSs were obtained by dissolving 1.5 g of PVP in 15 ml of DMF, sonicating the resulting solution and putting it on ice after, under constant shaking. Then, 40 µL of $HAuCl_4$ (100.9 mM) were added to this solution, monitored by the addition of 320 µL of Au-seed (1.5 mM), and kept under stirring for 1 MIPs. The excess of PVP was removed by three centrifugation-dispersion cycles with ethanol (3500 rpm, 40 min). The resulting AuNSs were store at 4ºC until use (Figure 14). The final concentration of AuNSs was calculated according *Scarabelli et al*. using absorbance method UV-Vis [241], [242].

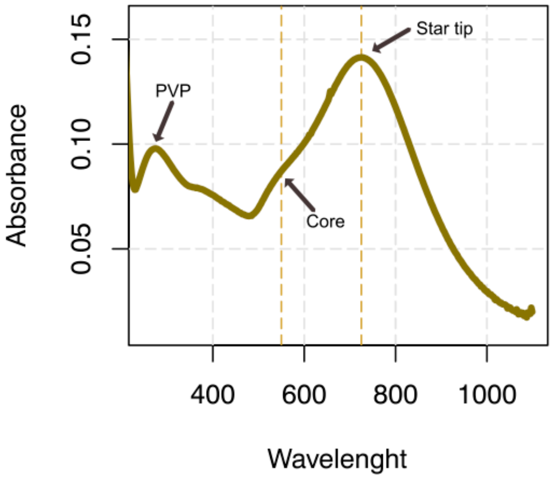

Figure 14: UV-Vis spectra of AuNSs.

3.2.7 Raman probe assembly

The Raman probe (Au-NPs/4-ATP/Ab-CEA) was setup by following the method reported by [243]. First, 4-ATP (1.0×10^{-5} M, in absolute ethanol) and AuNSs (0.6 mM) were mixed, in 1:1 ratio, and the resulting mixture was shaken for 4 hrs, at 25ºC. The resulting solution was centrifuged at 4500 rpm, for 20 min, at 25ºC, to remove the excess of unbound 4-ATP. The pellet (AuNSs/4-ATP) was re-suspended in 100 µL of PBS buffer (pH 7.4) and added of 20 µL of Ab-CEA. This solution was stirred overnight, at room temperature, yielding the formation of AuNSs/4-ATP/Ab-CEA. With the purpose of removing the unbound Ab-CEA, the solution followed the same centrifugation procedure described before. The pellet was re-suspended in 200 µL of PBS, yielding the ready to use solution of AuNSs/4-ATP/Ab-CEA.

3.2.8 SERS measurements

Electrodes with the Raman probe AuNSs/4-ATP/Ab-CEA incubated on the sensing surface (Figure 13 C) were analysed without prior treatment. Experiments were conducted with a 785 nm laser, hitting the samples with a power of 3 mW and considering a slit aperture of 50 µm. The laser spot was about 0.8 µm and defined as focused by the 100× lens objective. Photobleaching was set to 5 min and the Raman spectra were collected with an integration time of 2s and 5 accumulations, in the range 800-2000 cm^{-1}. The collected data was analysed in OMNIC software (Thermo Fisher Scientific).

3.3 Results and Discussions

3.3.1 Immunosensor assembly

The immunosensor assembly followed the several stages described in Figure 13 A. In general, these include (i) cleaning stage, (ii) preparation of the electrode to receive the antibody, (iii) antibody binding, and (iv) the blocking the non-specific interaction. Each of these stages was monitored by EIS, in order to monitor and control the progresses of each stage of modification upon the immunosensor assembly.

3.3.1.1 Amine layer

The next stage consisted in preparing the gold WE to receive the antibody, Ab-CEA. Cys was selected for this purpose. It binds to the gold surface through –SH bonds and organizes itself by self-assembly [244] in a monolayer arrangement, exposing amine groups to the outer surface. Moreover, amine surfaces are suitable for protein binding [245], [246].

The successful binding of Cys was confirmed by the decreasing semicircles in the EIS spectra (Figure 15). This behaviour corresponded to a decrease in the R_{ct} of the standard hexacyanoferrate redox-probe (negatively charged), most likely reflecting the positively charged amine groups at the electrode surface. Overall, this agrees with previous results reported in the literature [247].

3.3.1.2 Antibody binding

The Ab orientation in the gold surface is of fundamental importance for the correct performance of the immunosensor. One may find in the literature several orientation types for antibodies including *flat-on* (random adsorption attached on surface) or *tail-on* (Fc fragment attached on surface) [248]. *Flat-on* is a straightforward approach, as it requires only random adsorption of the antibody. *Tail-on* allows, in principle, that both Fab fragments in the antibody are available for binding, yielding therefore more sensitive responses [248]. This requires previous treatment of the antibody, which may include activating the carboxylic groups distributed in the antibody, including those existing in the Fc terminal, to allow its subsequent covalent binding to the amine surface at the immunosensor through an imine bond.

Both orientations were tested herein. In the *flat-on* approach, the antibodies were just let stand at the amine surface, overnight, at 4ºC. In the *tail-on* approach, the -COOH groups of the antibody were activated by EDAC/NHS chemistry, in MES buffer, and then incubated in the amine sensing area. The data obtained by these two approaches is shown in Figure 15 and suggested the selection of the *tail-on* binding. When compared to *flat-on*, the *tail-on* approach yielded a higher R_{ct} increase, thereby suggesting that the number of antibodies accommodated in the same sensing area were higher. This may be justified by an oriented binding of these antibodies, which would accommodate a higher number of proteins per unit area. Moreover, antibodies could partially cross-link through the activated carboxylic groups and their inherent amine groups, but the side effect of this activation chemistry would implicate a higher number of antibodies bound at the immunosensing surface and probably a higher number of CEA-binding sites.

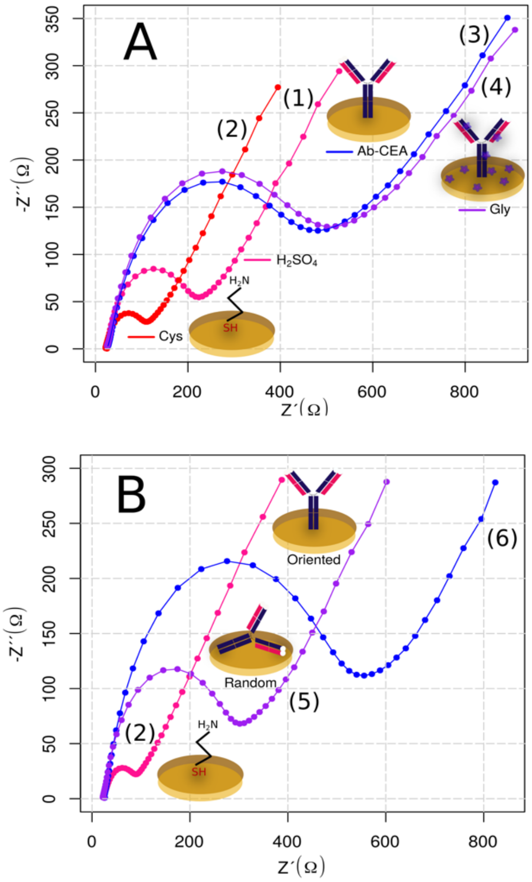

Figure 15: EIS spectra of the different stages of the immunosensor assembly (A) and the form of binding the antibody (B). (1) Electrochemical cleaning with H_2SO_4; (2) Cys layer on gold surface (Au-SPEs/Cys); (3) Oriented Ab-CEA immobilisation (Au-SPEs/Cys/Ab-CEA); (4) Gly adsorption to block non-specific sites (Au-SPEs/Cys/Ab-CEA/Gly); (5) using random adsorption of antibody; (6) oriented binding of the antibody, in which –COOH groups at the Fc terminal were activated for subsequent reaction with the amine groups in Cys.

3.3.1.3 Blocking non-specific binding

Sites on the Au-SPEs/Cys/Ab-CEA that could lead to non-specific binding (towards another chemical species other than CEA) should be blocked to avoid positive bias. This was achieved by incubating the modified surface in Gly. After this, EIS data evidenced an increase in the R_{ct} (Figure 15), thereby suggesting that Gly was bound to the surface. In this, activated carboxyl groups from the Ab-CEA were blocked and electrostatic/ionic interactions promoted by the amine and carboxyl groups in Gly were established with the different chemical moieties on the sensing layer.

3.3.2 pH dependence of the immunosensor response

The response of the CEA immunosensor was tested under different pH conditions. Values of 4.5, 6.0, and 7.5 pH were selected for this study, trying to combine opposite charge features of CEA, a glycosylated protein with an isoelectric point ~6 [247]. Overall, CEA has a positive dominant charge at pHs below 6 and a negative dominant charge at pHs above 6. To this end, the histidine conserved residues in CEA play a fundamental role in the pH-dependent binding through the imidazole chain, which at physiological pH is neutral and at acidic pH is positively charged [249].

This pH effect was tested by calibrating the immunosensor with CEA standard solutions of increasing concentrations, from 0.25 to 250 ng/ml, prepared in PBS buffer of the corresponding pH. Each standard solution was incubated for 30 minutes on the sensing surface and this solution replaced by the hexacyanoferrate redox probe for checking the EIS response. The representative data so obtained herein is shown in Figure 16.

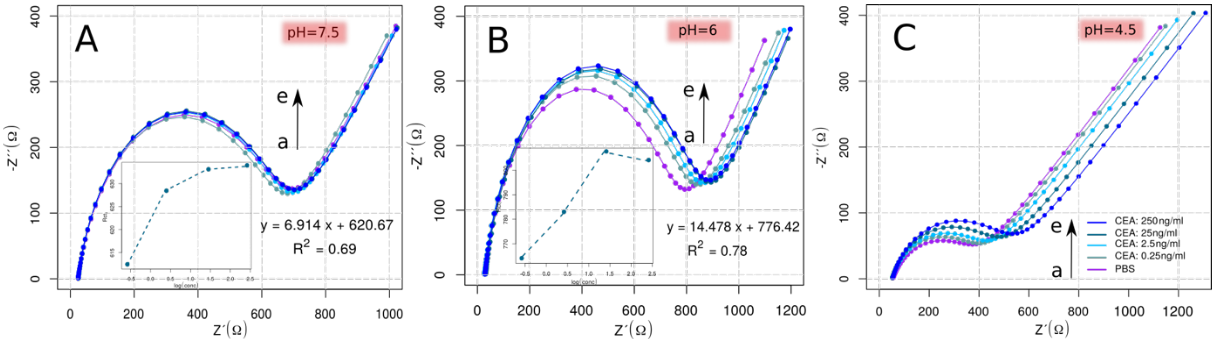

Figure 16: EIS spectra of CEA calibrations made under different pH conditions, namely 7.5 (A); 6.0 (B) and 4.5 (C), for a CEA concentration range of 0.25 to 250 ng/ml.

Overall, the best calibration features were obtained for pH 4.5 (Figure 16 C), with average slopes of 39.8 Ω/decade, squared correlation coefficients >0.99 and a lower limit of linear range (LLLR) of 0.25 ng/ml. In contrast, calibrations in pH 6 (Figure 16 B) had a narrower linear response and calibrations in pH 7.5 (Figure 16 A) showed steady signals for the increasing CEA concentrations, thereby displaying an insensitive behaviour for the target protein.

Thus, it was clear that decreasing pH values were linked to the increasing sensitivity of the calibration curve, reflected by the increasing changes of the R_{ct} for the same concentration interval. This could be logically related to the increasing positive charge of the CEA structure, as the pH is lower than the natural isoelectric point of the protein. However, when the calibrations under different pH values are compared, the greatest difference comes from the blank signal, which decreased significantly when the pH was 4.5. Thus, it is likely that the observed behavior was directly linked to the protonation of Gly used to block the non-specific binding, with an isoelectric point of ~6.1 and already present in the sensing surface. This positively charged surface could decrease the R_{ct} of the negatively charged hexacyanoferrate redox probe. In addition to this, the presence of the protein would also contribute to an increase in the R_{ct} of the sensing surface for being a non-conductive material, but its positive charge at pH 4.5 could also contribute to decrease the R_{ct}. From these opposing effects, the experimental results indicated that the non-conductive feature of the protein prevailed. Moreover, these two opposing effects could also justify the moderate signal variation observed along the calibration.

Figure 17 A shows the typical Nyquist plots of the immunosensor against increasing CEA concentrations prepared in PBS buffer, pH 4.5, and Figure 17 B shows the corresponding EIS calibration curve, plotting R_{ct} [Au-SPEs/Cys/Ab-CEA] against the logarithm of CEA concentration. Linear responses were observed from 0.25 to 100 ng/ml, thereby including the typical physiological levels of CEA in serum samples, 3 to 5 ng/ml [250].

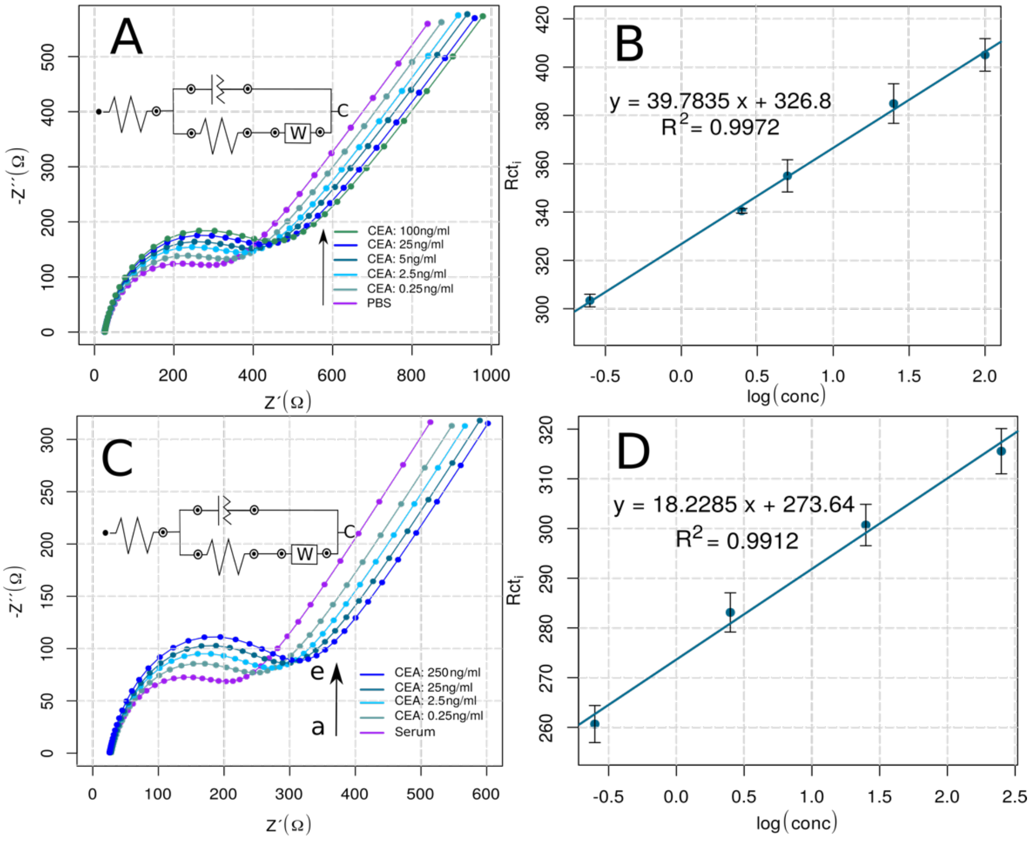

Figure 17: EIS spectra of the immunosensor calibration in PBS (A,B) or FBS (C,D), pH 4.5, after incubation of the blank and increasing concentrations of CEA standard solutions, from 0.25 ng/ml to 100 ng/ml (A) or to 250 ng/ml (C), and the corresponding calibration curve (B,D).

3.3.3 Electrochemical response in serum

The calibration of the biosensor was further established in standard solutions that were prepared in a serum background. This had the purpose of ensuring a valid correspondence between standards and samples. To this end, FBS was used, which has a close composition to human serum, much closer than PBS. The results obtained under these conditions are shown in Figure 17 C. In general, serum samples showed good analytical features, displaying a linear range from 0.25 to 250 ng/ml, with a slope 18.23 Ω/decade concentration and a squared correlation coefficient of 0.9912. Compared to calibrations in PBS, the slope of the calibration decreased, but the linear response range remained the same.

In general, it is clear that the device showed a controlled response against CEA concentration in a complex background as FBS, suggesting that it may produce accurate date in the analysis of serum samples.

3.3.4 Selectivity study

The study of the effect of specific compounds of physiological fluids in the sensing device is fundamental, for an effective analytical application. This was evaluated by checking the EIS response against interfering species. The interfering species selected herein were creatinine and glucose, following the normal composition of serum samples. The concentrations of creatinine and glucose were set to 1.0×10^{-3} and 1.0×10^{-4} g/ml, respectively, considering a possible 10× dilution of an original serum sample. Each solution was incubated in the sensing layer for 30 min, the same time given for the standard solutions in the calibration procedure. Tests were made in two different conditions, using binary (CEA and interfering species) or single component (only interfering species) solutions.

The results obtained using single component solutions are shown in Figure 18 B, incubating separately the interfering species and comparing the data to the response of CEA (5.0 ng/ml). These conditions corresponded to the worst scenario, because there was no other ion competing for the sensing layer with the interfering compound, which would allow a significant non-specific rebinding response. Each assay was conducted in a different Au-SPEs/Cys/Ab-CEA biosensor, in order to circumvent contamination from previously bound CEA or interfering specie. The average % deviation produced was 4 % for creatinine and 3 % for glucose, thereby evidencing a negligible interference effect.

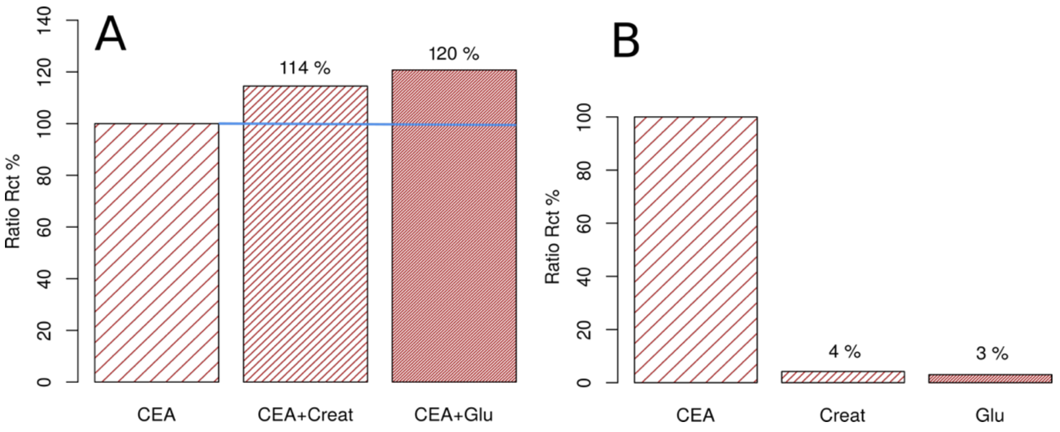

Figure 18: EIS signals obtained for a single solution of CEA, compared to solutions of interfering species (Creat and Glu) prepared in the presence of CEA (A) or without CEA (B).

The results obtained with the binary solutions are shown in Figure 18 A, checking the interference of Creatinine and Glucose in the response of a 0.25 ng/ml of CEA solution. To this end, the response of the immunosensor was evaluated both for solutions having only CEA and having CEA plus interfering species, where a competition between CEA and interfering species for the same paratope sites of the antibody was allowed. Again, this study used different Au-SPEs/Cys/Ab-CEA sensing units to test each condition. The average % deviation was 14 and 20% for creatinine and glucose, respectively. These results are most likely reflecting the variability of the different sensing units, rather than the interfering effect of any of these compounds. Yet, the obtained data confirmed the good selectivity of the devices. Overall, the results obtained evidenced the very good selectivity features of the sensing layer, thereby confirming that the immunosensor had a high affinity for the target molecule when in the presence of side-components.

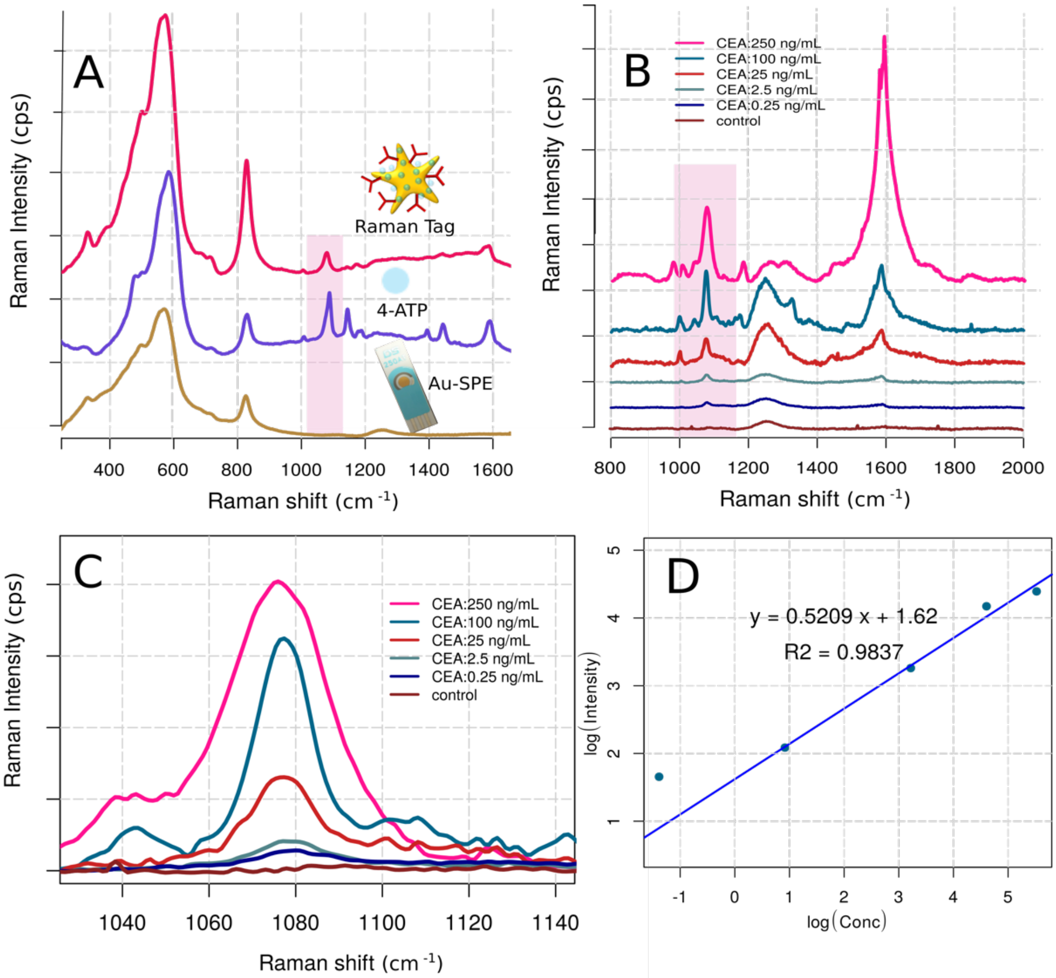

Figure 19: Raman spectra for testing the materials (A), including Au-SPEs, Au-SPEs with adsorbed 4-ATP and Au-SPEs with adsorbed Raman tag (AuNSs/4-ATP/Ab-CEA); and (B) after incubation of Au-SPEs/Cys/Ab-CEA in buffer or increasing concentrations of CEA (concentration 0.25, 2.5, 25, 50 and 250 ng/ml), subsequently incubated in the Raman tag; (C) highlighting a smaller Raman shift range of the data in (B); and (D) the corresponding calibration linear response.

3.3.5 SERS Probe assembly

Raman spectroscopy was used as a second analytical technique to evaluate the same sensing surface, having in mind both qualitative and quantitative data [251]. For this purpose, AuNSs were produced and modified with a suitable Raman reporter (4-ATP) and Ab-CEA, as described before. 4-ATP was bound covalently to the gold nanostructures through its thiol group. The antibodies were bound by adsorption to the AuNSs, which may involve different chemical functions at the outer surface of this protein.

Figure 19 A shows the spectra for a bare Au-SPEs, acting as control. The direct incubation of 4-ATP on this electrode is shown also in the same Figure 19 A and highlights a new peak at 1079 cm^{-1}, which is a characteristic peak of AuNSss4-ATP systems [252]. The other peaks present in the Au-SPEs remained and additional peaks with lower Raman intensity were also observed, also signalling the presence of the reporter. These less intense peaks appeared between 1500-1600 cm^{-1}, and were generated by aromatic ring vibrations [253].

Finally, when the probe AuNSs/4-ATP/Ab-CEA was incubated on the Au-SPEs, the same peak signalling the presence of 4-ATP at 1079 cm^{-1} was evidenced (Figure 19 A). Moreover, the other peaks signalling the background presence of the Au electrode were also enhanced, which probably resulted from a Raman enhanced effect from the AuNSs close to this surface. Overall, this data confirmed that the peak centred at 1079 cm^{-1} signalled the presence of the Raman tag, indirectly signalling the existence of CEA bound to the Au-SPEs/Cys/Ab-CEA sensing surface.

3.3.6 SERS AuNSs characterization

The AuNSs obtained here were characterized by TEM analysis. TEM images from isolated AuNSs showed a solid core bordered by several sharp, asymmetrical, and short branches (Figure 20). Moreover, images collected with several AuNSs suggested that the particles had similar sizes and were individually dispersed and not aggregated (Figure 20). Overall, the TEM images indicate that the medium average diameter of the AuNSs is ~30 nm.

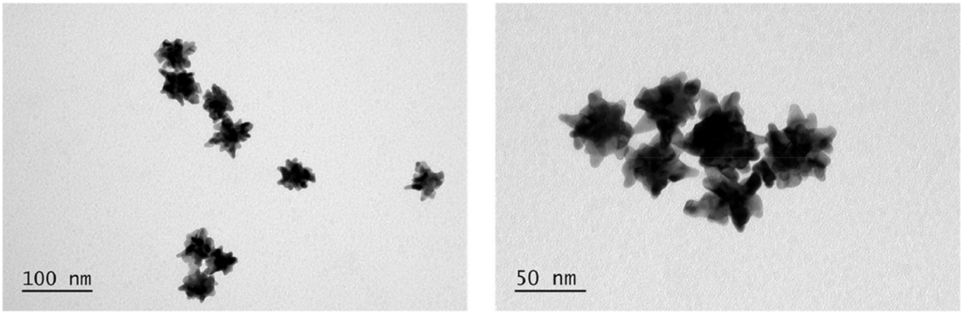

Figure 20: TEM images of the AuNSs.

3.3.7 SERS response in buffer

The immunosensor incubated in different concentrations of CEA (Au-SPEs/Cys/Ab-CEA/CEA), ranging from 0.025 to 250 ng/ml and prepared in PBS buffer pH 4.5, was exposed to the SERS tags. The Raman spectra collect by a power laser of 10 mW were collected in different spots in each WE (minimum n = 3), for each CEA concentration (Figure 21). The sensors showed a linear range lower than 0.025 ng/ml and a coefficient of correlation > 0.996. The peak intensity at 1079 cm^{-1} increased with increasing protein concentrations, demonstrating that a higher number of reporter probes were present. The overall increase in Raman intensity signal was about 6×.

Overall, the results obtained demonstrated that SERS detection improves the operational features of the biosensor when compared with EIS technique.

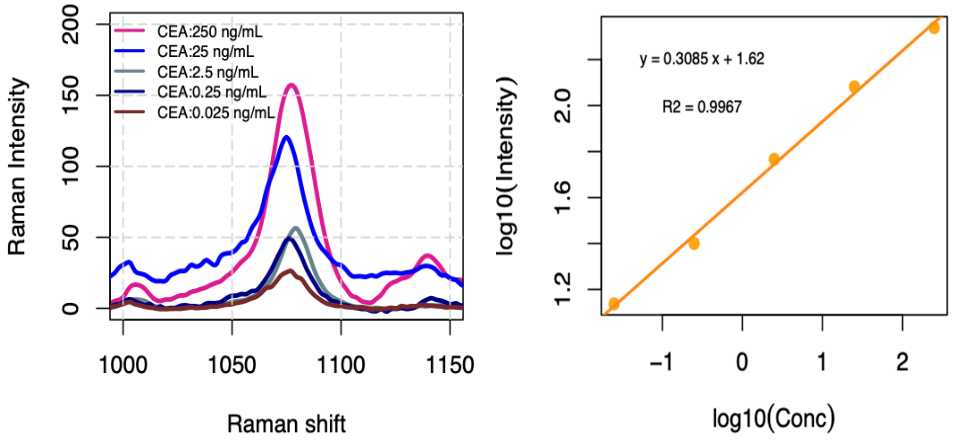

Figure 21: Raman spectra for testing the materials with adsorbed Raman tag (AuNSs/4-ATP/Ab-CEA); and (B) after incubation of Au-SPEs/Cys/Ab-CEA in buffer or increasing concentrations of CEA (concentration 0.025, 0.25, 2.5, 25, 50 and 250 ng/ml), subsequently incubated in the Raman tag.

3.3.8 SERS response in serum

The immunosensor incubated in different concentrations of CEA (Au-SPEs/Cys/Ab-CEA/CEA), ranging from 0.25 to 250 ng/ml and prepared in FBS, was exposed to the SERS tags. The Raman spectra were collected in different spots in each WE (minimum *n* = 3), for each CEA concentration (Figure 19 B). Then, the peak of 4-ATP was followed and used to estimate quantitative data about the concentration of CEA present (Figure 19 C).

In general, a higher amount of CEA in the surface yielded a higher peak intensity at 1079 cm^{-1}, thereby revealing that a higher number of reporter probes were present. This was valid from 0.25 to 250 ng/ml of CEA, the same concentration range of response for the EIS detection. Moreover, a linear correlation was established between the logarithm of the Raman intensity (*y*axis) against in the logarithm of the CEA concentration (*x* axis), as shown in Figure 22. The squared correlation coefficient of this linear trend confirmed a good agreement between the collected data, especially considering that different electrodes were used to construct this calibration.

Overall, the results obtained confirmed that the modification of common SPEs may be employed for a dual detection, combining EIS and SERS approaches as an *in-situ* validation of the analytical response obtained. This is mostly valuable under point-of-care conditions, in which accuracy is a critical point.

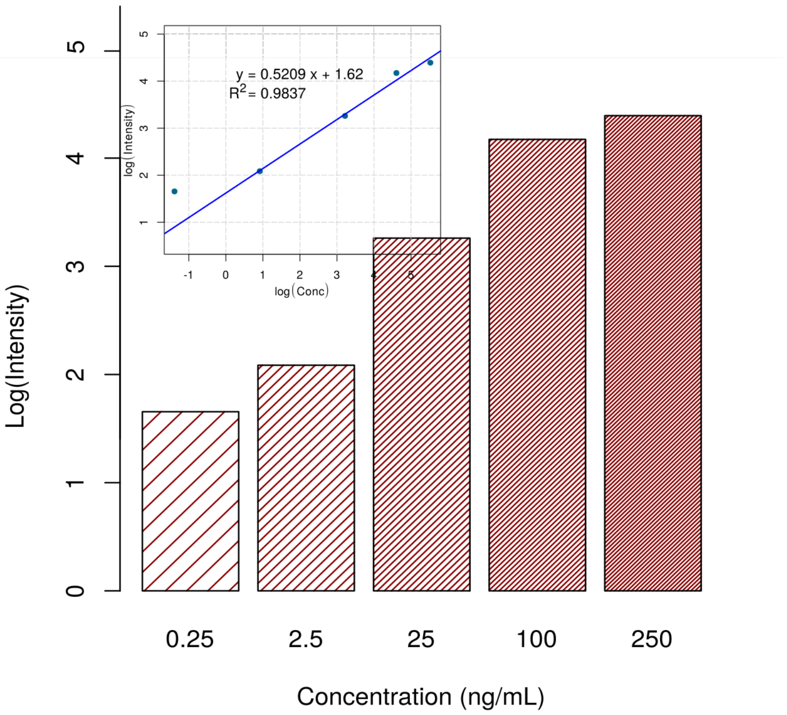

Figure 22: Raman bar plot corresponding to the logarithm of the Raman peak intensity at 1079 cm^{-1} versus the concentration of the CEA (ng/ml). Inset: the corresponding calibration curve, plotting in *x*-axis the logarithm of CEA concentration.

3.4 Conclusions

The experimental results showed that EIS was an adequate technique to follow the performance of the immunosensor. In general, this immunosensor was developed in a simple way, showing its potential for clinical applications. This sensor was used to determine CEA in a real serum matrix, showing sensitive response at concentrations within the physiological levels.

There are reports in the literature where the detection method manages to go to lower values than those presented in this work. However, the concentration of CEA in reference serum from healthy individuals is lower than 2.5 ng/ml, and patients with cancer are expected to have much higher levels. Thus, the sensitivity presented in this biosensor is more than enough to distinguish cancer patients from healthy ones. Moreover, this method is effective and presents a dual response using electrochemical techniques combined with Raman spectroscopy. Importantly, a straight comparison between both detection modes suggests that SERS yields a biosensor with improved operational features, when compared to EIS. In this regard, the LLLR of SERS analysis is 10× lower than that obtained by EIS.

In general, the combination of the selectivity of the antigen-antibody binding in an immunosensor with the novel detection capacity of the SERS technique appears highly promising. The technical approach described herein may be further evolved by combining different biorecognition elements in the same approach, for example, enzymes on the SPE and antibodies on the Raman tag. This would decrease even further the possibility of having an interfering effect of the sample. In addition, the present achievements represent the starting point for further improvements by extending the present approach to recent advanced metal electrode with Raman enhancers, such as the metal nanowire arrays and metal nanostars [254], which can be used as high sensitivity devices both for electrochemistry and SERS.

Overall, this device opens avenues for highly accurate readings the SERS-based technology providing strong reason to conceive, in the near future, the construction of reliable point-of-care devices that will contribute to the fast-developing field of personalized medicine.

Chapter 4. Poly(Thionine)-Modified Screen-Printed Electrodes for CA 19-9 Detection and Its Properties in Raman Spectroscopy

The results presented in this chapter are based on publication *“Poly (Thionine)- Modified Screen-Printed Electrodes for CA 19-9 Detection and Its Properties in Raman Spectroscopy*“ by **Castaño-Guerrero, Y**., Romanguera-Barcelay, Y., Moreira, F., Brito, W., R., Fortunato, E., Sales, M.G., Poly (Thionine)-Modified Screen-Printed Electrodes for CA 19-9 Detection and Its Properties in Raman Spectroscopy. Chemosensors (2022), 10 (3), 92. **doi:** 10.3390/CHEMOSENSORS10030092/S1. This chapter presents a study of electrochemical and spectroscopy properties of TH. PTH is used as monomer for MIP as well as electrochemical probe to reading. Finally, it discusses the potential use of PTH for SERS readings, as complementary information to electrochemical data.

4.1 Introduction

The use of conventional electrodes has evolved through several designs and one of the most used is based on chemically modified electrodes (CME). A CME is a necessary approach to solving sensitivity problems in the detection of analytes that are chemically similar [255]. The literature reports many examples of electrodes modified with nanomaterials [256] and molecules [257], [258], such as multiwall carbon nanotubes (MWCNTs) [259], carboxylic acid [260], poly(glutamic acid) [259], penicillamine [261], titanium oxide [262], and others [255], selected according to the intended need.

The possibility of creating polymeric structures in-situ to generate CMEs is currently finding wide interest, also in (bio)sensors with electrochemical detection. A wide range of polymers may be produced by electropolymerization, as long as electrical conditions that enable the formation of radical species at the electrode surface are applied to the electrochemical system. The resulting polymers so formed at the electrode surface change the electrical features of the receptor surface, which becomes either more conductive or more insulating. The resulting polymers may also display electroactive features, signalling the presence of the polymer.

PTH is among such polymers. It has received considerable attention as a polymeric film for sensing purposes, yielding improved sensitivity and lower limits of detection [255]. TH is its monomeric species, which is a redox dye that has been extensively studied [263]. PTH modified electrodes have been prepared in a simple way by CV having a solution of TH under potential sweep in the range of -0.4 to +0.4 V [264]; the specific potential range of interest depends on the electrical features of the receptor substrate. They may also be obtained by chronoamperometry, in which a constant oxidation potential is applied for a given time [265]. Overall, it has been accepted that the most probable mechanism for the electropolymerization of phenothiazine derivatives is the bond between the nitrogen atom of the amine group and the atom of the phenothiazine ring [266].

Still, the final electrochemical stability of the PTH modified electrodes is very critical in sensing and it depends greatly on the medium in which TH solutions were prepared (ionic content, type of ionic species and pH) and the electrochemical conditions applied. While PTH films prepared by applying constant positive voltage in 0.05 M H_2SO_4 are not stable when evaluated in a neutral medium, those prepared in two oxidation steps of constant potential and cyclic scanning in neutral PhB are stable [255]. In turn, *Ferreira et al.* conducted electrochemical characterization studies of PTH films produced by different scanning speeds and variations in the number of potential cycles. They concluded that the electroactivity and stability of the resulting PTH is pH dependent. In a wide range of pH values, 1.3 to 9, the authors demonstrated that when increasing the pH to more alkaline media, a lower electroactivity is observed that is associated with the loss of electroactive sites. In other words, the transfer of electrons between neighbouring sites is lower at more alkaline pH [267]. *Yang et al.* presented what may be called a hybrid approach to prepare PTH-modified electrodes [265], by using two steps of constant oxidation potential and scanning of cyclic potential in neutral phosphate solution. The authors refer to two electropolymerization steps when, firstly, they subjected the electrode to a fixed potential for a few minutes, as the second step, voltametric cycles in a potential range with a constant sweep. *Gao et al.* modified C-SPEs with PTH to determine the oxidation of nicotinamide adenine dinucleotide (NADH) [268]. The electropolymerization was conducted in PhB pH 7.0 with 25 scanning cycles. The authors considered that 25 CV cycles were adequate to control the electroactive residues in the PTH films. Considering the intended application of this work, the use of SPEs as substrates allowed producing a simple, inexpensive, and versatile analytical approach for monitoring NADH. Overall, there are different electrochemical routes and chemical conditions for preparing PTH, which must be selected appropriately according to the electrochemical system employed.

Thus, this work was directed to the use of PTH as polymeric material assembled in-situ in SPEs substrates. SPEs used herein had carbon or gold substrates on the WE, as commercially available. PTH was used to tailor MIPs for a relevant biomarker protein, which act as biomimetic materials for antibodies. TH acted not only as a functional monomer assembling the MIPs materials, but also as an indicator of the electrochemical signal, posing the possibility of having the electrochemical reading of the SPE self-indicated and label-free. This concept was explored for targeting CA 19-9, a cancer biomarker in PC undergoing the electropolymerization of TH in neutral PhB in the presence of CA19-9 to generate imprinted cavities in a molecular dimension within the polymeric network. Readings were made in PhB and CA19-9 binding was followed by DPV, as it allowed measuring the concentration of specific electroactive species. The resulting structure of PTH was evaluated using Raman spectroscopy, along with a control material prepared in the absence of CA19-9 and AuNSs modified with TH.

4.2 Experimental Section

4.2.1 Equipment

The electrochemical measurements were performed in the potentiostat/galvanostat from Metrohm Autolab (Ultrecht, Netherlands). The C-SPEs and Au-SPEs were from DropSens (Oviedo, Spain) (DRP-C110, DPR-250AT). The potentiostat interconnected with SPEs through a box was obtained from BioTID (Oviedo, Spain), Portugal. Raman spectra were collected in a Thermo Scientific DXR Raman Microscope (Wisconsin, U.S.A.) with a laser of 532 or 785 nm operated at a 5 mW power and a confocal microscope with a 50× objective lens. The parameters of the observed Raman modes (frequency, line width, and amplitude) were obtained, using Igor software, from the best fit of a sum of damped oscillator functions [269].

4.2.2 Reagents and solutions

All chemicals were of analytical grade and water ultrapure Milli-Q laboratory grade. Sodium phosphate dibasic dihydrate (Na_2HPO_4) and *ortho*-phosphoric acid 85% (H_3PO_4) were obtained from Riedel-de-Häen (North Carolina, U.S.A); carbohydrate antigen 19-9(250 KU) (Biorbyt, Cambridge, United Kingdom) from human metastatic liver carcinoma was obtained from Biorbyt; sodium phosphate dibasic dihydrate, 99.5% ($Na_2HPO_4 \cdot 2H_2O$) was from Panreac (Barcelona, Spain); sodium dihydrogen phosphate dehydrate ($NaH_2PO_4 \cdot 2H_2O$) was from Scharlau (Pamplona, Spain); sulfuric acid (H_2SO_4) was obtained from BDH (Dubai, UAE); thionin acetate from Acros Organics (Geel, Belgium); oxalic acid dihydrate (126.27 g/mol) was obtained from Merck (Branchburg, NJ, U.S.A.).

4.2.3 SERS measurements

The synthesis of AuNSs was performed according to *Castaño-Guerrero et al. 2021* [164]. Briefly, the first step consisted of the production of Au seeds. These were prepared with a solution of 0.5 mM of $HAuCl_4$, and 10 ml of 1% citrate solution was added under stirring. To the resulting solution, 10 ml of PVP (2.5 mM) was added and left under stirring overnight to form Au seeds. The Au seeds obtained were centrifuged (4500 rpm, 45 min) and concentrated to 1.5 mM.

The AuNSs were prepared with a solution with 1.5 g of PVP (2.5 mM) in 15 ml of N-N-Dimethylformamide (DMF) and sonicated. To this solution, 40 µL of $HAuCl_4$ (101 mM) was added, followed by the addition of 320 µL of the Au seeds (1.5 mM). After 1 MIPs of stirring, the solution was centrifuged to remove the excess of PVP, using three cycles of centrifugation-dispersion with ethanol (3500 rpm, 40 min). The resulting AuNSs was stored at 4 °C until use.

The Raman probe (AuNSs/TH) was set-up with a TH solution (1.0×10^{-3} M) in absolute ethanol mixed with the AuNSs (0.6 mM) solution, in a 1:1 ratio, and shaken for 1 MIPs, at 25 °C. The resulting solution was centrifuged at 4500 rpm for 20 min at 25 °C to remove the excess of unbound TH. The Raman probe AuNSs/TH was incubated until dry on the Au-SPEs.

4.2.4 MIPs assembly for CA 19-9

The electropolymerization of TH was made on C-SPEs or Au-SPEs (

Figure 23) to generate MIPs films for CA 19-9. These films were assembled in several steps. First SPEs underwent a cleaning stage by exposing the 3-electrode system to a H_2SO_4 solution (0.5 M), following 15 cycles of a CV procedure, between –0.2 and 1.2 V, at a scan rate of 0.05V/s. Then, the C-SPEs were modified by incubating a TH solution (10^{-3} M) on the WE, for 1 MIPs. The Au-SPEs were electrochemically modified by CV cycling of the same solution, under the potential range –0.4 to 1.2 V, at scan-rate of 0.05 V/s. The electropolymerization of TH for generating the MIPs material was the following step. To this end, the TH solution (10^{-3} M) was mixed with CA19-9 (1 KU) and incubated on the 3-electrodes, to undergo 15 CV cycles, from –0.4 to 0.4 V (C-SPEs) or –0.4 to 1.2 V (Au-SPEs), at scan rate of 0.05 V/s. Finally, the template was removed by incubating the WE in oxalic acid (0.5 M) for 1 MIPs. The same steps were followed in the construction of the control non-imprinted polymer (NIP), in which CA 19-9 was excluded from the procedure. Each step of the MIPs/NIP assembly was followed by DPV.

The resulting MIPs/NIP electrodes were calibrated against CA 19-9 standard solutions, ranging from 0.010 to 100 u/ml, prepared in PhB solution, pH 7.4. After a selected incubation time, the electrochemical reading of DPV was collected, using a pulse amplitude of 0.05 V, a pulse width of 0.0167 s, and pulse period of 0.1 s.

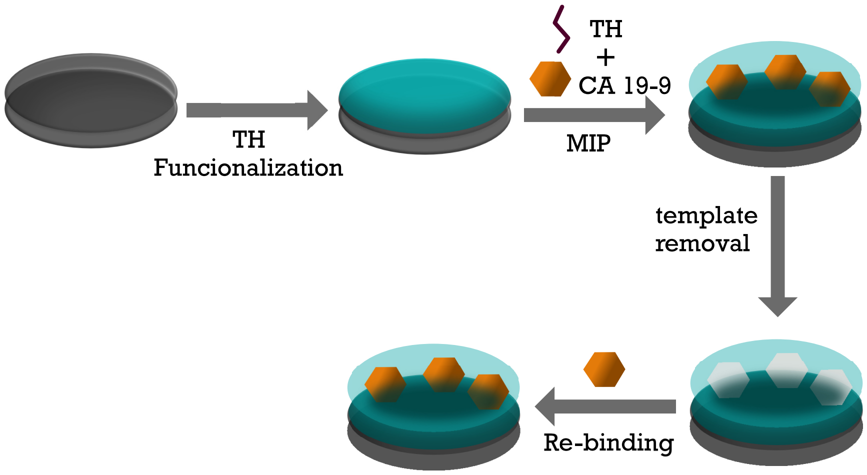

Figure 23: Schematic representation of the assembly of the biosensor. (A) clean electrode; (B) modification of the electrode with TH; (C) electropolymerization of TH to generate the MIPs materials with the template CA 19-9; (D) template removal; and (E) CA 19-9 rebinding to the imprinted sites.

4.3 Results and discussion

4.3.1 Formation and electrochemical studies of PTH on SPEs

The formation of the PTH film depends on the potential applied to the different substrates. In the first approaches reported it was indicated that one should not go below a potential of +1.1 V to undergo the electropolymerization of TH [265]. *Gao et al.* considered the upper potential limit in the potential sweep for preparation of PTH was the determining factor in obtaining PTH. On the other hand, it has been proposed that the oxidation potential should not be less than +0.9 V, because the potential of the electrode should be greater than the potential in which the oxidation of TH is occurring [268]. After various discussions, it was also accepted that the formation of PTH depends on the pre-anodization of the surface [264], from which a positive charge can accumulate at the electrode surface to generate the TH cationic radical. Thus, initial explorations over the TH electropolymerization were conducted to understand which potential would be required to oxidise TH between –0.4 and 1.2 V, at a scan rate of 0.050 V/s for 15 cycles. The results obtained herein are shown in Figure 24. A shoulder peak at a maximum potential of 0.9 V was evident in both substrates (C-SPEs and Au-SPEs). In the presence of thionine, around +0.9 V, an irreversible oxidation of the monomer occurred, generating a radical cation, starting polymerization. Globally, C-SPEs had more intense current signals than Au-SPEs (Figure 24 B), and it was also evident the formation of a pair of (apparently) quasi-reversible peaks (at +0.1 V and −0.2 V) was also evident. The formation of monomeric radicals occurred around +0.9 V as mentioned above. The redox couples that were most noticeable at the carbon electrodes (−0.2 V/+0.1 V) were attributed to the oxidation/reduction of the polymer. Other redox pairs at more negative potentials are also described in the literature [270], −0.23 V/−0.3 V, which was attributed to the oxidation/reduction of monomers but on CNT-modified surfaces, so these pairs of redox were not evident in our case. It was assumed that this monomer pair (not found) decreased in each voltammetry cycle, while the polymer pairs (−0.2 V/+0.1 V) increased, indicating the growth of PTH. The progressive blockage of electrons in the PTH layer was seen by the current decrease in consecutive CVs, with signals showing a tendency for an increased stabilization under an increasing number of CV cycles.

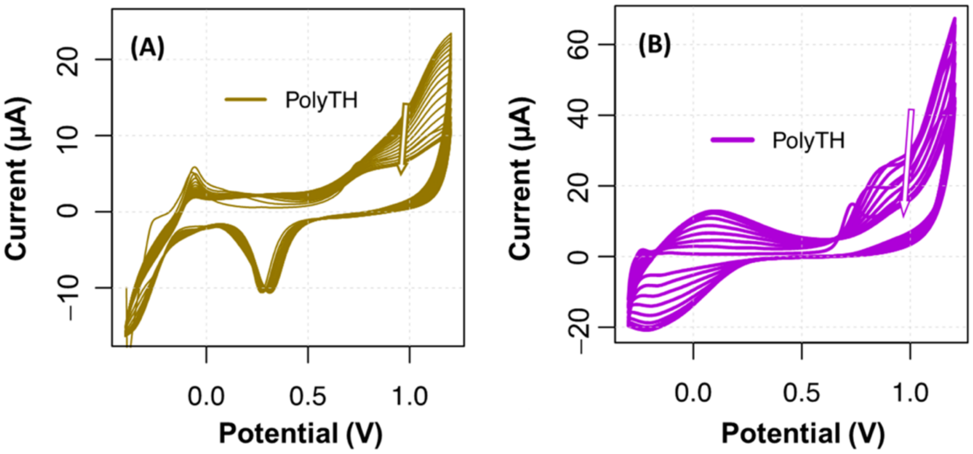

Figure 24: Consecutive voltammograms of a TH solution 1.0x10-3 M prepared in PhB, between -0.4 to 1.2 V, at scan rate 0.050 V/s for 15 cycles; (A) PTH, onto gold surface; (B) and carbon surface.

The electropolymerization curves on Au-SPEs showed two oxidation peaks (Figure 24 A), which are attributed to the redox reaction of the molecular layer being formed [271]. The anchor of TH to the Au-SPEs has been proposed to occur covalently when TH is first modified into a diazonium salt, which undergoes electrical reduction through nitrogen cleavage under cathodic conditions, at about 0.9 V [272]. Eventually, the TH may bind to the gold via sulphur or nitrogen atoms, which are quite common bonds that are energetically favoured.

It is known that by increasing the number of potential cycles during electropolymerization, the thickness of the polymeric film tends to be higher, but this is coupled to increased resistances that may hinder the electrochemical response. In the case of PTH, the increasing film thickness also causes a shift from electronic transfer in thin films to diffusion-controlled processes in thick films [267]. Yet, the purpose of having a first layer of TH/PTH was to have a stable binding between the electrode substrate (carbon or gold) and the subsequent MIPs or NIP film. Thus, no matter the number of cycles, the important aspect here was to have TH bound to the surface. From the studies made, it was clear that a stable PTH film was obtained for 15 CV cycles.

4.3.2 Preparation of an imprinted film of PTH for CA 19-9

The imprinted film was obtained by in-situ electropolymerization of TH in the presence of CA 19-9 (MIPs). First, both gold and carbon electrodes were modified with TH polymeric films formed under applied potentials or by simple casting, to ensure that the MIPs film was strongly bound to the electrode surface. The use of PTH to generate a MIPs material was also meant to have an electrochemical probe at the sensing material, which would avoid the need for an external redox probe. In this regard, *Cheng et al.*, explored the properties of TH in a biosensor for DNA recognition by integrating zirconia-reduced graphene oxide nanocomposites [273]. Another use of TH as an electrochemical probe is the study reported by *Zhou et al.*, in which graphene oxide was modified with TH [274].

The presence of CA 19-9 within the polymeric film being formed caused a displacement of the redox peaks towards more positive potentials in the cyclic voltammogram, both on carbon and gold substrates. This is shown in Figure 25, evidencing potential shifts of 50 mV in the C-SPEs and 100 mV in the Au-SPEs. It is important to note that the upper potential value of electropolymerization in the C-SPEs was decreased from +1.2 V to + 0.4 V (C-SPEs). This was done because the [255] reported that the formation of the polymer may be obtained under this narrower potential after subjecting the carbon surface to +1.2V, which took place at the cleaning stage [255], [268].

The fact that C-SPEs generated higher current values, could be turn out advantageous in terms of sensitivity of the analytical readings. C-SPEs are also less expensive than devices produced with gold-based inks.

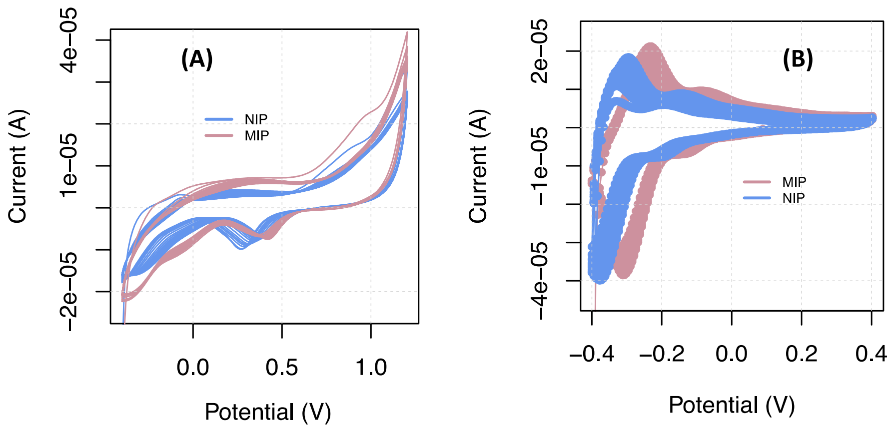

Figure 25: Consecutive voltammograms of a TH solution 1.0x10^{-3} M prepared in PhB, pH 7.4, with CA 19-9 (MIPs, pink), without CA 19-9 (NIP, blue), on the (A) gold electrode and the (B) carbon electrode.

4.3.3 Raman studies of TH on C-SPEs

Raman spectroscopy is one of the most powerful techniques for this purpose and has been widely used to study graphite and graphene. A characteristic Raman spectrum of the carbon electrodes is shown in Figure 26. The results showed that while the Raman peaks in crystalline graphene were the G (1579 cm^{-1})-associated symmetric E2g Raman mode [22], the intense peak at 1350 cm^{-1}, called the D band, is related to the A1g breathing mode, and it was observed because graphite oxidation and the subsequent reduction of graphene oxide significantly alter the basal plane structure of graphene [23]. The shoulder in the spectrum was interpreted to be peak D″ (1512 cm^{-1}), which has been reported for some carbon-based materials. In addition, some weak peaks at 1165 cm^{-1} were observed in graphene oxide flakes and powders. Raman's modes for graphene were also observed with different kinds of defects, such as rings with different numbers of C atoms and configurations of C-O bonds. In these cases, a peak at 1615 cm^{-1}, D′ band, has been attributed to the disorder-induced phonon mode due to crystal defects and defects in the graphene oxides [24].

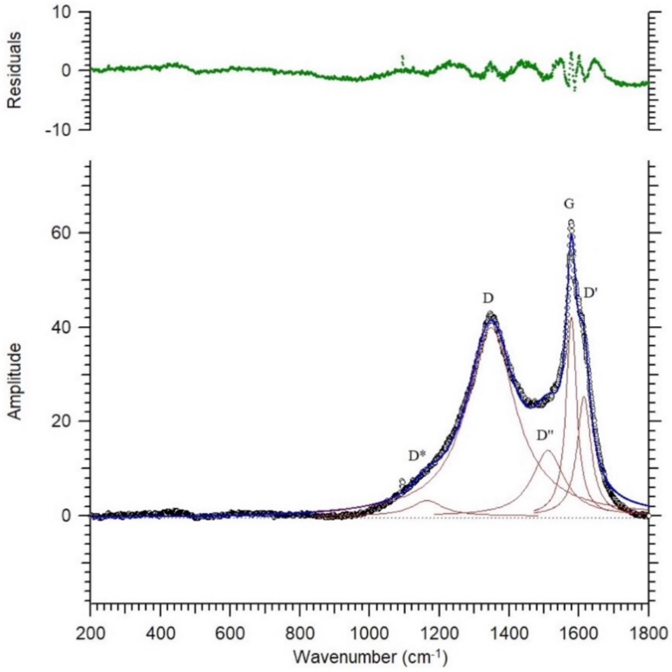

Figure 26: Raman spectra of the carbon electrode at room temperature, signaling peaks G, D, D', D''and D*.

By evaluating the Raman spectra of the same carbon electrode modified with TH, one may determine if it is present and if TH interaction with carbon is covalent or noncovalent in nature. This was carried out by observing the D band (1360 cm^{-1}) and following the alterations that may appear [25], as shown in Figure 27. The spectra of TH casted on carbon electrode is shown in Figure 28 b. It showed the Raman bands at 1350 and 1579 cm^{-1}, being a combination of both the characteristic bands of carbon and TH. The band at 1384 cm^{-1} corresponds to the 24 cm^{-1} Raman shift from the D band; this band is the defect band of carbon, and it was visible in the Raman spectrum. As such, one could confirm the noncovalent interaction hypothesis, given that functionalization with TH does not introduce defects in the carbon network. In agreement with the construction of the biosensor, the first layer deposited was by absorption of TH on the surface, and apparently no covalent bonds were established.

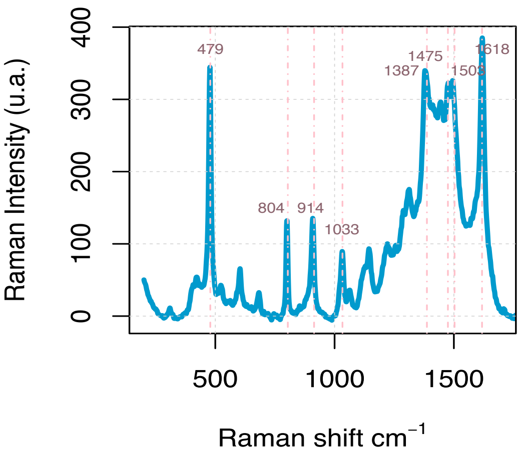

Figure 27: SERS spectra of TH powder showing the most relevant peaks.

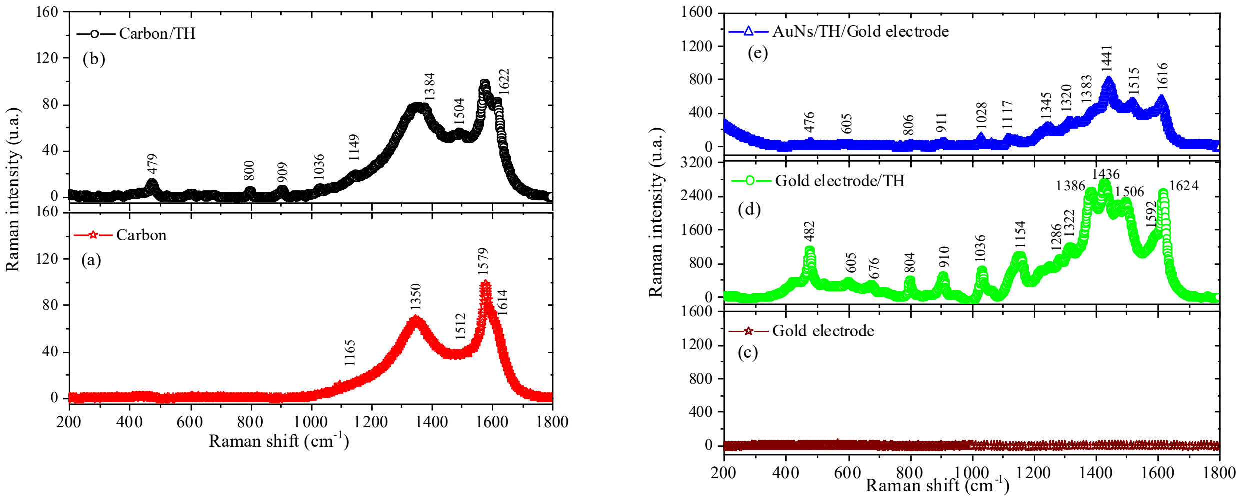

Figure 28: Raman spectra of carbon electrodes (a) or carbon electrodes modified with TH (b), along with gold electrodes (c) or gold electrodes modified with TH (d), and SERS of AuNSs with TH (e).

The eight main bands related to the presence of TH are shown in Table 1. Hutchinson et al. reported a band at 480 cm^{-1} that correlates well with the band at 479 cm^{-1} in the collected spectrum. This band was assigned to stretching of the C-S bond, central ring breathing, and Namino-H bond rocking [275]. Another band of TH was located 909 cm^{-1} and was assigned to ring breathing. The band at 1149 cm^{-1} was attributed to ring vibrations together with stretching vibrations of the N-H bond in the amino group. Finally, the important bands at 1504 and 1622 cm^{-1} were assigned to the aromatic ring stretching and Namino-H bending [272], [276].

Table 1: Raman bands of a TH solution on carbon or gold substrate assigning its presence and TH solid.

Thionine Solid (λ_{exe} = 645 nm)	**Thionine/ Carbon**	**Thionine/ Gold**	**AuNSs/Thionine/ Gold**	**Assignments**
1618	1622	1624	1616	$\nu(\text{C-C})_{\text{ring}} + \nu_{as}(\text{C-N-C})_{\text{ring}} + \delta(\text{N}_{\text{amino}}\text{-H})$
1503	1504	1506	1515	$\nu(\text{C-C})_{\text{ring}} + \delta(\text{N}_{\text{amino}}\text{-H})$
1475		1475	1476	$\nu(\text{C–C})_{\text{ring}}$
		1436	1441	$\nu(\text{C-C})_{\text{ring}} + \nu_{as}(\text{C-N=C})_{\text{ring}} + \text{rock}(\text{N}_{\text{bridge}}\text{-H})$
1387	1384	1386	1386	H-bending + ring-stretching
1320		1322	1320	rock (C-H) + $\delta(\text{N}_{\text{amino}}\text{-H})$
1283		1286		$\nu(\text{C-C})_{\text{ring}} + \nu(\text{N}_{\text{ring}}\text{-H})$
1224		1228	1214	β(C-H)+wag(C-H)
1150	1149	1154		$\nu(\text{C-C})_{\text{ring}}$
		1132	1137	$\nu(\text{C-C})_{\text{di(thionine)}}$
		1059	1114	$\nu(\text{N}_{\text{amino}}\text{-H})$
1033	1036		1028	$\beta(\text{C-H}) + \nu_{as}(\text{C-S})$ + rock (C-H)
887	909	910	889	ring breathing
804	800	804	802	
685		676		ring breathing +ν(C-S) + ν(C-H)
605		605	605	β(C-C) + rock (N_{amino}-H) + rock (C-H)
479	479	482	480	ν(C-S) + central ring breathing + rock (N_{amino}-H)

Moreover, there was an insignificant difference between the ratio I_D/I_G for 0.94 (carbon) and 1.04 (TH-carbon) presented in Table 2. As such, one could confirm the noncovalent interaction hypothesis, given that functionalization with TH does not introduce defects in the carbon network.

4.3.4 Raman Studies of TH on Au-SPEs

The Raman spectra collected for the gold electrode substrate (Figure 28 c) had no relevant peaks to comment, as expected for a gold material observed in Raman spectroscopy. In contrast, the modification of this gold electrode with TH solution that underwent the CV procedure yielded a spectrum with a wide range of vibrations, as evidenced in Figure 28 d.

The presence of TH on the gold electrode was evidenced by four main bands at 482, 1059, 1386, and 1624 cm^{-1} and twelve weaker bands at 605, 676, 804, 910, 1132, 1154, 1228, 1286, 1322, 1436, 1476, and 1506 cm^{-1}; the location of the bands as well as their respective assignments are represented in Table 1. The first four bands can be grouped by their vibration caused by stretching of the C-S bond, central ring breathing, and Namino-H bond rocking. The second one includes the contribution of stretching of C-N-C together with C-NH vibrations, whereas the last arises from aromatic ring stretching and Namino-H bending [272], [275], [276].

Table 2: Information about ratio between intensities and amplitude of carbon bands, D, D'',and G.

Carbon band	Frequency (cm^{-1})	Amplitude (comk-0unt)	FWHM (cm^{-1})	Area	ID”/IG	AD”/AG	ID/IG	AD/AG
D	1350	39,76	169,34	10575,5				
D”	1512	13,84	109,22	2374,9				
G	1579	42,04	35,73	2359,7				
					0,33	1,01	0,94	4,48
Carbon+TH band					ID”/IG	AD”/AG	ID/IG	AD/AG
D	1350	72,68	190,68	21769,3				
D”	1504	30,62	101,12	4871,44				
G	1580	70,18	44,79	4937,025				
					0,43	0,99	1,04	4,41

The band at 1506 cm^{-1} corresponded to central ring breathing, and Namino-H bond rocking of the amino group and the band at 1436 cm^{-1} were assigned to the formation of amino bridges between two phenothiazine molecules [272]. The bands of leucothionine were at 1154, 1228, and 1386 cm^{-1}. The signal corresponding to the vibrations of the ring of the dimeric structure formed was evidenced with the band at 1132 cm^{-1}. The band located near 605 cm^{-1} corresponded to the oscillation of the amino group [272]. The band at 1436 cm^{-1} arising from the asymmetric stretching vibrations of the C=N bond in the central ring, together with that at 1475 cm^{-1}, connected with the vibrations of quinoid rings, which suggest the transformation of grafted TH into the oxidized form [272]. Overall, the presence of TH on the gold substrate (as well as on the carbon) was clearly validated by the Raman studies.

4.3.5 Response of the MIPs Film to CA 19-9 in C-SPEs

For most dyes, including TH, the simplest immobilization technique consists of their adsorption to suitable substrates, such as carbon. In addition, monolayers of these molecules have been shown to be stably adsorbed on gold surfaces [277]. Thus, TH was first adsorbed into the carbon electrodes, by casting the TH solution along 1 h. This adsorption would allow a strong binding between the carbon substrate and the MIPs layer formed after, thereby contributing to increase the stability of the electrochemical response. Considering that TH was not chemically modified, it is possible that the molecule established π−π stack interactions with the aromatic rings on the carbon substrate and electrostatic interactions between the -S- and the three amine groups on TH and the oxidized functional groups on the carbon substrate (which were likely to be present after acidic cleaning).

The DPV technique was used to follow the TH peak on the substrate, confirmed by the appearance of a peak at around −0.35 V (Figure 29). The formation of the MIPs film was suggested by the increasing reduction current produced by the electrodes and a potential shift. In contrast, the NIP yielded a more intense potential shift for a lower peak current.

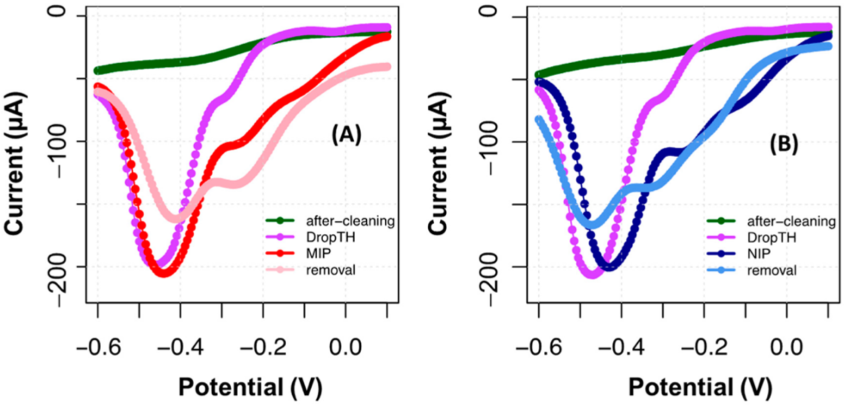

Figure 29: DPV voltammogram of C-SPEs after cleaning of surface (green), drop-casting TH (violet), electropolymerizing TH with or without CA 19-9 (red, MIPs, and blue, NIP), and removing the template (coral, MIPs, and light-blue, NIP). (**A**) represents the MIPs assembly and (**B**) the NIP assembly.

After template removal, a significant current decrease was observed, along with a shift in peak potentials. This tendency was more evident in the NIP, which was also subject to a template removal procedure, only for control purposes. This behaviour of the NIP evidenced the extraction from the electrode surface of di- to oligomeric compounds to TH that were not firmly attached. It could also signal chemical changes occurring on PTH after contact with oxalic acid. In addition, the peak shifting to −0.25 V in the NIP also became more intense than that in MIPs. By comparing this behaviour with the control NIP, the changes in the MIPs could be related to the fact that some protein molecules remained entrapped within the polymeric network.

The ability of the MIPs film to bind CA 19-9 was tested by performing calibration curves with standard solutions of the protein. This was performed only after stabilization of the MIPs/TH surface, by successive incubations in PhB, for 20 min, until a stable reading was reached. The calibration was made from the lowest to the highest concentration, incubating consecutively each standard solution in the same electrode. The standard solutions of CA 19-9 prepared for this purpose had 0.010, 0.030, 0.10, 0.30, 1.0, 3.0, 10, 31, and 100 u/ml.

The results obtained are shown in Figure 30. In general, from the two peaks observed in the voltammograms of the MIPs, the peak current at about −0.4 V decreased its intensity with increasing concentrations of CA 19-9, while the peak at −0.25 V displayed a random behaviour. In contrast, the voltammograms of the NIP displayed a more intense peak at about −0.25 V, which also displayed a random behaviour, and a negligible peak current at about −0.4 V. This global random behaviour of the NIP suggested the absence of specific binding sites on the polymeric network to capture CA 19-9.

Overall, a greater difference between MIPs and NIP films was observed at the peak located at about −0.4 V. This peak also displayed more intense peak current changes for consecutive concentration variations, thereby generating calibrations of greater sensitivity. Having calibrations plotted under this condition, the analytical performance of the biosensor in C-SPEs showed a linear trend in the concentration range studied, up to 10 u/ml (Figure 30 C). The average linear regression was I (A) = 7.6×10^{-6} × Log (CA 19-9, u/ml) + 2×10^{-5}, with an R squared >0.98, down to 0.010 u/ml. The calibrations in the NIP displayed a random response, as mentioned, thereby confirming that the response of the MIPs was selective for CA 19-9.

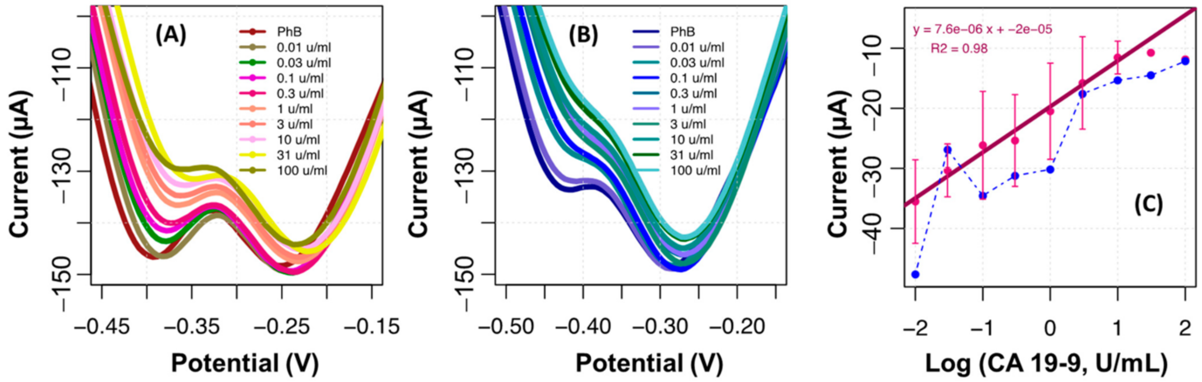

Figure 30: DPV voltammograms of MIPs (**A**) and NIP (**B**) films assembled on C-SPEs and incubated consecutively with increasing concentrations of CA 19-9 standard solutions, from 0.10 to 100 u/ml, along with the corresponding average calibration plots (**C**) plotting MIPs as dark-pink, and NIP as light-blue.

4.3.6 Response of the MIPs Film to CA 19-9 in Au-SPEs

The first layer with TH was made by casting the solution and allowing adsorption and by electropolymerization of TH on top of the electrodes. From the two approaches, electropolymerization yielded the most stable response and was therefore selected [228]. After electropolymerization of TH, the gold electrode displayed an increase in the current value, along with the appearance of a potential peak around −0.45 V (Figure 31 A). This suggests the formation of the polymeric film of TH, which seemed to be corroborated by the intense purple coloration obtained in the WE (Figure 31 A, pictured in inset that is stable within time and after washing).

The formation of the MIPs was confirmed by a marked increase in the reducing current in the potential peak that appeared at −0.5 V. As can be seen in Figure 31, the increase in the conductivity of the electrode in the MIPs was much greater with respect to the NIP. Another difference marked by the presence of CA 19-9 was the small shift in the peak to more negative potentials in the MIPs, while in the NIP, it shifted to more positive potentials.

The removal of CA 19-9 is a fundamental step to obtain the imprinted cavities that are directly related to the sensitivity of the biosensor. The removal of the protein was conducted by incubating oxalic acid on the WE for 1 h. The correct formation of cavities in the sensor was verified by decreasing the reduction peak and shifting to higher potentials. The NIP also yielded decreasing currents; however, the peak obtained had little resolution compared to the background signal.

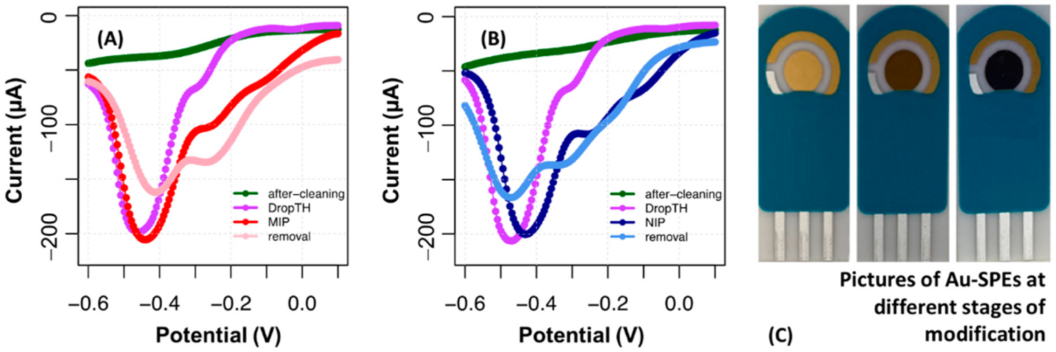

Figure 31: DPV voltammogram of Au-SPEs after cleaning of surface (green), PTH (violet), electropolymerizing TH with or without CA 19-9 (red, MIPs, and blue, NIP), and removing the template (coral, MIPs, and light-blue, NIP). MIPs represented in (**A**) and NIP in (**B**). SPE with the colour changes in the WE in the different construction phases (**C**).

The response of the MIPs film on Au-SPEs to CA 19-9 was tested by calibration curves, which were made similarly to the studies made with C-SPEs. The typical results so obtained are shown in Figure 32. Overall, the reduction peak signalling the presence of PTH was also the presence at about −0.5 V (it is important to note that the solutions were deaerated with nitrogen before reading) and the reduction peak tended to decrease in the presence of CA 19-9. This tendency showed a linear dependency with log CA 19-9 concentration from 0.10 u/ml to 100 u/ml. As before, the NIP displayed a random behaviour, thereby confirming that the response obtained for CA 19-9 depended mostly on interactions between the target protein and the binding sites.

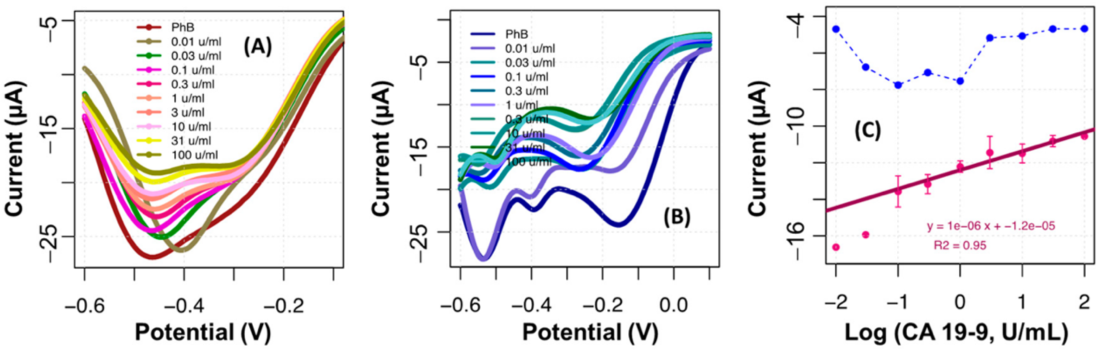

Figure 32: DPV voltammograms of MIPs (**A**) and NIP (**B**) films assembled on Au-SPEs and incubated consecutively with increasing concentrations of CA 19-9 standard solutions, from 0.10 to 100 u/ml, along with the corresponding average calibration plots (**C**), plotting MIPs as dark-pink, and NIP as light-blue.

4.3.7 SERS on TH Readings

Attempts to increase the signal by SERS studies were made by casting on the gold substrate TH linked to AuNSs. The TEM shown in Figure 33 confirmed the formation of AuNSs. The typical Raman band of TH was observed in the spectra obtained and shown in Table 1. The intensity of the spectrum obtained by SERS was two times lower than that obtained with TH casted directly on the gold electrode (Figure 28 e).

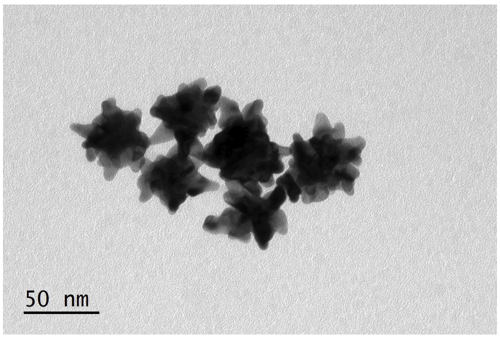

Figure 33: TEM images of AuNSs

The Raman spectra shown in Figure 34 A corresponds to the absorption of TH in glass and in the carbon substrate. In the other graph, Figure 34 B, the absorption of TH followed by electropolymerization is shown in carbon electrodes, TH/PTH. It is interesting to note that the spectra were apparently quite similar, showing the strong Raman bands of the TH. The most predominant bands observed were found at 486, 811, 914, 1036, 1389, 1504, and 1625 cm^{-1}, and their vibrational characteristics are listed in Table 1.

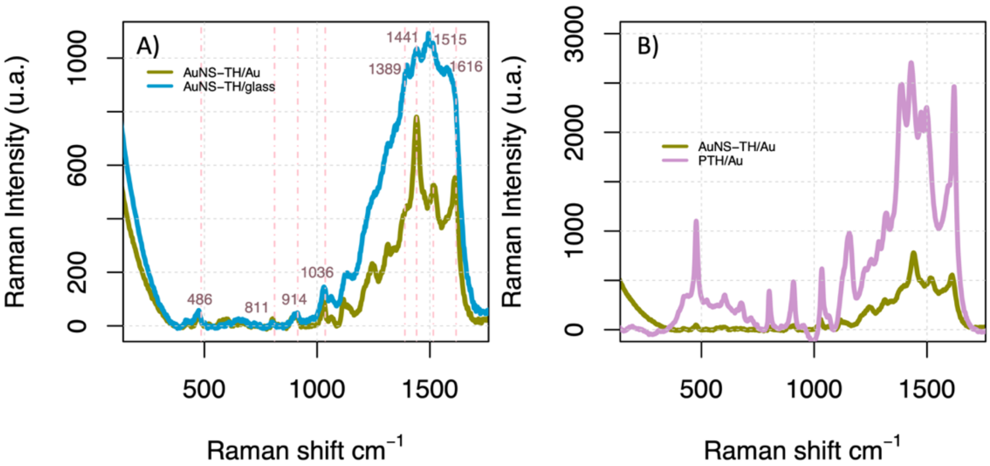

Figure 34: Raman spectra of TH, A) (blue) on carbon electrodes and (green) on glass, both substrates drop with TH, B) (pink) spectra of PTH on carbon substrate.

In the SERS spectrum, it was expected that the Raman bands would be more visible (Figure 35 B), that is, an increase in intensity would be observed throughout the spectrum. This may be since the distribution of the AuNSs was not homogeneous throughout the surface of the electrode. As the AuNSs/TH layer was not homogeneously distributed on the surface, it was difficult to observe the SERS effect (Figure 35 A), unlike the spectrum observed on the surface of the gold electrodes (Figure 35 B), where the intensity of the spectrum of the TH bands appeared with greater intensity compared to SERS.

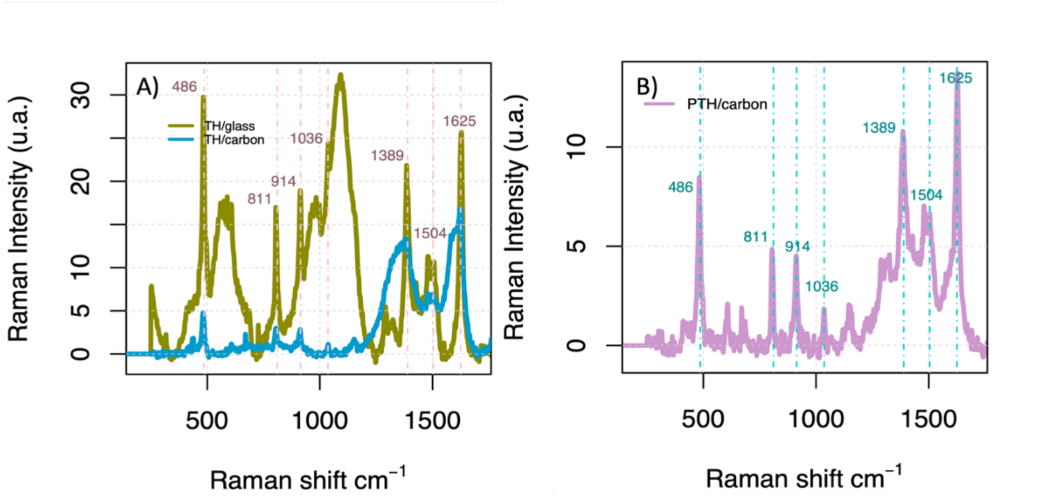

Figure 35: SERS spectra of A) TH/AuNSs, (blue) on glass and (green) on gold, B) (pink) spectra of PTH on gold substrate.

Hence, we can conclude that the distribution of the AuNSs/TH did not occur homogeneously throughout the surface. However, on the surface of the gold electrodes, we had a homogeneous layer of PTH that covered the entire surface of the gold. Any reading point of the Raman laser will find PTH deposited, and its effect intensified by the surface of the gold in which it was absorbed.

The band located at 1616 cm^{-1} corresponded to a shift of 8 cm^{-1} of the band corresponding to aromatic ring stretching and Namino-H bending for TH on Au-SPEs (1624 cm^{-1}). The band located at 1515 cm^{-1} could be attributed to central ring breathing, and Namino-H bond rocking of the amino group such as TH on the Au-SPEs band was located at 1506 cm^{-1}. The band at 1441 cm^{-1} attributed to the asymmetric stretching vibrations of C=N bond in the central ring decreased by 5 cm^{-1} in TH on Au-SPEs (1436 cm^{-1}). The greatest decrease corresponded to the attributed band vibrations of the ring of the dimeric at 1214 cm^{-1}, being 14 cm^{-1} for TH on Au-SPEs (1228 cm^{-1}). Despite the peaks appearing with less intensity in both spectra, this displacement of the band can be associated with loss or gains of energy between the atomic vibrations.

Overall, the signal obtained by direct reading to TH on the gold electrode was greater than that observed with the TH on the AuNSs. In fact, there was no reasonable explanation for this observation, considering that the gold AuNSs had a much greater surface area than the eventually flat gold surface on the Au-SPEs (which has great roughness because it was produced by printing a gold electrode on a ceramic substrate). Likely, this comparison was not valid and should require additional studies with increasing concentrations of the AuNSs/TH, but this was also made to work very expensively, which is not desired for a POC system.

Overall, the results obtained demonstrate that the Au-SPEs/TH substrate had potential to undergo a SERS reading to CA 19-9 binding in consecutive incubations of standard solutions, which would lead to a complementary and dual response on the same sensing unit. After incubation of the standard solutions, the electrochemical reading (which is non-destructive) could be followed by a SERS reading for providing additional information, in a similar approach to that described *in Castaño-Guerrero et al.* [164] (without AuNSs and having the signal enhancement at the substrate). This would help increase the accuracy of the analytical response.

4.4 Conclusions

A new MIPs material for CA 19-9 was presented for electrochemical reading of this cancer biomarker. When compared to a control, the MIPs showed selective and sensitive responses in reduction peak currents of the sensing film that were concentration dependent. The materials obtained were monitored by DPV and analysed by Raman spectroscopy, aiming to confirm the presence of TH and possible derived species. Raman spectroscopy was useful to determine the presence of TH and its different interactions with respect to each substrate studied. The results obtained from the characterization of the TH bands suggest wide range of potential applications.

Importantly, TH was efficient as an indicator of the electrochemical signal, revealing the SPEs to be self-indicated and label-free to detect CA 19-9. DPV was a useful technique to monitor the effect of CA 19-9 on the electrode, being an overly sensitive technique. Moreover, studies made with SERS suggested that the gold substrate with TH could further lead to complementary data, in a dual-detection scheme on the same electrode.

Chapter 5. Sensitive SERS detection of L1CAM using Ag-microsporous plasmon capsules on am imprinted film

The results presented in this chapter are based on work *" Sensitive SERS detection of L1CAM using Ag-microsporous plasmon capsules on an imprinted film* " by **Castaño-Guerrero, Y**., Andrea Mariño-Lopez, Felismina T.C. Moreira, Miguel A. Correa-Duarte, A.C. Marques[6], M. Goreti F. Sales. To along this chapter has shown a potential in biosensor application of SERS with MIPs technology. A plasmonic AgNCs were synthesized starting from Au cores continuing with the growth of Ag. The MBA as Raman reporter, in combination with the AgNCs modify with the antibody for L1CAM, make possible to recognize the cavities in the MIPs by SERS.

5.1 Introduction

Many chemical modifications of metallic NPs aim to improve their chemical/mechanical stability and fine-tune the surface properties in terms of electrical charge or chemical functionalities [278]. This can include layered core structures [279], [280], [281], which prevent agglomeration or deformation of the metallic NPs. Mesoporous silica coatings of metallic NPs have gained attention in this context, due to their numerous advantages, such as high surface area, controllable pore size, high thermal stability and easy surface functionalization [282].

NPs with a metallic core and a suitably designed protective shell are of interest for SERS, which aims to maximize the signal enhancement of specific Raman reporter molecules [283]. AuNPs have been used in SERS in many forms and with many coatings, including silica, with different thicknesses, sizes, and shapes of the plasmonic core, confirming high enhancement factors [284], [285]. Despite the many studies on AuNPs, silver nanoparticles (AgNPs) have also been used [286], [287] and outperform AuNPs due to their special optical properties [281]; AgNPs have a much sharper and stronger plasmon resonance compared to AuNPs.

The use of AgNPs in SERS is hindered by the low chemical stability of Ag [288], [289], for which core-shell Ag nanostructures have been developed [286], [287], [290], [291]. A shell with a bimetallic core of Au/Ag can further combine the advantages of both metals in terms of Raman signal output. In particular, the combination of Au and Ag provides easy morphology control and strong plasmonic properties, leading to higher SERS intensity than the pure NPs alone [292].

When these metal NPs are used for SERS sensing, a biological recognition element is desired to improve the accuracy of the determination. Molecularly imprinted polymers (MIPs) have been shown to be successful biological recognition elements in this context [293]. MIPs are prepared by forming a complex between the target molecule and selected functional monomers that undergoes appropriate polymerization. When the target molecule is removed, the vacancies formed on the polymeric network can selectively capture the imprinted target molecules [294][295].

Since the first report on MIPs-SERS sensors in 2003 by *Kostrewa et al.* [296], special attention has continued to be paid to this area. According to the recent review by Guo et al, particle-based MIPs-SERS sensors are divided into three categories [294]. First, there are the MIPs-over-SERS sensors (M-o-S) [297], [298], [299], which are characterized by presenting SERS NPs coated by MIPs surface imprinting. Secondly, there are SERS on MIPs (S-o-M) [300], in which a well-tuned number of NPs create a "hot spot" in the sensor structure. And finally, the MIPs mixed with SERS (M-m-S) [301], which are easier to fabricate compared to the previous ones and avoid complex SERS substrates.

This work describes a novel chip-based MIPs-SERS sensor that is fabricated in the same way as particle-based sensors and provides a larger surface area compared to particle-based sensors [294][295], [302], using a novel microporous plasmonic AgNCs material. It is assembled in a similar way as reported in [285] and provides stronger amplification of the SERS signal than conventional AuNPs or AgNPs. To this end, Au-AgNPs coated with silica and MBA, which are absorbed by the Ag surface as Raman tags, were used as the SERS substrate. This is demonstrated in a direct application to detect the L1CAM in a MIPs sensor platform electrochemically constructed on C-SPEs and by binding L1CAM antibodies to the SERS substrate to perform sandwich detection combining MIPs and antibody. The system was optimized with respect to several variables in accordance with the EIS and SERS data.

5.2 Experimental Section

5.2.1 Equipment

The Potentiostat/Galvanostat from Metrohm Autolab was used for electrochemical measurements. It is equipped with an impedimetric module and controlled by NOVA 2.0 software [237]. Commercially available C-SPEs were used (DropSens, DRP-C110), which combined WE and CE made of carbon as well as RE and electrical contacts made of silver.

Raman spectra were recoded using a Renishaw Invia system using a high-resolution grating of 1200 g-cm-1 and an acquisition time of 10 s. The laser (785 nm) was focused on the samples through a 50x objective with a power of 2.47 mW. Transmission electron microscopy (TEM) was performed using a JEOL JEM 1010 transmission electron microscope operating at an accelerating voltage of 100 kV.

5.2.2 Reagents and solutions

All chemicals were of analytical grade and water ultrapure Milli-Q laboratory grade. Potassium hexacyanoferrate III ($K_3[Fe(CN)_6]$), potassium hexacyanoferrate II ($K_4[Fe(CN)_6]$) trihydrate, sodium phosphate dibasic dihydrate (Na_2HPO_4), and Ortho-phosphoric acid 85% (H_3PO_4) were obtained from Riedel-de-Häen; sodium chloride (NaCl), ascorbic acid, 4-mercaptobenzoic acid, polyvinylpyrrolidone, poly(diallyldimethylammonium chloride) solution 20 wt. % in H_2O (MW: 400000-500000), L1CAM Antigen (4.7 mg/ml, 34 kDa) and Anti-L1CAM (IgG, polyclonal, produced in rabbit) were obtained from SigmaAldrich; silver nitrate (AgNO3) from Fluka; Sodium phosphate dibasic dihydrate, 99.5% ($Na_2HPO_4.2H_2O$) from Panreac; Sodium dihydrogen phosphate dihidrate ($NaH_2PO_4.2H_2O$) from Scharlau; foetal bovine serum from Alfa Aesar. Sulphuric acid (H_2SO_4) was obtained from BDH; thionine acetate from Acros Organics.

5.2.3 Synthesis of the Ag/SiO_2 m-capsules

Au-based silica shells with Au seeds in their inner cavity (void/Au/mSiO_2 composite) were prepared as described elsewhere [285]. Silver nitrate (10 mM, 1 ml) was added to 0.5 ml of the void/Au/mSiO_2 suspension (1.25 mg/ml) with vigorous stirring. After 5 min, 10 µL of ascorbic acid (10 mM) were added to the solution, which caused a colour change from red to brown due to the reduction of Ag^+. The sample was stirred for 5 min and then centrifuged and washed with ethanol (3500 rpm, 10 min) to remove the excess reagents and obtain the AgNCs.

The Raman reporter solution (MBA, 1.0×10^{-4} M) was added to the AgNCs and mixed for 1 h in the dark. The solution was washed with ethanol and water (3500 rpm, 10 min) to remove unbound MBA.

For coating with polyvinylpyrrolidone (PVP), 25 mg of PVP-30k were dissolved in 0.75 ml of water. 375 µL of this polymer solution were added to the AgNCs (625 mg) and stirred 18 h at room temperature.

Subsequently, the PVP excess was removed by three centrifugations and redispersing cycles with water (3500 rpm, 10 min). Finally, the product was dispersed again in water (0.5 ml).

The obtained structures (Au-Ag/MBA/$mSiO_2$/PVP) were functionalized with poly(diallyldimethylammonium chloride) solution 20 wt. % in H_2O (PDDA, MW: 400000-500000). For this purpose, PDDA was dissolved in a 0.5 M NaCl solution (pH 5.0) with a final polymer concentration of 2 mg/ml. Then 1.5 mL of the positively charged solution was added to the capsules (625 mg) and stirred for 30 minutes at room temperature. The excess of reagents was removed by three cycles of centrifugation-redispersion (3500 rpm, 10 minutes) the first two with water and the last with PhB, as this was the appropriate medium for the addition of the antibody for L1CAM (Ab). This polyelectrolyte film provided the necessary electrostatic charge surface to facilitate the subsequent adsorption of the antibody.

The AgNCs were redispersed in 200 µl PhB and 100 µl Ab (0.03 mg/ml) was added. The whole was stirred for 1 hour, followed by three cycles of centrifugation and redispersion with PhB. Finally, the resulting material was redispersed in 200 µl buffer (3.125 mg/ml).

5.2.4 SERS and electrochemical measurements

For the SERS measurements, a volume of 5 µl of the solution containing the dispersed Ag/MBA/$mSiO_2$/PVP/PDDA/Ab material (3.125 mg/ml) was used, which was poured overnight onto the biosensor with different concentrations of L1CAM. Then the surface was washed, and the biosensor was prepared for Raman calibration with different concentrations of L1CAM as described below for the electrochemical calibration curves.

The electrochemical measurements were used to follow the construction of the biosensor and its calibration. For this purpose, CV and EIS were used in the presence of a standard redox probe, $[Fe(CN)_6]^{3-/4-}$ covering the 3-electrode system. EIS shows the electron transfer and diffusion processes at the electrode/electrolyte interface in the form of a Nyquist plot. CV shows the current changes as a function of a series of applied potentials. In the EIS tests, a frequency range of 0.1 to 1x105 Hz was used, with an amplitude of 0.01 V and a number of 50 frequencies.

5.2.5 Preparation of MIPs

The MIPs synthesis was supported electrochemically and carried out on the C-SPEs surface. A schematic representation can be found in Figure 36. In general, the preparation of MIPs involved several steps: (i) purification, (ii) preparation of the electrode to receive the protein, (iii) protein binding, (iv) electropolymerization of the monomer, and (v) removal of the protein template. Each of these phases was monitored by EIS.

In the cleaning phase, a H_2SO_4 solution (0.5 M) was used and the electrodes were subjected to 15 cycles of CV between -0.2 and +1.2 V at a scan rate of 0.05 V/s. Then the WE was covered with TH (10^{-3} M) for 1 hour at room temperature.

Subsequently, the C-SPEs modified with TH (C-SPEs/TH) was incubated with L1CAM (0.01 mg/ml) for 1 hour. Electropolymerization was performed with TH solution dripped onto the 3-electrodes. A CV between -0.4 and +0.4 V was used at a scan rate of 0.050 V/s for 15 cycles. Subsequently, the polymer-modified electrode was incubated with oxalic acid (0.5 M) for 2 hours to remove the L1CAM template, as described in a previous study [263]. A control sample, a NIP, was prepared using the same procedure without L1CAM.

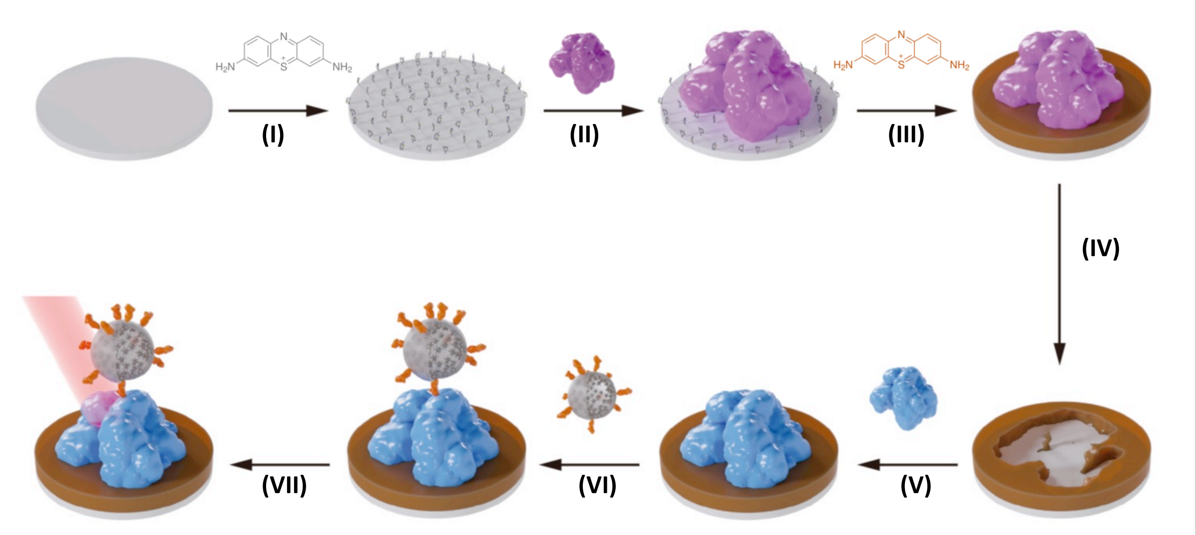

Figure 36: Schematic representation of the biosensor setup followed by incubation of L1CAM and Raman probe for SERS readings. (I) casting of TH on the clean C-SPEs; (II) casting of L1CAM; (III) electropolymerization of TH; (IV) removal of L1CAM; (V) binding with L1CAM (from samples or standards); (VI) binding of AgNCs with Ab; (VII) and SERS measurement in a confocal Raman spectroscope.

5.2.6 Electrochemical measurements

The electrochemical measurements to calibrate the biosensor were performed in a 5mM $[Fe(CN)_6]^{3-/4-}$ solution prepared in PhB 0.1 M with a pH of 7.4 (0.0754 M Na_2HPO_4 and 0.0246 M NaH_2PO_4). The L1CAM standard solutions used in the calibrations ranged from 0.1 to 100 ng/ml and were prepared by diluting the commercial protein in PhB buffer or in FBS diluted in PhB (1:100). Each solution was allowed to stand on the electrode for 20 minutes at room temperature. The selectivity study was performed in a similar manner with interfering species. The interfering solutions, also prepared in PhB, were 7.0×10^{-4} g/ml glucose, 1.0×10^{-3} g/ml creatinine, and 37 u/ml CA 19-9.

5.3 Results and discussions

5.3.1 Assembly of Ag/NPs

PS spheres of about 500 nm were used as templates for the electrostatic deposition of 3 nm AuNPs. The AuNPs were then coated with a layer of mesoporous silica, creating an ordered matrix with improved SERS and high signal reproducibility. After addition of Ag+ and ascorbic acid, Ag+ was reduced and grew around the Au core. The subsequent addition of MBA molecules allowed Ag to bind to Ag via thiol groups and generate an intense SERS signal. The resulting nanospheres were characterized by TEM Figure 37. The TEM images show mesoporous silica capsules with a size of about 500 nm in diameter and Ag-based particles in their inner cavity.

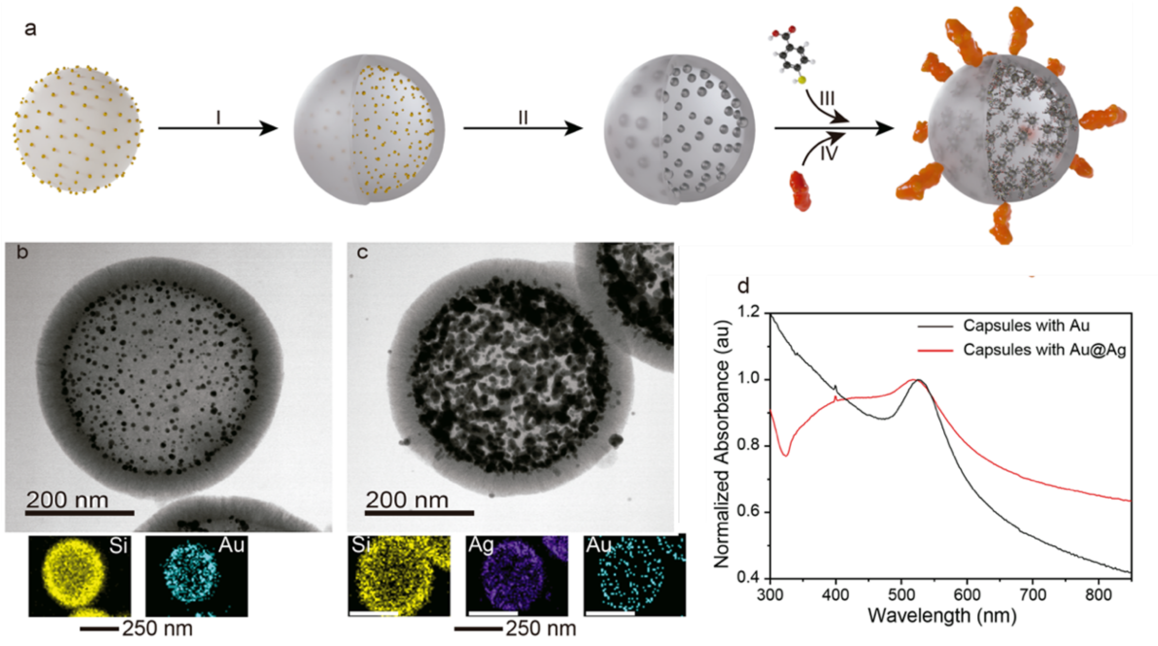

Figure 37: Schematic representation of the synthetic approach to obtain the Raman probe on the AgNCs (a), the transmission electron microscopy images of Si-Au (seed) (b) and Si/Au-AgNCs(c); and the UV-Vis spectra of aqueous dispersions of Si-Au and Si-AgNCs (d).

The resulting SERS spectra confirmed that MBA was adsorbed/attached to the Ag surface (Figure 38). The characteristic spectrum of MBA showed two Raman bands at 1078 and 1585 cm^{-1}, which were associated with the characteristic vibrations of the C-H bond of the aromatic ring and the C=C vibrations, respectively [292], [303]. The bands at 845 and 1420 cm-^{1} belong to δ (COO−) and ν(COO^{-}), respectively. The band observed at 719 cm^{-1} was assigned to the vibration γ(CCC) outside the aromatic ring [304].

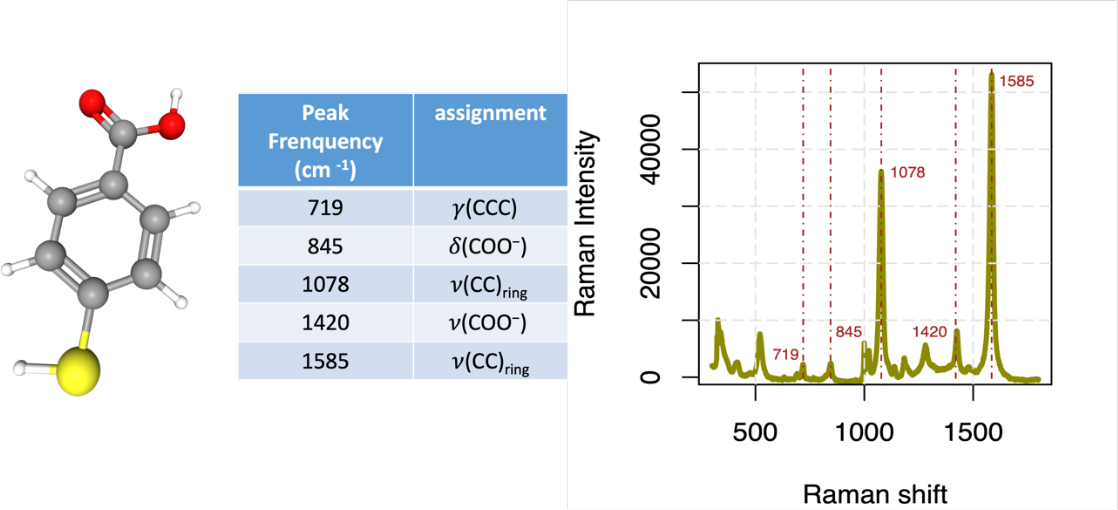

Peak Frenquency (cm $^{-1}$)	assignment
719	$\gamma(CCC)$
845	$\delta(COO^{-})$
1078	$\nu(CC)_{ring}$
1420	$\nu(COO^{-})$
1585	$\nu(CC)_{ring}$

Figure 38: Chemical structure of MBA (left), the characteristics Raman peaks for MBA (centre) and the typical Raman spectra obtained for MBA (right).

The antibody bound to the AgNCs was previously prepared in a background solution of PhB. This solution was prepared with phosphate salts and did not contain electrolytes such as NaCl or KCl. These electrolytes destabilized the formation of the AgNCs, as may be seen in Figure 39. Thus, a positively charged PDDA was added before the antibody, which as a stabilizer for the AgNCss and facilitated the binding of the Ab in the PhB solution.

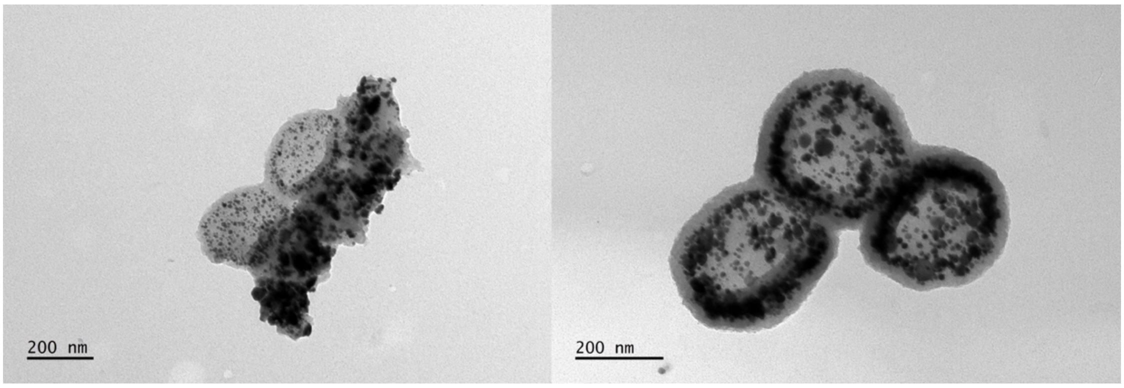

Figure 39: TEM for AgNPs with AB, without the PDDA.

Overall, the intensity of the spectra was high when compared to the typical Raman signal of the MBA alone. This confirmed the attainment of a strong electromagnetic field around the silver, referred to as a “hot spot” [294]. This effect was further enhanced because each AgNCs acted as a second amplifier of the “hot spots”, as a single capsule contained multiple hot spots of MBA molecules next to the Ag, most of which should produce a Raman signal. Since a single capsule may be signalling a single L1CAM protein, the Raman signal generated by a single protein is immensely amplified with our approach. In addition, the shell around the silver is expected to have a protective effect against silver oxidation, which may contribute to extend the self-life of the Raman probe.

5.3.2 SERS response of the nanoprobes

To monitor the signal enhancement produced by seeding Ag around Au, AgNCs or MBA-labeled AuNC were tested to monitor L1CAM for C-SPEs. The obtained SERS spectra are shown in Figure 40, signalling that the peak at 1078 cm^{-1} was the most adequate to follow the intensity changes in MBA, for concentrations of L1CAM ranging from 0.1 to 100 ng/ml. The highest L1CAM concentration showed SERS intensities of 21276 and 28020 when AuNC or AgNCs were used, respectively; at the lowest L1CAM concentration, the corresponding SERS intensities were 832 and 3157, respectively. As shown by the comparative results of the two metal nanomaterials, the growth of Ag-based nanostructures around AuNPs favoured the SERS signal enhancement by~4×.

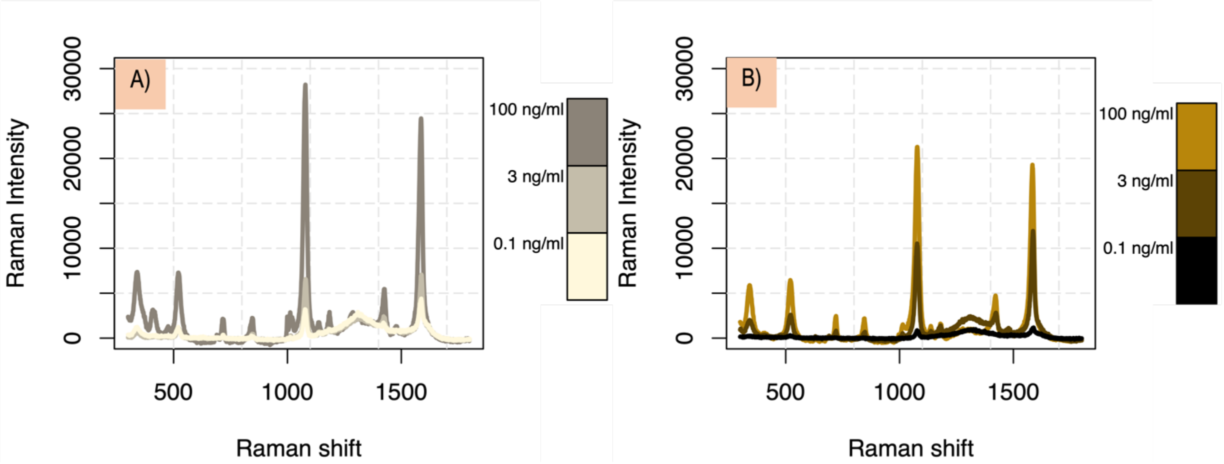

Figure 40: SERS spectra obtained by using the different Raman probes incubated on the biosensor with 0.1, 3 and 100 ng/ml of L1CAM. (A) Au-Ag/MBA/PVP/PDDA/Ab or (B) Au/MBA/PVP/PDDA/Ab.

5.3.3 Electrochemical studies in MIPs

In general, MIPs synthesis requires complex formation between L1CAM and a suitable functional monomer, which is subsequently polymerised. After removal of L1CAM, the resulting empty cavities are expected to have a shape and stereochemistry complementary to the imprinted protein. These cavities are therefore able to bind L1CAM, which can be followed up by electrochemical detection [294].

The first step in the construction of the biosensor was to clean the C-SPEs (Figure 36 I). This was done with successive CVs under a sulphuric acid solution. The resulting Nyquist plots and cyclic voltammograms are shown in Figure 41. They show increasing R_{ct} values and lower current magnitudes and larger peak-to-peak potential differences, respectively, reflecting the oxidation of the carbon substrate at the surface of the electrode. The signals obtained offer higher reproducibility within different C-SPEs units than when using the commercially available C-SPEs units without a pre-purification step.

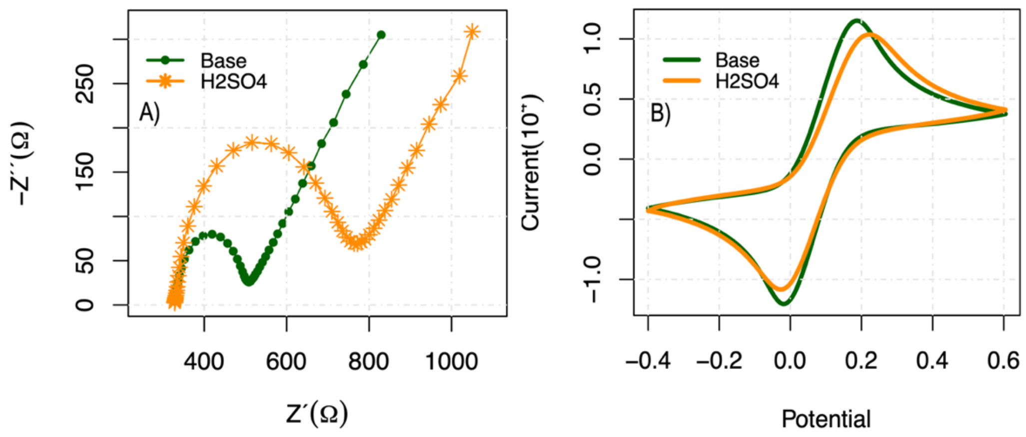

Figure 41: Nyquist plots (left) and CV voltammograms (right) of the pristine C-SPEs (Base) and the resulting electrochemical cleaning with 0.5 M H_2SO_4.

The next step in the construction of the biosensor was to cast TH onto the WE (Figure 36 II). TH belongs to the group of phenothiazine dyes with two amino groups and is a molecule with good electron transfer capacity and high solubility in water. TH acts as a cross-linking element between the carbon (on the SPEs) and the PTH MIPs to ensure the formation of a stable MIPs film: a) TH binds to the carbon electrode via non-covalent functionalisation [263] by establishing van der Walls interactions between the aromatic rings of carbon and TH; b) TH also allows subsequent binding to L1CAM via hydrogen bonding interactions with the chemical functions containing N-H and O-H atoms. The absorption of TH at the C-SPEs was confirmed by the increase in conductivity at the electrode surface Figure 42, as TH and the redox probe are oppositely charged.

The next step was the MIPs assembly (Figure 36 III). There are a variety of strategies for the fabrication of MIPs [305] of which surface imprinting by electropolymerisation was chosen. Surface imprinting makes it possible to increase the number of imprinted sites, which can increase sensitivity. This requires the incubation of L1CAM on the C-SPEs modified with TH, resulting in electrodes with higher R_{ct} values (Figure 42). Electropolymerisation makes it possible to control the size of the polymer film by controlling the electrochemical parameters such as the SR, the number of cycles and the potential window, which proves to be an advantage in terms of reproducibility [306]. The monomer selected for this purpose was TH [267], which offers 2 main advantages in terms of MIPs construction. Firstly, it contains two amino groups in alpha positions with N-H bonds that allow the formation of hydrogen bonds with multiple functional groups in L1CAM, facilitating complex formation [307]. Secondly, it yields a conductive polymer, PTH, which is expected to improve the electrochemical sensitivity. The higher R_{ct} values observed on the electrodes were indeed due to the formation of PTH, as the same electrodes incubated in PhB (instead of TH) and treated the same way showed much lower R_{ct} values.

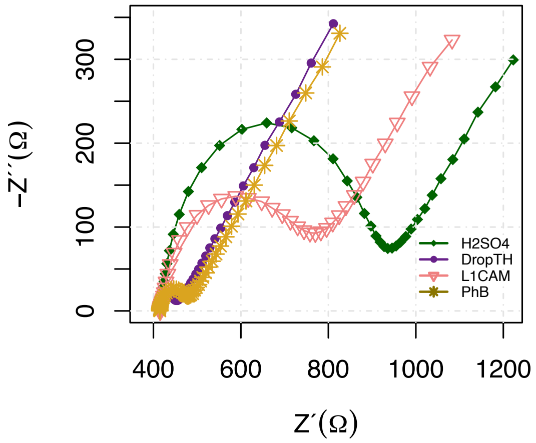

Figure 42: Nyquist plots after cleaning the electrode surface (green), drop casting of TH, 10-3 M (violet), and binding of L1CAM, 0.1 mg/ml, (coral) or PhB pH 7.4 (gold).

The MIPs of PTH was obtained by CV, where previous information on the conductive/electroactive properties of TH made the electropolymerization process simple, stable and satisfactorily reproducible [308]. It was originally assumed that the potential sweep would have an upper limit of 0.9 V, as TH would not polymerise at lower potentials [268], and that the potential of the electrode should be greater than the potential at which oxidation of the NH_2 groups occurred. In an initial exploration of the potential, a well-defined shoulder peak was observed at a maximum potential of 0.9 V with a pair of new reversible peaks (Epc = -0.2 V, Epa = 0.1) with potentials between -0.3 and 1.2 V at a scan rate of 0.050 V/s for 15 cycles (Figure 43).

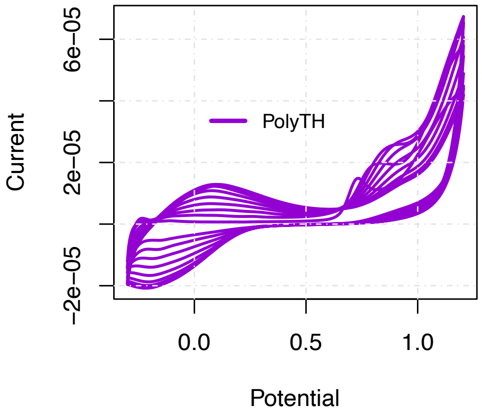

Figure 43: Cyclic voltammogram of the growth process of PTH film, between -0.4 to 1.2 V, at scan rate 0.050 V/s for 15 cycles (consecutive cycles generated greater current signals).

As the number of cycles increased, a gradual increase in peak height and a tendency towards stabilisation of peak current on successive scans was observed, confirming the formation of a polymer film of TH on the C-SPEs (Figure 43). Considering that the peak at around 0.9 V showed irreversible behaviour, the potential range of the CV was narrowed down to obtain only the reversible peaks. A CV between -0.4 and +0.4 V was sufficient to cause the formation of PTH, as evidenced by the purple colour on the surface of the electrode and the electrochemical properties of the electrode (Figure 44). In terms of the number of cycles that regulate the polymer thickness, the current increases with the number of cycles up to 15, after which the current can be slightly reduced [255]. Therefore, a total number of 15 cycles was chosen as the optimum number of cycles for the experiments. As expected, the Nyquist diagrams of the PTH before removal of the template show very low R_{ct} values, which is due to the high conductivity of the polymer materials (Figure 42).

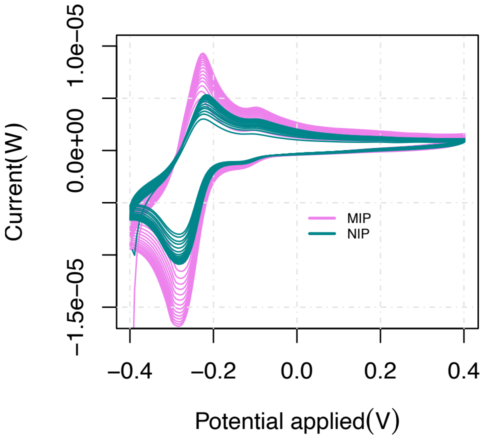

Figure 44: Cyclic voltammogram of the growth process of PTH film in MIPs and NIP, (violet) with L1CAM and (green) PhB pH 7.4, containing 1x10^{-3} M of TH.

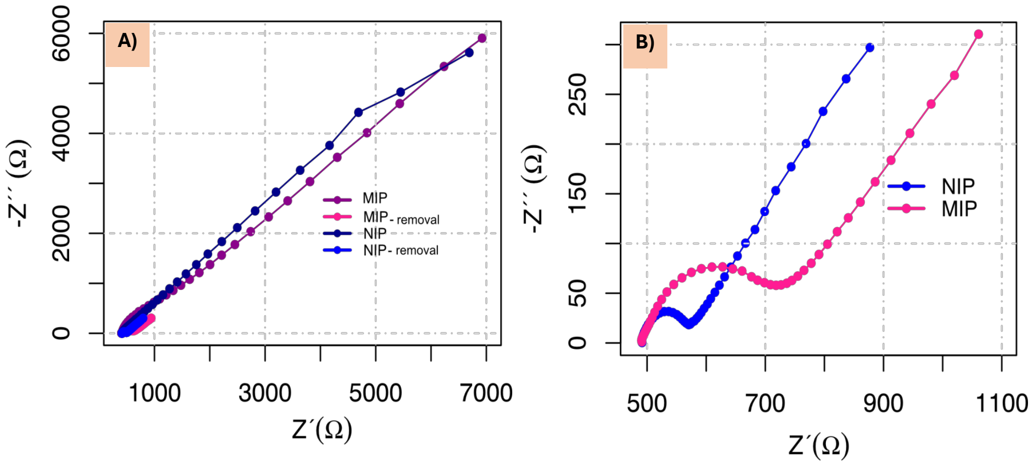

Figure 45: EIS plot for MIPs and NIP, A) after formation of polymeric network between L1CAM and TH; B) removal step with oxalic acid (0.5 M).

The subsequent stage was template removal (Figure 36 IV), which was performed with oxalic acid. This chemical treatment may have altered the intrinsic conductivity properties of the polymer films, as the overall R_{ct} values increased. Compared to the NIP, the MIPs biosensor has intrinsically higher R_{ct} values (Figure 45 B), which could be due to the presence of L1CAM proteins within the polymeric network or the fact that the presence of L1CAM hindered the formation of the polymer.

The stability of the signal generated by the sensor was ensured by successive 20-minute incubations in PhB. Only when a stable signal was achieved were the L1CAM standard solutions incubated in the sensor layer to record the calibration curves. The concentrations of the L1CAM standard solutions ranged from 0.1 to 100 ng/ml. As expected, the binding of L1CAM to the complementary MIPs cavities contributed to an increase in the R_{ct} value, which was more pronounced with increasing L1CAM concentration (Figure 46 A). The greater sensitivity of MIPs was confirmed by a slope of ~57 Ω/decade, compared to less than half the slope of NIP (Figure 46 B). This confirms that the dominant response of MIPs is due to the binding of L1CAM to the imprinted sites and not to non-specific sites in the polymer film. The linear response of NIP showed much smaller slopes and the quality of the linear fit was poor with a squared correlation coefficient of 0.96.

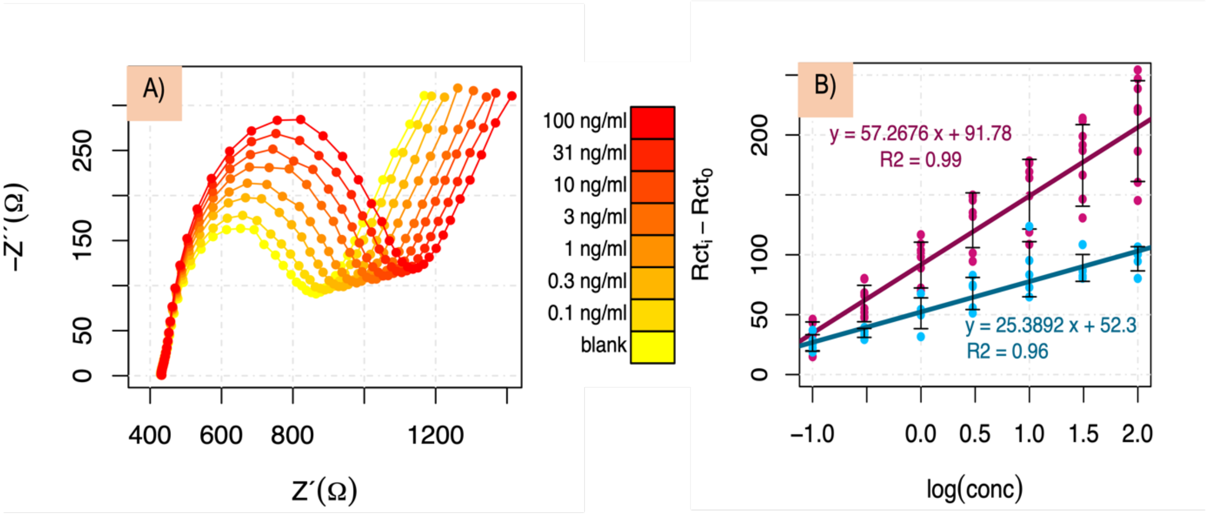

Figure 46: Electrochemical data for calibration with L1CAM standard solutions ranging from 0.1 ng/ml to 100 ng/ml prepared in PhB using the MIPs biosensor. (A) Nyquist plots for incubations in the MIPs film of increasing concentrations of L1CAM, from 0.1 ng/ml to 100 ng/ml; (B) corresponding calibration curves with linear plots, for (darkpink) MIPs and (lightblue) NIP.

5.3.4 SERS studies in MIPs

In the SERS assays, the Raman probe, Au-Ag/MBA/mSiO$_2$/PVP/PDDA/Ab, was incubated in the C-SPEs biosensor with a specific concentration of L1CAM. The probe was bound to the electrode surface via the Ab, which binds to the L1CAM already present at the imprinted sites. This binding was evaluated for biosensors with L1CAM concentrations ranging from 0.010 to 31 ng/ml, tracking the characteristic peak of MBA at 1078 cm^{-1}. For this end, the Raman spectra of each concentration were collected at various locations of the WE. The intensity of the Raman signal was also considered to obtain estimated quantitative data on the concentration of L1CAM. Thus, the SERS intensity value at 1078 cm^{-1} (y-axis) was plotted against the logarithm of the L1CAM concentration (x-axis). The use of the logarithmic concentration is related to the typical behaviour of MIPs materials.

Overall, the Raman spectra showed an increasing intensity of the band at 1078 cm-1 with increasing protein concentration (Figure 47 A). This increase in SERS signal corresponded to a series of consecutive events, starting with the higher number of probes Au-Ag/MBA/$mSiO_2$/PVP/PDDA/Ab on the surface, bound to a higher number of L1CAM protein structures, occupying a higher number of binding positions on the MIPs. From an analytical point of view, the results obtained showed an improvement over the electrochemical technique. While the sensor was able to detect up to 0.1 ng/ml L1CAM with the electrochemical technique, the SERS detection reached 0.01 ng/ml (Figure 47 B), which means that the detection capacity was improved 10-fold.

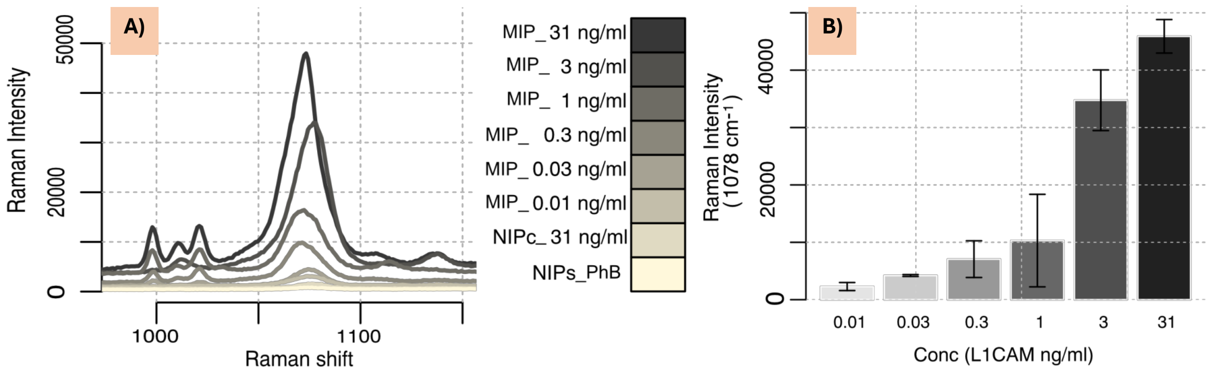

Figure 47: SERS spectra obtained using Raman lens and the Raman probe Ag/MBA/PVP/PDDA/Ab for MIPs films incubated with standard solutions of L1CAM of 0.01, 0.03, 0.3, 1, 31 ng/mL or for NIP films incubated with PhB or 31 ng/mL. A) Raman spectra ranging from 980 to 1150 cm^{-1}; B) Bar graph for the intensity of the Raman peak at 1078 cm^{-1} for each concentration of L1CAM analysed in the MIPs films.

Since the Raman laser beam only irradiated a small portion of each electrode, it was possible that the SERS signals did not reveal a representative surface of the biosensor. To complement these results, the spectra were also recorded using a Raman lens that covered a larger area of the electrode surface. Figure 48 shows the resulting SERS spectra for buffer and L1CAM standard solutions of 0.01, 10 and 100 ng/ml. In general, it was interesting to note that for buffered solutions incubated at the surface, the Raman signal at 1078 cm^{-1} provided no relevant intensity. As for the response of the MIPs to L1CAM, the observed response was also a linear trend as a function of log concentration, suggesting that the surface provided a similar overall response in analytical terms (although the strength of the Raman signal decreased when the signal acquisition conditions were changed).

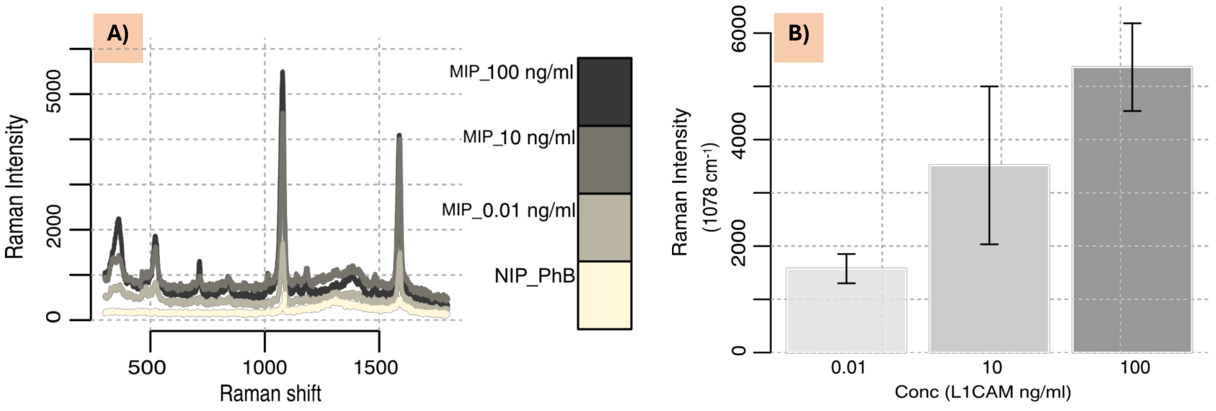

Figure 48: SERS spectra obtained for concentration solution of L1CAM, range 0.01, 10, 100 ng/ml, and NIP; using Ag/MBA/PVP/PDDA/AB, for more diameter of lent , A) spectra in 980 to 1150 cm-1 , B) Barplot for the same range of protein concentration.

SEM images were added to the Raman data to understand the differences in the analytical response between MIPs and NIP in terms of the the density of the nanocapsules on the biosensor surface. The typical images obtained are shown in Figure 49. In general, the differences between MIPs and NIP electrodes are not obvious when viewed by SEM, but the presence of nanocapsules highlights these differences and signals L1CAM binding sites. The images obtained are in general agreement with the results obtained in SERS. The MIPs showed a greater distribution and higher density of AgNCs over the entire surface compared to the NIP. The presence of some AgNCs on the surface of the NIPs indicates non-specific interactions (albeit to a very small extent compared to the MIPs). There is also some heterogeneous distribution of the nanocapsules over the electrode surface. This effect is eliminated analytically by having multiple measurement points on each electrode and selecting the most representative response (higher intensity) or a single Raman measurement (lower intensity).

5.3.5 Serum study

The biosensor was calibrated in standard solutions prepared in a 100-fold dilution of serum (Figure 50). Foetal bovine serum, which is similar in composition to human serum, was used for this purpose. In general, the serum calibrations showed good analytical properties. They exhibited a linear range from 0.1 to 31 ng/ml, with a slope of 349 Ω/decade and a squared correlation coefficient of 0.99. It is clear that the biosensor is sensitive to increasing concentrations of L1CAM, when compared to the analysis made in buffered solutions. This high electrochemical sensitivity was likely due to the presence of additional ionic species in the solutions from the diluted serum and the non-specific binding by coexisting proteins. This was supported by the fact that initial stabilisation with a blank solution was very difficult to achieve.

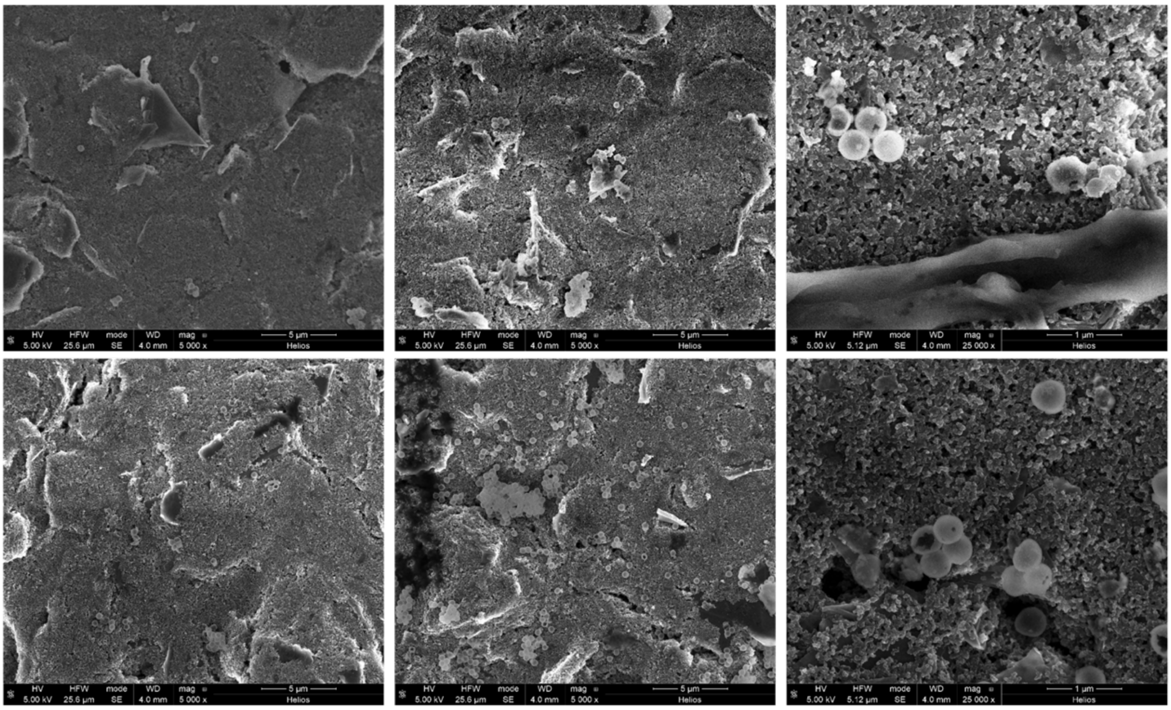

Figure 49: SEM images of the NIP (top, after incubation in buffer solution) and MIPs (bottom, after incubation in 100 ng/ml) films, with Raman probes incubated on the surface of the electrode. The images on the left and in the centre correspond to different locations on each electrode; the image on the right corresponds to a higher magnification.

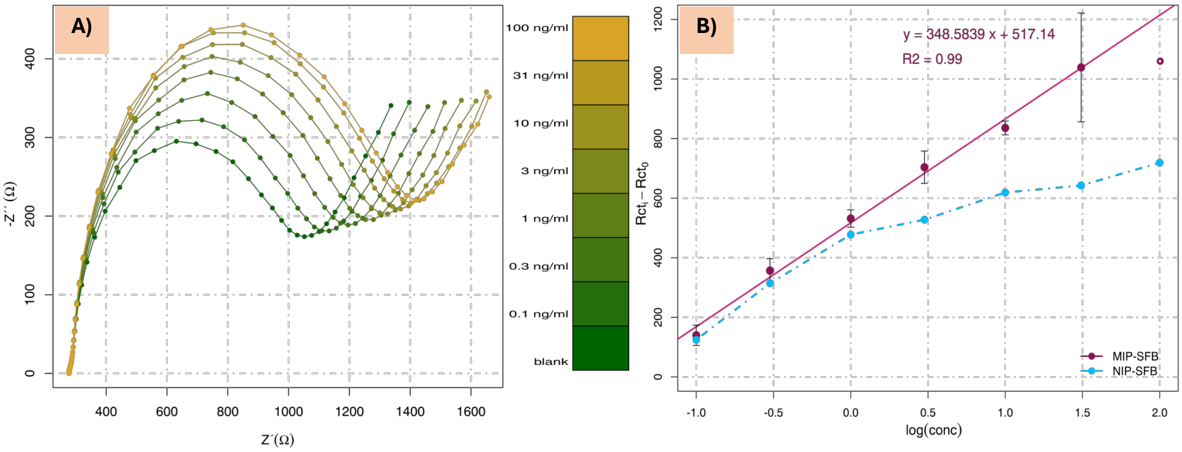

Figure 50: Electrochemical data for calibration with L1CAM standard solutions ranging from 0.1 ng/ml to 100 ng/ml prepared in 100-fold diluted foetal bovine serum using the MIPs biosensor. (A) Nyquist diagrams. (B) Calibration plots for relativa R_{ct} to the blank of the MIPs (dark pink) and NIP (light blue).

When analysing the layer that comes into contact with the sample, it was found that the sulphur atom on the TH could undergo side reactions with functional groups in non-specific proteins in the serum. To eliminate this possible non-specific adsorption of components in the serum, a solution of 3-MPA was added to the construction of the MIPs prior to protein removal. It was hypothesised that it could bind free -SH in the MIPs layer and thus provide a more stable platform against incubation in serum.

As expected, an improvement in the stabilization of the MIPs layer incubated with serum was observed, but this addition of a new layer led to a change in the signal during calibration.

As shown in Figure 51 A, with the successive increase in L1CAM concentration two incomplete semi-circles became visible. This was reflected in the frequency/phase plots, in Figure 51 B and C, where this behaviour was much more pronounced for the MIPs. Using data for a fixed frequency of 2.95 Hz, the linear curve obtained for the MIPs was very different from that of the NIP, corresponding to a linear range from 0.3 to 100 ng/ml with more than double the sensitivity (Figure 51 D). Thus, an increase in the phase value with increasing L1CAM concentration is observed, with the R-squared being 0.99.

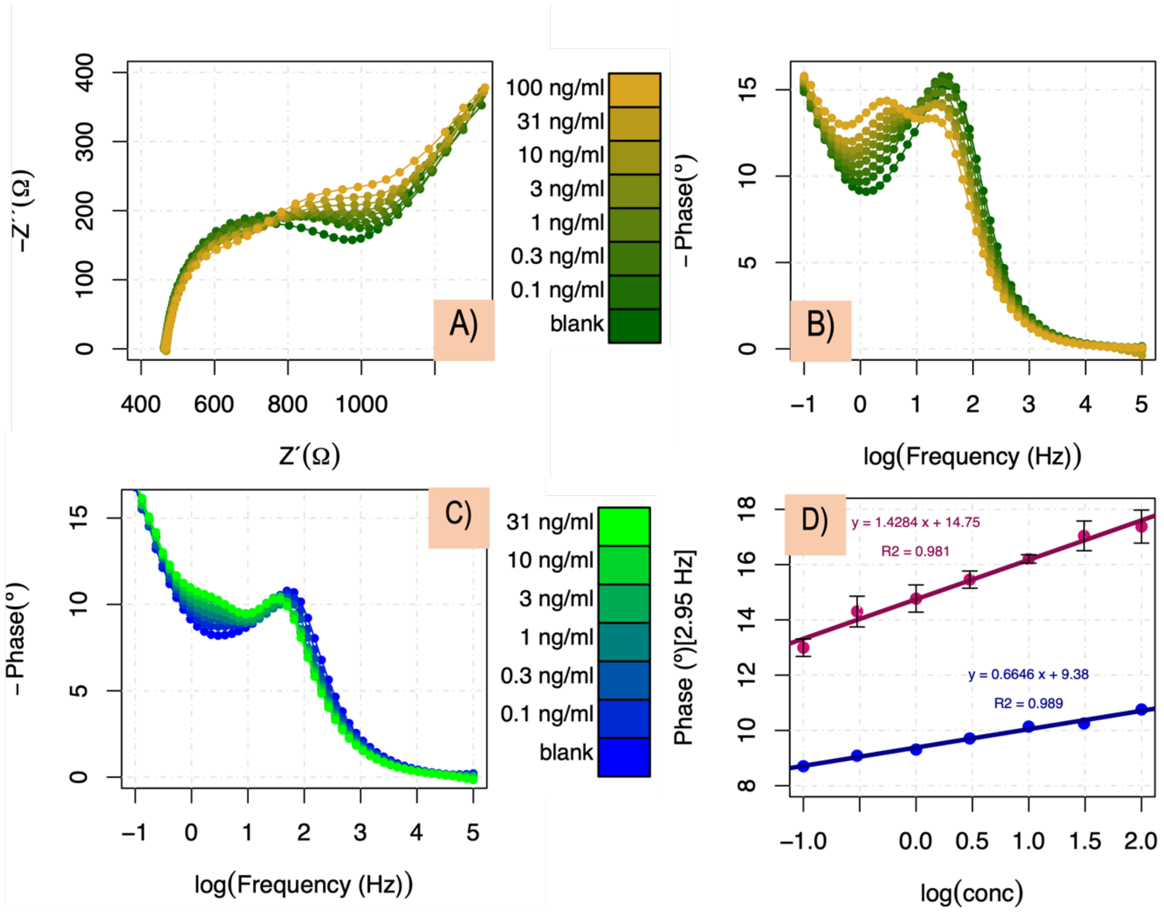

Figure 51: Electrochemical data for calibration with L1CAM standard solutions ranging from 0.1 ng/ml to 100 ng/ml prepared in 100-fold diluted foetal bovine serum using the MIPs biosensor modified with a layer of 3-MPA. (A) Nyquist diagrams. (B) Frequency-phase diagram of the MIPs. (C) Frequency-phase diagram of the NIP. (D) Calibration plots for a fixed frequency of 2.95 Hz of the MIPs (dark pink) and NIP (light blue).

5.3.6 Selectivity study

Selectivity studies were performed to understand the ability of the analytical system to discriminate between L1CAM and coexisting compounds in biological fluids. The potential interferents selected for this study were creatinine, glucose and CA 19-9 and their concentrations were adjusted to 1.0 × 10^{-3} g/ml,

7.0×10^{-4} g/ml and 37 u/ml, respectively. These solutions were prepared in PhB and incubated separately on the sensor for 20 minutes. This is the same time given for the standard solutions of L1CAM in the calibration procedure. These results of the separate incubation of the individual interfering substances were compared with the response of the device to L1CAM (10 ng/ml).

The average percentage of the response was 1.3 % for creatinine, 9.9 % for glucose and 10.8 % for CA 19-9, compared to L1CAM, indicating a negligible interfering effect (Figure 52). This was an excellent result considering that this separate interference test corresponds to the worst-case scenario of the device, as the lack of competition with the target molecule could allow a significant non-specific response.

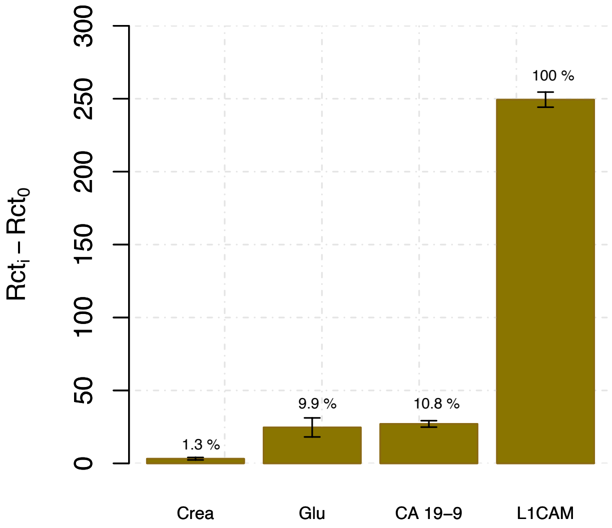

Figure 52: Relative R_{ct} data extracted from the Nyquist plots for L1CAM standard solutions and other possible interfering species (creatinine, glucose and CA 19-9).

In general, the results obtained showed that MIPs has high selectivity characteristics, maintaining a high affinity for the target molecule in relation to secondary components.

5.4 Conclusion

A new material with a porous silica-based structure covering the AgNPs seeded on Au has been developed. The silica-shell so formed contributed to the stability of the Ag particles against oxidation and protected them to some extent from external contamination. A Raman tag and an antibody were bound to the AgNPs inside the silicon to ensure the desired functionality. Since a single nanocapsule contained a large number of hot spots, it enabled intense SERS signal amplification.

The MIPs sensor for L1CAM constructed with PTH showed high sensitivity in PhB, where pretreatment with a thiol-based compound was required in serum samples to avoid non-specific binding of coexisting compounds. The biosensor had good electrochemical sensitivity in the clinical range of interest to patients. This electrochemical response was complemented by Raman spectroscopy data after the Raman probe was added. SERS detection improved the detection capacity at least 10 times the concentration of the protein.

Overall, the combination of electrochemistry/SERS and MIPs/antibodies is expected to provide an exceptionally reliable answer. The selectivity imposed by the MIPs is monitored by electrochemistry and further validated by immunoassay with SERS to perform a “sandwich-like” assay between a MIPs (commonly known as a plastic antibody) and a naturally derived antibody. This dual detection capability combined with dual recognition can be extended to other biomarkers, especially when it is important to avoid negative/positive errors.

Chapter 6. Silent-region SERS tag detects CA 19-9 captured in a MIPs surface using the Coomassie Brilliant Blue dye

The results presented in this chapter are based on work “*Silent-region SERS tag detects CA 19-9 captured in a MIP surface using the Coomassie Brilliant Blue dye*” by **Castaño-Guerrero, Y**., Correa-Duarte, M., Águas, H., Sales, M.G. This work used the background knowledge of plasmonic AgNCs and the MIP technology to detect CA 19-9. The most innovative part of this work is related to the use of CBB incubated with the protein before the addition of the monomer 3AP. Also, the Raman tag MBN was employed, displaying a characteristic peak outside of “fingerprint region”. The reporter Raman signal increased with the increasing of CA 19-9 concentrations and confirmed the recognition of proteins bond to the MIPs by the AgNCs with antibodies.

6.1 Introduction

As explained, there is a low precision in a single biomarker detection for monitoring the installation and aggressiveness of PC, making the development of a multi-biomarker system for PC very important. In this work, a new device for CA19-9 was implemented. CA 19-9 is the only biomarker approved by the US FDA for PC in clinical diagnostic [309]. Elevated levels of this biomarker in blood plasma are not always (and only) associated with PC. High levels of CA 19-9 have occurred in oncological and non-oncological cases, as well as in other types of tumors, or diseases such as pancreatitis and obstructive jaundice [310]. Thus, the level of CA 19-9 in serum is used as prognosis and to follow the response to chemotherapy. Normal serum levels of CA 19-9 have been established under 37 u/ml [311].

Overall, there is a need to find a sensitive and selective technique to detect low levels of CA 19-9, with particular focus on the early detection of changes in the CA 19-9 levels in blood [312]. Among the techniques developed for the detection of CA 19-9, one can find enzyme-linked immunosorbent assays [313], electrochemical immunoassays [314], [315], [316], and immunoassays using quantum dots [312]. Most of these provide low detection limits, but they maintain the inconvenience of a long time to response, high costs and low selectivity in terms of recognition. In line with the previous works, it would be interesting to explore the capacity of having a MIPs/immunoassay testing with SERS detection.

In terms of MIPs assembly, it is important to have a monomeric compound with high affinity for CA19-9. The dye used in the well-known Bradford assay for protein quantification [317], CBB, displays high affinity for specific amino acids such as arginine, histidine, lysine, phenylamine, tyrosine and tryptophan, making this a potential candidate for tailoring MIPs for proteins. CBB forms a stable complex with proteins through electrostatic interactions with the amino and carboxyl groups of the proteins [318]. In 2015 [319], CBB was used for the electrochemical polymerization of CBB on carbon paste electrodes. The modified electrode showed an excellent electrocatalytic activity towards the oxidation of the target molecules. Electrode modification with CBB also showed good stability, sensitivity, selectivity, and reproducibility, which are also the key parameters for the good operation of the modified electrode [319].

In terms of SERS detection, the use of AgNCs seems advantageous, following the previous work. However, the Raman reporter signaling the presence of the protein can be changed to improve the selectivity [320]. In general, the Raman spectra ranges from 500 to 3000 cm^{-1} Raman shift, which can be split into different regions: (a) the “fingerprint-region” (500 to 1800 cm^{-1}) that signals the vibrations of most of the molecules; (b) the “silent-region” (1800 to 2800 cm^{-1}) in which only triple-bond vibrations exist and no cellular vibrations from functional groups are detected; (c) and the “high-frequency region” (> 2800 cm^{-1}) that corresponds to C–H stretching vibrations (CH, CH_2, CH_3) [320]. As the biological materials include different biomolecules, the resulting Raman spectra is complex and contains overlapping signals. This makes the identification of just one molecule very difficult, unless it is found in large quantities or has a unique signature that distinguishes it from other molecules. Particularly, Raman tags with signal in the so-called “silent-regions” are an interesting choice. The functional groups in this region have a strong signal and can be discriminated among endogenous biomolecules. The chemical structures with functional groups like deuterium (stretching vibration −C–D), alkynes (stretching vibration −C≡C–) and nitriles (stretching vibration −C≡N), are candidates to Raman tags due to their chemical stability, small size, and synthetic availability [320].

This, this work uses CBB to build a biosensor with high selectivity for CA 19-9. Since the CBB dye has high affinity for proteins, it is possible to create a binding site in the MIP with greater stability and selectivity for CA 19-9. CBB also protects the protein from radical attack during the polymerization because it forms a complex with the protein and only after 3AP monomers will form polymeric films around this complex by electrical stimulation. The binding sites in the MIPs are obtained after removing the protein, and keep the dye attached to the polymer, facilitating the formation of the reversible complex between the protein and the CBB. In this way, the plastic antibody will be more sensitive to detect CA 19-9. The MIPs was used as plastic antibody to retain the target to be detect using AgNCs (see Figure 53). The surface of AgNCs was modified with anti-CA 19-9 antibody and the SERS signal was followed using the MBN as Raman tag.

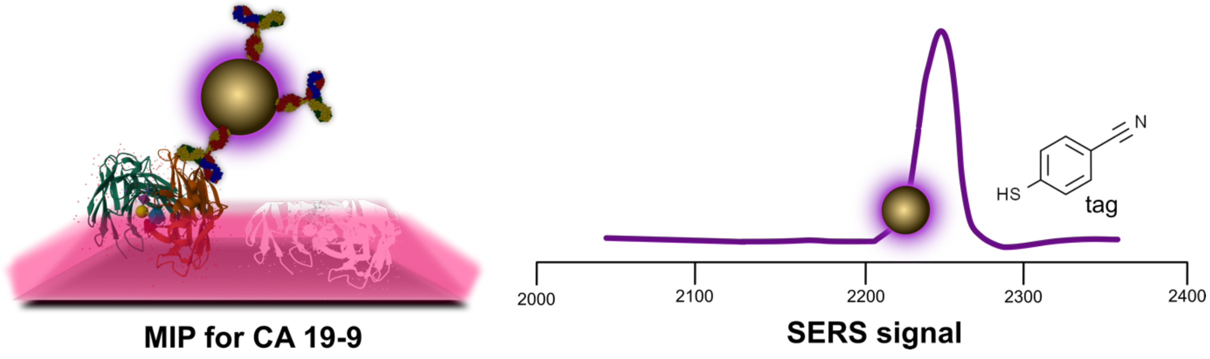

Figure 53: Schematic representation of the MIPs for CA 19-9 with the detection of protein through SERS using AgNCs (left) and the peak signal obtained for the Raman tag bond to the AgNCs (right).

6.2 Experimental Section

6.2.1 Equipment

Electrochemical measurements were made with the Potentiostat/Galvanostat from Metrohm Autolab controlled by NOVA 2.0 software [237]. The C-SPEs were acquired from DropSens, DRP-C110. The commercially C-SPEs have a three-electrode system, the WE and CE are made with carbon and the reference is silver material. The control box connecting these SPEs to the potentiostat was from BioTID, Portugal.

Raman spectra were acquired with a Thermo Scientific DXR Raman Microscope. The laser (785 nm) was focused on the samples through a 50x objective with a power of 15 mW.

6.2.2 Reagents and solutions

All solutions were prepared with ultrapure water Milli-Q laboratory grade. Potassium hexacyanoferrate III ($K_3[Fe(CN)_6]$), potassium hexacyanoferrate II ($K_4[Fe(CN)_6]$) trihydrate from Riedel-de-Häen; Sodium phosphate dibasic dihydrate, 99.5% ($Na_2HPO_4.2H_2O$) from Panreac; Sodium dihydrogen phosphate dihydrate ($NaH_2PO_4.2H_2O$) from Scharlau; foetal bovine serum and Glucose were obtained from Alfa Aesar. Sulphuric acid (H_2SO_4) was obtained from BDH; 3-Aminophenol, 99% from Acros Organics; Coomassie Brilliant Blue G 250 from Panreac; CA 19-9 obtained from Biotbyt; Carcinoembryonic Antigen from EastCoastBio; Creatinine obtained from Fluka; Anti-CA 19-9 antibody from Abcam; Ascorbic Acid, Polyvinylpyrrolidone, Poly(diallyldimethylammonium chloride) solution 20 wt. % in H_2O (PDDA, MW: 400000-500000), Gold (III) chloride trihydrate 99 % ($HAuCl_4.H_2O$), Latex beads Polystyrene, Poly(allylamine hydrochloride), Oxalic acid dihydrate and Tetrakis hydroxymethyl phosphonium chloride solution, were obtained from SigmaAldrich. Silver nitrate ($AgNO_3$) from Fluka; 4-mercaptobenzonitrile obtained by Apollo-Scientific; Sodium Hydroxide (NaOH) obtained from EKA; Sodium Chloride (NaCl) obtained by Normapur.

6.2.3 Preparation of Biosensor

The biosensor for CA 19-9 detection was assembled electrochemically on C-SPEs surface using MIPs technology. The performance of biosensor in each step of construction was followed by EIS.

The C-SPEs were previously cleaning through an electrochemical oxidation in H_2SO_4 solution (0.5 M), made by CV, between -0.5 and 1.5 V, at a scan rate of 0.05V/s for 10 cycles.

Then, for the polymerizingn solutions consisted of a solution 1:1 (v:v) with CBB (0.01mM) and 3AP (0.5mM) in PhB solution (0.1 M). The PhB solution was prepared at pH 7.4 using 0.0754 M of Na_2HPO_4 and 0.0246 M of NaH_2PO_4. Previously, 150 µl of CBB solution was shaken during 20 min with 50 µl of CA 19-9 (10 $ku \cdot ml^{-1}$). Then 200 µl of 3AP was added to obtain the polymerizing solution yielding the MIPs. The same procedure was used to prepare the NIP solution replacing the protein solution by PhB. The electrode was covered with polymerizing solution and was electropolymerization was made by CV, scanning the potentials between -0.3 to 0.8 V, at a scan rate of 0.050 V/s, fot 10 cycles. To protein was removed to form the imprinted cavities in the same way as in the previous works [321]. The modified electrode was incubated during 1 hour with oxalic acid (0.5 M).

6.2.4 Electrochemical measurements

The calibrations of the biosensor were evaluatedout with electrochemical measurements usinga 5nM standard solution of $[Fe(CN)6]^{3-/4-}$, prepared in PhB. The EIS was used at frequency range of 0.1 to $1x10^5$ Hz, with 0.01 V of amplitude and a number of frequencies of 50.

The calibration curves were performed with CA 19-9 standard solution ranging from 0.006 to 100 u/ml prepared in PhB or in FBS diluted 1:100. Each standard solution was incubated for 30 min onto the electrode before electrochemical reading. The selectivity studies evaluated the response of interfering solutions in PhB with 7.0×10^{-4} g/ml of Glucose, 1.0×10^{-3} g/m of Creatinine, and 2.5 mg/ml of CEA.

6.2.5 Synthesis of the Ag/SiO$_2$ capsules

The AgNCs shelled with silica and Au seeds in the inner cavity (void/Au/mSiO$_2$) were prepared according to [285].Under vigorous stirring, a silver nitrate solution (10 mM, 1 ml) was added to 0.5 ml of void/Au/mSiO$_2$ solution (1.25 mg/ml$^-$). After 5 min, 10 µL of ascorbic acid (10 mM) were added to the solution under stirring, resulting in a colour change from red to brown as consequence of Ag+ reduction. The solution was kept under agitation during 5 min. The excess of reagent was removed by centrifugation-redispersion cycles with ethanol (3500 rpm, 10 min).

The Raman reporter, MBN (10^{-3}M), was added to the AgNCs and mixed for 1 h in dark. The solution was centrifuged (3500 rpm, 10 min) in ethanol twice and the last centrifugation was resuspended in 0.5 ml of water.

PVP was used to coat the AgNCs. The PVP solution was prepared by dissolving 25 mg of PVP dissolved in 0.75 ml of water. 375 µL of PVP solution was added to the AgNCs and stirred during 18 h at room temperature. The excess of PVP was removed by centrifugation-redispersion cycles (4500 rpm, 10 min) in ethanol, and then redispersed in 0.5 ml of water.

The final material structure (Au-Ag/MBN/mSiO$_2$/PVP) was functionalized with PDDA, (MW: 400000-500000) to provide of AgNCs surface the necessary electrostatic charge for the subsequent adsorotion of the antibody. First, the PDDA solution was prepared to final concentration of 2 mg/ml, being dissolved in 0.5 M of NaCl (pH 5.0). 1.5 ml of polymer solution were added to the AgNCs and left under stirring for 30 minutes. Then, the solution was centrifugated three times (4500 rpm, 10 min), first in water and the last in PhB, the appropriate medium for Anti-CA 19-9 antibody binding.

The AgNCs were redispersed in 200 µL of PhB and 100 µL of Anti-CA 19-9 antibody (0.02 mg/ml) was added. The solution was stirred for 1 h, followed by three centrifugation-redispersion cycles with PhB. Finally, they were redispersed in 200 µL of buffer and 5 µL of the final dispersion were drop casted on each electrode (3.125 mg/ml).

6.2.6 SERS measurements

In calibrations with SERS, each C-SPEs was pre-incubated with a specific CA 19-9 standard solution concentration at the WE surface, as described for the electrochemical calibration curves. A volume of 5 µL of the Raman probe dispersion (Au-Ag/MBN/mSiO$_2$/PVP/PDDA/Ab, 3.125 mg/ml) was deposited on the electrode overnight, to bind to the protein at the electrode surface. Then, the electrode surface was washed with water.

6.3 Results and Discussion

6.3.1 Electrochemical studies

The MIP polymer was assembled using electropolymerization of 3AP. The electrochemical behaviour of aminophenol is variable depending on the groups (-NH$_2$ and -OH) susceptible to oxidation [322],

[323]. These groups can occupy *ortho*-, *meta*- and *para*- positions, conferring each compound different electrochemical properties [324]. Studies about the mechanism of electropolymerization through the -NH_2 group [325], and mediated by the -OH group [323], [326] have been reported in the literature. Polymerization can occur by any of the electroactive groups [326]. The electropolymerization of the phenols takes place in the vicinity of the electrodes and not exactly on top of the electrode. So, the adsorption of the molecules that react on the surface of the electrode will be facilitated by the lone pair of electrons found in the molecule. In this way, the -OH group would be free to anchor itself on the surface of the electrode [325]. However, experimentally [325] the opposite effect has been observed.

The electropolymerization process of derivatives of phenols, especially aminophenol, produces polymeric films with insulating properties [327], [328], [329]. Several factors affect the result of the polymer, such as the pH of the electrolyte [330]. In the acid medium, the amino group is responsible for the polymerization process while in the basic and neutral medium the process is mediated by the phenoxyl radicals (Figure 54) [325].

Under our electropolymerization conditions, according to *Franco et al. it* is most likely that the polymerization of 3AP occurs through the attack of nitrogen on the aromatic ring [322]. Theoretically, this would be a possible oxidation mechanism, as we have no studies on functional groups on the surface of the electrode to confirm this statement.

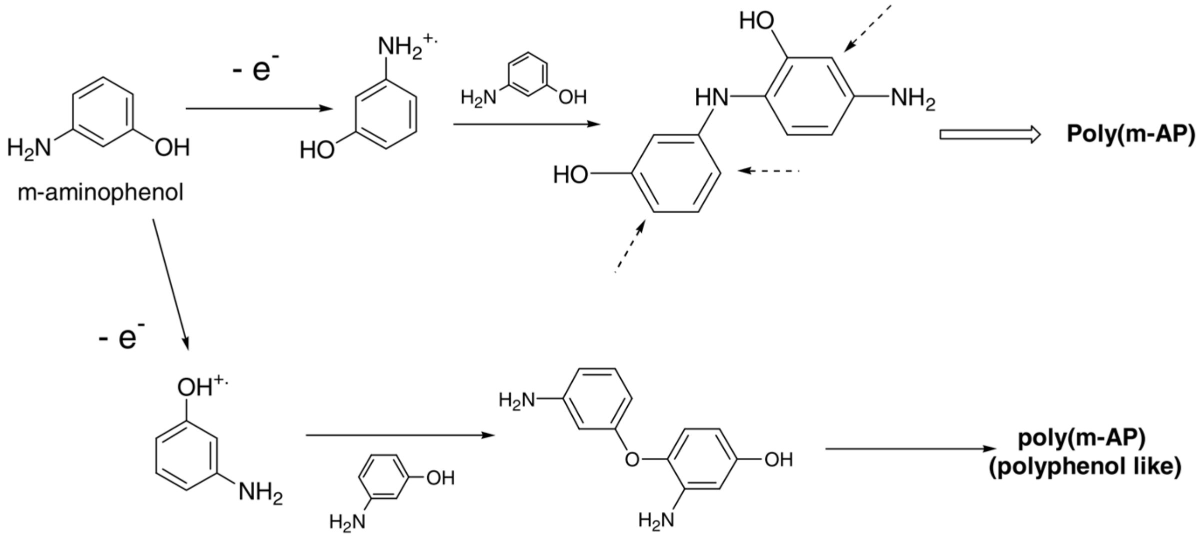

Figure 54: Proposed mechanism of Poly(3AP) reproduced from [325].

6.3.2 Formation and electrochemical characterization of MIPs

The electrochemical behaviour of 3AP on carbon electrodes at pH 7.0 is shown in Figure 55. The first cycle illustrates a single irreversible wave at 0.44 V, and during continuous potential cycling a gradual decrease in its oxidation is observed. The peak current decreases with the increasing number of potential cycles indicating the formation of polymeric film onto the electrode surface. The quick decrease of oxidation current in the successive CV of electropolymerization suggests that these films is insulating and may be of self-limited growth. The results in the literature agree that these polymers form a very thin film, continuous, and usually results in low permeability of compounds inside of them [331]. Figure 55 A to D shows the electropolymerization of 3AP varying the SR. The increase of SR increases the oxidation peak current, revealing in Figure 55 E a more conductive surface when the current of the oxidation peak is higher. The results indicate that with increasing the SR, the poly(3AP) formed presents more permeability to compounds. Since the polymeric surface formed with 50 mv/s allows better charge transfer, this condition was chosen to perform the subsequent tests.

In the work developed by *Chetankumar et al.* reported in [332], CBB was used to modify a carbon-paste electrode (CPE) by electropolymerization with CV. This study confirmed the growth of polymeric films of CBB on CPEs using specific parameters [332]. In work of *Chetankumar et al.,* used as supporting electrolyte to undergo the electropolymerization a solution of 0.1 M NaOH. The supporting electrolyte is critical to define the way the electropolymerization is established, because it defines the polarization of the monomeric species and determines its reactivity and the atoms/bonds involved in the radical polymerization. However, this work cannot use an alkaline condition, because the protein must co-exist with the polymerizing medium. Herein, a solution of 0.1 M PhB was used instead. Under this condition, there was no evidence of the formation of a polymeric film when the electropolymerization of CBB was conducted by CV (Figure 56). On the contrary, if the voltammograms were zoomed in, there are a pair of peaks in the lower potential range that look like a quasi-reversible redox reaction, although in little extent because the currents produced tend to be small.

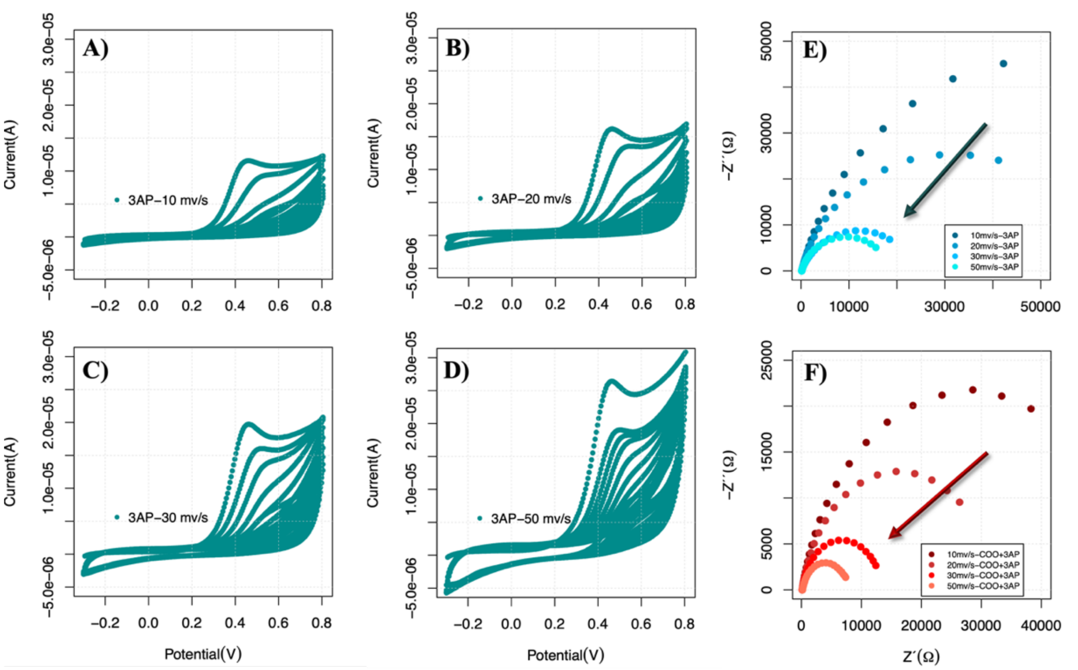

Figure 55: Potential cycling of electropolymerization of 3AP. Increasing scan rate, A) 10 mv/s, B) 20 mv/s, C) 30 mv/s and D) 50 mv/s. EIS for each scan rate for E) 3AP and F) CBB+3AP.

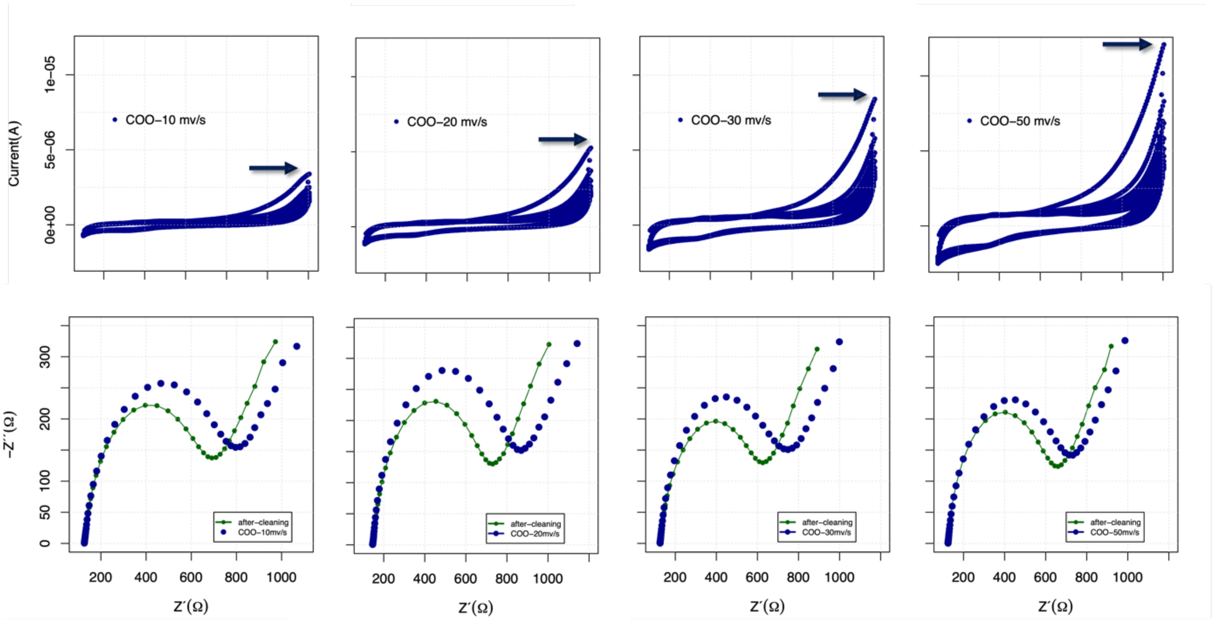

Figure 56: CV voltammograms (top) of the electropolymerization of CBB (0.01mM in 0.1 M PhB, named as COO) on C-SPEs, made with different SR, and the corresponding Nyquist plots (bottom), including the signals obtained with the cleaned electrodes, before electropolymerization.

Still, CBB was selected because it holds a special affinity for proteins, well-known via the Bradford assay, which is used for determining protein concentration [333]. The assay is based on absorbance emitted by the complex formed between proteins and CBB. The mechanism of CBB binding to proteins is widely described [334], [335], mediated by electrostatic and hydrophobic interactions through the radical groups of the amino acid in the proteins. Thus, the presence of CBB in the assembly of the MIP can improve its detection features, because it holds great affinity for CA 19-9 and enables a reversible binding of the protein.

The voltammograms obtained for the polymerization of a solution containing a mixture of CBB and 3AP at different SR (10, 20, 30 and 50 mv/s) is shown in Figure 57. This test was made first to understand the progress of the polymerization with the SR for this mixture, before adding CA 19-9 to the MIP assembly. From this study, a SR of 50 mv/s was chosen, because the C-SPE presented a better electron transfer capacity, displaying a more conductive surface.

The electropolymerization is then made with a mixture of 3AP, CBB and CA 19-9, drop casted onto the electrode surface and undergoing several CV cycles. Figure 58 shows an oxidation peak that belongs to 3AP. This peak in decreasing in intensity with the increasing of potential cycles, leading to the formation of an insulating polymeric film. The MIP is obtained after removing the template from the polymeric network, achieved by incubation in oxalic acid. The formation of binding sites is evidenced by the decreasing R_{ct} values, which reveal the exit of the protein (the polymer becomes more porous and less resistant to charge transfer). This decreasing is also observed in the NIP but with a lower magnitude. This can mean that some polymeric chains were lost after oxalic acid treatment or that some chemical change or protonation may have changed in the course of this process. Overall, the difference between these events in the MIP and the NIP correspond to the exit of the CA19-9 from the polymeric network.

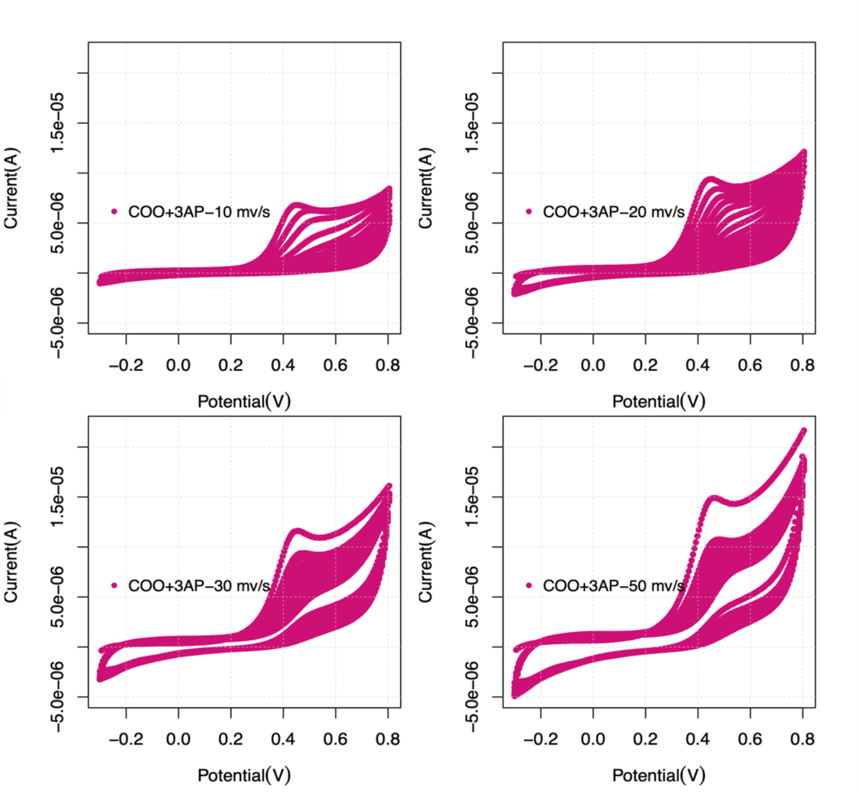

Figure 57: Study at different Scan Rate 10, 20, 30 and 50 mv/s of electropolymerizing CBB and 3AP solution in 0.1 M PhB.

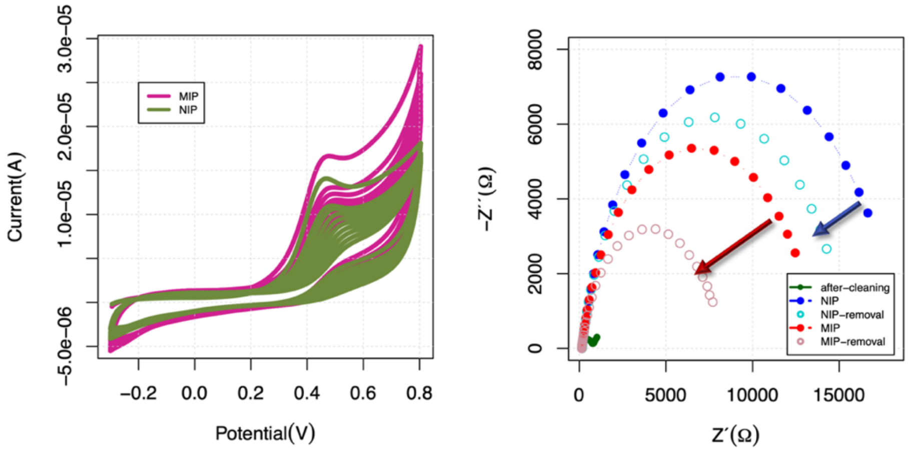

Figure 58: CV during the process of film formation for MIPs and NIP onto the electrode surface (left). EIS for each steps of assembly of biosensor for CA 19-9 (right), shows the MIPs, NIP and after removal of template in the surface.

6.3.3 Performance of MIPs in the detection of CA 19-9

To capacity of the biosensor to respond to the target analyte was evaluated by electrochemical calibrations. The biosensor was calibrated by using increasing concentrations of CA 19-9, in a range of 0.006 to 100 u/ml. Different background solutions were tested: PhB (Figure 59 A) and FBS (Figure 59 B). PhB was used to check the response of the biosensor and optimize it in case of need; FBS was used to simulate the complexity of human serum and predict how the biosensor would behave in this medium.

Figure 59 shows how the R_{ct} decreases with the increasing concentrations of CA 19-9, resulting in a surface that allows more easily the occurrence of charge transfer. The rebinding of CA 19-9 to the complementary cavities in the MIP produced increasing currents in the surface, which must be related to the fact that the superficial charge of protein improved the conductivity of the surface of biosensor. The calibration in buffer had a higher slope than in FBS, which accounts the possibility of having some coexisting proteins occupying some of the binding sites tailored for CA 19-9. Overall, both conditions the biosensor was able to detect low concentration of CA 19-9, obtaining a higher sensitivity in PhB (higher slope). The calibration of the NIP does not display a linear trend, evidencing non-specific binding events, but only to a small extent.

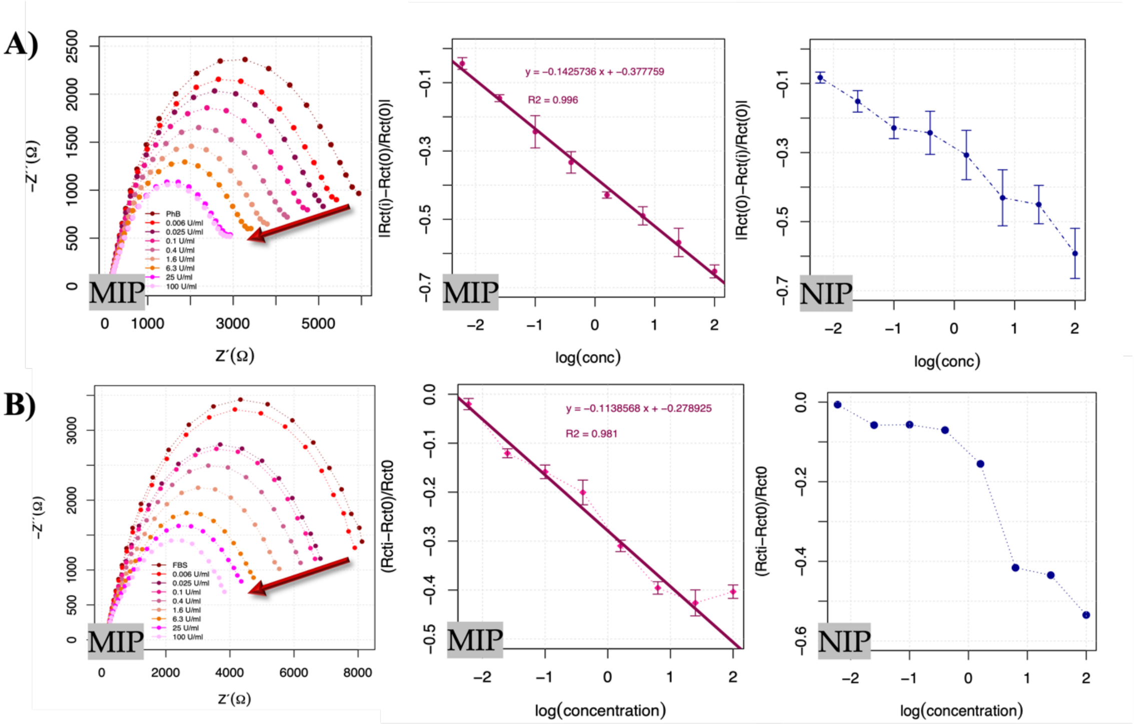

Figure 59: Calibration of biosensor with ranging solution of CA 19-9 between 0.006 to 100 u/ml presented the R_{ct} of MIPs and the linear plot for MIPs (pink) and NIP (blue), prepared in PhB A) and in FBS B) solution.

The effect of CBB in this response was checked by evaluating the response of biosensors produced in the same way but without this component. The typical response obtained is shown in Figure 60 and indicates a completely different behaviour. First, the polymerization of the MIPs was significantly hindered by the presence of CA 19-9, when considering that the R_{ct} values in PhB are very low (compared to the MIPs prepared with CBB). Somehow, this effect may suggest the protective effect of CBB upon CA 19-9 because 3AP did not interact directly with the protein. About the NIP, the non-specific binding observed explains the response of the MIP when CBB was present. 3AP was the component in the system that was responsible for the non-specific binding.

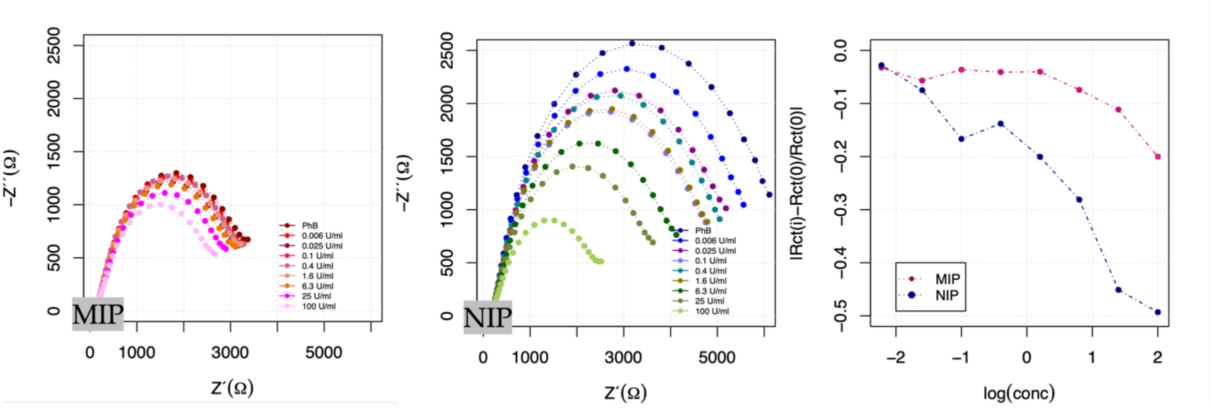

Figure 60: Calibration of MIPs and NIP with 3AP without CBB.

6.3.4 AgNCs SERS signal

Recent efforts have been directed to include Raman reporter molecules with anti-interfering properties [336]. This can be achieved by avoiding spectral interferences with biological molecules when using chemical structures with characteristic peak(s) in the Raman-silent region (1800-2700 cm^{-1}). The silent region is different from fingerprint region because no endogenous biomolecules show peaks in this region. In the silent region the principal vibrational modes are contributes from stable isotopes or triple bonds (e.g. alkyne, cyanide, nitrile) [337]. Particularly, MBN [338] shows a strong peak in the Raman-silent region and was chosen as tag to coat the AgNCs. In addition to this, MBN produces a strong intensity of peak and allows easy conjugation with silver through the thiol groups.

The Raman spectra in Figure 61 A, show the molecule’s characteristic peaks at around 489, 577, 1017, 1072, 1182, 1480, 1584 and 2231 cm^{-1}, which confirms the successful binding of MBN to the AgNCs. This typical Raman spectrum presents stretching vibrations of the cyano-group ($C \equiv N$), with acceptable peak intensities at 2231 cm^{-1}.

The AgNCs were also modified with an antibody against CA 19-9 allow the recognition of this protein at the electrode surface by Raman spectroscopy techniques. To this end, the C-SPEs was incubated with the respective concentration of CA 19-9 (0.006, 6.3 and 100 u/ml). Then, the solution of AgNCs modified with antibody and with the Raman tag were incubated overnight in the C-SPEs. As expected, the intensity of peak at 2231 cm^{-1} increased with the increasing concentration of protein in the C-SPEs surface (see Figure 61 B). As evidenced by SERS results, other high intensity peaks are noticeable in the MBN spectrum. The highest intensity peaks are in the spectrum located at 1072 and 1584 cm^{-1}, corresponding to v(C-S), v(C-C) aromatic skeleton stretching vibration, respectively [339], [340], [341]. However, these peaks coincide with vibrations corresponding to chemical structures of various origins, like proteins, lipids, nucleic acids, and others Raman reporters.

These peaks could be markers of surface concentration of CA 19-9, however, as we already know, the contribution in this region does not come only from the reporter. Hence it is more reliable to follow the intensity variations of the peak coming from v(C≡N) vibration, where we know that only this vibration comes from.

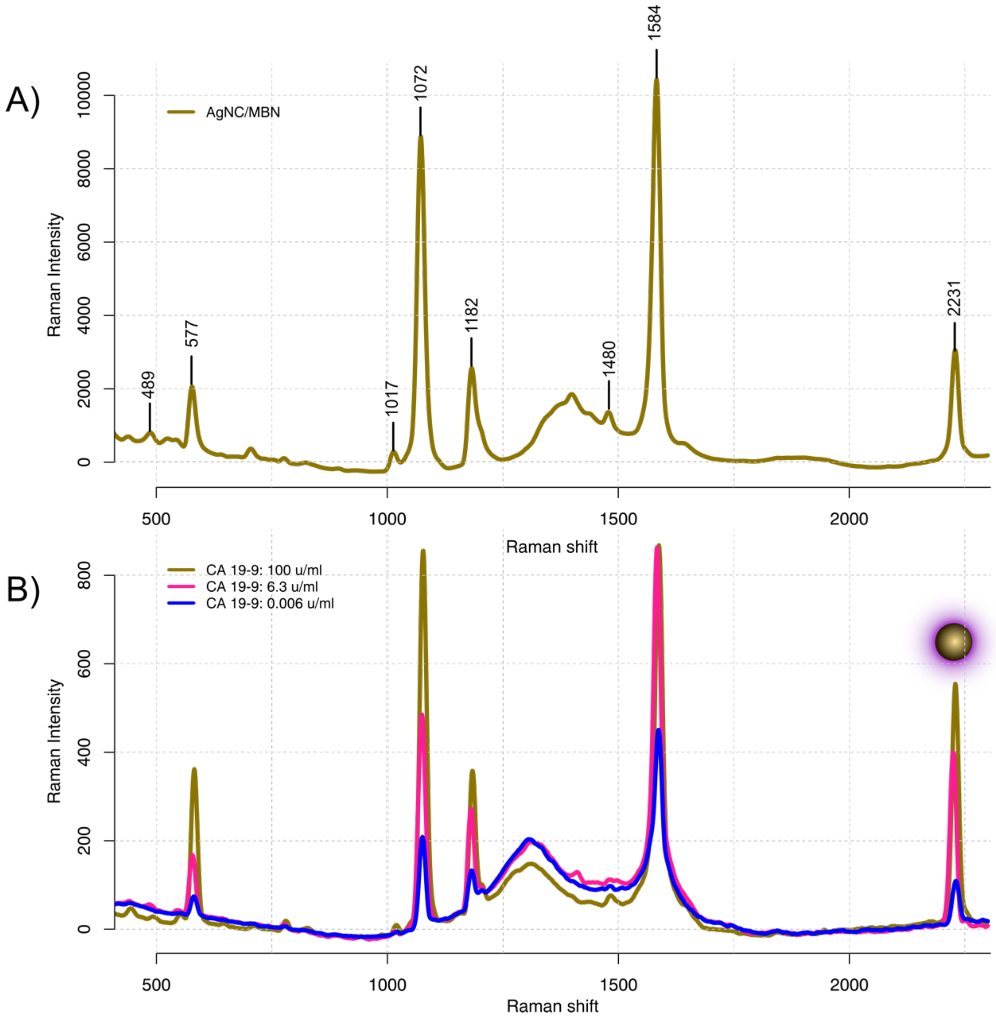

Figure 61: Characteristic SERS spectra for Raman tag MBN A), and the spectrum of AgNCs onto C-SPEs for different concentrations of CA-19-9.

6.3.5 Selectivity Studies

The selectivity is a relevant characteristic of any biosensor. It evaluates the capacity of a bioreceptor to discriminate the target analyte in a complex solution containing other compounds, with more or less structural similarity [342]. The conventional representation of a selectivity assay is the interaction between antigen-antibody. The antibody acts as bioreceptor, then it is exposed to biological solution that contains the antigen, and the antibody only interacts with the specific target antigens.

In this work, the selectivity of the biosensor was evaluated against CEA, creatinine, and glucose, as regular components in complex biological solutions. Figure 62 shows the results obtained using these interfering compounds in terms of relative R_{ct} to the blank. The concentration of the interfering molecules was established at 2.5 ng/ml for CEA, 1.0×10^{-3} g/ml for creatinine and 7.0×10^{-4} g/ml for glucose. Each concentration was prepared in PhB and incubated in different sensing unit, for 20 min. The results obtained for each interfering species were compared with the response of the sensor for CA 19-9 (37 u/ml).

Overall, the interfering components played a little interfering effect upont the response of CA 19-9. First, the singal of the interfering species was only up to 13% of the signal obtained with CA 19-9. Second, the interfering effect should be even smaller when there is a competing effect with CA 19-9, which was absent in this study because all solutions were tested individually.

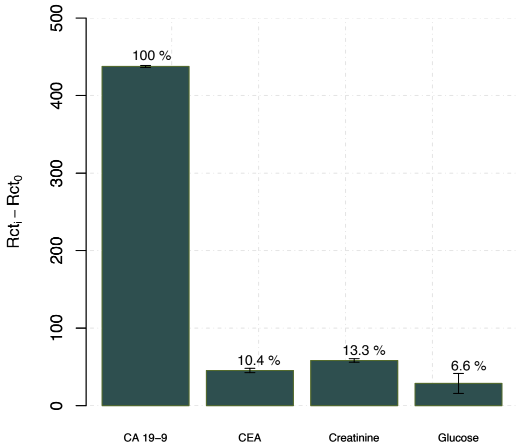

Figure 62: Relative R_{ct} values from Nyquist plots obtained for a single solution of L1CAM, compared with single solutions of interfering species (CEA, Creatinine and Glucose).

6.4 Conclusions

The combination of 3AP as monomer with CBB presents improved the sensitivity of the biosensor for detecting CA 19-9. CBB promoted stability to the MIP structure and protected the protein during the assembly of polymer by radical polymerization under an electrical stimulus. The absence of CBB in the polymerization stage was critical for the analytical detection of CA 19-9. The capacity of the MIPs to concentrate CA 19-9 for subsequent SERS binding is evidenced by the response obtained at very low concentrations and by the increasing intensities obtained with the increasing concentrations.

The AgNCs were synthesized as before, yielding a strong plasmonic signal for a new Raman tag in a special region of the spectra. The large number of hot spots inside of nanostructure resulted in SERS signals of good intensity, recognizing the presence of the protein bond to the MIPs.

The sensitivity of sensor to detect CA 19-9 in a complex matrix like FBS was effective at physiological level concentrations. EIS confirmed to be a suitable technique to follow the change in the sensor development process.

Overall, the sensor displayed good sensitivity and capacity to differentiate alterations in CA 19-9 concentrations by SERS, and also evaluate small changes in concentrations when assessed by electrochemical methods. The combination of MIPs and antibodies with a special Raman tag was successful, and can be extended to a multiplex domain, to be explored in the next chapter.

Chapter 7. Multiplex detection of CA 19-9 and GPC1 with Raman reporters in the silent and fingerprint region

The results presented in this chapter are based on the intitled work *“Multiplex detection of CA 19-9 and GPC1 with Raman reporters in the silent and fingerprint region“* by **Castaño-Guerrero, Y**., Correa-Duarte, M., Aguas, H., Sales, M.G. In this work was used the previously synthetized plasmonic AgNCs to implement a novel multiplex SERS detection. The MIPs technology was used to build the biosensor and concentrate the biomarkers on its surface. The biomarkers were previously added to CBB solution and after some time the monomer 3AP was added. Both reporters previously used were employed here, involving a differentiated Raman peak in the “silent-region” and in the “fingerprint-region”. Raman reporters MBN and 4-ATP were used to identify the presence of CA 19-9 and GPC1 in the surface of biosensor.

7.1 Introduction

The idea of analysing multiple biomarkers for cancer screening and monitoring has been under development for some years. Most biomarkers are not specific for a given type of cancer; together with the genetic variability of human, false positives are obtained, making the result no longer reliable. Hence, multiplex cancer biomarker assays are considered an alternative for a more reliable use in health settings [343].

There are several multiplex-based works using SERS. In these, there is a specific Raman reporter for each compound detected. Finding reporters to his combined detection is a difficult task, because the characteristic peaks of each reporter should not overlap with the background signals or with each other, which is a real challenge. *Koo et al.* [344], reported the simultaneous detection of several molecules in a one-pot, using five reporters with well-separated peaks in the fingerprint region. Other authors have chosen to design and synthesize SERS tags with triple bonds (C≡N and C≡C) to keep the relevant Raman signals outside the fingerprint region [345], [346].

Thus, this work presents a multiplex SERS (Figure 63) analysis to detect two biomarkers of relevance in PC. The approach taken is similar to the previous chapter but included two distinct Raman probes with the respective antibodies, to signal only one of the biomarkers present. The detection of CA 19-9 and GPC1 is achieved individually and simultaneously on the surface of C-SPEs, linked to AgNCs modified with MBN and 4-ATP as reporters, respectively.

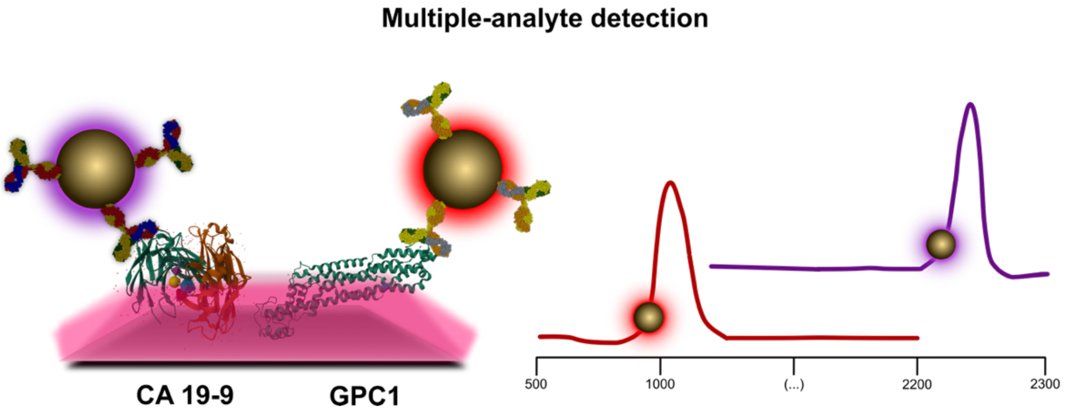

Figure 63: Schematic representation of multiplex MIPs and SERS detection using as Raman tags MBN and 4-ATP.

7.2 Experimental Section

7.2.1 Equipament

A Potentiostat/Galvanostat from Metrohm Autolab controlled by NOVA 2.0 software was used in the electrochemical assays [237]. The commercially C-SPEs were acquired from DropSens, DRP-C110, component by three-electrode system. The interface connector between C-SPEs and Autolab was made in a homade box. The Raman studies were made in Renishaw Invia system using a laser of 785 nm, focused on the samples through a 20x objective with a power of 5.60 mW.

7.2.2 Reagents and solutions

All chemicals solutions were prepared with ultrapure water, Milli-Q laboratory grade. Potassium hexacyanoferrate III ($K_3[Fe(CN)_6]$), potassium hexacyanoferrate II ($K_4[Fe(CN)_6]$) trihydrate from Riedel-de-Häen; sodium phosphate dibasic dihydrate, 99.5% ($Na_2HPO_4.2H_2O$) from Panreac; Sodium dihydrogen phosphate dihydrate ($NaH_2PO_4.2H_2O$) from Scharlau; sulphuric acid (H_2SO_4) was obtained from BDH; 3-aminophenol, 99% from Acros Organics; Coomassie Brilliant Blue G 250 from Panreac; CA 19-9 obtained from Biotbyt; anti-CA 19-9 antibody from Abcam; ascorbic acid, polyvinylpyrrolidone, poly(diallyldimethylammonium chloride) solution 20 wt. % in H_2O (MW: 400000-500000), gold (III) chloride trihydrate 99 % ($HAuCl_4.H_2O$), latex beads polystyrene, poly(allylamine hydrochloride), oxalic acid dihydrate, anti-GPC1 antibody, GPC1 antigen and tetrakis hydroxymethyl phosphonium chloride solution, were obtained from Sigma-Aldrich; silver nitrate ($AgNO_3$) from Fluka; 4-mercaptobenzonitrile from Apollo-Scientific; sodium hydroxide (NaOH) obtained from EKA and sodium chloride (NaCl) from Normapur.

7.2.3 Synthesis of the Ag/SiO_2 capsules

The AgNCs coated with silica were synthetized from Au seed (void/Au/mSiO_2). The void/Au/mSiO_2 were prepared following the description elsewhere [285]. The synthesis of AgNCs was following the same procedure described in section 6.2.5. In this time were used two Raman reporters 4-ATP and MBN for the identification of GPC1 and CA 19-9, respectively. The final AgNCs redispersed in PhB was modified with the corresponding antibody (Anti-CA 19-9 antibody, 0.02 mg·ml^{-1}; Anti-GPC1 antibody, 0.05 mg/ml), as described in section 6.2.5.

7.2.4 Synthesis of multiplex MIPs

The same MIP approach were used to assembly the biosensor for GPC1 and multiplex the response for a combination of biomarkers, GPC1 and CA 19-9. The biosensor was produced electrochemically on C-SPEs electrodes, following the same procedure described in section 6.2.3, adapted herein to a different protein. To obtain a multiplex response, the MIP material was produced in the presence of a solution containing both biomarkers, GPC1 (1.2 µg·mL^{-1}) and CA 19-9 (10 ku·mL^{-1}).

The three electrodes of C-SPEs were covered with polymerizing solution and carried out the electropolymerization procedure using CV between -0.3 to 0.8 V, with SR of 0.050 V/s during 10 cycles. The removal of the biomarkers was made as previously reported [321], incubating during 1 hour with oxalic acid (0.5 M).

7.2.5 SERS measurements

The SERS measurements followed the same procedure as that described in previous chapters. The sensing surface was incubated with different concentrations of GPC1 and CA 19-9, washed and left overnight with 5 µL of the mixture of the Raman probe. In the following day, the surface was washed with water and the Raman spectra was collected.

7.3 Results

7.3.1 Characterization of SERS tags

Figure 64 illustrates the nanostructures obtained in the main stages of the synthesis of the AgNCs. In the first stage (A), the NCs contained Au NPs (3 nm) entrapped inside the silica shell. The AgNCs were obtained after Ag^+ reduction on top of AuNPs that acted as seeds (the right image, B). The final AgNCs looked more dense inside, due to the growth of silver around the gold seeds. The well-formed AgNCs had around 50 nm of diameter, with 10 nm of porous silica covering the outside.

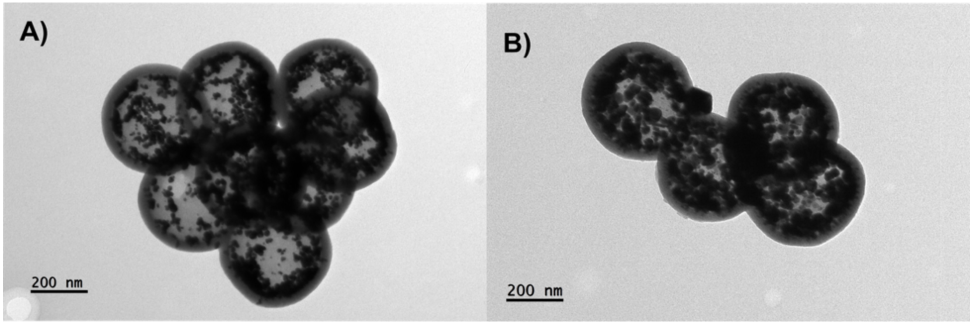

Figure 64: TEM images of the synthesized nanocapsules. A) NPs with the AuNPs inside de silica shell, B) nanocapsules with Ag grown inside on the AuNPs, which acted as seeding sites.

To evaluate the capacity of the SERS tags to enhance the detected signal, the Raman spectra were collected for the 4-ATP and MBN molecules. After immobilisation through the Ag-S bonding interaction on the surface of silver, the Raman intensity of both tags increased significantly, as shown in Figure 65. In MBN spectra, the most relevant peak is determined by the C≡N stretching frequency, which not only depends on the local electric fields but also on the environment to which the nitrile is exposed [347]. MBN evidences three strong bands localized in the fingerprint region at 1076, 1180 and 1586 cm^{-1}, corresponded to aromatic C=H stretching vibrations, C-H bending vibrations, and aromatic skeleton stretching vibration [341]. Also, the obvious peaks in the silent region appear at 2227 cm^{-1} corresponding to the asymmetric stretching of nitrile group ($v_{as}(C\equiv N)$).

The results confirmed that the SERS-tag contained AgNPs inside functionalized with 4-ATP or MBN molecules serving as a Raman reporters. The 4-ATP has been used in many studies and is a consistent Raman reporter [164], [348], [349], [350]. The peak in the Raman biological silent-region of SERS-tag with MBN indicated the correct functionalization of Raman reporter. The band at 2227 cm^{-1} is not the strongest signal but the band not overlapping with others and appear pure in biosilent region evidence without doubt the vibration mode of nitrile group. The results are consistent with previously report [351], [352].

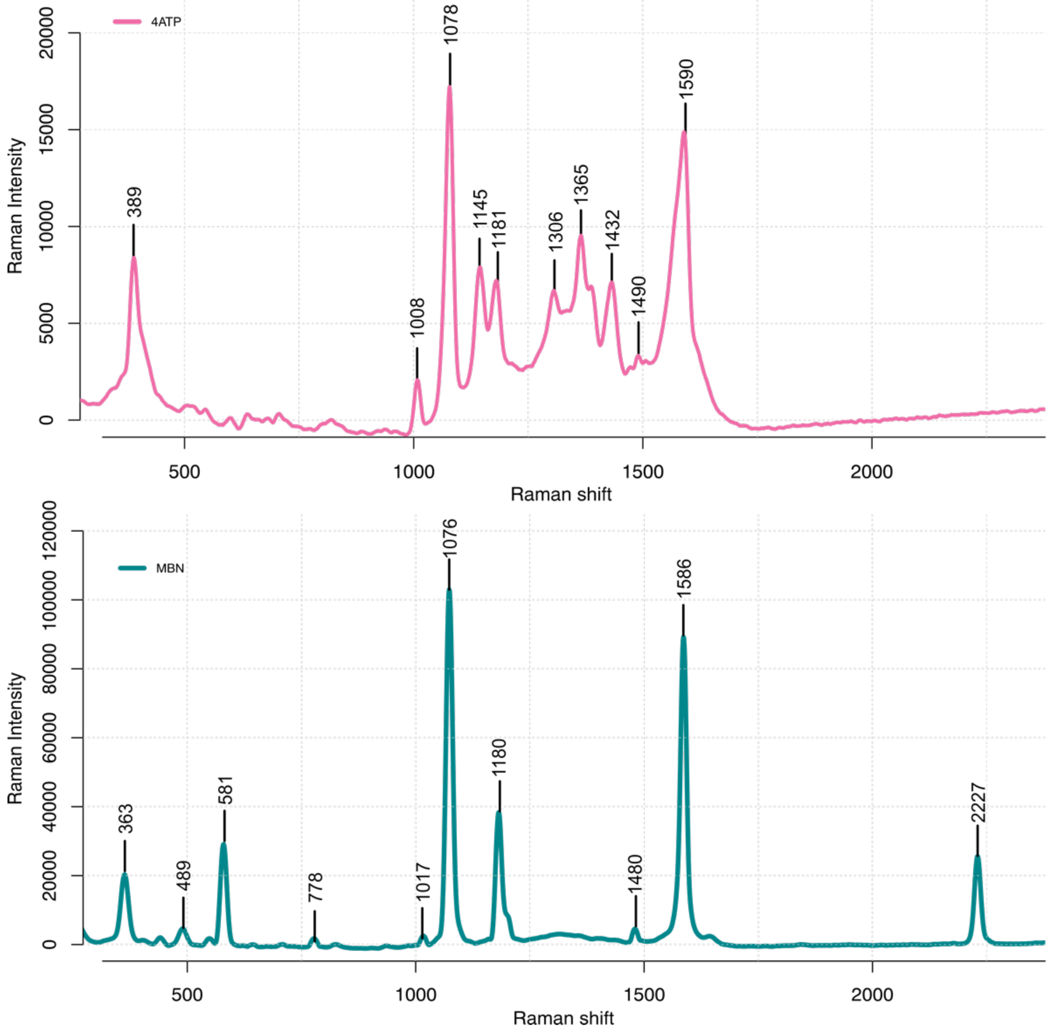

Figure 65: Raman spectra of SERS tags 4-ATP (top, in pink colour) and MBN (bottom, in green colour).

The fingerprint Raman region includes most of the vibrations from conventional SERS tags. When 4-ATP is used, the three more prominent bands at 389, 1078, and 1590 cm^{-1}. According to the literature the intensities of peaks at 389 cm^{-1} and 1590 cm^{-1} are attributed to δ(C–S) and v(C–C) vibrations, respectively [339], [340]. The strongest peak observed at 1078 cm^{-1} is assigned to C (benzene-ring)-S stretching vibration. The spectra showed other bands at 1008, 1145, 1181, 1306, 1365, 1432, 1490 cm^{-1}, whose vibration modes assignment are described in Table 3.

Table 3: Raman peak of a SERS tags 4-ATP, MBN and both tags, on the carbon electrode.

4-ATP/ AgNCs	MBN/ AgNCs	4-ATP+MBN/ AgNCs	Assignments
	2227	2228	ν(C≡N)
1590	1586	1586	ν(C-C) + ν(C-H)
1490	1480	1480	ν(C-C) + δ(C-H)
1432		1439	δ(C-H) + ν(C-C)
1365			ν(C-C) + δ(C-H)
1305		1315	ν(C-N)
1181	1180	1182	δ(C-H)
1145		1143	δ(C-H)
1078	1076	1075	ν(C-S)
1008	1017	1015	γ(C-C) + γ(C-C-C)
	581	581	δ(C-C)
	489		ν(C-N) + ν(C-S) + γ(C-C-C)
	418	418	γ(C-C-C)
389	363	364	δ(C-S)

7.3.2 Multiplex antigens of SERS detection

Multiplex SERS detection of antigens was achieved using two types of antibody-modified tags. The SERS tags were conjugated with specific antibodies to detect the presence of GPC1 and CA 19-9 simultaneously. The SERS tags used were 4-ATP for GPC1, and MBN for CA19-9. Each tag provided very different signals in term of Raman shift.

Under optimized conditions, two different concentrations of antigens were analysed, according to the linear responses expected and the clinical levels of interest. The lowest detectable concentrations of GPC1 and CA 19-9 were 0.01 ng/ml and 0.006 u/ml, respectively, shown in Figure 66. The system in therefore of interest to clinical settings, as the concentration at the physiological limit of each protein in serum is 5 ng/ml [353] and 37 u/ml [354], for GPC1 and CA 19-9, respectively.

As showed the Figure 66 the peak of 4-ATP at 1078 cm^{-1} increases the intensity with the increasing concentration of GPC1. The characteristic peaks of tag that follow in intensity at 1590 and 389 cm^{-1} also show the same behavior, increase the intensity when we go from the lower concentration to cut-off of the protein. In this case, for the conjugate of the SERS tag with 4-ATP it is evident to differentiate between two protein concentrations using the strong peak. Although there are other bands overlap in this region, they remain between the medium to weak signals, which is not an interference problem.

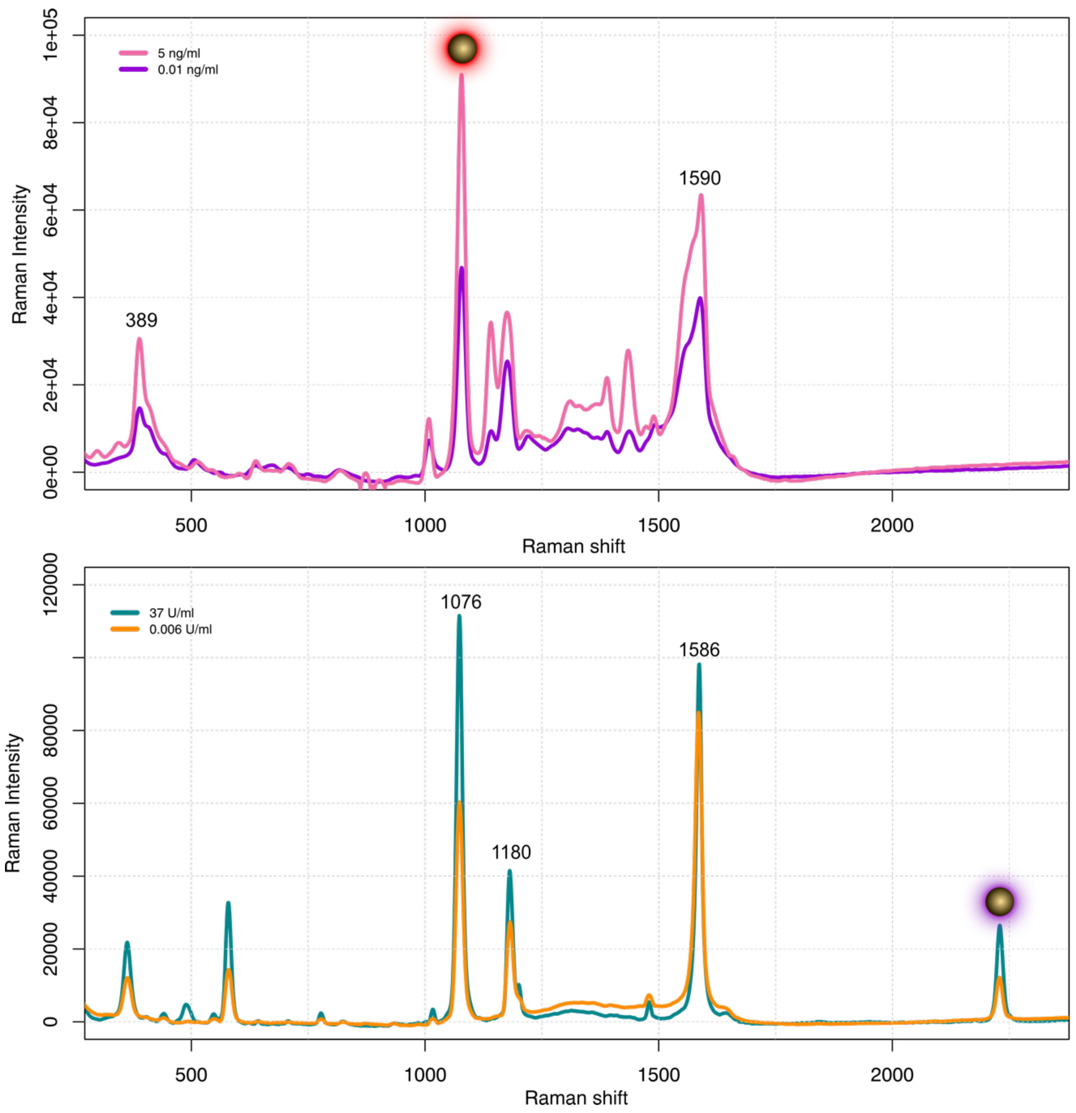

Figure 66: Raman spectra of AgNCs conjugated with 4-ATP and MBN, to detect GPC1 (top, 0.01 and 5 ng/ml) and CA 19-9 (bottom, 0.006 and 37 u/ml).

The SERS tag for MBN shows a strong signal located at approximately the same point as 4-ATP at 1076 cm^{-1}. As these peaks differ in only 2 cm^{-1}, which would be a problem in term of analytical evaluation of each biomarker, MBN was selected. The thiol group in MBN also allows easy conjugation with AgNCs, because it produces an evident SERS signal at 2227 cm^{-1}. The characteristic peak of the MBN molecule is easy to distinguish and does not overlap with the peaks of 4-ATP.
Analysing the spectra in term of Raman intensity, the characteristic peaks located at 1076, 1180, and 1586 cm^{-1} seen in the spectra of MBN would seem useful for detection of CA 19-9. These peaks would be capable to discriminating better lower and higher concentrations of CA 19-9. However, the objective of this work is a multiplex detection of the two proteins on the same surface. Thus, overlapping of Raman peaks is not acceptable. The peaks chosen to follow in the multiplex assays are 1078 cm^{-1} for GPC1 and 2227 cm^{-1} for CA 19-9.

The multiplex detection assay was carried out with the value of the cut-off concentrations of both proteins, and a second reading of a solution diluted 10 times. The capture platform was produced using the MIPs technology, aiming to simultaneously capture of biomarkers GPC1 and CA 19-9. After the biomarkers were captured by the MIPs, the Raman signal was obtained through the SERS tags deposited on the surface of the electrode overnight. It was expected that the MIPs would bind both proteins, because it was assembled with a mixture of GPC1 and CA 19-9 at the polymerization stage. The selectivity for each protein was not critical in this case, as the main purpose was to concentrate these proteins. Any cross-response would not limit the accuracy of the response, because the final signalling was established by the antibodies bond to the AgNCs with the respective Raman tag.

The characteristic Raman spectra obtained in multiplex readings are shown in Figure 67, with an asterisk (4-ATP) and inverted triangle (MBN). The main spectral peaks of 4-ATP were observed at 418, 1143 and 1439 cm^{-1}, while the main peaks of MBN were observed at 581 and 2228 cm^{-1}. Despite some overlaps, from the contribution of the two tags the spectrum shows the profile of the characteristic peaks. Considering the peaks at 1075 cm^{-1} for 4-ATP and at 2228 cm^{-1} for MBN (Figure 67), both peaks evidenced the presence of the antigens trapped in the MIPs platform.

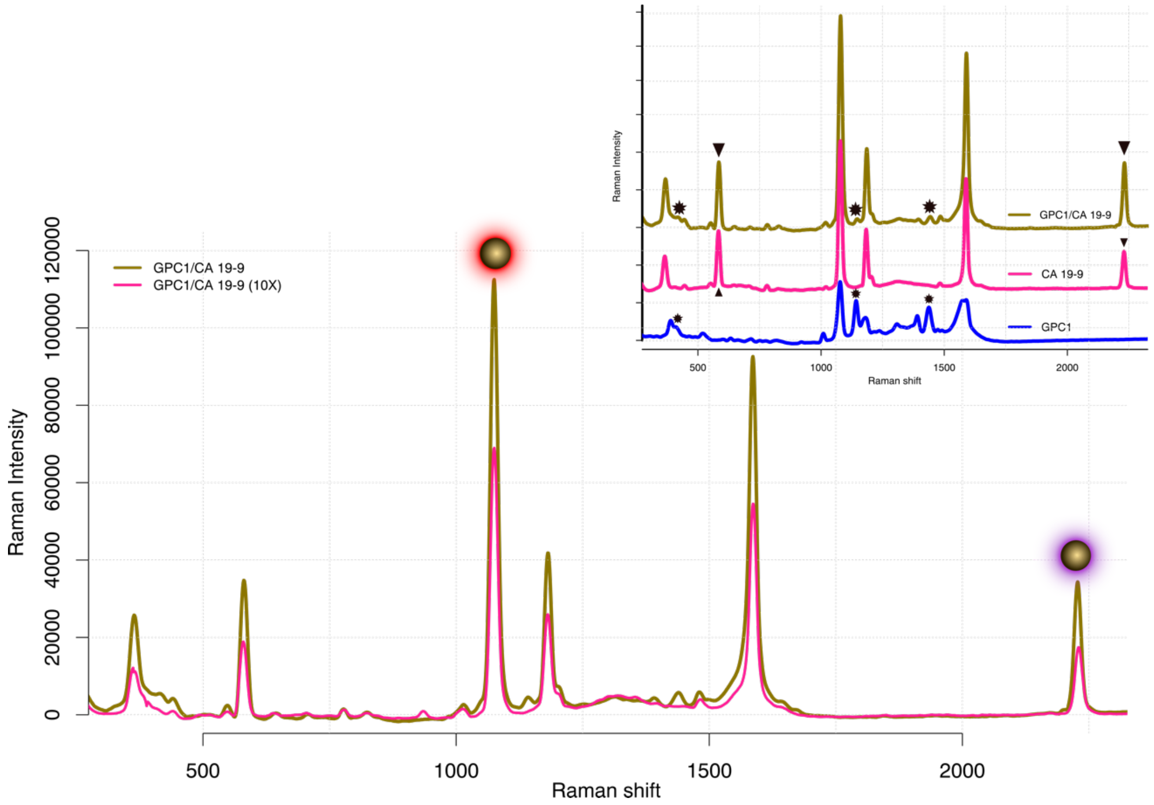

Figure 67: Multiplex SERS spectra for GPC1 and CA 19-9, in concentration of physiological values and dilute 10 times. In the small frame represent the spectrum of SERS tags individually (4-ATP, MBN) and a mixture (4-ATP+ MBN).

Figure 67 confirmed the selective antigen-antibody binding, specifically detecting the GPC1 and CA 19-9 proteins. In terms of quantitative output, the intensity of the Raman peaks decreased upon the 10-fold dilution of the solution containing the mixture of biomarkers. This was as expected, considering that the

MIPs response is typical a linear trend with the log concentrations. The peaks at 1075 and 2228 cm^{-1} evidenced some deviation to the original peaks of the tags in single detection, which could be a result of the combination of the signals from both labels that complement each other.

7.3.3 Single antigen detection

In multiplex SERS detection, GPC1 and CA 19-9 were simultaneously detected and identified using characteristics peaks of SERS tags. In single SERS detection, the focus is detecting a only GPC1. The single detection of CA 19-9 is already discussed in section 6.3.4. The typical Raman spectra of the calibration for GPC1 in SERS is presented in Figure 68.

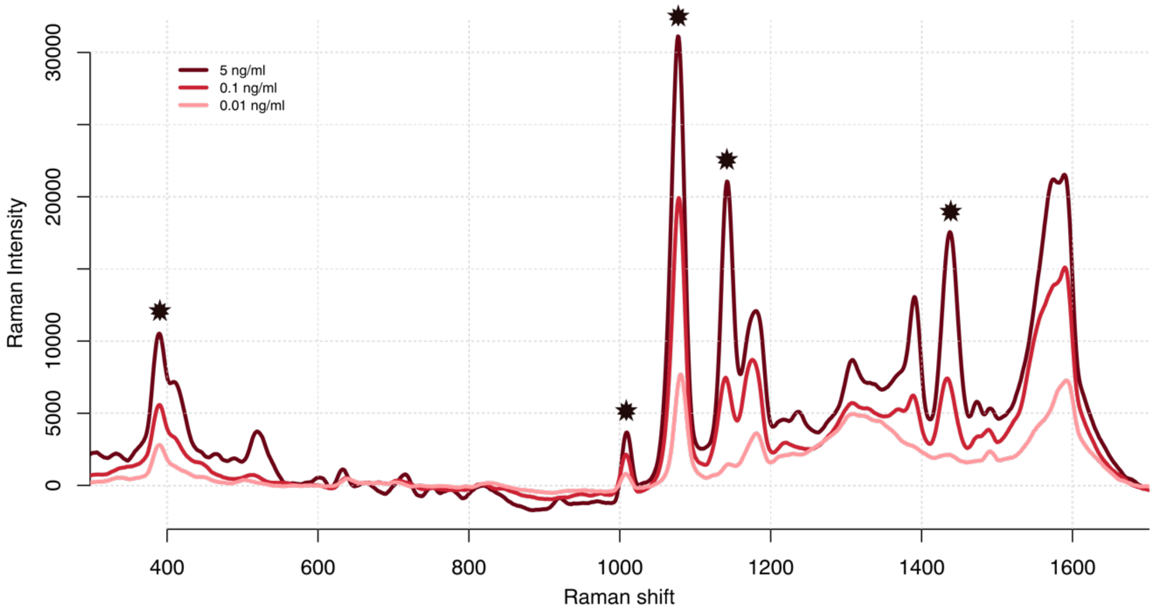

Figure 68: Spectrum of SERS tag for detection of GPC1 in concentration of 0.01, 0.1 and 5 ng/ml.

The principal peaks characteristics of 4-ATP are identified by asterisk in the spectrum, located at 389, 1008,1078, 1145 and 1432 cm^{-1}. The most intense band (1078 cm^{-1}) evidenced a decrease of Raman intensity corresponding to the decrease in the concentration of GPC1. The other representative bands of the Raman reporter evidenced a similar behaviour to the decreasing concentration of biomarker. The result in SERS against GPC1 corroborated the correct assembly using the MIPs technique through electrical stimulation. The calibration of MIPs for GPC1 was further performed with EIS, for different concentrations (0.01, 0.05, 0.1, 0.5, 1, and 5 ng/ml). The typical data is shown in Figure 69. As the concentration of GPC1 increased, the R_{ct} decreased which meant that the surface was more susceptible to charge transfer. The rebinding of protein into the complementary hole in the MIPs allowed a more conductive behaviour at the electrode surface. The possible explanation of behaviour is the way to the protein rebinding into the cavities of the MIPs and the surface charges exposed. Similar response for

CA 19-9 was observed in the previous (chapter, 6.3.3.) confirming that the electropolymerization of the 3AP monomer mixed with the CBB dye promotes these results.

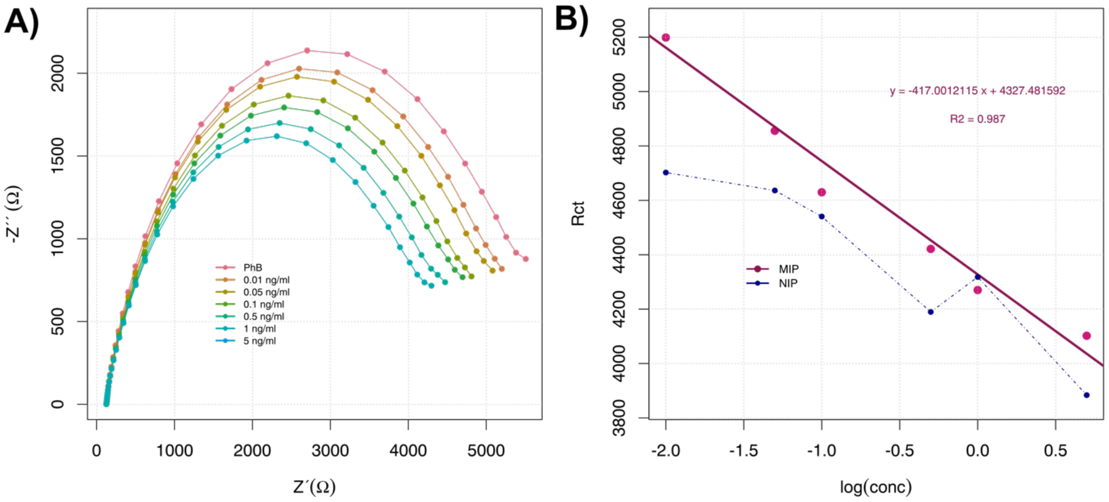

Figure 69: A) EIS reading for GPC1 in a range of concentrations: 0.01, 0.05, 0.1, 0.5, 1, and 5 ng/ml. B) Linear plot of MIPs and NIP.

The 3AP is considered a non-conducting polymer [322] that produced insulating electropolymerized films. As a non-conductive polymer 3AP shows high resistivity properties, self-limiting growth which produces thinner polymer films. In relation to electrical conductivity, non-conducting polymers do not have a strict definition because it depends on many factors such as the level of electron and proton doping. Hence, the concept of conductive or non-conductive polymers is interchangeable [322]. So, the polymeric film produced by 3AP can have conductive or non-conductive properties depending on variables such as: the pH of the polymerization solution [183], the substrate and particularly in our case the polymerization mixture.

The CBB dye has been explored in modifications on electrodes demonstrating considerable improvement in sensitivity, stability and improving the electron transfer reaction [332]. Surfaces modified with CBB acquire conductive properties. Therefore, the combination of the 3AP monomer with CBB contributes to a polymeric film with improved charge transfer properties.

7.4 Conclusion

Multiplex SERS detection is advantageous in scenarios where one wants to analyse a complex mixture of analytes or multiple targets need to be identified/quantified at the same time. It allows the simultaneous detection of various biomarkers in a single experiment.

The MIP technique was efficient in terms of capturing a single biomarker or both analytes at the same time. EIS readings were shown to be sensitive in detecting low levels of GPC1, for concentrations down to 0.01 ng/ml. The multiplex MIP for the biomarkers GPC1 and CA 19-9 was able to bind both proteins, allowing their subsequent detection by SERS tags.

The SERS technique proved to be efficient and sensitive enough to distinguish the signals coming from each protein. In addition to detecting GPC1 and CA 19-9 on the same surface in 10 times more diluted samples, the SERS signals were also strong enough to suggest the specific detection of the biomarkers.

Chapter 8. Conclusion and Futures Progress

The results presented in this thesis culminate with the conclusions and future perspectives that may outcome from the overall work presented.

In general, this thesis proposed development of a low-cost screen platform for detection of biomarkers for PC, which was accomplished. Specifically, the recognition of biomarkers combining the electrochemical and SERS as a detection mechanism was implemented successfully. The development of an immunosensor for the detection of CEA using SERS meets the clinical requirements intended herein, mainly in terms of sensitivity, reproducibility, and selectivity. Furthermore, the combination of electrochemical detection with SERS greatly improved the sensitivity to detect CEA. The introduction of NPs for SERS allowed obtaining the expected detection limits for this complex electrochemical system based in SERS. Knowing that the SERS readings could be improved in relation to the hot spots found on the surface of the electrode, new NPs were incorporated in the following work. The NPs combined with Ag/Au coated with silica allowed obtaining better reproducibility for a better detection capacity. The plasmonic AgNCs allowed recognizing L1CAM with high sensitivity, derived from the evident and strong Raman peak.

In part, the success of the construction of a biosensor based in MIPs was related to the compatibility between the monomer and the molecule used as template. Thus, in the following work, a new monomer was incorporated to detect CA 19-9, the TH dye. This work showed the potential use of TH both in Raman, as an electropolymerizable monomer and as a self-indicating probe in electrochemical assays. Despite obtaining promising results with its utility as an electrochemical probe, there were some problems with the reproducibility of the assays.

Going forward, it is important to note that the sensitivity is controlled by the interactions between the monomer and the template. Hence, it was important to look for more specific chemical interactions between monomers and the intended biomarker. The idea was used the CBB to create a protective layer for CA 19-9 when monomer 3AP underwent electropolymerization. CBB is commonly used in protein assays because of its capacity to bind to proteins and form protein-dye complexes with high affinity and non-covalent interactions. Hence, our work used this dye-protein complex to create a more specific recognition template for the protein. The complex allowed the polymer to grow around it, creating a high affinity hole for CA 19-9 once the molecule was removed. Once the protein was rebound to the imprinted sites, the AgNCs could detect bind to it and single its presence by the characteristic MBN Raman tag peaks.

Combining previous works, a multiplex biosensor was developed to detect two biomarkers on the same spot, CA 19-9 and GPC1, using the same MIP as biorecognition element. Once the plastic antibodies were obtained on the WE, the translation of the previously technology for this multiple approach was straightforward. Through SERS detection, the use of well-selected Raman reporters, showing relevant peaks in different Raman shift positions, allowed the simultaneous detection of both biomarkers.

In the future, the great potential of this technique may be explored in terms of Raman reports, considering the need to have individual peaks avoid interference from other components. A special attention is given to Raman reporters with relevant characteristic peaks in the silent region, which is a fairly unstudied topic. The idea is to design and synthetize new Raman reporters with other characteristic peaks in the silent region, and high affinity for metals, such as Au and Ag, to enable a strong and stable binding over time.

Bibliography

[1] D. Crosby *et al.*, “Early detection of cancer,” *Science (1979)*, vol. 375, no. 6586, Mar. 2022, doi: 10.1126/SCIENCE.AAY9040/ASSET/0A3087E0-148F-45C4-B9D9-5558E774A080/ASSETS/IMAGES/LARGE/SCIENCE.AAY9040-F6.JPG.

[2] Y. Yan, G. Fu, and L. Ming, “Role of exosomes in pancreatic cancer,” *Oncol Lett*, vol. 15, no. 5, p. 7479, May 2018, doi: 10.3892/OL.2018.8348.

[3] E. A. Armstrong *et al.*, “Exosomes in Pancreatic Cancer: from Early Detection to Treatment,” *Journal of Gastrointestinal Surgery*, vol. 22, no. 4, pp. 737–750, Apr. 2018, doi: 10.1007/S11605-018-3693-1/TABLES/3.

[4] S. Afzal, M. Hassan, S. Ullah, H. Abbas, F. Tawakkal, and M. A. Khan, “Breast Cancer; Discovery of Novel Diagnostic Biomarkers, Drug Resistance, and Therapeutic Implications,” *Front Mol Biosci*, vol. 9, p. 161, Feb. 2022, doi: 10.3389/FMOLB.2022.783450/BIBTEX.

[5] A. Tarasiuk, T. Mackiewicz, E. Małecka-Panas, and J. Fichna, “Biomarkers for early detection of pancreatic cancer – miRNAs as a potential diagnostic and therapeutic tool?,” *Cancer Biol Ther*, vol. 22, no. 5–6, p. 347, 2021, doi: 10.1080/15384047.2021.1941584.

[6] S. Kato and K. Honda, “Use of Biomarkers and Imaging for Early Detection of Pancreatic Cancer,” *Cancers (Basel)*, vol. 12, no. 7, pp. 1–21, Jul. 2020, doi: 10.3390/CANCERS12071965.

[7] S. Hamada and T. Shimosegawa, “Biomarkers of Pancreatic Cancer,” *Pancreatology*, vol. 11, no. 2, pp. 14–19, Apr. 2011, doi: 10.1159/000323479.

[8] N. Habbe *et al.*, “MicroRNA miR-155 is a biomarker of early pancreatic neoplasia,” *Cancer Biol Ther*, vol. 8, no. 4, p. 340, Feb. 2009, doi: 10.4161/CBT.8.4.7338.

[9] Y. Sadakari *et al.*, “MicroRNA Expression Analyses in Preoperative Pancreatic Juice Samples of Pancreatic Ductal Adenocarcinoma,” *JOP*, vol. 11, no. 6, pp. 587–592, Nov. 2010, doi: 10.6092/1590-8577/3402.

[10] S. Yue, W. Mu, U. Erb, and M. Zöller, “The tetraspanins CD151 and Tspan8 are essential exosome components for the crosstalk between cancer initiating cells and their surrounding,” *Oncotarget*, vol. 6, no. 4, p. 2366, 2015, doi: 10.18632/ONCOTARGET.2958.

[11] S. A. Melo *et al.*, “Glypican1 identifies cancer exosomes and facilitates early detection of cancer,” *Nature*, vol. 523, no. 7559, p. 177, Jul. 2015, doi: 10.1038/NATURE14581.

[12] M. Liu *et al.*, “Cell-specific biomarkers and targeted biopharmaceuticals for breast cancer treatment,” *Cell Prolif*, vol. 49, no. 4, pp. 409–420, Aug. 2016, doi: 10.1111/CPR.12266.

[13] F. T. C. Moreira, M. J. M. S. Ferreira, J. R. T. Puga, and M. G. F. Sales, “Screen-printed electrode produced by printed-circuit board technology. Application to cancer biomarker detection by means of plastic antibody as sensing material,” *Sens Actuators B Chem*, vol. 223, pp. 927–935, Feb. 2016, doi: 10.1016/J.SNB.2015.09.157.

[14] F. T. C. Moreira, S. Sharma, R. A. F. Dutra, J. P. C. Noronha, A. E. G. Cass, and M. G. F. Sales, “Smart plastic antibody material (SPAM) tailored on disposable screen printed electrodes for protein recognition: Application to myoglobin detection,” *Biosens Bioelectron*, vol. 45, no. 1, pp. 237–244, Jul. 2013, doi: 10.1016/J.BIOS.2013.02.012.

[15] D. Wang *et al.*, “Simultaneous electrochemical immunoassay using graphene–Au grafted recombinant apoferritin-encoded metallic labels as signal tags and dual-template magnetic molecular imprinted polymer as capture probes,” *Biosens Bioelectron*, vol. 65, pp. 78–82, Mar. 2015, doi: 10.1016/J.BIOS.2014.09.085.

[16] K. Mori *et al.*, “A Pretreatment-Free, Polymer-Based Platform Prepared by Molecular Imprinting and Post-Imprinting Modifications for Sensing Intact Exosomes,” *Angew Chem Int Ed Engl*, vol. 58, no. 6, pp. 1612–1615, Feb. 2019, doi: 10.1002/ANIE.201811142.

[17] R. A. Alvarez-Puebla and L. M. Liz-Marzán, “SERS-Based Diagnosis and Biodetection,” *Small*, vol. 6, no. 5, pp. 604–610, Mar. 2010, doi: 10.1002/SMLL.200901820.

[18] F. Wang, S. Cao, R. Yan, Z. Wang, D. Wang, and H. Yang, “Selectivity/Specificity Improvement Strategies in Surface-Enhanced Raman Spectroscopy Analysis,” *Sensors (Basel)*, vol. 17, no. 11, Nov. 2017, doi: 10.3390/S17112689.

[19] G. M. Cooper, “The Development and Causes of Cancer,” 2000, Accessed: Aug. 24, 2022. [Online]. Available: https://www.ncbi.nlm.nih.gov/books/NBK9963/

[20] L. Chen, A. M. Bode, and Z. Dong, “Circulating tumor cells: Moving biological insights into detection,” *Theranostics*, vol. 7, no. 10, pp. 2606–2619, 2017, doi: 10.7150/THNO.18588.

[21] R. L. Siegel, K. D. Miller, H. E. Fuchs, and A. Jemal, “Cancer statistics, 2022,” *CA Cancer J Clin*, vol. 72, no. 1, pp. 7–33, Jan. 2022, doi: 10.3322/CAAC.21708.

[22] K. D. Miller *et al.*, “Cancer treatment and survivorship statistics, 2022,” *CA Cancer J Clin*, vol. 72, no. 5, pp. 409–436, Sep. 2022, doi: 10.3322/CAAC.21731.

[23] S. Wu, W. Zhu, P. Thompson, and Y. A. Hannun, “Evaluating intrinsic and non-intrinsic cancer risk factors,” *Nature Communications 2018 9:1*, vol. 9, no. 1, pp. 1–12, Aug. 2018, doi: 10.1038/s41467-018-05467-z.

[24] E. Bender, “Will a test to detect early pancreatic cancer ever be possible?,” *Nature*, vol. 579, no. 7800, pp. S12–S13, Mar. 2020, doi: 10.1038/D41586-020-00846-3.

[25] “Cancer Tomorrow.” Accessed: Jul. 19, 2022. [Online]. Available: https://gco.iarc.fr/tomorrow/en/dataviz/bars?types=0&sexes=0&mode=population&group_populations=0&multiple_populations=1&multiple_cancers=1&cancers=13&populations=903_904_905_908_909_935&apc=cat_ca20v1.5_ca23v-1.5&group_cancers=1

[26] V. Goral, “Pancreatic Cancer: Pathogenesis and Diagnosis,” *Asian Pac J Cancer Prev*, vol. 16, no. 14, pp. 5619–5624, 2015, doi: 10.7314/APJCP.2015.16.14.5619.

[27] A. McGuigan, P. Kelly, R. C. Turkington, C. Jones, H. G. Coleman, and R. S. McCain, “Pancreatic cancer: A review of clinical diagnosis, epidemiology, treatment and outcomes,” *World J Gastroenterol*, vol. 24, no. 43, p. 4846, Nov. 2018, doi: 10.3748/WJG.V24.I43.4846.

[28] A. Bengtsson, R. Andersson, and D. Ansari, “The actual 5-year survivors of pancreatic ductal adenocarcinoma based on real-world data,” *Sci Rep*, vol. 10, no. 1, p. 16425, Dec. 2020, doi: 10.1038/S41598-020-73525-Y.

[29] R. S. O'Neill and A. Stoita, "Biomarkers in the diagnosis of pancreatic cancer: Are we closer to finding the golden ticket?," *World J Gastroenterol*, vol. 27, no. 26, p. 4045, Jul. 2021, doi: 10.3748/WJG.V27.I26.4045.

[30] D. Giannis, D. Moris, and A. S. Barbas, "Diagnostic, Predictive and Prognostic Molecular Biomarkers in Pancreatic Cancer: An Overview for Clinicians," *Cancers 2021, Vol. 13, Page 1071*, vol. 13, no. 5, p. 1071, Mar. 2021, doi: 10.3390/CANCERS13051071.

[31] "Definition of biomarker - NCI Dictionary of Cancer Terms - NCI." Accessed: Jun. 27, 2023. [Online]. Available: https://www.cancer.gov/publications/dictionaries/cancer-terms/def/biomarker

[32] N. L. Henry and D. F. Hayes, "Cancer biomarkers," *Mol Oncol*, vol. 6, no. 2, p. 140, 2012, doi: 10.1016/J.MOLONC.2012.01.010.

[33] F. N. Al-Shaheri *et al.*, "Blood biomarkers for differential diagnosis and early detection of pancreatic cancer," *Cancer Treat Rev*, vol. 96, p. 102193, May 2021, doi: 10.1016/J.CTRV.2021.102193.

[34] E. Boschetti, A. D'Amato, G. Candiano, and P. G. Righetti, "Protein biomarkers for early detection of diseases: The decisive contribution of combinatorial peptide ligand libraries," *J Proteomics*, vol. 188, pp. 1–14, Sep. 2018, doi: 10.1016/J.JPROT.2017.08.009.

[35] "Top 10: What are the heaviest organs in the human body? | BBC Science Focus Magazine." Accessed: Jan. 23, 2023. [Online]. Available: https://www.sciencefocus.com/the-human-body/top-10-what-are-the-heaviest-organs-in-the-human-body/

[36] A. K. Füzéry, J. Levin, M. M. Chan, and D. W. Chan, "Translation of proteomic biomarkers into FDA approved cancer diagnostics: Issues and challenges," *Clin Proteomics*, vol. 10, no. 1, pp. 1–14, Oct. 2013, doi: 10.1186/1559-0275-10-13/FIGURES/2.

[37] H. Koprowski, Z. Steplewski, K. Mitchell, M. Herlyn, D. Herlyn, and P. Fuhrer, "Colorectal carcinoma antigens detected by hybridoma antibodies," *Somatic Cell Genetics 1979 5:6*, vol. 5, no. 6, pp. 957–971, Nov. 1979, doi: 10.1007/BF01542654.

[38] K. S. Goonetilleke and A. K. Siriwardena, "Systematic review of carbohydrate antigen (CA 19-9) as a biochemical marker in the diagnosis of pancreatic cancer," *European Journal of Surgical Oncology (EJSO)*, vol. 33, no. 3, pp. 266–270, Apr. 2007, doi: 10.1016/J.EJSO.2006.10.004.

[39] S. Nikolaou, S. Qiu, F. Fiorentino, S. Rasheed, P. Tekkis, and C. Kontovounisios, "Systematic review of blood diagnostic markers in colorectal cancer," *Tech Coloproctol*, vol. 22, no. 7, p. 481, Jul. 2018, doi: 10.1007/S10151-018-1820-3.

[40] S. Ning *et al.*, "Clinical significance and diagnostic capacity of serum TK1, CEA, CA 19-9 and CA 72-4 levels in gastric and colorectal cancer patients," *J Cancer*, vol. 9, no. 3, p. 494, 2018, doi: 10.7150/JCA.21562.

[41] B. George, M. Kent, A. Surinach, N. Lamarre, and P. Cockrum, "The Association of Real-World CA 19-9 Level Monitoring Patterns and Clinical Outcomes Among Patients With Metastatic Pancreatic Ductal Adenocarcinoma," *Front Oncol*, vol. 11, p. 3979, Oct. 2021, doi: 10.3389/FONC.2021.754687/BIBTEX.

[42] U. K. Ballehaninna and R. S. Chamberlain, "The clinical utility of serum CA 19-9 in the diagnosis, prognosis and management of pancreatic adenocarcinoma: An evidence based appraisal," *J Gastrointest Oncol*, vol. 3, no. 2, pp. 105–119, 2012, doi: 10.3978/J.ISSN.2078-6891.2011.021.

[43] A. Barhli, J. Cros, L. Bartholin, and C. Neuzillet, "Prognostic stratification of resected pancreatic ductal adenocarcinoma: Past, present, and future," *Digestive and Liver Disease*, vol. 50, no. 10, pp. 979–990, Oct. 2018, doi: 10.1016/J.DLD.2018.08.009.

[44] X. G. Ni *et al.*, "The clinical value of serum CEA, CA19-9, and CA242 in the diagnosis and prognosis of pancreatic cancer," *European Journal of Surgical Oncology (EJSO)*, vol. 31, no. 2, pp. 164–169, Mar. 2005, doi: 10.1016/J.EJSO.2004.09.007.

[45] Z. Wei, X. Cai, W. Cui, and J. Zhang, "Electrochemical Immunoassay for Tumor Marker CA19-9 Detection Based on Self-Assembled Monolayer," *Molecules 2022, Vol. 27, Page 4578*, vol. 27, no. 14, p. 4578, Jul. 2022, doi: 10.3390/MOLECULES27144578.

[46] Z. Huang *et al.*, "Simple and effective label-free electrochemical immunoassay for carbohydrate antigen 19-9 based on polythionine-Au composites as enhanced sensing signals for detecting different clinical samples," *Int J Nanomedicine*, vol. 12, p. 3049, Apr. 2017, doi: 10.2147/IJN.S131805.

[47] P. GOLD and S. O. FREEDMAN, "DEMONSTRATION OF TUMOR-SPECIFIC ANTIGENS IN HUMAN COLONIC CARCINOMATA BY IMMUNOLOGICAL TOLERANCE AND ABSORPTION TECHNIQUES," *J Exp Med*, vol. 121, no. 3, p. 439, Feb. 1965, doi: 10.1084/JEM.121.3.439.

[48] D. M. P. Thomson, J. Krupey, S. 0 Freedman, and P. Goldt, "THE RADIOIMMUNOASSA Y OF CIRCULATING CARCINOEMBRYONIC ANTIGEN OF THE HUMAN DIGESTIVE SYSTEM*," 1969.

[49] A. M. Kabel, "Tumor markers of breast cancer: New prospectives," *Journal of Oncological Sciences*, vol. 3, no. 1, pp. 5–11, Apr. 2017, doi: 10.1016/J.JONS.2017.01.001.

[50] H. Kato *et al.*, "Role of Serum Carcinoma Embryonic Antigen (CEA) Level in Localized Pancreatic Adenocarcinoma: CEA Level before Operation is a Significant Prognostic Indicator in Patients with Locally Advanced Pancreatic Cancer Treated with Neoadjuvant Therapy Followed by Surgical Resection: A Retrospective Analysis," *Ann Surg*, vol. 275, no. 5, pp. E698–E707, May 2022, doi: 10.1097/SLA.0000000000004148.

[51] Y. Jo *et al.*, "Clinical Significance of Early Carcinoembryonic Antigen Change in Patients With Nonmetastatic Colorectal Cancer," *Front Oncol*, vol. 12, p. 2104, May 2022, doi: 10.3389/FONC.2022.739614/BIBTEX.

[52] M. Imamura *et al.*, "Independent prognostic impact of preoperative serum carcinoembryonic antigen and cancer antigen 15-3 levels for early breast cancer subtypes," *World J Surg Oncol*, vol. 16, no. 1, pp. 1–11, Feb. 2018, doi: 10.1186/S12957-018-1325-6/FIGURES/6.

[53] M. Grunnet and J. B. Sorensen, "Carcinoembryonic antigen (CEA) as tumor marker in lung cancer," *Lung Cancer*, vol. 76, no. 2, pp. 138–143, May 2012, doi: 10.1016/J.LUNGCAN.2011.11.012.

[54] A. aroon Lertkhachonsuk, S. Buranawongtrakoon, N. Lekskul, N. Rermluk, W. W. Wee-Stekly, and C. Charakorn, “Serum CA19-9, CA-125 and CEA as tumor markers for mucinous ovarian tumors,” *Journal of Obstetrics and Gynaecology Research*, vol. 46, no. 11, pp. 2287–2291, Nov. 2020, doi: 10.1111/JOG.14427.

[55] V. L. Kankanala and S. K. R. Mukkamalla, “Carcinoembryonic Antigen,” *StatPearls*, Jan. 2022, Accessed: Dec. 02, 2022. [Online]. Available: https://www.ncbi.nlm.nih.gov/books/NBK578172/

[56] H. Wang, A. M. Meng, S. H. Li, and X. L. Zhou, “A nanobody targeting carcinoembryonic antigen as a promising molecular probe for non-small cell lung cancer,” *Mol Med Rep*, vol. 16, no. 1, p. 625, Jul. 2017, doi: 10.3892/MMR.2017.6677.

[57] L. van Manen *et al.*, “Elevated CEA and CA19-9 serum levels independently predict advanced pancreatic cancer at diagnosis,” *Biomarkers*, vol. 25, no. 2, pp. 186–193, Feb. 2020, doi: 10.1080/1354750X.2020.1725786/SUPPL_FILE/IBMK_A_1725786_SM1532.PDF.

[58] F. G. Rathjen and M. Schachner, “Immunocytological and biochemical characterization of a new neuronal cell surface component (L1 antigen) which is involved in cell adhesion.,” *EMBO J*, vol. 3, no. 1, p. 1, 1984, doi: 10.1002/J.1460-2075.1984.TB01753.X.

[59] R. Wachowiak *et al.*, “Increased L1CAM (CD171) levels are associated with glioblastoma and metastatic brain tumors,” *Medicine (United States)*, vol. 97, no. 38, Sep. 2018, doi: 10.1097/MD.0000000000012396.

[60] H. Kiefel *et al.*, “L1CAM,” *https://doi.org/10.4161/cam.20832*, vol. 6, no. 4, pp. 374–384, 2012, doi: 10.4161/CAM.20832.

[61] M. K. E. Schäfer and P. Altevogt, “L1CAM malfunction in the nervous system and human carcinomas,” *Cellular and Molecular Life Sciences*, vol. 67, no. 14, pp. 2425–2437, Jul. 2010, doi: 10.1007/S00018-010-0339-1/FIGURES/2.

[62] H. Asou, M. Miura, M. Kobayashi, and K. Uyemura, “The cell adhesion molecule L1 has a specific role in neural cell migration,” *Neuroreport*, vol. 3, no. 6, pp. 481–484, 1992, doi: 10.1097/00001756-199206000-00006.

[63] P. M. Wood, M. Schachner, and R. P. Bunge, “Inhibition of Schwann cell myelination in vitro by antibody to the L1 adhesion molecule,” *Journal of Neuroscience*, vol. 10, no. 11, pp. 3635–3645, Nov. 1990, doi: 10.1523/JNEUROSCI.10-11-03635.1990.

[64] S. Inaguma *et al.*, “Expression of neural cell adhesion molecule L1 (CD171) in neuroectodermal and other tumors: An immunohistochemical study of 5155 tumors and critical evaluation of CD171 prognostic value in gastrointestinal stromal tumors,” *Oncotarget*, vol. 7, no. 34, pp. 55276–55289, Jul. 2016, doi: 10.18632/ONCOTARGET.10527.

[65] S. Izumoto *et al.*, “A new mutation of the L1CAM gene in an X-linked hydrocephalus family,” *Child’s Nervous System 1996 12:12*, vol. 12, no. 12, pp. 742–747, 1996, doi: 10.1007/BF00261591.

[66] E. De Angelis, A. Watkins, M. Schäfer, T. Brümmendorf, and S. Kenwrick, “Disease-associated mutations in L1 CAM interfere with ligand interactions and cell-surface expression,” *Hum Mol Genet*, vol. 11, no. 1, pp. 1–12, Jan. 2002, doi: 10.1093/HMG/11.1.1.

[67] M. Mustapic *et al.*, “Plasma extracellular vesicles enriched for neuronal origin: A potential window into brain pathologic processes,” *Front Neurosci*, vol. 11, no. MAY, p. 278, May 2017, doi: 10.3389/FNINS.2017.00278/BIBTEX.

[68] E. J. Goetzl *et al.*, “Altered lysosomal proteins in neural-derived plasma exosomes in preclinical Alzheimer disease,” *Neurology*, vol. 85, no. 1, pp. 40–47, Jul. 2015, doi: 10.1212/WNL.0000000000001702.

[69] G. G. Daaboul *et al.*, “Digital Detection of Exosomes by Interferometric Imaging,” *Scientific Reports 2016 6:1*, vol. 6, no. 1, pp. 1–10, Nov. 2016, doi: 10.1038/srep37246.

[70] M. Fogel *et al.*, “L1 expression as a predictor of progression and survival in patients with uterine and ovarian carcinomas,” *The Lancet*, vol. 362, no. 9387, pp. 869–875, Sep. 2003, doi: 10.1016/S0140-6736(03)14342-5.

[71] F. K. F. Kommoss *et al.*, “L1CAM further stratifies endometrial carcinoma patients with no specific molecular risk profile,” *British Journal of Cancer 2018 119:4*, vol. 119, no. 4, pp. 480–486, Jul. 2018, doi: 10.1038/s41416-018-0187-6.

[72] M. Wojciechowski, E. Głowacka, M. Wilczyński, A. Pękala-Wojciechowska, and A. Malinowski, “The sL1CAM in sera of patients with endometrial and ovarian cancers,” *Arch Gynecol Obstet*, vol. 295, no. 1, pp. 225–232, Jan. 2017, doi: 10.1007/S00404-016-4226-3/TABLES/6.

[73] P. Altevogt, K. Doberstein, and M. Fogel, “L1CAM in human cancer,” *Int J Cancer*, vol. 138, no. 7, pp. 1565–1576, Apr. 2016, doi: 10.1002/IJC.29658.

[74] S. Bondong *et al.*, “Prognostic significance of L1CAM in ovarian cancer and its role in constitutive NF-κB activation,” *Annals of Oncology*, vol. 23, no. 7, pp. 1795–1802, Jul. 2012, doi: 10.1093/ANNONC/MDR568.

[75] Aktas B, Kasimir-Bauer S, Wimberger P, Kimmig R, and Heubner M, “Utility of mesothelin, L1CAM and Afamin as biomarkers in primary ovarian cancer - PubMed,” *Anticancer Res*, vol. 33, no. 1, pp. 329–36, Jan. 2013, Accessed: Jun. 07, 2023. [Online]. Available: https://pubmed.ncbi.nlm.nih.gov/23267165/

[76] D. T. Alexandrescu *et al.*, “Melanoma-Specific Marker Expression in Skin Biopsy Tissues as a Tool to Facilitate Melanoma Diagnosis,” *Journal of Investigative Dermatology*, vol. 130, no. 7, pp. 1887–1892, Jul. 2010, doi: 10.1038/JID.2010.61.

[77] D. Talantov *et al.*, “Novel Genes Associated with Malignant Melanoma but not Benign Melanocytic Lesions,” *Clinical Cancer Research*, vol. 11, no. 20, pp. 7234–7242, Oct. 2005, doi: 10.1158/1078-0432.CCR-05-0683.

[78] R. Wachowiak *et al.*, “Increased L1CAM (CD171) levels are associated with glioblastoma and metastatic brain tumors,” *Medicine (United States)*, vol. 97, no. 38, Sep. 2018, doi: 10.1097/MD.0000000000012396.

[79] M. Deichmann, H. Kurzen, U. Egner, P. Altevogt, and W. Hartschuh, “Adhesion molecules CD171 (L1CAM) and CD24 are expressed by primary neuroendocrine carcinomas of the skin (Merkel cell carcinomas),” *J Cutan Pathol*, vol. 30, no. 6, pp. 363–368, Jul. 2003, doi: 10.1034/J.1600-0560.2003.00073.X.

[80] C. Schröder *et al.*, “Expression and prognostic value of L1-CAM in breast cancer,” *Oncol Rep*, vol. 22, no. 5, pp. 1109–1117, Nov. 2009, doi: 10.3892/OR_00000543/HTML.

[81] D. H. Suh *et al.*, “L1 Cell Adhesion Molecule Expression Is Associated With Pelvic Lymph Node Metastasis and Advanced Stage in Diabetic Patients With Endometrial Cancer: A Matched Case Control Study,” *J Cancer Prev*, vol. 19, no. 3, p. 231, Sep. 2014, doi: 10.15430/JCP.2014.19.3.231.

[82] D. L. Chen *et al.*, “L1cam promotes tumor progression and metastasis and is an independent unfavorable prognostic factor in gastric cancer,” *J Hematol Oncol*, vol. 6, no. 1, pp. 1–14, Jun. 2013, doi: 10.1186/1756-8722-6-43/FIGURES/6.

[83] F. Bergmann *et al.*, “Elevated L1CAM expression in precursor lesions and primary and metastastic tissues of pancreatic ductal adenocarcinoma,” *Oncol Rep*, vol. 24, no. 4, pp. 909–915, Oct. 2010, doi: 10.3892/OR_00000936.

[84] S. Sebens Müerköster *et al.*, “Drug-induced expression of the cellular adhesion molecule L1CAM confers anti-apoptotic protection and chemoresistance in pancreatic ductal adenocarcinoma cells,” *Oncogene 2007 26:19*, vol. 26, no. 19, pp. 2759–2768, Nov. 2006, doi: 10.1038/sj.onc.1210076.

[85] C. Geismann *et al.*, “Up-regulation of L1CAM in pancreatic duct cells is transforming growth factor β1- and slug-dependent: Role in malignant transformation of pancreatic cancer,” *Cancer Res*, vol. 69, no. 10, pp. 4517–4526, May 2009, doi: 10.1158/0008-5472.CAN-08-3493/654809/P/UP-REGULATION-OF-L1CAM-IN-PANCREATIC-DUCT-CELLS-IS.

[86] S. Wang, Y. Qiu, and B. Bai, “The Expression, Regulation, and Biomarker Potential of Glypican-1 in Cancer,” *Front Oncol*, vol. 9, p. 614, Jul. 2019, doi: 10.3389/FONC.2019.00614/BIBTEX.

[87] R. V. Iozzo and R. D. Sanderson, “Proteoglycans in cancer biology, tumour microenvironment and angiogenesis,” *J Cell Mol Med*, vol. 15, no. 5, p. 1013, May 2011, doi: 10.1111/J.1582-4934.2010.01236.X.

[88] S. Wang, Y. Qiu, and B. Bai, “The Expression, Regulation, and Biomarker Potential of Glypican-1 in Cancer,” *Front Oncol*, vol. 9, p. 614, Jul. 2019, doi: 10.3389/FONC.2019.00614.

[89] Q. Truong *et al.*, “Glypican-1 as a Biomarker for Prostate Cancer: Isolation and Characterization,” *J Cancer*, vol. 7, no. 8, p. 1002, 2016, doi: 10.7150/JCA.14645.

[90] F. O. F. O. Alshammari, Y. M. Al-Saraireh, A. M. M. Youssef, Y. M. Al-Sarayra, and H. M. Al-rawashdeh, “<p>Glypican-1 Overexpression in Different Types of Breast Cancers</p>,” *Onco Targets Ther*, vol. 14, pp. 4309–4318, Jul. 2021, doi: 10.2147/OTT.S315200.

[91] S. A. Melo *et al.*, “Glypican-1 identifies cancer exosomes and detects early pancreatic cancer,” *Nature 2015 523:7559*, vol. 523, no. 7559, pp. 177–182, Jun. 2015, doi: 10.1038/nature14581.

[92] J. P. Hinestrosa *et al.*, “Early-stage multi-cancer detection using an extracellular vesicle protein-based blood test,” *Communications Medicine 2022 2:1*, vol. 2, no. 1, pp. 1–9, Mar. 2022, doi: 10.1038/s43856-022-00088-6.

[93] J. Dai *et al.*, “Exosomes: key players in cancer and potential therapeutic strategy,” *Signal Transduction and Targeted Therapy 2020 5:1*, vol. 5, no. 1, pp. 1–10, Aug. 2020, doi: 10.1038/s41392-020-00261-0.

[94] C. Hu *et al.*, “Potentiality of Exosomal Proteins as Novel Cancer Biomarkers for Liquid Biopsy,” *Front Immunol*, vol. 13, p. 2356, Jun. 2022, doi: 10.3389/FIMMU.2022.792046/BIBTEX.

[95] M. T. Hsu, Y. K. Wang, and Y. J. Tseng, “Exosomal Proteins and Lipids as Potential Biomarkers for Lung Cancer Diagnosis, Prognosis, and Treatment,” *Cancers 2022, Vol. 14, Page 732*, vol. 14, no. 3, p. 732, Jan. 2022, doi: 10.3390/CANCERS14030732.

[96] W. Li *et al.*, “Role of exosomal proteins in cancer diagnosis,” *Mol Cancer*, vol. 16, no. 1, Aug. 2017, doi: 10.1186/S12943-017-0706-8.

[97] R. Vaz, V. M. Serrano, Y. Castaño-Guerrero, A. R. Cardoso, M. F. Frasco, and M. G. F. Sales, “Breaking the classics: Next-generation biosensors for the isolation, profiling and detection of extracellular vesicles,” *Biosens Bioelectron X*, vol. 10, p. 100115, May 2022, doi: 10.1016/J.BIOSX.2022.100115.

[98] H. Lu, F. Niu, F. Liu, J. Gao, Y. Sun, and X. Zhao, “Elevated glypican-1 expression is associated with an unfavorable prognosis in pancreatic ductal adenocarcinoma,” *Cancer Med*, vol. 6, no. 6, p. 1181, Jun. 2017, doi: 10.1002/CAM4.1064.

[99] S. Wang, Y. Qiu, and B. Bai, “The Expression, Regulation, and Biomarker Potential of Glypican-1 in Cancer,” *Front Oncol*, vol. 9, p. 614, Jul. 2019, doi: 10.3389/FONC.2019.00614.

[100] Y. Dai, K. Abbasi, M. DePietro, S. Butler, and C. C. Liu, “Advanced fabrication of biosensor on detection of Glypican-1 using S-Acetylmercaptosuccinic anhydride (SAMSA) modification of antibody,” *Sci Rep*, vol. 8, no. 1, p. 13541, Dec. 2018, doi: 10.1038/S41598-018-31994-2.

[101] G. Xiao *et al.*, “Light-addressable photoelectrochemical sensors for multichannel detections of GPC1, CEA and GSH and its applications in early diagnosis of pancreatic cancer,” *Sens Actuators B Chem*, vol. 372, p. 132663, Dec. 2022, doi: 10.1016/J.SNB.2022.132663.

[102] V. Naresh and N. Lee, “A Review on Biosensors and Recent Development of Nanostructured Materials-Enabled Biosensors,” *Sensors (Basel)*, vol. 21, no. 4, pp. 1–35, Feb. 2021, doi: 10.3390/S21041109.

[103] A. D. McNaught and A. Wilkinson., *UPAC. Compendium of Chemical Terminology, 2nd ed. (the “Gold Book”)*. Oxford : Blackwell Scientific Publications, 1997.

[104] P. Tetyana, P. M. Shumbula, Z. Njengele-Tetyana, P. Tetyana, P. M. Shumbula, and Z. Njengele-Tetyana, “Biosensors: Design, Development and Applications,” *Nanopores*, Jun. 2021, doi: 10.5772/INTECHOPEN.97576.

[105] S. Vigneshvar, C. C. Sudhakumari, B. Senthilkumaran, and H. Prakash, “Recent advances in biosensor technology for potential applications - an overview,” *Front Bioeng Biotechnol*, vol. 4, no. FEB, p. 11, Feb. 2016, doi: 10.3389/FBIOE.2016.00011/BIBTEX.

[106] C. Karunakaran, R. Rajkumar, and K. Bhargava, “Introduction to Biosensors,” *Biosens Bioelectron*, pp. 1–68, Jan. 2015, doi: 10.1016/B978-0-12-803100-1.00001-3.

[107] S. N. Sawant, “Development of Biosensors From Biopolymer Composites,” *Biopolymer Composites in Electronics*, pp. 353–383, Jan. 2017, doi: 10.1016/B978-0-12-809261-3.00013-9.

[108] K. Ramanathan and B. Danielsson, “Principles and applications of thermal biosensors,” *Biosens Bioelectron*, vol. 16, no. 6, pp. 417–423, Aug. 2001, doi: 10.1016/S0956-5663(01)00124-5.

[109] V. Naresh and N. Lee, “A Review on Biosensors and Recent Development of Nanostructured Materials-Enabled Biosensors,” *Sensors (Basel)*, vol. 21, no. 4, pp. 1–35, Feb. 2021, doi: 10.3390/S21041109.

[110] M. A. Morales and J. M. Halpern, “Guide to Selecting a Biorecognition Element for Biosensors,” *Bioconjug Chem*, vol. 29, no. 10, p. 3231, Oct. 2018, doi: 10.1021/ACS.BIOCONJCHEM.8B00592.

[111] T. Sajini and B. Mathew, “A brief overview of molecularly imprinted polymers: Highlighting computational design, nano and photo-responsive imprinting,” *Talanta Open*, vol. 4, p. 100072, Dec. 2021, doi: 10.1016/J.TALO.2021.100072.

[112] S. Akgönüllü, S. Kılıç, C. Esen, and A. Denizli, “Molecularly Imprinted Polymer-Based Sensors for Protein Detection,” *Polymers 2023, Vol. 15, Page 629*, vol. 15, no. 3, p. 629, Jan. 2023, doi: 10.3390/POLYM15030629.

[113] U. Chadha *et al.*, “Recent progress and growth in biosensors technology: A critical review,” *Journal of Industrial and Engineering Chemistry*, vol. 109, pp. 21–51, May 2022, doi: 10.1016/J.JIEC.2022.02.010.

[114] X. Song, D. Wang, and M. Kim, “Development of an immuno-electrochemical glass carbon electrode sensor based on graphene oxide/gold nanocomposite and antibody for the detection of patulin,” *Food Chem*, vol. 342, p. 128257, Apr. 2021, doi: 10.1016/J.FOODCHEM.2020.128257.

[115] Q. Yan *et al.*, “A highly sensitive uric acid electrochemical biosensor based on a nano-cube cuprous oxide/ferrocene/uricase modified glassy carbon electrode,” *Scientific Reports 2020 10:1*, vol. 10, no. 1, pp. 1–10, Jun. 2020, doi: 10.1038/s41598-020-67394-8.

[116] A. Krajewska, J. Radecki, and H. Radecka, “A Voltammetric Biosensor Based on Glassy Carbon Electrodes Modified with Single-Walled Carbon Nanotubes/Hemoglobin for Detection of Acrylamide in Water Extracts from Potato Crisps,” *Sensors (Basel)*, vol. 8, no. 9, p. 5832, Sep. 2008, doi: 10.3390/S8095832.

[117] W. Białobrzeska *et al.*, “Electrochemical Immunosensors Based on Screen-Printed Gold and Glassy Carbon Electrodes: Comparison of Performance for Respiratory Syncytial Virus Detection,” *Biosensors 2020, Vol. 10, Page 175*, vol. 10, no. 11, p. 175, Nov. 2020, doi: 10.3390/BIOS10110175.

[118] R. Daly, T. Narayan, H. Shao, A. O’riordan, and P. Lovera, “Platinum-based interdigitated microelectrode arrays for reagent-free detection of copper,” *Sensors*, vol. 21, no. 10, p. 3544, May 2021, doi: 10.3390/S21103544/S1.

[119] G. C. M. de Oliveira, J. H. de S. Carvalho, L. C. Brazaca, N. C. S. Vieira, and B. C. Janegitz, “Flexible platinum electrodes as electrochemical sensor and immunosensor for Parkinson’s

disease biomarkers," *Biosens Bioelectron*, vol. 152, p. 112016, Mar. 2020, doi: 10.1016/J.BIOS.2020.112016.

[120] Y. Feng, D. Zhou, L. Gao, and F. He, "Electrochemical biosensor for rapid detection of bacteria based on facile synthesis of silver wire across electrodes," *Biosens Bioelectron*, vol. 168, p. 112527, Nov. 2020, doi: 10.1016/J.BIOS.2020.112527.

[121] A. Sánchez-Calvo, M. C. Blanco-López, and A. Costa-García, "Paper-Based Working Electrodes Coated with Mercury or Bismuth Films for Heavy Metals Determination," *Biosensors 2020, Vol. 10, Page 52*, vol. 10, no. 5, p. 52, May 2020, doi: 10.3390/BIOS10050052.

[122] A. Saenchoopa *et al.*, "A disposable electrochemical biosensor based on screen-printed carbon electrodes modified with silver nanowires/hpmc/chitosan/urease for the detection of mercury (II) in water," *Biosensors (Basel)*, vol. 11, no. 10, p. 351, Oct. 2021, doi: 10.3390/BIOS11100351/S1.

[123] R. Mesa, S. Khan, M. D. P. T. Sotomayor, and G. Picasso, "Using Carbon Paste Electrode Modified with Ion Imprinted Polymer and MWCNT for Electrochemical Quantification of Methylmercury in Natural Water Samples," *Biosensors (Basel)*, vol. 12, no. 6, p. 376, Jun. 2022, doi: 10.3390/BIOS12060376/S1.

[124] R. Rejithamol and S. Beena, "Carbon Paste Electrochemical Sensors for the Detection of Neurotransmitters," *Frontiers in Sensors*, vol. 3, p. 15, May 2022, doi: 10.3389/FSENS.2022.901628.

[125] A. Jędrzak, T. Rębiś, Ł. Klapiszewski, J. Zdarta, G. Milczarek, and T. Jesionowski, "Carbon paste electrode based on functional GOx/silica-lignin system to prepare an amperometric glucose biosensor," *Sens Actuators B Chem*, vol. 256, pp. 176–185, Mar. 2018, doi: 10.1016/J.SNB.2017.10.079.

[126] A. Saenchoopa *et al.*, "A Disposable Electrochemical Biosensor Based on Screen-Printed Carbon Electrodes Modified with Silver Nanowires/HPMC/Chitosan/Urease for the Detection of Mercury (II) in Water," *Biosensors (Basel)*, vol. 11, no. 10, Oct. 2021, doi: 10.3390/BIOS11100351.

[127] A. Saenchoopa *et al.*, "A Disposable Electrochemical Biosensor Based on Screen-Printed Carbon Electrodes Modified with Silver Nanowires/HPMC/Chitosan/Urease for the Detection of Mercury (II) in Water," *Biosensors (Basel)*, vol. 11, no. 10, Oct. 2021, doi: 10.3390/BIOS11100351.

[128] B. W. Park, D. S. Kim, and D. Y. Yoon, "Surface modification of gold electrode with gold nanoparticles and mixed self-assembled monolayers for enzyme biosensors," *Korean Journal of Chemical Engineering*, vol. 28, no. 1, pp. 64–70, Jan. 2011, doi: 10.1007/S11814-010-0349-6/METRICS.

[129] K. Kuntamung, J. Jakmunee, and K. Ounnunkad, "A label-free multiplex electrochemical biosensor for the detection of three breast cancer biomarker proteins employing dye/metal ion-loaded and antibody-conjugated polyethyleneimine-gold nanoparticles," *J Mater Chem B*, vol. 9, no. 33, pp. 6576–6585, Aug. 2021, doi: 10.1039/D1TB00940K.

[130] C. Pothipor, J. Jakmunee, S. Bamrungsap, and K. Ounnunkad, "An electrochemical biosensor for simultaneous detection of breast cancer clinically related microRNAs based on a gold nanoparticles/graphene quantum dots/graphene oxide film," *Analyst*, vol. 146, no. 12, pp. 4000–4009, Jun. 2021, doi: 10.1039/D1AN00436K.

[131] R. G. Mahmudunnabi, F. Z. Farhana, N. Kashaninejad, S. H. Firoz, Y. B. Shim, and M. J. A. Shiddiky, “Nanozyme-based electrochemical biosensors for disease biomarker detection,” *Analyst*, vol. 145, no. 13, pp. 4398–4420, Jul. 2020, doi: 10.1039/D0AN00558D.

[132] M. L. Yola, “Sensitive sandwich-type voltammetric immunosensor for breast cancer biomarker HER2 detection based on gold nanoparticles decorated Cu-MOF and Cu2ZnSnS4 NPs/Pt/g-C3N4 composite,” *Mikrochim Acta*, vol. 188, no. 3, Mar. 2021, doi: 10.1007/S00604-021-04735-Y.

[133] C. Pothipor, S. Bamrungsap, J. Jakmunee, and K. Ounnunkad, “A gold nanoparticle-dye/poly(3-aminobenzylamine)/two dimensional MoSe2/graphene oxide electrode towards label-free electrochemical biosensor for simultaneous dual-mode detection of cancer antigen 15-3 and microRNA-21,” *Colloids Surf B Biointerfaces*, vol. 210, p. 112260, Feb. 2022, doi: 10.1016/J.COLSURFB.2021.112260.

[134] D. Pimalai, T. Putnin, W. Waiwinya, C. Chotsuwan, N. Aroonyadet, and D. Japrung, “Development of electrochemical biosensors for simultaneous multiplex detection of microRNA for breast cancer screening,” *Mikrochim Acta*, vol. 188, no. 10, Oct. 2021, doi: 10.1007/S00604-021-04995-8.

[135] L. C. Clark and C. Lyons, “ELECTRODE SYSTEMS FOR CONTINUOUS MONITORING IN CARDIOVASCULAR SURGERY,” *Ann N Y Acad Sci*, vol. 102, no. 1, pp. 29–45, Oct. 1962, doi: 10.1111/J.1749-6632.1962.TB13623.X.

[136] M. H. Son, S. W. Park, H. Y. Sagong, and Y. K. Jung, “Recent Advances in Electrochemical and Optical Biosensors for Cancer Biomarker Detection,” *BioChip Journal 2022*, pp. 1–24, Nov. 2022, doi: 10.1007/S13206-022-00089-6.

[137] H. S. Magar, R. Y. A. Hassan, and A. Mulchandani, “Electrochemical Impedance Spectroscopy (EIS): Principles, Construction, and Biosensing Applications,” *Sensors (Basel)*, vol. 21, no. 19, Oct. 2021, doi: 10.3390/S21196578.

[138] M. Sönmezler *et al.*, “How Reliable Is the Electrochemical Readout of MIP Sensors?,” *Sensors 2020, Vol. 20, Page 2677*, vol. 20, no. 9, p. 2677, May 2020, doi: 10.3390/S20092677.

[139] “Electrochemical Techniques-Based approaches for Mycobacterium Tuberculosis Detection: Last Decade Review”, doi: 10.1088/1757-899X/705/1/012019.

[140] P. Chooto and P. Chooto, “Cyclic Voltammetry and Its Applications,” *Voltammetry*, Jan. 2019, doi: 10.5772/INTECHOPEN.83451.

[141] C. F. G. C. Geraldes, “Introduction to Infrared and Raman-Based Biomedical Molecular Imaging and Comparison with Other Modalities,” *Molecules 2020, Vol. 25, Page 5547*, vol. 25, no. 23, p. 5547, Nov. 2020, doi: 10.3390/MOLECULES25235547.

[142] G. S. Bumbrah and R. M. Sharma, “Raman spectroscopy – Basic principle, instrumentation and selected applications for the characterization of drugs of abuse,” *Egypt J Forensic Sci*, vol. 6, no. 3, pp. 209–215, Sep. 2016, doi: 10.1016/J.EJFS.2015.06.001.

[143] A. Orlando *et al.*, “A Comprehensive Review on Raman Spectroscopy Applications,” *Chemosensors 2021, Vol. 9, Page 262*, vol. 9, no. 9, p. 262, Sep. 2021, doi: 10.3390/CHEMOSENSORS9090262.

[144] G. S. Bumbrah and R. M. Sharma, “Raman spectroscopy – Basic principle, instrumentation and selected applications for the characterization of drugs of abuse,” *Egypt J Forensic Sci*, vol. 6, no. 3, pp. 209–215, Sep. 2016, doi: 10.1016/J.EJFS.2015.06.001.

[145] “unit of wavelength - Overview, Structure, Properties & Uses.” Accessed: Sep. 20, 2023. [Online]. Available: https://school.careers360.com/physics/unit-of-wavelength-topic-pge

[146] “Principles of Raman spectroscopy (3) Raman spectroscopy measurements | JASCO Global.” Accessed: Jun. 15, 2023. [Online]. Available: https://www.jasco-global.com/principle/principles-of-raman-spectroscopy-3-raman-spectroscopy-measurements/

[147] “How to Choose a Raman Spectroscopy Laser.” Accessed: Jun. 15, 2023. [Online]. Available: https://novantaphotonics.com/how-choose-raman-spectroscopy-laser/

[148] V. Voliani *et al.*, “Cancer phototherapy in living cells by multiphoton release of doxorubicin from gold nanospheres,” *J Mater Chem B*, vol. 1, no. 34, pp. 4225–4230, Aug. 2013, doi: 10.1039/C3TB20798F.

[149] H. Shi and P. J. Sadler, “How promising is phototherapy for cancer?,” *British Journal of Cancer 2020 123:6*, vol. 123, no. 6, pp. 871–873, Jun. 2020, doi: 10.1038/s41416-020-0926-3.

[150] I. Kozak and J. K. Luttrull, “Modern retinal laser therapy,” *Saudi Journal of Ophthalmology*, vol. 29, no. 2, p. 137, Apr. 2015, doi: 10.1016/J.SJOPT.2014.09.001.

[151] D. Palanker and M. S. Blumenkranz, “Chapter 39 - Retinal Laser Therapy: Biophysical Basis and Applications,” *Retina*, pp. 746–760, 2013, doi: 10.1016/B978-1-4557-0737-9.00039-4.

[152] I. Pence and A. Mahadevan-Jansen, “Clinical instrumentation and applications of Raman spectroscopy,” *Chem Soc Rev*, vol. 45, no. 7, p. 1958, Mar. 2016, doi: 10.1039/C5CS00581G.

[153] “Principles of Raman spectroscopy (1) What is Raman spectroscopy? | JASCO Global.” Accessed: Sep. 20, 2023. [Online]. Available: https://www.jasco-global.com/principle/1-what-is-raman-spectroscopy/

[154] K. Hanna, E. Krzoska, A. M. Shaaban, D. Muirhead, R. Abu-Eid, and V. Speirs, “Raman spectroscopy: current applications in breast cancer diagnosis, challenges and future prospects,” *British Journal of Cancer 2021 126:8*, vol. 126, no. 8, pp. 1125–1139, Dec. 2021, doi: 10.1038/s41416-021-01659-5.

[155] D. W. Shipp, F. Sinjab, and I. Notingher, “Raman spectroscopy: techniques and applications in the life sciences,” *Advances in Optics and Photonics, Vol. 9, Issue 2, pp. 315-428*, vol. 9, no. 2, pp. 315–428, Jun. 2017, doi: 10.1364/AOP.9.000315.

[156] N. K. Howell, G. Arteaga, S. Nakai, and E. C. Y. Li-Chan, “Raman Spectral Analysis in the C-H Stretching Region of Proteins and Amino Acids for Investigation of Hydrophobic Interactions,” 1999, doi: 10.1021/jf981074l.

[157] L. and S. D. and K. R. and Z. M. Nasdala, “Raman spectroscopy: Analytical perspectives in mineralogical research,” *EMU Notes in Mineralogy*, vol. 12, pp. 281–343, 2004.

[158] G. M. Das, S. Managò, M. Mangini, and A. C. De Luca, “Biosensing Using SERS Active Gold Nanostructures,” *Nanomaterials 2021, Vol. 11, Page 2679*, vol. 11, no. 10, p. 2679, Oct. 2021, doi: 10.3390/NANO11102679.

[159] S. Schlücker, “Surface-Enhanced Raman Spectroscopy: Concepts and Chemical Applications,” *Angewandte Chemie International Edition*, vol. 53, no. 19, pp. 4756–4795, May 2014, doi: 10.1002/ANIE.201205748.

[160] S. Fateixa, H. I. S. Nogueira, and T. Trindade, “Hybrid nanostructures for SERS: materials development and chemical detection,” *Physical Chemistry Chemical Physics*, vol. 17, no. 33, pp. 21046–21071, Aug. 2015, doi: 10.1039/C5CP01032B.

[161] H. Ko, S. Singamaneni, and V. V. Tsukruk, “Nanostructured Surfaces and Assemblies as SERS Media,” *Small*, vol. 4, no. 10, pp. 1576–1599, Oct. 2008, doi: 10.1002/SMLL.200800337.

[162] T. Jiang, X. Wang, L. Zhang, J. Zhou, and Z. Zhao, “Synthesis and improved SERS performance of silver nanoparticles-decorated surface mesoporous silica microspheres,” *Appl Surf Sci*, vol. 378, pp. 181–190, Aug. 2016, doi: 10.1016/J.APSUSC.2016.03.225.

[163] G. Zhu, L. Cheng, G. Liu, and L. Zhu, “Synthesis of Gold Nanoparticle Stabilized on Silicon Nanocrystal Containing Polymer Microspheres as Effective Surface-Enhanced Raman Scattering (SERS) Substrates,” *Nanomaterials 2020, Vol. 10, Page 1501*, vol. 10, no. 8, p. 1501, Jul. 2020, doi: 10.3390/NANO10081501.

[164] Y. Castaño-Guerrero, F. T. C. Moreira, A. Sousa-Castillo, M. A. Correa-Duarte, and M. G. F. Sales, “SERS and electrochemical impedance spectroscopy immunoassay for carcinoembryonic antigen,” *Electrochim Acta*, vol. 366, p. 137377, Jan. 2021, doi: 10.1016/J.ELECTACTA.2020.137377.

[165] B. Andreiuk *et al.*, “Design and synthesis of gold nanostars-based SERS nanotags for bioimaging applications,” *Nanotheranostics*, vol. 6, no. 1, p. 10, 2022, doi: 10.7150/NTNO.61244.

[166] J. Reguera, D. Jiménez De Aberasturi, N. Winckelmans, J. Langer, S. Bals, and L. M. Liz-Marzán, “Synthesis of Janus plasmonic–magnetic, star–sphere nanoparticles, and their application in SERS detection,” *Faraday Discuss*, vol. 191, no. 0, pp. 47–59, Oct. 2016, doi: 10.1039/C6FD00012F.

[167] M. K. Singh *et al.*, “Synthesis of rod-shaped Au-Cu intermetallic nanoparticles and SERS detection,” *Mater Lett*, vol. 249, pp. 33–36, Aug. 2019, doi: 10.1016/J.MATLET.2019.04.065.

[168] Y. Zhang, C. Li, Z. Fakhraai, B. Moosa, P. Yang, and N. M. Khashab, “Synthesis of Spiked Plasmonic Nanorods with an Interior Nanogap for Quantitative Surface-Enhanced Raman Scattering Analysis,” *ACS Omega*, vol. 3, no. 10, pp. 14399–14405, Oct. 2018, doi: 10.1021/ACSOMEGA.8B01153/ASSET/IMAGES/LARGE/AO-2018-01153C_0004.JPEG.

[169] C. R. Rekha, V. U. Nayar, and K. G. Gopchandran, “Synthesis of highly stable silver nanorods and their application as SERS substrates,” *Journal of Science: Advanced Materials and Devices*, vol. 3, no. 2, pp. 196–205, Jun. 2018, doi: 10.1016/J.JSAMD.2018.03.003.

[170] Y. Pang, C. Wang, L. C. Lu, C. Wang, Z. Sun, and R. Xiao, “Dual-SERS biosensor for one-step detection of microRNAs in exosome and residual plasma of blood samples for diagnosing

pancreatic cancer," *Biosens Bioelectron*, vol. 130, pp. 204–213, Apr. 2019, doi: 10.1016/J.BIOS.2019.01.039.

[171] J. Li *et al.*, "Highly Sensitive Exosome Detection for Early Diagnosis of Pancreatic Cancer Using Immunoassay Based on Hierarchical Surface-Enhanced Raman Scattering Substrate," *Small Methods*, vol. 6, no. 6, p. 2200154, Jun. 2022, doi: 10.1002/SMTD.202200154.

[172] N. Banaei, A. Foley, J. M. Houghton, Y. Sun, and B. Kim, "Multiplex detection of pancreatic cancer biomarkers using a SERS-based immunoassay," *Nanotechnology*, vol. 28, no. 45, p. 455101, Oct. 2017, doi: 10.1088/1361-6528/AA8E8C.

[173] D. Braun, "Origins and Development of Initiation of Free Radical Polymerization Processes," *Int J Polym Sci*, vol. 2009, pp. 1–10, 2009, doi: 10.1155/2009/893234.

[174] A. Ravve, *Principles of Polymer Chemistry*, Third edit. Springer US, 2012. doi: 10.1007/978-1-4899-1283-1.

[175] H. Riazi, A. A. Shamsabadi, P. Corcoran, M. C. Grady, A. M. Rappe, and M. Soroush, "On the thermal self-initiation reaction of η-Butyl acrylate in free-radical polymerization," *Processes*, vol. 6, no. 1, p. 3, Jan. 2018, doi: 10.3390/pr6010003.

[176] A.-H. Bonardi *et al.*, "Thermal Initiators as Additives for Photopolymerization of Methacrylates upon Blue Light," *Coatings 2020, Vol. 10, Page 478*, vol. 10, no. 5, p. 478, May 2020, doi: 10.3390/COATINGS10050478.

[177] A. Eibel, D. E. Fast, and G. Gescheidt, "Choosing the ideal photoinitiator for free radical photopolymerizations: predictions based on simulations using established data," *Polym Chem*, vol. 9, no. 41, pp. 5107–5115, Oct. 2018, doi: 10.1039/C8PY01195H.

[178] Wei-Fang Su, "Radical Chain Polymerization," in *Principles of Polymer Design and Synthesis*, Springer Berlin Heidelberg, 2013, pp. 137–183. [Online]. Available: https://doi.org/10.1007/978-3-642-38730-2_7

[179] M. Roushani and Z. M. Karazan, "Novel Electrochemical Sensor Based on Electropolymerized Dopamine Molecularly Imprinted Polymer for Selective Detection of Pantoprazole," *IEEE Sens J*, vol. 22, no. 7, pp. 6263–6269, Apr. 2022, doi: 10.1109/JSEN.2022.3150222.

[180] "Electrochemical Determination of Naloxone Using Molecularly Imprinted Poly(para-phenylenediamine) Sensor," 2020, doi: 10.1149/1945-7111/abbb0d.

[181] I. F. Abo-Elmagd *et al.*, "Impedimetric Sensors for Cyclocreatine Phosphate Determination in Plasma Based on Electropolymerized Poly(o-phenylenediamine) Molecularly Imprinted Polymers," vol. 6, pp. 31282–31291, 2021, doi: 10.1021/acsomega.1c05098.

[182] K. Namsheer and C. S. Rout, "Conducting polymers: a comprehensive review on recent advances in synthesis, properties and applications," *RSC Adv*, vol. 11, no. 10, pp. 5659–5697, Feb. 2021, doi: 10.1039/D0RA07800J.

[183] G. Ziyatdinova, E. Guss, and E. Yakupova, "Electrochemical Sensors Based on the Electropolymerized Natural Phenolic Antioxidants and Their Analytical Application," *Sensors 2021, Vol. 21, Page 8385*, vol. 21, no. 24, p. 8385, Dec. 2021, doi: 10.3390/S21248385.

[184] Y. Wang and M. Li, “Controlled electropolymerization based on self-dimerizations of monomers,” *Curr Opin Electrochem*, vol. 33, p. 100952, Jun. 2022, doi: 10.1016/J.COELEC.2022.100952.

[185] R. O. Akinyeye *et al.*, “Electrochemical Synthesis and Characterization of 1,2-Naphthaquinone-4-Sulfonic Acid Doped Polypyrrole”, doi: 10.1002/elan.200603732.

[186] C. Liao, “Electrochemical polymerization,” *Chemistry Bulletin / Huaxue Tongbao*, vol. 63, no. 2, pp. 37–41, 2000, doi: 10.1007/978-3-319-95987-0_3/COVER.

[187] F. Saouti, S. Belaaouad, A. Cherqaoui, and Y. Naimi, “Polyaniline Thin Film Prepared by Electrochemical Polymerization Method,” vol. 12, pp. 5523–5533, 2022, doi: 10.33263/BRIAC124.55235533.

[188] A. Korent, K. Ž. Soderžnik, S. Šturm, and K. Ž. Rožman, “A Correlative Study of Polyaniline Electropolymerization and its Electrochromic Behavior,” *J Electrochem Soc*, vol. 167, no. 10, p. 106504, Jun. 2020, doi: 10.1149/1945-7111/AB9929.

[189] N. Casado and D. Mecerreyes, “Chapter 1 Introduction to Redox Polymers: Classification, Characterization Methods and Main Applications,” *RSC Polymer Chemistry Series*, vol. 2021-January, no. 24, pp. 1–26, 2020, doi: 10.1039/9781788019743-00001.

[190] N. Jaffrezic-Renault, C. Ariño, and R. Y. A Hassan, “Advances in Electrochemical Nano-Biosensors for Biomedical and Environmental Applications: From Current Work to Future Perspectives,” *Sensors 2022, Vol. 22, Page 7539*, vol. 22, no. 19, p. 7539, Oct. 2022, doi: 10.3390/S22197539.

[191] A. Raziq, A. Kidakova, R. Boroznjak, J. Reut, A. Öpik, and V. Syritski, “Development of a portable MIP-based electrochemical sensor for detection of SARS-CoV-2 antigen,” *Biosens Bioelectron*, vol. 178, Apr. 2021, doi: 10.1016/J.BIOS.2021.113029.

[192] A. R. Cardoso, M. H. De Sá, M. Goreti, and F. Sales, “An impedimetric molecularly-imprinted biosensor for Interleukin-1β determination, prepared by in-situ electropolymerization on carbon screen-printed electrodes,” 2019, doi: 10.1016/j.bioelechem.2019.04.017.

[193] F. W. Scheller, X. Zhang, A. Yarman, U. Wollenberger, and R. E. Gyurcsányi, “Molecularly imprinted polymer-based electrochemical sensors for biopolymers,” *Curr Opin Electrochem*, vol. 14, pp. 53–59, Apr. 2019, doi: 10.1016/J.COELEC.2018.12.005.

[194] Y. Lai, Y. Deng, G. Yang, S. Li, C. Zhang, and X. Liu, “Molecular Imprinting Polymers Electrochemical Sensor Based on AuNPs/PTh Modified GCE for Highly Sensitive Detection of Carcinomaembryonic Antigen,” *J Biomed Nanotechnol*, vol. 14, no. 10, pp. 1688–1694, Oct. 2018, doi: 10.1166/JBN.2018.2617.

[195] M. C. C. G. Carneiro, A. Sousa-Castillo, M. A. Correa-Duarte, and M. G. F. Sales, “Dual biorecognition by combining molecularly-imprinted polymer and antibody in SERS detection. Application to carcinoembryonic antigen,” *Biosens Bioelectron*, vol. 146, p. 111761, Dec. 2019, doi: 10.1016/J.BIOS.2019.111761.

[196] A. Castro-Grijalba, V. Montes-García, M. J. Cordero-Ferradás, E. Coronado, J. Pérez-Juste, and I. Pastoriza-Santos, “SERS-Based Molecularly Imprinted Plasmonic Sensor for Highly Sensitive PAH Detection,” *ACS Sens*, vol. 5, no. 3, pp. 693–702, Mar. 2020, doi: 10.1021/ACSSENSORS.9B01882/ASSET/IMAGES/LARGE/SE9B01882_0005.JPEG.

[197] P. G. Etchegoin and E. C. L. Ru, “Basic Electromagnetic Theory of SERS,” *Surface Enhanced Raman Spectroscopy: Analytical, Biophysical and Life Science Applications*, pp. 1–37, Dec. 2010, doi: 10.1002/9783527632756.CH1.

[198] I. O. Sosa, C. Noguez, and R. G. Barrera, “Optical properties of metal nanoparticles with arbitrary shapes,” *Journal of Physical Chemistry B*, vol. 107, no. 26, pp. 6269–6275, Jul. 2003, doi: 10.1021/JP0274076/ASSET/IMAGES/MEDIUM/JP0274076E00012.GIF.

[199] M. Muldarisnur, N. Fridayanti, E. Oktorina, E. Zeni, E. Elvaswer, and S. Syukri, “Effect of nanoparticle geometry on sensitivity of metal nanoparticle based sensor,” *IOP Conf Ser Mater Sci Eng*, vol. 578, no. 1, p. 012036, Sep. 2019, doi: 10.1088/1757-899X/578/1/012036.

[200] M. T. Yaraki *et al.*, “Biomimetic Metallic Nanostructures for Biomedical Applications, Catalysis, and beyond,” *Ind Eng Chem Res*, vol. 61, no. 22, pp. 7547–7593, Jun. 2022, doi: 10.1021/ACS.IECR.2C00285/ASSET/IMAGES/LARGE/IE2C00285_0016.JPEG.

[201] J. Zhang *et al.*, “Ultrasensitive Detection of Circulating Tumor DNA of Lung Cancer via an Enzymatically Amplified SERS-Based Frequency Shift Assay,” *ACS Appl Mater Interfaces*, vol. 11, no. 20, pp. 18145–18152, May 2019, doi: 10.1021/ACSAMI.9B02953/ASSET/IMAGES/LARGE/AM-2019-02953D_0005.JPEG.

[202] Y. Yang *et al.*, “Rapid Detection of SARS-CoV-2 RNA in Human Nasopharyngeal Specimens Using Surface-Enhanced Raman Spectroscopy and Deep Learning Algorithms,” *ACS Sens*, vol. 8, no. 1, pp. 297–307, Jan. 2023, doi: 10.1021/ACSSENSORS.2C02194/SUPPL_FILE/SE2C02194_SI_001.PDF.

[203] H. N. Wang, B. M. Crawford, A. M. Fales, M. L. Bowie, V. L. Seewaldt, and T. Vo-Dinh, “Multiplexed Detection of MicroRNA Biomarkers Using SERS-Based Inverse Molecular Sentinel (iMS) Nanoprobes,” *J Phys Chem C Nanomater Interfaces*, vol. 120, no. 37, p. 21047, Sep. 2016, doi: 10.1021/ACS.JPCC.6B03299.

[204] S. Weng *et al.*, “Highly sensitive and reliable detection of microRNA for clinically disease surveillance using SERS biosensor integrated with catalytic hairpin assembly amplification technology,” *Biosens Bioelectron*, vol. 208, p. 114236, Jul. 2022, doi: 10.1016/J.BIOS.2022.114236.

[205] W. Ma *et al.*, “A microfluidic-based SERS biosensor with multifunctional nanosurface immobilized nanoparticles for sensitive detection of MicroRNA,” *Anal Chim Acta*, vol. 1221, p. 340139, Aug. 2022, doi: 10.1016/J.ACA.2022.340139.

[206] Y. Sun, L. Fang, Y. Yi, A. Feng, K. Zhang, and J. J. Xu, “Multistage nucleic acid amplification induced nano-aggregation for 3D hotspots-improved SERS detection of circulating miRNAs,” *J Nanobiotechnology*, vol. 20, no. 1, pp. 1–12, Dec. 2022, doi: 10.1186/S12951-022-01500-Y/FIGURES/5.

[207] S. K. Gahlaut, D. Savargaonkar, C. Sharan, S. Yadav, P. Mishra, and J. P. Singh, “SERS Platform for Dengue Diagnosis from Clinical Samples Employing a Hand Held Raman Spectrometer,” *Anal Chem*, vol. 92, no. 3, pp. 2527–2534, Feb. 2020, doi: 10.1021/ACS.ANALCHEM.9B04129/ASSET/IMAGES/LARGE/AC9B04129_0006.JPEG.

[208] F. Bray, J. Ferlay, I. Soerjomataram, R. L. Siegel, L. A. Torre, and A. Jemal, "Global cancer statistics 2018: GLOBOCAN estimates of incidence and mortality worldwide for 36 cancers in 185 countries," *CA Cancer J Clin*, vol. 68, no. 6, pp. 394–424, Nov. 2018, doi: 10.3322/CAAC.21492.

[209] J. Marrugo-Ramírez, M. Mir, and J. Samitier, "Blood-Based Cancer Biomarkers in Liquid Biopsy: A Promising Non-Invasive Alternative to Tissue Biopsy," *International Journal of Molecular Sciences 2018, Vol. 19, Page 2877*, vol. 19, no. 10, p. 2877, Sep. 2018, doi: 10.3390/IJMS19102877.

[210] E. A. Armstrong *et al.*, "Exosomes in Pancreatic Cancer: from Early Detection to Treatment," *Journal of Gastrointestinal Surgery 2018 22:4*, vol. 22, no. 4, pp. 737–750, Feb. 2018, doi: 10.1007/S11605-018-3693-1.

[211] S. A. Soper *et al.*, "Point-of-care biosensor systems for cancer diagnostics/prognostics," *Biosens Bioelectron*, vol. 21, no. 10, pp. 1932–1942, Apr. 2006, doi: 10.1016/J.BIOS.2006.01.006.

[212] Z. Huang *et al.*, "Simultaneous quantitation of carbohydrate antigen 125 and carcinoembryonic antigen in human serum via time-resolved fluoroimmunoassay," *Clinica Chimica Acta*, vol. 483, pp. 222–226, Aug. 2018, doi: 10.1016/J.CCA.2018.05.003.

[213] A.-U.-R. Fnu and M. W. Saif, "Elevated Level of Serum Carcinoembryonic Antigen (CEA) and Search for a Malignancy: A Case Report", doi: 10.7759/cureus.648.

[214] W. S. Wang *et al.*, "EIA versus RIA in detecting carcinoembryonic antigen level of patients with metastatic colorectal cancer.," *Hepatogastroenterology*, vol. 51, no. 55, pp. 136–141, Jan. 2004, Accessed: Aug. 30, 2023. [Online]. Available: https://europepmc.org/article/med/15011849

[215] N. J. Ronkainen, H. B. Halsall, and W. R. Heineman, "Electrochemical biosensors," *Chem Soc Rev*, vol. 39, no. 5, pp. 1747–1763, Apr. 2010, doi: 10.1039/B714449K.

[216] A. P. F. Turner, "Biosensors: sense and sensibility," *Chem Soc Rev*, vol. 42, no. 8, pp. 3184–3196, Mar. 2013, doi: 10.1039/C3CS35528D.

[217] S. N. Topkaya, M. Azimzadeh, and M. Ozsoz, "Electrochemical Biosensors for Cancer Biomarkers Detection: Recent Advances and Challenges," *Electroanalysis*, vol. 28, no. 7, pp. 1402–1419, Jul. 2016, doi: 10.1002/ELAN.201501174.

[218] C. Zhang *et al.*, "Sandwich-type electrochemical immunosensor for sensitive detection of CEA based on the enhanced effects of Ag NPs@CS spaced Hemin/rGO," *Biosens Bioelectron*, vol. 126, pp. 785–791, Feb. 2019, doi: 10.1016/J.BIOS.2018.11.039.

[219] H. Y. Lin, J. Rick, and T. C. Chou, "Optimizing the formulation of a myoglobin molecularly imprinted thin-film polymer—formed using a micro-contact imprinting method," *Biosens Bioelectron*, vol. 22, no. 12, pp. 3293–3301, Jun. 2007, doi: 10.1016/J.BIOS.2006.11.015.

[220] L. A.A.N.A. Truta and M. Goreti F. Sales, "Sol-Gel Chemistry in Biosensing Devices of Electrical Transduction: Application to CEA Cancer Biomarker".

[221] J. Li, X. Wang, H. Duan, Y. Wang, Y. Bu, and C. Luo, "Based on magnetic graphene oxide highly sensitive and selective imprinted sensor for determination of sunset yellow," *Talanta*, vol. 147, pp. 169–176, Jan. 2016, doi: 10.1016/J.TALANTA.2015.09.056.

[222] S. Aslan and Ü. Anik, “Development of TiO2 and Au Nanocomposite Electrode as CEA Immunosensor Transducer,” *Electroanalysis*, vol. 26, no. 6, pp. 1373–1381, Jun. 2014, doi: 10.1002/ELAN.201400086.

[223] Y. Zou, L. X. Sun, and F. Xu, “Biosensor based on polyaniline–Prussian Blue/multi-walled carbon nanotubes hybrid composites,” *Biosens Bioelectron*, vol. 22, no. 11, pp. 2669–2674, May 2007, doi: 10.1016/J.BIOS.2006.10.035.

[224] X. Li, R. Yuan, Y. Chai, L. Zhang, Y. Zhuo, and Y. Zhang, “Amperometric immunosensor based on toluidine blue/nano-Au through electrostatic interaction for determination of carcinoembryonic antigen,” *J Biotechnol*, vol. 123, no. 3, pp. 356–366, May 2006, doi: 10.1016/J.JBIOTEC.2005.11.023.

[225] G. Paniagua *et al.*, “Amperometric aptasensor for carcinoembryonic antigen based on the use of bifunctionalized Janus nanoparticles as biorecognition-signaling element,” *Anal Chim Acta*, vol. 1061, pp. 84–91, Jul. 2019, doi: 10.1016/J.ACA.2019.02.015.

[226] N. Gan, L. Jia, and L. Zheng, “A Sandwich Electrochemical Immunosensor Using Magnetic DNA Nanoprobes for Carcinoembryonic Antigen,” *International Journal of Molecular Sciences 2011, Vol. 12, Pages 7410-7423*, vol. 12, no. 11, pp. 7410–7423, Oct. 2011, doi: 10.3390/IJMS12117410.

[227] J. C. Kemmegne-Mbouguen, E. Ngameni, P. G. Baker, T. T. Waryo, B. Kgarebe, and E. I. Iwuoha, “Carcinoembryonic Antigen Immunosensor Developed with Organoclay Nanogold Composite Film,” *Int J Electrochem Sci*, vol. 9, no. 1, pp. 478–492, Jan. 2014, doi: 10.1016/S1452-3981(23)07733-7.

[228] Y. Li, W. K. Yang, M. Q. Fan, and A. Liu, “A sensitive label-free amperometric CEA immunosensor based on graphene-Nafion nanocomposite film as an enhanced sensing platform,” *Analytical Sciences*, vol. 27, no. 7, pp. 727–731, Jul. 2011, doi: 10.2116/ANALSCI.27.727/METRICS.

[229] L. A. A. N. A. Truta, F. T. C. Moreira, and M. G. F. Sales, “A dye-sensitized solar cell acting as the electrical reading box of an immunosensor: Application to CEA determination,” *Biosens Bioelectron*, vol. 107, pp. 94–102, Jun. 2018, doi: 10.1016/J.BIOS.2018.02.011.

[230] X. Pei, B. Zhang, J. Tang, B. Liu, W. Lai, and D. Tang, “Sandwich-type immunosensors and immunoassays exploiting nanostructure labels: A review,” *Anal Chim Acta*, vol. 758, pp. 1–18, Jan. 2013, doi: 10.1016/J.ACA.2012.10.060.

[231] N. Li *et al.*, “An ultrasensitive electrochemical immunosensor for CEA using MWCNT-NH 2 supported PdPt nanocages as labels for signal amplification,” *J Mater Chem B*, vol. 3, no. 9, pp. 2006–2011, Feb. 2015, doi: 10.1039/C4TB01695E.

[232] Y. Wang *et al.*, “Sandwich-type electrochemical immunosensor for CEA detection based on Ag/MoS2@Fe3O4 and an analogous ELISA method with total internal reflection microscopy,” *Sens Actuators B Chem*, vol. 266, pp. 561–569, Aug. 2018, doi: 10.1016/J.SNB.2018.03.178.

[233] Å. Larsson, R. Ghosh, and S. Hammarström, “Relative positions of some epitopes on carcinoembryonic antigen,” *Cancer Immunology Immunotherapy*, vol. 30, no. 2, pp. 92–96, Mar. 1989, doi: 10.1007/BF01665959/METRICS.

[234] Y. Lin, G. Xu, F. Wei, A. Zhang, J. Yang, and Q. Hu, “Detection of CEA in human serum using surface-enhanced Raman spectroscopy coupled with antibody-modified Au and γ-Fe2O3@Au nanoparticles,” *J Pharm Biomed Anal*, vol. 121, pp. 135–140, Mar. 2016, doi: 10.1016/J.JPBA.2016.01.027.

[235] H. Ilkhani, T. Hughes, J. Li, C. J. Zhong, and M. Hepel, “Nanostructured SERS-electrochemical biosensors for testing of anticancer drug interactions with DNA,” *Biosens Bioelectron*, vol. 80, pp. 257–264, Jun. 2016, doi: 10.1016/J.BIOS.2016.01.068.

[236] M. Meneghello, E. Papadopoulou, P. Ugo, and P. N. Bartlett, “Using Electrochemical SERS to Measure the Redox Potential of Drug Molecules Bound to dsDNA—a Study of Mitoxantrone,” *Electrochim Acta*, vol. 187, pp. 684–692, Jan. 2016, doi: 10.1016/J.ELECTACTA.2015.11.121.

[237] “NOVA | Metrohm.” Accessed: Jan. 31, 2024. [Online]. Available: https://www.metrohm.com/en/service/software-center/nova.html

[238] J. Kang and P. A. Rowntree, “Gold film surface preparation for self-assembled monolayer studies,” *Langmuir*, vol. 23, no. 2, pp. 509–516, Jan. 2007, doi: 10.1021/LA0518804/ASSET/IMAGES/LARGE/LA0518804F00006.JPEG.

[239] M. F. M. Noh and I. E. Tothill, “Development and characterisation of disposable gold electrodes, and their use for lead(II) analysis,” *Anal Bioanal Chem*, vol. 386, no. 7–8, pp. 2095–2106, Dec. 2006, doi: 10.1007/S00216-006-0904-5/FIGURES/7.

[240] L. M. Fischer *et al.*, “Gold cleaning methods for electrochemical detection applications,” *Microelectron Eng*, vol. 86, no. 4–6, pp. 1282–1285, Apr. 2009, doi: 10.1016/J.MEE.2008.11.045.

[241] P. Senthil Kumar, I. Pastoriza-Santos, B. Rodríguez-González, F. Javier García De Abajo, and L. M. Liz-Marzán, “High-yield synthesis and optical response of gold nanostars,” *Nanotechnology*, vol. 19, no. 1, p. 015606, Nov. 2007, doi: 10.1088/0957-4484/19/01/015606.

[242] L. Scarabelli, A. Sánchez-Iglesias, J. Pérez-Juste, and L. M. Liz-Marzán, “A ‘Tips and Tricks’ Practical Guide to the Synthesis of Gold Nanorods,” *Journal of Physical Chemistry Letters*, vol. 6, no. 21, pp. 4270–4279, Nov. 2015, doi: 10.1021/ACS.JPCLETT.5B02123/SUPPL_FILE/JZ5B02123_LIVESLIDES.MP4.

[243] A. R. Bizzarri, I. Moscetti, and S. Cannistraro, “Surface enhanced Raman spectroscopy based immunosensor for ultrasensitive and selective detection of wild type p53 and mutant p53R175H,” *Anal Chim Acta*, vol. 1029, pp. 86–96, Oct. 2018, doi: 10.1016/J.ACA.2018.04.049.

[244] X. Hu, A. Guiseppi-Elie, and C. Z. Dinu, “Biomolecular interfaces based on self-assembly and self-recognition form biosensors capable of recording molecular binding and release,” *Nanoscale*, vol. 11, no. 11, pp. 4987–4998, Mar. 2019, doi: 10.1039/C8NR10090J.

[245] F. T. C. Moreira, S. Sharma, R. A. F. Dutra, J. P. C. Noronha, A. E. G. Cass, and M. G. F. Sales, “Protein-responsive polymers for point-of-care detection of cardiac biomarker,” *Sens Actuators B Chem*, vol. 196, pp. 123–132, Jun. 2014, doi: 10.1016/J.SNB.2014.01.038.

[246] F. T. C. Moreira, R. A. F. Dutra, J. P. Noronha, and M. G. F. Sales, “Novel sensory surface for creatine kinase electrochemical detection,” *Biosens Bioelectron*, vol. 56, pp. 217–222, Jun. 2014, doi: 10.1016/J.BIOS.2013.12.052.

[247] F. A. Engler *et al.*, "'Catch-and-Release' Anti-Carcinoembryonic Antigen Monoclonal Antibody Leads to Greater Plasma and Tumor Exposure in a Mouse Model of Colorectal Cancer," *Journal of Pharmacology and Experimental Therapeutics*, vol. 366, no. 1, pp. 205–219, Jul. 2018, doi: 10.1124/JPET.117.246900.

[248] N. S. Ferreira and M. G. F. Sales, "Disposable immunosensor using a simple method for oriented antibody immobilization for label-free real-time detection of an oxidative stress biomarker implicated in cancer diseases," *Biosens Bioelectron*, vol. 53, pp. 193–199, Mar. 2014, doi: 10.1016/J.BIOS.2013.09.056.

[249] J. T. Andersen *et al.*, "Anti-carcinoembryonic antigen single-chain variable fragment antibody variants bind mouse and human neonatal Fc receptor with different affinities that reveal distinct cross-species differences in serum half-life," *Journal of Biological Chemistry*, vol. 287, no. 27, pp. 22927–22937, Jun. 2012, doi: 10.1074/jbc.M112.355131.

[250] N. Laborla *et al.*, "Amperometric immunosensor for carcinoembryonic antigen in colon cancer samples based on monolayers of dendritic bipodal scaffolds," *Anal Chem*, vol. 82, no. 5, pp. 1712–1719, Mar. 2010, doi: 10.1021/AC902162E/ASSET/IMAGES/LARGE/AC-2009-02162E_0010.JPEG.

[251] G. S. Bumbrah and R. M. Sharma, "Raman spectroscopy – Basic principle, instrumentation and selected applications for the characterization of drugs of abuse," *Egypt J Forensic Sci*, vol. 6, no. 3, pp. 209–215, Sep. 2016, doi: 10.1016/J.EJFS.2015.06.001.

[252] F. Domenici, A. R. Bizzarri, and S. Cannistraro, "SERS-based nanobiosensing for ultrasensitive detection of the P53 tumor suppressor," *Int J Nanomedicine*, vol. 6, pp. 2033–2042, 2011, doi: 10.2147/IJN.S23845.

[253] "Infrared and Raman Characteristic Group Frequencies: Tables and Charts - George Socrates - Google Books." Accessed: Aug. 30, 2023. [Online]. Available: https://books.google.pt/books?hl=en&lr=&id=LDoAAjMn-wEIC&oi=fnd&pg=PR17&ots=Cq8ZV0OzbM&sig=5zzlgmt-mWm1cqP-m_APvL0J7BM&redir_esc=y#v=onepage&q&f=false

[254] M. R. Krumholz *et al.*, "Preparation and characterization of Ag-nanostars@Au-nanowires hierarchical nanostructures for highly sensitive surface enhanced Raman spectroscopy," *Nano Express*, vol. 1, no. 2, p. 020006, Jul. 2020, doi: 10.1088/2632-959X/ABA104.

[255] A. J. S. Ahammad, M. M. Rahman, G. R. Xu, S. Kim, and J. J. Lee, "Highly sensitive and simultaneous determination of hydroquinone and catechol at poly(thionine) modified glassy carbon electrode," *Electrochim Acta*, vol. 56, no. 14, pp. 5266–5271, May 2011, doi: 10.1016/J.ELECTACTA.2011.03.004.

[256] N. Baig and T. A. Saleh, "Electrodes modified with 3D graphene composites: a review on methods for preparation, properties and sensing applications," vol. 185, no. 6, p. 283, doi: 10.1007/s00604-018-2809-3.

[257] V. Katic *et al.*, "3D Printed Graphene Electrodes Modified with Prussian Blue: Emerging Electrochemical Sensing Platform for Peroxide Detection," *ACS Appl Mater Interfaces*, vol. 11, no. 38,

pp. 35068–35078, Sep. 2019, doi: 10.1021/ACSAMI.9B09305/ASSET/IMAGES/LARGE/AM9B09305_0007.JPEG.

[258] E. Demir, H. Silah, and B. Uslu, “Phthalocyanine Modified Electrodes in Electrochemical Analysis,” *Crit Rev Anal Chem*, vol. 0, no. 0, pp. 1–37, Sep. 2020, doi: 10.1080/10408347.2020.1806702.

[259] D. P. Santos, M. V. B. Zanoni, M. F. Bergamini, A. M. Chiorcea-Paquim, V. C. Diculescu, and A. M. Oliveira Brett, “Poly(glutamic acid) nanofibre modified glassy carbon electrode: Characterization by atomic force microscopy, voltammetry and electrochemical impedance,” *Electrochim Acta*, vol. 53, no. 11, pp. 3991–4000, Apr. 2008, doi: 10.1016/J.ELECTACTA.2007.08.072.

[260] A. Özcan, S. İlkbaş, and A. Atılır Özcan, “Development of a disposable and low-cost electrochemical sensor for dopamine detection based on poly(pyrrole-3-carboxylic acid)-modified electrochemically over-oxidized pencil graphite electrode,” vol. 165, pp. 489–495, doi: 10.1016/j.talanta.2017.01.007.

[261] C. Pérez-Ràfols, N. Serrano, J. Manuel Díaz-Cruz, C. Ariño, and M. Esteban, “Penicillamine-modified sensor for the voltammetric determination of Cd(II) and Pb(II) ions in natural samples,” vol. 144, pp. 569–573, doi: 10.1016/j.talanta.2015.06.083.

[262] A. Benvidi, M. Banaei, M. D. Tezerjani, H. Molahosseini, and S. Jahanbani, “Impedimetric PSA aptasensor based on the use of a glassy carbon electrode modified with titanium oxide nanoparticles and silk fibroin nanofibers,” vol. 185, no. 1, p. 50, doi: 10.1007/s00604-017-2589-1.

[263] T. A. S. L. De Sousa *et al.*, “Thionine Self-Assembled Structures on Graphene: Formation, Organization, and Doping,” *Langmuir*, vol. 34, no. 23, pp. 6903–6911, Jun. 2018, doi: 10.1021/ACS.LANGMUIR.8B00506/ASSET/IMAGES/LARGE/LA-2018-005066_0009.JPEG.

[264] E. Dempsey, D. Diamond, and A. Collier, “Development of a biosensor for endocrine disrupting compounds based on tyrosinase entrapped within a poly(thionine) film,” vol. 20, no. 2, pp. 367–377, doi: 10.1016/j.bios.2004.02.007.

[265] R. Yang, C. Ruan, W. Dai, J. Deng, and J. Kong, “Electropolymerization of thionine in neutral aqueous media and H2O2 biosensor based on poly(thionine),” vol. 44, no. 10, pp. 1585–1596, doi: 10.1016/S0013-4686(98)00283-7.

[266] E. Topçu and M. Alanyalioğlu, “Electrochemical formation of poly(thionine) thin films: The effect of amine group on the polymeric film formation of phenothiazine dyes,” *J Appl Polym Sci*, vol. 131, no. 1, p. 39686, Jan. 2014, doi: 10.1002/APP.39686.

[267] V. Ferreira, A. Tenreiro, and L. M. Abrantes, “Electrochemical, microgravimetric and AFM studies of polythionine films: Application as new support for the immobilisation of nucleotides,” *Sens Actuators B Chem*, vol. 119, no. 2, pp. 632–641, Dec. 2006, doi: 10.1016/J.SNB.2006.01.024.

[268] Q. Gao, X. Cui, F. Yang, Y. Ma, and X. Yang, “Preparation of poly(thionine) modified screen-printed carbon electrode and its application to determine NADH in flow injection analysis system,” *Biosens Bioelectron*, vol. 19, no. 3, pp. 277–282, Nov. 2003, doi: 10.1016/S0956-5663(03)00212-4.

[269] Y. Romaguera-Barcelay, J. Agostinho Moreira, G. González-Aguilar, A. Almeida, J. P. Araujo, and J. Pérez De La Cruz, “Synthesis of orthorhombic rare-earth manganite thin films by a novel chemical solution route,” *J Electroceram*, vol. 26, no. 1–4, pp. 44–55, Jun. 2011, doi: 10.1007/S10832-010-9626-3/FIGURES/8.

[270] M. E. Ghica and C. M. A. Brett, “Poly(brilliant green) and poly(thionine) modified carbon nanotube coated carbon film electrodes for glucose and uric acid biosensors,” vol. 130, pp. 198–206, doi: 10.1016/j.talanta.2014.06.068.

[271] R. Li, L. Cao, C. Liang, S. Sun, H. Liu, and P. Yan, “Development and modeling of an ultrasensitive label-free electrochemical immunosensor for okadaic acid based on polythionine-modified three-dimensional gold nanoelectrode ensembles,” vol. 26, no. 9, pp. 4661–4670, doi: 10.1007/s11581-020-03599-1.

[272] A. Blacha-Grzechnik, K. Piwowar, P. Zassowski, R. Motyka, and J. Zak, “In-situ Raman spectroelectrochemical studies on thionine layer electrochemically grafted to the gold surface,” vol. 245, pp. 902–911, doi: 10.1016/j.electacta.2017.05.132.

[273] Z. Chen, X. Liu, D. Liu, F. Li, L. Wang, and S. Liu, “Ultrasensitive Electrochemical DNA Biosensor Fabrication by Coupling an Integral Multifunctional Zirconia-Reduced Graphene Oxide-Thionine Nanocomposite and Exonuclease I-Assisted Cleavage,” vol. 8, doi: 10.3389/fchem.2020.00521.

[274] Q. Zhou, G. Li, Y. Zhang, M. Zhu, Y. Wan, and Y. Shen, “Highly Selective and Sensitive Electrochemical Immunoassay of Cry1C Using Nanobody and π–π Stacked Graphene Oxide/Thionine Assembly,” vol. 88, no. 19, pp. 9830–9836, doi: 10.1021/acs.analchem.6b02945.

[275] K. Hutchinson, R. E. Hester, W. J. Albery, and A. R. Hillman, “Raman spectroscopic studies of a thionine-modified electrode,” vol. 80, no. 8, pp. 2053–2071, doi: 10.1039/F19848002053.

[276] M. E. Yu, B. S. Cheong, and H. G. Cho, “SERS Spectroscopy and DFT Studies of Thionine and its Derivatives Adsorbed on Silver Colloids: Which N Atom is Used for Coordination of a Phenothiazine-Based Natural Dye to Electron-Deficient Metal Surface?,” *Bull Korean Chem Soc*, vol. 38, no. 8, pp. 928–934, Aug. 2017, doi: 10.1002/BKCS.11205.

[277] R. Mažeikienė, G. Niaura, O. Eicher-Lorka, and A. Malinauskas, “Raman spectroelectrochemical study of Toluidine Blue, adsorbed and electropolymerized at a gold electrode,” vol. 47, no. 2, pp. 105–112, doi: 10.1016/j.vibspec.2008.02.018.

[278] Y. C. Cao, Z. Wang, X. Jin, X. F. Hua, M. X. Liu, and Y. Di Zhao, “Preparation of Au nanoparticles-coated polystyrene beads and its application in protein immobilization,” *Colloids Surf A Physicochem Eng Asp*, vol. 334, no. 1–3, pp. 53–58, Feb. 2009, doi: 10.1016/J.COLSURFA.2008.10.002.

[279] J. S. Han and G. S. An, “Preparation of Dual-Layered Core–Shell Fe3O4@SiO2 Nanoparticles and Their Properties of Plasmid DNA Purification,” *Nanomaterials 2021, Vol. 11, Page 3422*, vol. 11, no. 12, p. 3422, Dec. 2021, doi: 10.3390/NANO11123422.

[280] J. Lin *et al.*, “Crystal-Amorphous Core-Shell Structure Synergistically Enabling TiO2 Nanoparticles’ Remarkable SERS Sensitivity for Cancer Cell Imaging,” *ACS Appl Mater Interfaces*, vol.

12, no. 4, pp. 4204–4211, Jan. 2020, doi: 10.1021/ACSAMI.9B17150/ASSET/IMAGES/LARGE/AM9B17150_0006.JPEG.

[281] S. bin Lee, S. M. Paek, and J. M. Oh, “Porous Hybrids Structure between Silver Nanoparticle and Layered Double Hydroxide for Surface-Enhanced Raman Spectroscopy,” *Nanomaterials*, vol. 11, no. 2, pp. 1–15, Feb. 2021, doi: 10.3390/NANO11020447.

[282] J. Chen, R. Zhang, L. Han, B. Tu, and D. Zhao, “One-pot synthesis of thermally stable gold@mesoporous silica core-shell nanospheres with catalytic activity,” *Nano Research 2013 6:12*, vol. 6, no. 12, pp. 871–879, Sep. 2013, doi: 10.1007/S12274-013-0363-1.

[283] Y. Wang, B. Yan, and L. Chen, “{SERS} Tags: Novel Optical Nanoprobes for Bioanalysis,” vol. 113, no. 3, pp. 1391–1428, doi: 10.1021/cr300120g.

[284] Z. Gao, N. D. Burrows, N. A. Valley, G. C. Schatz, C. J. Murphy, and C. L. Haynes, “In solution SERS sensing using mesoporous silica-coated gold nanorods,” *Analyst*, vol. 141, no. 17, pp. 5088–5095, Aug. 2016, doi: 10.1039/C6AN01159D.

[285] A. Mariño-Lopez *et al.*, “Microporous Plasmonic Capsules as Stable Molecular Sieves for Direct {SERS} Quantification of Small Pollutants in Natural Waters,” vol. 5, no. 1, pp. 46–50, doi: 10.1002/cnma.201800355.

[286] S. Shim, X. H. Pham, M. G. Cha, Y. S. Lee, D. H. Jeong, and B. H. Jun, “Size effect of gold on Ag-coated Au nanoparticle-embedded silica nanospheres,” *RSC Adv*, vol. 6, no. 54, pp. 48644–48650, May 2016, doi: 10.1039/C6RA04296A.

[287] M. Żygieło, P. Piotrowski, M. Witkowski, G. Cichowicz, J. Szczytko, and A. Królikowska, “Reduced Self-Aggregation and Improved Stability of Silica-Coated Fe3O4/Ag SERS-Active Nanotags Functionalized With 2-Mercaptoethanesulfonate,” *Front Chem*, vol. 9, p. 448, Jun. 2021, doi: 10.3389/FCHEM.2021.697595/BIBTEX.

[288] C. Gao *et al.*, “Highly Stable Silver Nanoplates for Surface Plasmon Resonance Biosensing,” *Angewandte Chemie International Edition*, vol. 51, no. 23, pp. 5629–5633, Jun. 2012, doi: 10.1002/ANIE.201108971.

[289] M. Zhao *et al.*, “Silica Cladding of Ag Nanoparticles for High Stability and Surface-Enhanced Raman Spectroscopy Performance,” vol. 11, no. 1, p. 403, doi: 10.1186/s11671-016-1604-5.

[290] J. E. S. van der Hoeven, H. Gurunarayanan, M. Bransen, D. A. M. de Winter, P. E. de Jongh, and A. van Blaaderen, “Silica-Coated Gold Nanorod Supraparticles: A Tunable Platform for Surface Enhanced Raman Spectroscopy,” *Adv Funct Mater*, p. 2200148, 2022, doi: 10.1002/ADFM.202200148.

[291] D. Lupa, M. Oćwieja, N. Piergies, A. Baliś, C. Paluszkiewicz, and Z. Adamczyk, “Gold nanoparticles deposited on silica microparticles - Electrokinetic characteristics and application in SERS,” *Colloid Interface Sci Commun*, vol. 33, p. 100219, Nov. 2019, doi: 10.1016/J.COLCOM.2019.100219.

[292] Z. Pan *et al.*, “Au@Ag nanoparticle sensor for sensitive and rapid detection of glucose,” vol. 45, no. 6, pp. 3059–3066, doi: 10.1039/D0NJ04489J.

[293] N. Alizadeh and A. Salimi, “Ultrasensitive Bioaffinity Electrochemical Sensors: Advances and New Perspectives,” *Electroanalysis*, vol. 30, no. 12, pp. 2803–2840, Dec. 2018, doi: 10.1002/ELAN.201800598.

[294] X. Guo, J. Li, M. Arabi, X. Wang, Y. Wang, and L. Chen, “Molecular-Imprinting-Based Surface-Enhanced Raman Scattering Sensors,” vol. 5, no. 3, pp. 601–619, doi: 10.1021/acssensors.9b02039.

[295] M. C. C. G. Carneiro, A. Sousa-Castillo, M. A. Correa-Duarte, and M. G. F. Sales, “Dual biorecognition by combining molecularly-imprinted polymer and antibody in SERS detection. Application to carcinoembryonic antigen,” *Biosens Bioelectron*, vol. 146, p. 111761, Dec. 2019, doi: 10.1016/J.BIOS.2019.111761.

[296] S. Kostrewa, M. Emgenbroich, D. Klockow, and G. Wulff, “Surface-Enhanced Raman Scattering on Molecularly Imprinted Polymers in Water,” vol. 204, no. 3, pp. 481–487, doi: 10.1002/macp.200390015.

[297] Y. Guo, L. Kang, S. Chen, and X. Li, “High performance surface-enhanced Raman scattering from molecular imprinting polymer capsulated silver spheres.”, doi: 10.1039/c5cp00206k.

[298] Y. Lv, Y. Qin, F. Svec, and T. Tan, “Molecularly imprinted plasmonic nanosensor for selective {SERS} detection of protein biomarkers,” vol. 80, pp. 433–441, doi: 10.1016/j.bios.2016.01.092.

[299] H. Li *et al.*, “A polydopamine-based molecularly imprinted polymer on nanoparticles of type {SiO}2@{rGO}@Ag for the detection of λ-cyhalothrin via {SERS},” vol. 185, no. 3, p. 193, doi: 10.1007/s00604-017-2604-6.

[300] P. Liu, R. Liu, G. Guan, C. Jiang, S. Wang, and Z. Zhang, “Surface-enhanced Raman scattering sensor for theophylline determination by molecular imprinting on silver nanoparticles,” vol. 136, no. 20, pp. 4152–4158, doi: 10.1039/c1an15318h.

[301] T. Shahar, T. Sicron, and D. Mandler, “Nanosphere molecularly imprinted polymers doped with gold nanoparticles for high selectivity molecular sensors,” vol. 10, no. 3, pp. 1056–1063, doi: 10.1007/s12274-016-1366-5.

[302] X. Tu *et al.*, “Molecularly Imprinted Polymer-Based Plasmonic Immunosandwich Assay for Fast and Ultrasensitive Determination of Trace Glycoproteins in Complex Samples,” vol. 88, no. 24, pp. 12363–12370, doi: 10.1021/acs.analchem.6b03597.

[303] I. Ragheb *et al.*, “Surface Enhanced Raman Scattering on Regular Arrays of Gold Nanostructures: Impact of Long-Range Interactions and the Surrounding Medium,” vol. 10, no. 11, p. 2201, doi: 10.3390/nano10112201.

[304] Z. Gu *et al.*, “Surface enhanced Raman scattering of molecules related to highly ordered gold cavities,” *Journal of Raman Spectroscopy*, vol. 44, no. 12, pp. 1682–1688, Dec. 2013, doi: 10.1002/JRS.4384.

[305] M. Gao *et al.*, “Recent Advances and Future Trends in the Detection of Contaminants by Molecularly Imprinted Polymers in Food Samples,” *Front Chem*, vol. 8, p. 1142, Dec. 2020, doi: 10.3389/FCHEM.2020.616326/BIBTEX.

[306] P. Rebelo *et al.*, “Molecularly imprinted polymer-based electrochemical sensors for environmental analysis,” *Biosens Bioelectron*, vol. 172, p. 112719, Jan. 2021, doi: 10.1016/J.BIOS.2020.112719.

[307] Q. Huang *et al.*, “Molecularly imprinted poly(thionine)-based electrochemical sensing platform for fast and selective ultratrace determination of patulin,” *Anal Chem*, vol. 91, no. 6, pp. 4116–4123, Mar. 2019, doi: 10.1021/ACS.ANALCHEM.8B05791/ASSET/IMAGES/LARGE/AC-2018-05791Y_0006.JPEG.

[308] Z. Jahromi, M. Afzali, A. Mostafavi, R. Nekooie, and M. Mohamadi, “Electropolymerization of thionine as a stable film along with carbon nanotube for sensitive detection of tetracycline antibiotic drug,” *Iranian Polymer Journal (English Edition)*, vol. 29, no. 3, pp. 241–251, Mar. 2020, doi: 10.1007/S13726-020-00788-7/TABLES/3.

[309] W. D. Hazelton and E. G. Luebeck, “Biomarker-based early cancer detection: is it achievable?,” *Sci Transl Med*, vol. 3, no. 109, p. 109fs9, Nov. 2011, doi: 10.1126/scitranslmed.3003272.

[310] K. Baryeh, S. Takalkar, M. Lund, and G. Liu, “Development of quantitative immunochromatographic assay for rapid and sensitive detection of carbohydrate antigen 19-9 (CA 19-9) in human plasma,” *J Pharm Biomed Anal*, vol. 146, pp. 285–291, Nov. 2017, doi: 10.1016/j.jpba.2017.09.004.

[311] U. K. Ballehaninna and R. S. Chamberlain, “Serum CA 19-9 as a Biomarker for Pancreatic Cancer—A Comprehensive Review,” *Indian J Surg Oncol*, vol. 2, no. 2, pp. 88–100, Jun. 2011, doi: 10.1007/s13193-011-0042-1.

[312] N. A. Alarfaj, M. F. El-Tohamy, and H. F. Oraby, “CA 19-9 Pancreatic Tumor Marker Fluorescence Immunosensing Detection via Immobilized Carbon Quantum Dots Conjugated Gold Nanocomposite,” *Int J Mol Sci*, vol. 19, no. 4, Apr. 2018, doi: 10.3390/ijms19041162.

[313] R. Passerini *et al.*, “The Pitfalls of CA19-9: Routine Testing and Comparison of Two Automated Immunoassays in a Reference Oncology Center,” *Am J Clin Pathol*, vol. 138, no. 2, pp. 281–287, 2012, doi: 10.1309/AJCPOPNPLLCYR07H.

[314] D. Du, F. Yan, S. Liu, and H. Ju, “Immunological assay for carbohydrate antigen 19-9 using an electrochemical immunosensor and antigen immobilization in titania sol–gel matrix,” *J Immunol Methods*, vol. 283, no. 1, pp. 67–75, 2003, doi: 10.1016/j.jim.2003.08.014.

[315] M. L. Yola and N. Atar, “Carbohydrate antigen 19-9 electrochemical immunosensor based on 1D-MoS2 nanorods/LiNb3O8 and polyoxometalate-incorporated gold nanoparticles,” *Microchemical Journal*, vol. 170, p. 106643, Nov. 2021, doi: 10.1016/j.microc.2021.106643.

[316] Z. Huang *et al.*, “Simple and effective label-free electrochemical immunoassay for carbohydrate antigen 19-9 based on polythionine-Au composites as enhanced sensing signals for detecting different clinical samples,” *Int J Nanomedicine*, vol. 12, pp. 3049–3058, Apr. 2017, doi: 10.2147/IJN.S131805.

[317] B. MM, “A rapid and sensitive method for the quantitation of microgram quantities of protein utilizing the principle of protein-dye binding,” *Anal Biochem*, vol. 72, no. 1–2, pp. 248–254, May 1976, doi: 10.1006/ABIO.1976.9999.

[318] K. S. Shalini Devi, N. Anusha, S. Raja, and A. Senthil Kumar, “A New Strategy for Direct Electrochemical Sensing of a Organophosphorus Pesticide, Triazophos, Using a Coomassie Brilliant-Blue Dye Surface-Confined Carbon-Black-Nanoparticle-Modified Electrode,” *ACS Appl Nano Mater*, vol. 1, no. 8, pp. 4110–4119, Aug. 2018, doi: 10.1021/ACSANM.8B00861/ASSET/IMAGES/LARGE/AN-2018-00861K_0002.JPEG.

[319] P. S. Ganesh and B. E. Kumara Swamy, “Simultaneous electroanalysis of hydroquinone and catechol at poly(brilliant blue) modified carbon paste electrode: A voltammetric study,” *Journal of Electroanalytical Chemistry*, vol. 756, pp. 193–200, Nov. 2015, doi: 10.1016/J.JELECHEM.2015.08.027.

[320] K. Dodo, K. Fujita, and M. Sodeoka, “Raman Spectroscopy for Chemical Biology Research,” *J Am Chem Soc*, vol. 144, no. 43, pp. 19651–19667, Nov. 2022, doi: 10.1021/JACS.2C05359/ASSET/IMAGES/LARGE/JA2C05359_0008.JPEG.

[321] Y. Castaño-Guerrero, Y. Romaguera-Barcelay, F. T. C. Moreira, W. R. Brito, E. Fortunato, and M. G. F. Sales, “Poly(Thionine)-Modified Screen-Printed Electrodes for CA 19-9 Detection and Its Properties in Raman Spectroscopy,” *Chemosensors*, vol. 10, no. 3, p. 92, Mar. 2022, doi: 10.3390/CHEMOSENSORS10030092/S1.

[322] D. L. Franco *et al.*, “Electropolymerization of 3-aminophenol on carbon graphite surface: Electric and morphologic properties,” *Mater Chem Phys*, vol. 107, no. 2–3, pp. 404–409, Feb. 2008, doi: 10.1016/J.MATCHEMPHYS.2007.08.006.

[323] M. Yuqing, C. Jianrong, and W. Xiaohua, “Using electropolymerized non-conducting polymers to develop enzyme amperometric biosensors,” *Trends Biotechnol*, vol. 22, no. 5, pp. 227–231, May 2004, doi: 10.1016/J.TIBTECH.2004.03.004.

[324] C. Ö. Dinç, S. Yalçınkaya, H. Altuntaş, and N. Çolak, “Synthesis and characterization of poly(m-aminophenol)-succinat,” 2014, doi: 10.1080/15685551.2014.907617.

[325] H. J. Salavagione, J. Arias, P. Garcés, E. Morallón, C. Barbero, and J. L. Vázquez, “Spectroelectrochemical study of the oxidation of aminophenols on platinum electrode in acid medium,” *Journal of Electroanalytical Chemistry*, vol. 565, no. 2, pp. 375–383, Apr. 2004, doi: 10.1016/J.JELECHEM.2003.11.005.

[326] S. Taj, M. F. Ahmed, and S. Sankarapapavinasam, “Electro-oxidative polymerization of m-aminophenol,” *Synth Met*, vol. 52, no. 2, pp. 147–158, Oct. 1992, doi: 10.1016/0379-6779(92)90303-Z.

[327] Z. Zhang, H. Liu, and J. Deng, “A glucose biosensor based on immobilization of glucose oxidase in electropolymerized o-aminophenol film on platinized glassy carbon electrode,” *Anal Chem*, vol. 68, no. 9, pp. 1632–1638, 1996, doi: 10.1021/AC950431D/ASSET/IMAGES/MEDIUM/AC950431DE00005.GIF.

[328] Y. Nakabayashi and H. Yoshikawa, “Amperometric biosensors for sensing of hydrogen peroxide based on electron transfer between horseradish peroxidase and ferrocene as a mediator,” *Analytical Sciences*, vol. 16, no. 6, pp. 609–613, Jun. 2000, doi: 10.2116/ANALSCI.16.609/METRICS.

[329] Y. Nakabayashi, M. Wakuda, and H. Imai, “Amperometric Glucose Sensors Fabricated by Electrochemical Polymerization of Phenols on Carbon Paste Electrodes Containing Ferrocene as an Electron Transfer Mediator,” *Analytical Sciences*, vol. 14, no. 6, pp. 1069–1076, Dec. 1998, doi: 10.2116/ANALSCI.14.1069/METRICS.

[330] T. Gopalasamy, M. Gopalswamy, M. Gopichand, and J. Raj, “Poly Meta-Aminophenol: Chemical Synthesis, Characterization and Ac Impedance Study,” *J Polym*, vol. 2014, pp. 1–11, Jan. 2014, doi: 10.1155/2014/827043.

[331] D. L. Franco *et al.*, “Electropolymerization of 3-aminophenol on carbon graphite surface: Electric and morphologic properties,” *Mater Chem Phys*, vol. 107, no. 2–3, pp. 404–409, Feb. 2008, doi: 10.1016/J.MATCHEMPHYS.2007.08.006.

[332] K. Chetankumar, B. E. Kumara Swamy, S. C. Sharma, and H. Adarsha, “Coomassie brilliant blue G 250 modified carbon paste electrode sensor for the voltammetric detection of dihydroxybenzene isomers,” *Scientific Reports 2021 11:1*, vol. 11, no. 1, pp. 1–14, Aug. 2021, doi: 10.1038/s41598-021-95347-2.

[333] X. X. Han, Y. Xie, B. Zhao, and Y. Ozaki, “Highly sensitive protein concentration assay over a wide range via surface-enhanced raman scattering of coomassie brilliant blue,” *Anal Chem*, vol. 82, no. 11, pp. 4325–4328, Jun. 2010, doi: 10.1021/AC100596U/SUPPL_FILE/AC100596U_SI_001.PDF.

[334] C. D. Georgiou, K. Grintzalis, G. Zervoudakis, and I. Papapostolou, “Mechanism of Coomassie brilliant blue G-250 binding to proteins: A hydrophobic assay for nanogram quantities of proteins,” *Anal Bioanal Chem*, vol. 391, no. 1, pp. 391–403, May 2008, doi: 10.1007/S00216-008-1996-X/TABLES/2.

[335] E. Brunelle *et al.*, “Coomassie Brilliant Blue G-250 Dye: An Application for Forensic Fingerprint Analysis,” *Anal Chem*, vol. 89, no. 7, pp. 4314–4319, Apr. 2017, doi: 10.1021/ACS.ANALCHEM.7B00510/ASSET/IMAGES/LARGE/AC-2017-00510Y_0003.JPEG.

[336] K. Plakas *et al.*, “Design and evaluation of Raman reporters for the Raman-silent region,” *Nanotheranostics*, vol. 6, no. 1, p. 1, 2022, doi: 10.7150/NTNO.58965.

[337] J. Xu *et al.*, “Unveiling Cancer Metabolism through Spontaneous and Coherent Raman Spectroscopy and Stable Isotope Probing,” *Cancers 2021, Vol. 13, Page 1718*, vol. 13, no. 7, p. 1718, Apr. 2021, doi: 10.3390/CANCERS13071718.

[338] L. Huang, D. W. Sun, Z. Wu, H. Pu, and Q. Wei, “Reproducible, shelf-stable, and bioaffinity SERS nanotags inspired by multivariate polyphenolic chemistry for bacterial identification,” *Anal Chim Acta*, vol. 1167, p. 338570, Jul. 2021, doi: 10.1016/J.ACA.2021.338570.

[339] J. Zheng, Y. Zhou, X. Li, Y. Ji, T. Lu, and R. Gu, “Surface-enhanced Raman scattering of 4-aminothiophenol in assemblies of nanosized particles and the macroscopic surface of silver,” *Langmuir*, vol. 19, no. 3, pp. 632–636, Feb. 2003, doi: 10.1021/LA011706P/ASSET/IMAGES/LARGE/LA011706PF00005.JPEG.

[340] X. Hu, T. Wang, L. Wang, and S. Dong, “Surface-Enhanced Raman Scattering of 4-Aminothiophenol Self-Assembled Monolayers in Sandwich Structure with Nanoparticle Shape

Dependence: Off-Surface Plasmon Resonance Condition," *Journal of Physical Chemistry C*, vol. 111, no. 19, pp. 6962–6969, May 2007, doi: 10.1021/JP0712194.

[341] S. Chen, M. Lv, J. Fan, Y. Huang, G. Liang, and S. Zhang, "Bioorthogonal surface-enhanced Raman scattering flower-like nanoprobe with embedded standards for accurate cancer cell imaging," *Anal Chim Acta*, vol. 1246, p. 340895, Mar. 2023, doi: 10.1016/J.ACA.2023.340895.

[342] N. Bhalla, P. Jolly, N. Formisano, and P. Estrela, "Introduction to biosensors," *Essays Biochem*, vol. 60, no. 1, p. 1, Jun. 2016, doi: 10.1042/EBC20150001.

[343] L. Li, C. Liu, X. Cao, L. Tan, and W. Lu, "Multiplexing determination of cancer-associated biomarkers by surface-enhanced Raman scattering using ordered gold nanohoneycomb arrays," *Bioanalysis*, vol. 9, no. 20, pp. 1561–1572, Oct. 2017, doi: 10.4155/BIO-2016-0237/ASSET/IMAGES/LARGE/FIGURE8.JPEG.

[344] K. M. Koo, E. J. H. Wee, P. N. Mainwaring, Y. Wang, and M. Trau, "Toward Precision Medicine: A Cancer Molecular Subtyping Nano-Strategy for RNA Biomarkers in Tumor and Urine," *Small*, vol. 12, no. 45, pp. 6233–6242, Dec. 2016, doi: 10.1002/SMLL.201602161.

[345] J. Li, F. Liu, C. He, F. Shen, and J. Ye, "Orthogonal gap-enhanced Raman tags for interference-free and ultrastable surface-enhanced Raman scattering," *Nanophotonics*, vol. 11, no. 8, pp. 1549–1560, Mar. 2022, doi: 10.1515/NANOPH-2021-0689/ASSET/GRAPHIC/J_NANOPH-2021-0689_FIG_006.JPG.

[346] X. R. Bai *et al.*, "Accurate Clinical Diagnosis of Liver Cancer Based on Simultaneous Detection of Ternary Specific Antigens by Magnetic Induced Mixing Surface-Enhanced Raman Scattering Emissions," *Anal Chem*, vol. 91, no. 4, pp. 2955–2963, Feb. 2019, doi: 10.1021/ACS.ANALCHEM.8B05153/ASSET/IMAGES/LARGE/AC-2018-05153J_0006.JPEG.

[347] G. Schkolnik, J. Salewski, D. Millo, I. Zebger, S. Franzen, and P. Hildebrandt, "Vibrational Stark Effect of the Electric-Field Reporter 4-Mercaptobenzonitrile as a Tool for Investigating Electrostatics at Electrode/SAM/Solution Interfaces," *International Journal of Molecular Sciences 2012, Vol. 13, Pages 7466-7482*, vol. 13, no. 6, pp. 7466–7482, Jun. 2012, doi: 10.3390/IJMS13067466.

[348] H. Zhang, H. Lai, G. Li, and Y. Hu, "4-Aminothiophenol capped halloysite nanotubes/silver nanoparticles as surface-enhanced Raman scattering probe for in-situ derivatization and selective determination of nitrite ions in meat product," *Talanta*, vol. 220, p. 121366, Dec. 2020, doi: 10.1016/J.TALANTA.2020.121366.

[349] Z. Guo *et al.*, "Chemometrics coupled 4-Aminothiophenol labelled Ag-Au alloy SERS off-signal nanosensor for quantitative detection of mercury in black tea," *Spectrochim Acta A Mol Biomol Spectrosc*, vol. 242, p. 118747, Dec. 2020, doi: 10.1016/J.SAA.2020.118747.

[350] L. Sun, Z. Yu, and M. Lin, "Synthesis of polyhedral gold nanostars as surface-enhanced Raman spectroscopy substrates for measurement of thiram in peach juice," *Analyst*, vol. 144, no. 16, pp. 4820–4825, Aug. 2019, doi: 10.1039/C9AN00687G.

[351] C. Chen, Y. Zhang, X. Wang, X. Qiao, G. I. N. Waterhouse, and Z. Xu, "A core-satellite self-assembled SERS aptasensor containing a 'biological-silent region' Raman tag for the accurate

and ultrasensitive detection of histamine," *Food Science and Human Wellness*, vol. 13, no. 2, pp. 1029–1039, Mar. 2024, doi: 10.26599/FSHW.2022.9250089.

[352] M. Li *et al.*, "Alkyne- and Nitrile-Anchored Gold Nanoparticles for Multiplex SERS Imaging of Biomarkers in Cancer Cells and Tissues," *Nanotheranostics*, vol. 3, no. 1, p. 113, 2019, doi: 10.7150/NTNO.30924.

[353] C. Wang, Y. Han, and X. Li, "Glypican-1 may be a plasma biomarker for predicting the rupture of small intracranial aneurysms.," *J Proteomics*, vol. 293, p. 105060, Feb. 2024, doi: 10.1016/J.JPROT.2023.105060.

[354] T. Yamada, T. Minami, M. Yamada, and Y. Terauchi, "Proposed carbohydrate antigen 19-9 (CA19-9) cut-off values for the detection of pancreatic cancer in patients with poorly controlled diabetes: a real-world study," *Endocr J*, vol. 70, no. 11, pp. 1069–1075, 2023, doi: 10.1507/ENDOCRJ.EJ23-0186.